AFOSR-TR- 89-1051

DTIC FILE COPY

WAES-TR-89-0010

DTIC
S ELECTE AUG 1 0 1989 D
D

AD-A211 406

(2)

Advanced Energy Systems

AN INVESTIGATION OF THE IRRADIATION SWELLING MECHANISMS IN REFRACTORY METALS AT HIGH TEMPERATURES

FINAL SCIENTIFIC REPORT

PREPARED FOR

THE AIR FORCE OFFICE OF SCIENTIFIC RESEARCH (AFSC)

UNDER CONTRACT

F49620-85-C-0060

DISTRIBUTION STATEMENT A
Approved for public release;
Distribution Unlimited

JUNE 1989

Westinghouse Electric Corporation
Advanced Energy Systems
P.O. Box 10864
Pittsburgh, Pennsylvania 15236

89 8 10 056

DISCLAIMER

SECURITY CLASSIFICATION OF THIS PAGE

REPORT DOCUMENTATION PAGE

Form Approved
OMB No. 0704-0188

1a. REPORT SECURITY CLASSIFICATION
UNCLASSIFIED

1b. RESTRICTIVE MARKINGS

2a. SECURITY CLASSIFICATION AUTHORITY

2b. DECLASSIFICATION / DOWNGRADING SCHEDULE

3. DISTRIBUTION / AVAILABILITY OF REPORT
Approved for public release;
distribution is unlimited.

4. PERFORMING ORGANIZATION REPORT NUMBER(S)

5. MONITORING ORGANIZATION REPORT NUMBER(S)
AFOSR-TR- 89-1051

6a. NAME OF PERFORMING ORGANIZATION
Westinghouse Electric Corporation

6b. OFFICE SYMBOL *(If applicable)*

7a. NAME OF MONITORING ORGANIZATION
AFOSR/NP

6c. ADDRESS *(City, State, and ZIP Code)*
Advanced Energy Systems
Pittsburgh, PA 15236

7b. ADDRESS *(City, State, and ZIP Code)*
Building 410, Bolling AFB DC
20332-6448

8a. NAME OF FUNDING / SPONSORING ORGANIZATION
AFOSR

8b. OFFICE SYMBOL *(If applicable)*
NP

9. PROCUREMENT INSTRUMENT IDENTIFICATION NUMBER
F49620-85-C-0060

8c. ADDRESS *(City, State, and ZIP Code)*
Building 410, Bolling AFB DC
20332-6448

10. SOURCE OF FUNDING NUMBERS

PROGRAM ELEMENT NO.	PROJECT NO.	TASK NO.	WORK UNIT ACCESSION NO.
61102F	2301	A7	

11. TITLE *(Include Security Classification)*
(U) AN INVESTIGATION OF THE IRRADIATION SWELLING MECHANISMS IN REFRACTORY METALS AT HIGH TEMPERATURES

12. PERSONAL AUTHOR(S)
R. Bajaj, G. R. Fenske, B. O. Hall, J. C. Greggi, A. T. Taylor

13a. TYPE OF REPORT
Final

13b. TIME COVERED
FROM 3/1/85 TO 7/31/88

14. DATE OF REPORT *(Year, Month, Day)*
June 1989

15. PAGE COUNT
265

16. SUPPLEMENTARY NOTATION

17. COSATI CODES

FIELD	GROUP	SUB-GROUP
	11 02	

18. SUBJECT TERMS *(Continue on reverse if necessary and identify by block number)*
Swelling, irradiation, refractory metals, Niobium plus Nb Alloys, Dislocation Loops, Electron Microscopy

19. ABSTRACT *(Continue on reverse if necessary and identify by block number)*

See Other Side

20. DISTRIBUTION / AVAILABILITY OF ABSTRACT
☒ UNCLASSIFIED/UNLIMITED ☐ SAME AS RPT. ☐ DTIC USERS

21. ABSTRACT SECURITY CLASSIFICATION
UNCLASSIFIED

22a. NAME OF RESPONSIBLE INDIVIDUAL
Bruce L. Smith, Lt Col, USAF

22b. TELEPHONE *(Include Area Code)*
(202) 767-4908

22c. OFFICE SYMBOL
AFOSR/NP

DD Form 1473, JUN 86 *Previous editions are obsolete.* SECURITY CLASSIFICATION OF THIS PAGE

UNCLASSIFIED

19. Abstract (con)

A three-phase study of elevated temperature irradiation swelling in refractory metals was done with an objective of understanding swelling mechanisms and demonstrating practicality of swelling-resistant materials. During the first phase, a theoretical model was developed for the swelling in body-centered cubic (bcc) metals. Niobium was irradiated with Nb++ ions to 50 dpa and swelling was determined by transmission electron microscopy. A peak swelling at 900 degrees C of 7 percent and no swelling above 1300 degrees C was observed. Reasonable agreements were obtained between the experimental and theoretical swelling curve when niobium-oxygen interaction was included. Sink strength ratios were calculated from the data. The theoretical model during the second phase included loop growth/shrinkage in bcc metals. Experiments were performed at 800 degrees C and 1000 degrees C to 0.05 and 5 dpa. High densities of dislocation loops 10 nm in size were observed. Dislocation loops were predominantly interstitial in nature with a Burgers vector of a/2 111 with some vacancy loops. During the third phase, Nb-5Hf and Nb-5W were irradiated at 800 degrees - 1350 degrees C with Nb++ and with Nb++ + He+. Nb-5Hf showed swelling at high temperatures. Nb-5W showed no swelling up to 35 dpa, demonstrating that Nb-5W is a candidate alloy for nuclear reactor high temperature applications.

WAES-TR-89-0010

AN INVESTIGATION OF THE IRRADIATION SWELLING MECHANISMS IN REFRACTORY METALS AT HIGH TEMPERATURES

FINAL SCIENTIFIC REPORT

R. Bajaj
G. R. Fenske
J. C. Greggi
B. O. Hall
A. T. Taylor

APPROVED BY: W. P. Blankenship
W. P. Blankenship, Manager
Materials Science & Engineering

R. W. Buckman, Jr., Manager
Materials & Fuels Technology

C. R. Adkins
C. R. Adkins, Manager
Engineering

Prepared for the Air Force Office of Scientific Research (AFSC)

Under Contract

F49620-85-C-0060

JUNE 1989

Westinghouse Electric Corporation
Advanced Energy Systems
P. O. Box 10864
Pittsburgh, PA 15236-0864

TABLE OF CONTENTS

TABLE OF CONTENTS (Cont.)

TABLE OF CONTENTS (Cont.)

TABLE OF CONTENTS (Cont.)

LIST OF TABLES

LIST OF TABLES

LIST OF FIGURES

LIST OF FIGURES (Continued)

LIST OF FIGURES (Continued)

LIST OF FIGURES (Continued)

LIST OF FIGURES (Continued)

ABSTRACT

This report presents the results of an investigation of elevated temperature irradiation swelling in refractory metals with an objective of understanding swelling mechanisms in these materials and demonstrating practicality of swelling-resistant materials. The study was divided into three phases.

During the first phase, a theoretical model was developed for the swelling in body-centered cubic (bcc) metals. The model was based on chemical reaction rate formalism. Calculations were carried out on a model material, niobium, which was selected for the study. Experimental and theoretical work was conducted to determine the swelling mechanism. Niobium was irradiated with Nb$^{(++)}$ ions to a dose of 50 dpa and swelling was determined by transmission electron microscopy. A peak swelling at 900°C of 7% was observed. No swelling was observed above 1300°C. The experimental data were compared to those predicted by the theoretical model. Reasonable agreements were obtained between the experimental and theoretical swelling curve when niobium-oxygen interaction was included. Sink strength ratios were also calculated from the data.

The theoretical model was extended during the second phase to include loop growth/shrinkage in bcc metals. It was shown that the Little, Bullough, and Wood model was not strictly applicable. The difference in bias of <111> and <100> loops and the high initial dislocation density which decreases with time are not sufficient to explain <111> loop shrinkage. Experiments were carried out at 800° and 1000°C to 0.05 and 5 dpa. Dislocation loops were characterized. High densities, on the order of 10^{16} cm^{-3}, of dislocation loops ≈10 nm in size were observed at both temperatures. Dislocation loops were thoroughly characterized and found to be predominately interstitial in nature with a Burgers vector of $\frac{a}{2}\langle 111\rangle$ with some vacancy loops.

During the third phase of the program, two alloys, Nb-5Hf and Nb-5W, were irradiated with Nb$^{(++)}$ alone and with Nb$^{(++)}$ + He$^{(+)}$ over a temperature range of 800°-1350°C. Nb-5Hf showed swelling only at high temperatures. However, Nb-5W showed no swelling up to 35 dpa. It was thus demonstrated that Nb-5W is a candidate alloy for high temperature applications in a nuclear reactor environment.

Further work to extend both theoretical understanding and experimental verification of swelling resistance to higher doses is recommended for future work.

(AW)

1.0 INTRODUCTION

This is the final report of a three phase program on the investigation of swelling mechanisms in refractory metals at high temperature. The report is organized into three sections corresponding to each phase of the work. The Phase I and Phase II reports were published in February 1985 and June 1986 in references 1 and 2, respectively. During the first phase, a theoretical model was developed and a material, niobium, was selected. Experiments were carried out to determine high temperature (up to 0.6 T_m, where T_m = melting point in K) swelling and the model was refined to include effects of interstitial oxygen trapping. A reasonable agreement between the calculated and experimental swelling was obtained. The second phase of the program was devoted to the development of a model for loop growth/shrinkage. Experiments were carried out to investigate low dose microstructural evolution by irradiating niobium at elevated temperatures. Dislocation loop structure was characterized in detail. During the third phase of the program, emphasis was placed on developing swelling resistant compositions of refractory metal alloys based on niobium. Alloys containing hafnium and tungsten additions were irradiated to a high dose with self-ions alone and in combination with helium ions over a wide range of temperatures. This work showed that niobium-tungsten alloy is a highly swelling resistant material up to a temperature of 0.6 T_m. This is a promising material for applications in space nuclear reactors. The work on the extension and refinement of a swelling model developed for pure niobium compared to the alloys was deferred due to funding limitations. In sections 7.0, 8.0, and 9.0 each phase of the investigation is described in detail.

2.0 BACKGROUND

Refractory metals and their alloys offer distinct advantages for applications in nuclear systems where high temperatures are required because they exhibit high elevated temperature strength, better corrosion resistance in liquid metal coolants, and better thermophysical properties than other structural materials. In applications where high temperatures are accompanied by high neutron fluxes, these materials are expected to experience swelling which

which is caused by the agglomeration of irradiation-induced vacancies into cavities and by the production of gaseous transmutation products such as helium. Unfortunately swelling data for these materials are limited, also current theoretical treatments of swelling are not directly applicable to refractory metals since they were developed for face-centered cubic (fcc) rather than body-centered cubic (bcc) materials.

Recognizing the need for a mechanistic swelling model applicable to refractory metals, a three phase research program was developed with the objective of achieving an understanding of the swelling phenomenon that would apply to all bcc metals. This program builds upon the understanding of swelling in fcc materials, which have been studied extensively since the first discovery of voids in stainless steel, and also on the available swelling information for refractory metals and their alloys.

In the experimental area, this program adopts the techniques of self-ion irradiations developed for austenitic, iron, and nickel based alloys. This report summarizes the available literature on refractory metal swelling, details the development of the theoretical model and the experimental techniques and presents the experimental data generated on swelling and microstructure evolution in pure niobium at high and low displacement doses and in two alloys of niobium containing additions of hafnium and tungsten. The results of incorporating the data into the theoretical model are given and recommendations are made for future work.

3.0 PROGRAM OBJECTIVE

The primary objective of this program is to further the understanding of high temperature (from $0.3\ T_m$ - $0.6\ T_m$) cavity swelling and microstructural response of refractory metals to neutron irradiation. The ultimate goal is to acquire a theoretical understanding of swelling and through this to demonstrate the practicality of a low swelling alloy for elevated temperature service. This goal will be achieved by a close coupling of theory development and controlled experimental studies. The neutron-induced swelling was simulated by single and dual ion irradiations with self-ions, and self-ions plus helium, respectively.

4.0 SIMULATION TECHNIQUES

Over the last fifteen years, techniques have been developed for simulating neutron irradiation damage in small, transmission electron microscopy (TEM) size specimens. These techniques have been developed to a high degree of sophistication(3-7) and have been proven to be very useful in alloy design and modeling of microstructural evolution and swelling. Simulation techniques offer several advantages over in-reactor irradiations:

(a) They can be performed ex-reactor. Heavy ion bombardment is used to produce the simulated neutron damage. Ion bombardment can be performed at a number of accelerator facilities around the country.

(b) Irradiation times for a specific dose are three to four orders of magnitude shorter.

(c) Irradiation variables such as dose rate, temperature, helium to displacement per atom ratio (He/dpa) can be varied in a controlled manner.

(d) The technique is significantly less expensive than in-reactor irradiations.

(e) The irradiated specimens are not radioactive.

The versatility of the simulation method is of major importance in the type of work proposed here since a wide variation in irradiation conditions can be achieved and can be tailored to investigate specific aspects of theoretical models.

An important modification to the heavy ion bombardment technique is the use of self-ions. Although difficult to accomplish for refractory metals, the use of self-ions prevents the possibility of chemical interactions which might influence swelling behavior.

A second modification proposed in this work is the simultaneous bombardment of the specimens with self-ions and helium. In earlier work, the specimens were pre-injected with helium to simulate the transmutation-produced gas. More recently it was realized that nucleation of cavities and subsequent microstructural evolution in pre-injected specimens differ significantly from that in specimens under simultaneous bombardment.

In this work, the displacement damage produced by the energetic neutrons is simulated by high energy (5-6 MeV) self-ions, and the transmutation produced helium is simulated by irradiating the specimen simultaneously with a beam of high energy self-ions and a beam of helium ions. The energy of the latter is adjusted so that the displacement damage and the deposition of helium occur in the same location in the specimen.

5.0 REVIEW OF IRRADIATION TESTS ON REFRACTORY METALS

The refractory alloy systems are based on vanadium, niobium, molybdenum, tantalum, and tungsten. Swelling in these metals has received much less attention than in the austenitic materials, although some attention has been given to these metals because of their potential use in fusion reactors. Most of the studies have been limited to relatively low temperatures and the information in the range of 0.4-0.6 T_m is scant. The other drawbacks of these studies are that they deal with existing alloys or metals of uncontrolled purity and the ion irradiation studies utilized heavy ions of foreign metal (e.g., Ni in V, Ta in Mo) rather than self-ions. This latter factor clouds the results of these studies since foreign atoms are deposited in the damage region introducing microstructural features, such as precipitates, which would not be present in a neutron irradiation. Dual-ion irradiation data of refractory metals are very limited. In the following section, high temperature ion and neutron swelling results of Mo, Nb, V, Ta, and W and their alloys are presented. Earlier studies on helium pre-injected or uninjected specimens are also included.

5.1 Vanadium

High purity vanadium was neutron irradiated by Weber et al.(8) at temperatures from 600° to 750°C (0.4 to 0.46 T_m) to damage levels from 1 to 5 dpa. Voids and precipitates of vanadium carbide, VC, were observed. The voids increased in size and decreased in density with increasing temperature. At the peak swelling temperature of 650°C, a swelling of 2.5% was observed at 5 dpa. It was recommended that carbon contamination be minimized to avoid VC precipitation.

Agarwal and Taylor(9) irradiated high purity vanadium with vanadium ions at 650° and 700°C to 55 dpa and found the swelling fraction increased at first, attained a maximum (2% at 34 dpa), and decreased with increasing dose. The reduced swelling was explained on the basis of a change in bias due to precipitates requiring excess vacancies for accommodation. The effects of interstitial impurities were very significant in the study of vanadium.

In another study (on self-ion irradiated, pre-injected vanadium), Agarwal et al.(10), showed that nitrogen was most effective in controlling swelling with carbon and oxygen showing smaller effects. Fine precipitation was observed in specimens doped with C and O. The observations were analyzed in terms of solute segregation theory.

Santhanam et al.(11) investigated the effects of impurities and pre-injected helium content (10 and 100 ppm) on swelling of high purity and commercial vanadium ion-irradiated with Ni ions at temperatures from 650°-850°C (0.42 T_m to 0.51 T_m) to ≈60 dpa. A maximum void swelling of 3.5% was observed in commercial purity vanadium containing 10 appm He. The voids were cubic and their concentration was an order of magnitude larger in commercial purity material than high purity material at 650° and 700°C. However, the voids were smaller in the commercial purity material. The peak swelling temperatures (700°C for high purity and 750°C for commercial purity) coincided with the temperature at which precipitates were first observed. The effect of helium was significant only at 750°C (0.46 T_m) where the swelling decreased with increasing helium content. It was postulated that bubbles were formed by prior annealing at 750°C for one hour and acted as predominant sinks and competed with dislocations, thus causing low swelling. Also, it was suggested that helium bubbles were not good void nuclei in vanadium.

Lott et al.(12) investigated the effect of substitutional nickel and interstitial nitrogen on vanadium bombarded with Cu^{+++} ions without the presence of helium at relatively low temperatures of 450° to 650°C (0.26 to 0.34 T_m). Both of these elements reduced swelling in vanadium. It was suggested that the reduction in swelling was caused by precipitation phenomena observed in nickel-doped specimens. The precipitation increased the density of unbiased sinks and enhanced recombination. In the nitrogen-doped specimens, it was speculated that the small black dot (dislocation loop) damage caused the same effects as the precipitates.

In studies of neutron-irradiated vanadium, Bressers and van Witzenberg(13) irradiated single crystal and polycrystalline vanadium at 400°-800°C (0.31 - 0.49 T_m), after doping with 850 appm oxygen, to a fluence of 2.5 x 10^{22} n/cm^2 (E>1 MeV). A maximum swelling of 0.14% was observed in doped polycrystalline material. The effect of interstitial oxygen was greatest in the annealed single crystals and at the higher temperature range. Void lattice formation was not observed in any of the specimens.

Tyler and Goodhew(14) conducted annealing studies on helium pre-implanted vanadium, to study the bubble growth mechanism. Isothermal anneals were conducted for times up to 100 h at 950°C. Bubbles produced during annealing were faceted. It was concluded that the growth of bubbles occurred by migration and coalescence. The rate limiting parameter was impurity sensitive nucleation of atomic ledges on the bubble facets.

The alloys of vanadium were evaluated in both the U.S. and West Germany as candidate cladding materials for LMFBRs, and are currently being evaluated for use in fusion devices. As a result, there are more vanadium alloy data at elevated temperatures than for any other refractory alloy.

Van Witzenberg et al.(15) investigated the effects of pre-implanted helium (up to 1000 ppm) on neutron-irradiated vanadium and V-Cr-Ti alloys. The irradiations were carried out to 4.5×10^{22} n/cm^2 ($E > 0.1$ MeV) at a low temperature of 540°C (0.37 T_m). Helium caused decreased swelling and void concentrations and increased void sizes in pure vanadium irrespective of concentration, in qualitative agreement with oxygen in the previous study. In V-Cr-Ti, the opposite effect was found. Helium increased the void concentration and decreased the size irrespective of concentration. The swelling, however, was less in V-Cr-Ti than in pure vanadium with or without helium. The differences were explained on the basis of the critical cavity concept.

A number of vanadium alloys have been investigated in simulation tests to determine swelling behavior. These studies, reviewed by Gold et. al.(16), have concentrated on the V-Ti-Cr system which has shown a general resistance to void swelling in alloys containing titanium. In V-10Cr alloy, a maximum of 1% swelling was observed at a fluence of 1.5×10^{22} n/cm^2 at irradiation temperatures of 700° and 800°C. The VANSTAR-7 alloy has shown very low swelling. For alloys containing titanium, irradiated at temperatures from 470° to 780°C to fluences as high as 6×10^{22} n/cm^2, little or no swelling was observed.

The V-20 Ti composition is highly swelling resistant, however injection of 90-200 appm of helium results in void formation during subsequent neutron irradiation(17). The swelling was low, however, of the order of 0.03%, after 3×10^{22} n/cm^2. Recent ion bombardment experiments show that V-Cr binary alloys swell more than unalloyed vanadium while alloys containing Ti were completely swelling resistant(18), thus confirming the swelling resistance of Ti containing vanadium alloys for the range of ion bombardment temperatures 400° to 700°C, and damage levels to 50 dpa.

5.2 Niobium

In uninjected niobium and its alloys irradiated with Ni ions, Loomis et al.(19,20), found void swelling between 600° and 1150°C (0.31 T_m and 0.52 T_m respectively) with peak swelling occurring at 0.4 T_m in Nb and ≈1025°C (0.47 T_m) in Nb-1 Zr. Oxygen impurities reduced the swelling, promoted void ordering, and increased void nucleation.

Loomis and Gerber(21,22) irradiated niobium and its binary and ternary alloys with dual beams of Ni^+ and He^+ at temperatures as high as 950°C (0.47 T_m) and showed that Fe and Ni impurities that diffuse rapidly in Nb have a minor influence on swelling whereas those (e.g., Mo) that diffuse slowly decrease the swelling. Elements that getter oxygen (e.g., Ti) decreased the swelling, suggesting a strong role of oxygen in swelling in niobium.

Jang and Moteff(23) neutron irradiated Nb-1 Zr to $1x10^{22}$ n/cm^2 at temperatures varying from 430° to 1050°C (0.26 T_m to 0.48 T_m) and found void swelling at all temperatures. A maximum of 2% swelling was observed at 800°C (a shift of ≈200°C from ion data) at this relatively low dose. The swelling was analyzed in terms of reaction rate theory with a good agreement.

Bartlett et al.(24) reported results of swelling in Nb-5Zr and Nb-10Zr irradiated to a fluence of 3.6×10^{22} n/cm^2 at 450° to 600°C. They found no significant amount of swelling for any condition, although a few voids were observed for the irradiation at 550° and 600°C.

5.3 Tantalum

Unalloyed tantalum showed swelling under neutron bombardment between 400° and 1000°C(25). At a fluence of approximately 2.5×10^{22} n/cm^2, a swelling of 2.5% was observed(26). Murgatroyd(27) found swelling in tantalum irradiated at 500°C, however, the swelling decreased with increasing fluence. This recovery was attributed to the shrinkage of voids due to the transmutation of Ta to W, with a resulting reduction in lattice parameter.

Swelling in tantalum alloys has received little attention. No swelling was observed in T-111 irradiated at 450° and 600°C. The Ta-10W alloy showed some voids, but swelling was less than in the unalloyed metal(28).

5.4 Molybdenum

Brimhall and Simonen(29) studied swelling in uninjected Mo single crystals at temperatures up to 900°C (0.4 T_m) by ion bombardment with 7.5 MeV Ta^{+++} ions to doses as high as 150 dpa. A void swelling of ≈2% was observed at the highest dose. They found a maximum in void concentration occurring at relatively low dose and further swelling occurred by void growth. The dose dependence of swelling was less than linear. Void ordering was also observed.

Simonen and Brimhall(30) analyzed the swelling data on Mo irradiated to 1000°C (0.44 T_m) and concluded that the voids act as unbiased sinks. In another study, Bradley and Brimhall(31) found a good correlation between swelling with Ni ions and that with neutrons when the temperature shift was included. They also found little effect of free surfaces on the ion-bombarded specimens of Mo single crystals.

Recently, Brimhall, et al.(32) irradiated Mo at high temperature (0.44 T_m) in a dual beam facility and injected Ta^{+++} and He^{+} ions simultaneously to a dose of 80 dpa. Simultaneous injection of helium caused continuous nucleation of voids. The helium had little effect on the absolute magnitude of the swelling which was approximately 0.5%, and the dose dependence was similar to neutron irradiations at low dose levels.

The effect of an oversized atom (Zr) on void swelling at 700°-900°C in Mo was investigated by Liou, et al.(33) Zr appeared to reduce the stacking fault energy and ease loop nucleation. Solute-defect flux coupling caused precipitation of an incoherent phase.

Stubbins and Moteff(34) studied Mo and its alloys irradiated at the highest temperatures to 1425°C (≈0.55 T_m). Their study on the uninjected Mo and TZM (an alloy with Ti, Zr, and Mo) metal showed increasing swelling with increasing temperatures. The dose dependence of swelling varied with temperature and was not the same in different alloys. Over a temperature range of 850°-1000°C, TZM showed lower swelling than Mo-0.5Ti; also swelling in TZM showed less temperature dependence than in Mo-0.5Ti alloy.

In Mo and its alloys, neutron irradiated from 330° to 850°C to fluences of 1 and 3 x 10^{20} n/cm^2, Bentley, et al.(35,36) observed voids at all temperatures, and void growth with increasing temperature. In TZM, however, void shrinkage was observed at 750° and 850°C and the damage structure consisted of dislocation loops and almost a complete absence of voids. A strong influence of impurities with damage structure was envisaged, with oversize alloying elements segregating to the dislocation core. Pard and Garr(37) irradiated TZM to 8 x 10^{22} n/cm^2 (E > 0.1 MeV); however, their temperatures of irradiation were low and very little void swelling was observed. Sprague et al.(38) and Gelles et al.(39) also studied low temperature (650°C, 0.32 T_m) swelling in Mo and its alloys. A value of 3% swelling was found in Mo at a fluence of 5.4 x 10^{26} n/cm^2 (E > 0.1 MeV) by Sprague et al. Gelles et al. reported a swelling of 3% in TZM alloy at a fluence of 1.47 x 10^{23}n/cm^2 (E > 0.1 MeV); however, saturation was not predicted until 10^{24} n/cm^2 with 20% swelling.

5.5 Tungsten

Tungsten and its alloys have received the least amount of attention of the five refractory alloy systems. Neutron-irradiated tungsten showed swelling over the temperature range of 450° to 1300°C (0.2 to 0.43 T_m). Matolich et. al.(40) observed swelling of approximately 2% at 750°C, however, increasing swelling was suggested at temperatures >1200°C.

A tungsten-rhenium (W-25Re) alloy examined after exposure to a range of irradiation conditions showed no swelling(41). No void formation was observed in W containing 5 to 25% Re irradiated to a fluence of 4 to 5 x 10^{21} n/cm^2 at temperatures from 600°-1500°C.

A recent review paper by Wiffen(42) provides an excellent review of irradiation effects data in refractory metals.

5.6 Conclusions on the State of the Art of Refractory Metal Irradiation Data

From the literature survey of swelling in bcc refractory metals, it is clear that no controlled and systematic study is available from which to draw any definite conclusions on the swelling mechanisms in these metals. In addition, the data base on high temperature swelling under controlled conditions is meager at best. The present work is intended to fill the gap existing in the understanding of high temperature swelling in these materials.

6.0 SELECTION OF MATERIAL FOR STUDY

The technologically important refractory metals can generally be classified into two groups: i.e., Group V metals, vanadium, niobium, and tantalum, and Group VI metals, molybdenum and tungsten. All were considered in the selection of a model material. The choice was based on three major considerations: (1) theoretical, (2) experimental, and (3) practical; i.e., those related to the engineering application of these materials. In making the choice of material, the third consideration was weighted less than the first two.

The theoretical considerations involved the availability of the parameters needed for theoretical modelling of the swelling phenomenon. These parameters are related to dislocation bias, point defect diffusivities, sink strengths, binding energies, vacancy and interstitial migration and formation energies. In addition, an important consideration was the probability of formation of <100> loops. Based on these latter considerations V, Nb, and Mo were more desirable than Ta and W.

Among the experimental factors considered were the availability of a self-ion beam with sufficient ion current in an energy range of 4-8 MeV, the depth of penetration of the incoming self-ion, and susceptibility to contamination during the irradiation. These considerations favored niobium over all of the other candidates, since ion beams of sufficient current can be obtained using a novel approach which is described in Section 7.1. Peak damage due to self-ions in Nb occurs at a depth of approximately 1 μm, which is considered sufficiently removed from the surface to avoid surface sensitive effects. Also, the only other candidate material, V, is very susceptible to contamination during ion irradiation. Ta, Mo, and W were rejected because ion currents of sufficient intensity could not be obtained and because the penetration depth is limited due to their high atomic weights.

Practical or applications-oriented considerations favored Nb and Ta because alloys of these materials can be utilized up to high temperatures, 1200° and 1350°C, respectively, whereas V alloys are only usable to <800°C. W and Mo can be used at high temperatures, however, fabrication of their alloys is difficult and they undergo a transition from ductile to brittle behavior at relatively high temperatures, especially in the irradiated condition.

Based on these considerations niobium was chosen as the material for study. Table I summarizes the matrix used to make the selection of material for study.

Model calculations, which predict the swelling in niobium are provided in the next section.

TABLE I

Summary of Choice of Material Considerations

Metal	Theoretical	Experimental	Practical
V	O	X	X
Nb	O	O	O
Ta	X	X	O
Mo	O	X	X
W	X	X	X

O-Favorable

X-Less Favorable

7.0 PHASE I PROGRAM

7.1 Development of a Theoretical Model for Refractory Metals

Since the discovery of voids in irradiated stainless steel by Cawthorne and Fulton(43) in 1967, there has been considerable study of void and cavity nucleation and growth in metals. Classical steady state nucleation theory has been extended to treat nucleation when supersaturations of both vacancies and interstitials are present, and has been used to calculate nucleation rates for various irradiation conditions(44-46). Time dependent nucleation models, based on the chemical reaction rate formalism, have also been developed to predict nucleation rate as a function of time(47,48). Experimental data suggest that the classical separation of cavity evolution into nucleation and growth regimes is not a bad approximation, and theoretical models have been developed to predict growth of an average void or cavity after nucleation is complete(49,50). These growth models have recently been expanded to include equations that describe higher moments of the cavity size distribution function(51).

Although the details of crystal structure are not emphasized in rate theory model development, calculations are generally performed for face-centered cubic metals and have been quite successful in reproducing qualitative trends in the experimental data, including the temperature dependence of the nucleation and growth behavior, the general form of the size distribution function, nucleation times, and gross impurity effects. Little attention, on the other hand, has been given to body-centered cubic metals. In these metals, differences in the migration and formation energies of vacancies and interstitials, in surface energies, in development of the loop microstructure, and in impurity interactions can give rise to significant differences in cavity growth and swelling behavior. The purpose of the present work is to develop a cavity growth model specifically for body-centered cubic metals and to calculate growth rates and swelling behavior in refractory metals. The results of this effort are presented in this section.

7.1.1 Point Defect Concentrations

The rate equations for the concentrations of point defects - vacancies and interstitials - can be written as

$$\underset{\sim}{\nabla} \cdot \left(D_v \underset{\sim}{\nabla} C_v + \frac{D_v C_v}{kT} \underset{\sim}{\nabla} U_v\right) + G_v - RC_v C_I - K_v C_v = \frac{\partial C_v}{\partial t} \tag{1}$$

and

$$\underset{\sim}{\nabla} \cdot \left(D_I \underset{\sim}{\nabla} C_I + \frac{D_I C_I}{kT} \underset{\sim}{\nabla} U_I\right) + G_I - RC_v C_I - K_I C_I = \frac{\partial C_I}{\partial t} \tag{2}$$

where subscripts I and v denote inerstitials ad vacancies, D is a diffusion coefficient, C is concentration of point defects per unit volume, k is Boltzmann's constant, T is absolute temperature, U is the interaction energy of point defects with a sink, G is a point defect product rate per unit volume, R is the recombination coefficient, and K is a reaction rate constant. Time-dependent solutions of Eqs. (1) and (2) can be obtained using standard numerical techniques. Treatment of void swelling, however, does not require this since the relaxation times for changes in the point defect concentrations are short when compared with those required to change the microstructure. A quasi-steady state condition is generally assumed to hold, and the time derivatives are neglected. A second approximation that is invoked to simplify the problem is that the real material with its set of inhomogeneous sinks can be replaced by a continuum with a uniform sink distribution whose integrated effect on the point defect concentrations is the same as that of the discrete set. The spatial derivatives in Eqs. (1) and (2) are then eliminated, and an analytic solution can be obtained for the quasi-steady state point defect concentrations:

$$C_v = \frac{[K_I K_v + R(G_I - G_v)]}{2RK_v} \left(\left(1 + \frac{4RG_v K_I K_v}{[K_I K_v + R(G_I - G_v)]^2}\right)^{1/2} - 1\right) \tag{3}$$

$$C_I = \frac{[K_I K_v + R(G_v - G_I)]}{2RK_I} \left(\left(1 + \frac{4RG_I K K_v}{[K_I K_v + R(G_I - G_v)]^2}\right)^{1/2} - 1\right) \tag{4}$$

The steady state defect concentrations obtained from Eqs. (3) and (4) are functions of the point-defect production rates G_I and G_v and the sink strengths, K_I and K_v, which are determined by the microstructure. They enter the rate equations that describe the microstructural evolution as parameters that are self-consistently adjusted as the microstructure changes with time.

7.1.1.1 Sink Strengths

The model material is assumed to contain a variety of sinks for point defects: network dislocations (nd), interstitial dislocation loops (ℓ), cavities (c), precipitates (p), and grain boundaries (gb). The strength S_j of a given sink, j, is that quantity which, when multiplied by the point defect diffusion coefficient and concentration, gives the loss rate of defects to the sink. S_j is generally written as the product of three factors: a geometric parameter describing the sink, a capture efficiency Z_j, and a correction factor that accounts for interactions between sinks. The expressions that were used for S_j in the present work are

$$S_{I,v}^{nd} = LZ_{I,v}^{nd} , \tag{5}$$

where L is the network dislocation density;

$$S_{I,v}^{\ell} = 4\pi \ r_{\ell}^{*} N_{\ell} \ Z_{I,v}^{\ell} , \tag{6}$$

where N_ℓ is the loop density and r_ℓ^* is an effective capture radius, defined by $r_\ell^{*2} = \delta r_\ell/2$, where δ is the dislocation core radius and r_ℓ is the loop radius;

$$S_{I,v}^{c} = 4\pi \ r_c N_c \ Z_{I,v}^{c} \tag{7}$$

where r_c is the cavity radius, and N_c is the cavity density;

$$S_{I,v}^{p} = 4\pi \ r_p N_p \ Z_{I,v}^{p} \tag{8}$$

where r_p is the precipitate radius, and N_p is the precipitate density; and

$$S^{gb}_{I,v} = \frac{6S^{1/2}}{d} , \qquad (9)$$

where S is the sum of the strength of all sinks within the grain, and d is the grain diameter.

The capture efficiencies $Z_{I,v}$, which occur in Eqs. (5) through (9), are given by the ratio of the actual point-defect current to the sink to an ideal current, which would result if the sink were a perfect absorber and had no stress field to interact with that of the point defect. Attempts have been made to theoretically evaluate the capture efficiencies for a variety of sink types(52-55). The problem is a difficult one, however, and these calculations can be criticized because of oversimplifications, invalid approximations, and inconsistencies(56,57). For numerical calculations, the capture efficiencies are therefore treated as parameters: Z_v for a sink type is generally assumed to be 1, and Z_I for dislocations ranges between roughly 1.02 and 1.5, with Z_I for other sinks assumed to be 1.

The reaction-rate constants $K^j_{I,v}$ for each sink are obtained by multiplying the sink strengths by the appropriate point-defect diffusion coefficient:

$$K^j_{I,v} = S^j_{I,v} D_{I,v} , \qquad (10)$$

and the rate constants $K_{I,v}$, which appear in the equations for the point defect concentrations, are

$$K_{I,v} = \sum_j K^j_{I,v} \qquad (11)$$

The point-defect diffusion coefficients D_I and D_v are given by

$$D_{I,v} = D^o_{I,v} \exp [-Q_{I,v}/kT] , \qquad (12)$$

where $D^o_{I,v}$ is the pre-exponential factor, and $Q_{I,v}$ is the activation energy.

7.1.1.2 Defect Production Rates

In many swelling models, the production rates for interstitials and vacancies are assumed to be equal. The steady state defect concentrations can then be written as

$$C_v = \frac{K_V}{2R}\left(\left(1 + \frac{4RG}{K_I K_V}\right)^{1/2} - 1\right) \tag{13}$$

$$C_I = \frac{K_I}{2R}\left(\left(1 + \frac{4RG}{K_I K_V}\right)^{1/2} - 1\right) , \tag{14}$$

where $G_I = G_V = G$ is the production rate, and the ratio of concentrations, C_I/C_V, is equal to K_V/K_I. This assumption is valid in certain physical situations, specifically when vacancy loop formation in cascades is negligible and when interstitial injection does not occur. Most generally, the production rates can be written as

$$G_V = (1 - \epsilon_V)\, G \tag{15}$$

and

$$G_I = (1 + \epsilon_I)\, G, \tag{16}$$

where ϵ_V is the fraction of vacancies that form vacancy loops and ϵ_I is the fraction of additional interstitials due to self-ion injection. The latter parameter, ϵ_I, is non-zero only near the end of range, where the implanted ions come to rest.

7.1.2 Interstitial Dislocation Loops

Interstitial loops observed in body-centered cubic metals after irradiation are of two types. The type most frequently found is a perfect loop with $\frac{a}{2}\langle 111\rangle$ Burgers vector and a {111} habit plane(58-61). After ion or electron irradiation at high temperatures, however, perfect loops with a <100> Burgers vectors and {100} habit planes are seen in α-iron(62) and ferritic alloys(63).

Eyre and Bullough(64) proposed a mechanism for formation of interstitial loops in the body-centered cubic lattice. They suggested that <110> split dumbbell interstitials aggregate on {110} planes to form faulted loop nuclei with $\frac{a}{2}$ <110> Burgers vector. Due to a high stacking fault energy, the loops unfault by either of two reactions:

$$\frac{a}{2}\ [110] + \frac{a}{2}\ [1\bar{1}0] \rightarrow a\ [100] \tag{17}$$

or

$$\frac{a}{2}\ [110] + \frac{a}{2}\ [001] \rightarrow \frac{a}{2}\ [111] \tag{18}$$

The elastic energy of either product loop is further reduced by a rotation of the habit plane from {100} and {111} respectively. Bullough and Perrin(65) verified this model using a computer simulation of the α-iron lattice and found that $\frac{a}{2}$ <111> loop formation was energetically favored at all irradiation temperatures. In addition, their results showed that unfaulting occurred at very small loop sizes, below the resolution limit for conventional transmission electron microscopy.

Little, Bullough, and Wood(63) have recently used these ideas to explain the evolution of the damage structure and the observed swelling resistance in FV 448 martensitic stainless steel. After neutron irradiation to damage levels of 30 displacements per atom (dpa) at temperatures in the range 380° to 480°C, a homogeneous population of loops with a <100> Burgers vector was observed to exist in domains, which lay within the martensite matrix that retained a high (pre-irradiation) network dislocation density. The overall swelling of the alloy, estimated from measurements of void statistics, was <<0.1%, a value in agreement with bulk density determinations(66). The mechanism that Little, Bullough, and Wood proposed for the observed swelling suppression is based on theoretical calculations of bias factors for interstitial dislocation loops(52-55). According to these calculations, the bias of a dislocation depends on the magnitude of its Burgers vector. Hence, the bias of an a <100> type dislocation with $|\underset{\sim}{b}| = a$ is larger than that of a $\frac{a}{2}$ <111> type dislocation with $|\underset{\sim}{b}| = \sqrt{3}\ a/2$.

The $\frac{a}{2}$ <111> dislocations are relatively neutral sinks when compared with the a <100> dislocations and act to absorb the excess vacancies that would be available for void formation in their absence.

The mechanism of swelling suppression that occurs in the ferritic steels is applicable to the general class of body-centered cubic materials, including the technologically important refractory metals such as Nb, Mo, W, V, Ta, and their alloys. The requirements for the mechanism to be effective are (1) the presence of a high initial dislocation density, and (2) a sufficiently high probability for a <100> loop formation. Table II, which was taken from reference (63), contains a list of body-centered cubic metals with their lattice parameters, shear moduli, and the relative probability P for <100> loop formation, calculated from

$$P = \exp\left[(E^{<100>} - E^{<111>})/kT\right] , \tag{19}$$

where the loop energies $E^{<100>}$ and $E^{<111>}$ are given by

$$E^{<100>} = \frac{\mu a^3}{4\pi} (\alpha + \sin\alpha) + a^2 T (\sin\alpha \cos\alpha - \alpha) \tag{20}$$

TABLE II

Lattice Parameters, Shear Moduli, and Calculated Relative Probabilities for <100> Loop Formation in a Range of BCC Metals

Metal	Lattice Parameter, a (nm)	Shear Modulus μ (x 10 GPa)	Relative Probability, P
Nb	0.330	3.96	4.3×10^{-5}
V	0.304	4.73	5.5×10^{-5}
Fe	0.287	8.60	5.7×10^{-9}
Ta	0.330	7.07	7.9×10^{-11}
Mo	0.315	12.3	1.9×10^{-19}
W	0.317	16.0	1.4×10^{-27}

$$E^{<111>} = \frac{\mu a^3}{8\pi} (\beta + \sin\beta) + a^2 T (\sin\beta \cos\beta - \beta), \tag{21}$$

with

$$\alpha = 2 \sin^{-1} \left(\frac{\mu a}{16\pi T}\right)$$

$$b = 2 \sin^{-1} \left(\frac{\mu a}{32\pi T}\right) ,$$

where a is the lattice parameter, T is the stacking fault energy, and μ is the shear modulus.

V and Nb are clearly good candidates for swelling suppression via the loop mechanism, since the probability of <100> loop formation in these metals is roughly four orders of magnitude larger than that for α-iron. In Ta, Mo, and W, the mechanism should be relatively unimportant.

7.1.2.1 Rate Equations

The differential equations that describe the time evolution of the two types of interstitial loop are

$$\frac{dr_{\ell i}}{dt} = a^2 \left(Z_I^{\ell i} D_I C_I - Z_v^{\ell v} D_v (C_v - C_{v\ell i}^{th})\right) \qquad (22)$$

where $r_{\ell i}$ is the mean radius of the loops of type i.

$C_{v\ell i}^{th}$ is the thermal vacancy concentration at the loop, which is given by

$$C_{v\ell i}^{th} = C_v^{th} \exp \left[- (T + E_{\ell i} - \sigma a) a^2/kT\right], \qquad (23)$$

where C_v^{th} is the bulk thermal vacancy concentration, and σ is the hydrostatic stress. The elastic energy $E_{\ell i}$ of a circular loop is given by(67)

$$E_{\ell i} = A_1 \left(A_2 \left[\ell n\ (p/\delta) - \ell n\ (\pi/4) -2\right] + A_3\right), \qquad (24)$$

where p is the loop perimeter, and

$$A_1 = [\mu p/4\pi\ (1-\nu)]$$

$$A_2 = [(1-\nu/2)\ (b^2-b_z^2) + b_z^2]$$

$$A_3 = [-(1-2\nu)\ (b^2-b_z^2) + 2(3-2\nu)b_z^2]/8\ (1-\nu)\ ,$$

where ν is Poisson's ratio, b is the Burgers vector, b_z is the z-component of the Burgers vector, with the z-axis perpendicular to the loop plane, and δ is the dislocation core radius.

7.1.3 Helium

The presence of helium in a metal during irradiation can have a substantial effect on cavity nucleation(68,69). It is relatively insoluble, and the binding energy between vacancies and helium atoms is high, of the order of 3 eV. Helium is consequently trapped by small vacancy clusters. The gas then stabilizes the clusters by reducing the vacancy emission rate, and the clusters can grow until they reach the critical size. At this size, the excess flux of vacancies over interstitials is sufficient for continued growth.

The critical cavity size depends on temperature. At low temperatures, clusters with two or three vacancies are stable and the effect of helium is small. At higher temperatures, however, when clusters require ten or more vacancies to be stable, the presence of helium can determine whether cavity formation is possible.

As currently included in the theory of cavity growth the effect of helium is simply to decrease the thermal emission rate of vacancies from the cavity. The gas exerts a pressure opposing the surface tension, and the thermal equilibrium vacancy concentration C_{vc}^{th} at the cavity surface becomes

$$C_{vc}^{th} = C_v^{th} \exp\ [-(P_g - 2T/r_c)\ \Omega/kT]\ , \qquad (25)$$

where P_g is the gas pressure, and Ω is the atomic volume. The decrease in the thermal concentration, as given by Eq. (25), leads to cavity growth at higher temperatures.

Helium can also interact with other components of the microstructure, for example, dislocations and precipitates. Both experimental evidence(70) and theoretical calculations(51,71), however, indicate that vacancies or cavities are the dominant sink for the gas. In the present work, therefore, helium is assumed to be either mobile and occupying an interstitial site or trapped in a cavity, with the possibility of emission either by thermal detrapping or by knockout. The sink strength S of a cavity for helium is taken by

$$S_{He}^{c} = 4\pi \, r_c N_c \, . \tag{26}$$

The rate equation that governs the concentration of mobile helium is

$$\frac{dC_{He}}{dt} = \dot{n}_{He} - K_{He}^{v} \, C_{He} + X \tag{27}$$

for the concentration of free helium, where $\dot{n}_{He}$ is the helium injection rate, K_{He}^{v} is the reaction rate constant for loss of helium to cavities, and X is the rate at which helium is emitted from cavities. The equation for the concentration of helium trapped in cavities is

$$\frac{dC_{He}^{T}}{dt} = K_{He}^{v} \, C_{He} - X \tag{28}$$

The detrapping rate X is given by

$$X = \dot{n}_d + \nu_d C_{He}^{T} \, , \tag{29}$$

where $\dot{n}_d$ is the radiation displacement rate for helium from cavities, and ν_d is the thermal detrapping rate for a single helium atom.

7.1.4 Solutes

Solutes that interact with point defects can affect cavity growth in a metal in several ways. The most widely studied phenomenon is that of solute segregation to cavities(72,73), which occurs because of the coupled diffusion of point defects and solutes to sinks during irradiation. Theoretical calculations have shown that the presence of a solute at the cavity surface can decrease the vacancy capture efficiency of the cavity, leading to a reduction in the growth rate. This effect is difficult to model, however, and has not been substantiated by experimental evidence. It is therefore not included in the present work.

Solutes can also act as traps for either interstitials or vacancies or both types of point defect. As traps, solutes hinder diffusion and change the time scales of the basic nucleation and growth processes. Modification of the basic swelling model to include defect trapping is accomplished by means of an effective diffusion coefficient, D^+, which is given by(74)

$$D^{+}_{I,v} = D_{I,v} / [1 + 4\pi C_T R_T D_{I,v} (\tau_T - \tau_H)] , \tag{30}$$

where C_T is trap concentration, τ_H is the time spent at a host atom site during the diffusion process, τ_T is the time spent at a trap site, and R_T is the capture radius of the trap. A square well interaction potential is assumed, with a capture radius equal to a single jump distance. The time τ_T and τ_H are given by

$$\tau_T^{-1} = \upsilon_T = \upsilon_o \exp [-(E^m_{I,v} + E_B)/kT] \tag{31}$$

and

$$\tau_H^{-1} = \upsilon_H = \upsilon_o \exp (-(E^m_{I,v} /kT) \tag{32}$$

where υ_T and υ_H are jump frequencies, υ_o is the attempt frequency, $E_{I,v}$ are motion energies, and E_B is the solute-point defect binding energy.

Vacancy trapping by solute atoms generally leads to longer incubation times for cavity nucleation and higher cavity number densities$^{(74)}$. The cavity growth rate is reduced, and total swelling at a fixed fluence is lowered.

7.1.5 Cavities

The swelling rate $\dot{S}$ is given by

$$\dot{S} = 4\pi \; N_c r_c{}^2 \frac{dr_c}{dt} \tag{33}$$

where the time rate of change $\frac{dr_c}{dt}$ of the mean cavity radius r_c is

$$\frac{dr_c}{dt} = \frac{\Omega}{r_c} \quad \{Z_v^c \, D_v \, (C_v - C_{vc}^{th}) - Z_I^c \, D_I C_I\} \; , \tag{34}$$

where the thermal vacancy concentration C_{vc}^{th} at the cavity surface is given by Eq. (25).

Eqs. (22), (27), (28), and (34) are the basic set of differential equations for modelling swelling in body-centered cubic metals. They can be solved numerically using standard techniques such as those in the GEAR package$^{(75)}$.

7.1.6 Calculations for Niobium

As mentioned previously, one of the features that distinguishes the irradiation-induced microstructure in body-centered cubic metals from that found in face-centered cubic metals is the existence of two types of dislocation loops. The dominant type is of <111> orientation, but <100> loops can also form. The presence of several sinks in the system with positive but differing biases for interstitials complicates the microstructural evolution during irradiation. The relative values of the bias factors for the network dislocations, the <111> loops, and the <100> loops, for example, determine whether <100> loops grow or shrink in a given microstructural environment and affect the cavity growth rate. One purpose of the model was to quantitatively evaluate the effects of the loop bias or preference factors on the loop and cavity growth rates.

A second goal was to numerically assess the effect of helium on cavity growth. As in face-centered cubic metals, the presence of helium in sufficient quantity in body-centered cubic metals enhances the cavity growth rate and leads to increased swelling. The chemical reaction rate model was used to calculate cavity growth rates for cavities with different gas contents. The growth rates show a clear dependence on the gas content, and the impact of the results on the temperature dependence of cavity swelling in the presence of helium is outlined.

In the following section, numerical results of calculations performed with parameters appropriate for niobium are presented. Values that are used are presented in Table III.

7.1.7 Results of Calculations

7.1.7.1 Loop Capture Efficiencies

Calculations were performed to determine the sensitivity of the growth rates of voids and loops to the values assumed for the interstitial capture efficiencies $Z_I^{\ell 1}$ and $Z_I^{\ell 2}$ of the <100> and <111> interstitial dislocation loops. Values of $Z_I^{\ell 1}$ and $Z_I^{\ell 2}$ between 1.0 and 1.3 were considered; the capture efficiency Z_I^{nd} of the network dislocations was held fixed at 1.05, a value that is typically used for modeling work and is supported by experimental data in face-centered cubic metals(82). A listing of the possible cases for values $Z_I^{\ell 1}$ and $Z_I^{\ell 2}$ with respect to each other and to the value of the network capture efficiency Z_I^{nd} is given in Table IV and a schematic representation of these cases is shown in Fig. 1. Theoretical considerations may be used to limit the possibilities. Calculations of bias factors in several approximations(52,83,84) suggest that the capture efficiency of small dislocation loops is larger than that for network dislocations. In addition, the capture efficiency for a loop is proportional to the magnitude of its Burgers vector $\underset{\sim}{b}$; one may assume, therefore, that $Z_I^{\ell 1} > Z_I^{\ell 2}$ and, other factors being equal, $Z_I^{\ell 1} / Z_I^{\ell 2} = b_1/b_2$. These two considerations yield potential $(Z_I^{\ell 1}, Z_I^{\ell 2})$ values along the solid line in Fig. 1.

TABLE III
Parameters for Niobium

Quantity	Value
Lattice parameter, a	3.29×10^{-8} cm (76)
Atomic volume, Ω	1.78×10^{-23} cm^3 (76)
Nearest neighbor distance, d	2.85×10^{-8} cm(76)
Dislocation core radius, δ	2.85×10^{-8} cm
Shear modulus, μ	3.96×10^{11} dynes/cm^2 (77)
Poisson's ratio, υ	0.392 (77)
Surface energy, T	2.7×10^3 ergs/cm^2(63)
Vacancy formation energy, E_v^f	2.53 eV (78,79)
Vacancy migration energy, E_v^m	1.09 eV (78,79)
Vacancy formation prefactor, C_{vo}^{th}	$4/\Omega$
Vacancy diffusion prefactor, D_{vo}	0.008 cm^2/s (79)
Interstitial migration energy, E_I^m	0.115 eV (80)
Interstitial diffusion prefactor, D_{Io}	10^{13} $d^2/6$ cm^2/s (78)
Helium migration energy, E_{He}^m	0.2 eV (81)
Helium diffusion prefactor, D_{Heo}	10^{13} $d^2/6$ cm^2/s
Helium detrapping frequency, υ_D	$10^{13}\ e^{\frac{-3.8}{kT/s}}$ (80)

TABLE IV

Possible Regimes for Capture Efficiencies (see Fig. 1)

(Condensed notation: $Z_I^{\ell 1} > Z_1$; $Z_I^{\ell 2} = Z_2$; $Z_I^{nd} = Z_n$)

Regime	Definition	Dimensionality
I	$Z_1 = 1$; $Z_2 = 1$	point
IIa	$Z_1 = 1$; $1 < Z_2 < Z_n$	line
IIb	$Z_1 = 1$; $Z_2 = Z_n$	point
IIc	$Z_1 = 1$; $Z_2 > Z_n$	line
IIIa	$Z_2 = 1$; $1 < Z_1 < Z_n$	line
IIIb	$Z_2 = 1$; $Z_1 = Z_n$	point
IIIc	$Z_2 = 1$; $Z_1 > Z_n$	line
IVa	$1 > Z_1 > Z_n$; $Z_2 < Z_1$	area
IVb	$Z_1 = Z_2 < Z_n$	line
IVc	$Z_1 = Z_2 = Z_n$	point
IVd	$1 < Z_1 < Z_n$; $Z_1 > Z_2$	area
IVe	$1 < Z_1 < Z_n$; $Z_2 = Z_n$	line
IVf	$1<Z_z < Z_n$; $Z_1 = Z_n$	line
Va	$1 < Z_1 < Z_n$; $Z_2 > Zn$	area
Vb	$Z_1 = Z_n$; $Z_2 > Z_1$	line
VIa	$Z_n < Z_1$; $1 < Z_2 < Z_n$	area
VIb	$Z_n < Z_1$; $Z_2 = Z_n$	line
VIIa	$Z_n < Z_1$; $Z_n < Z_2 < Z_1$	area
VIIb	$Z_n < Z_1$; $Z_2 = Z_1$	line
VIIc	$Z_n < Z_1$; $Z_2 > Z_1$	area

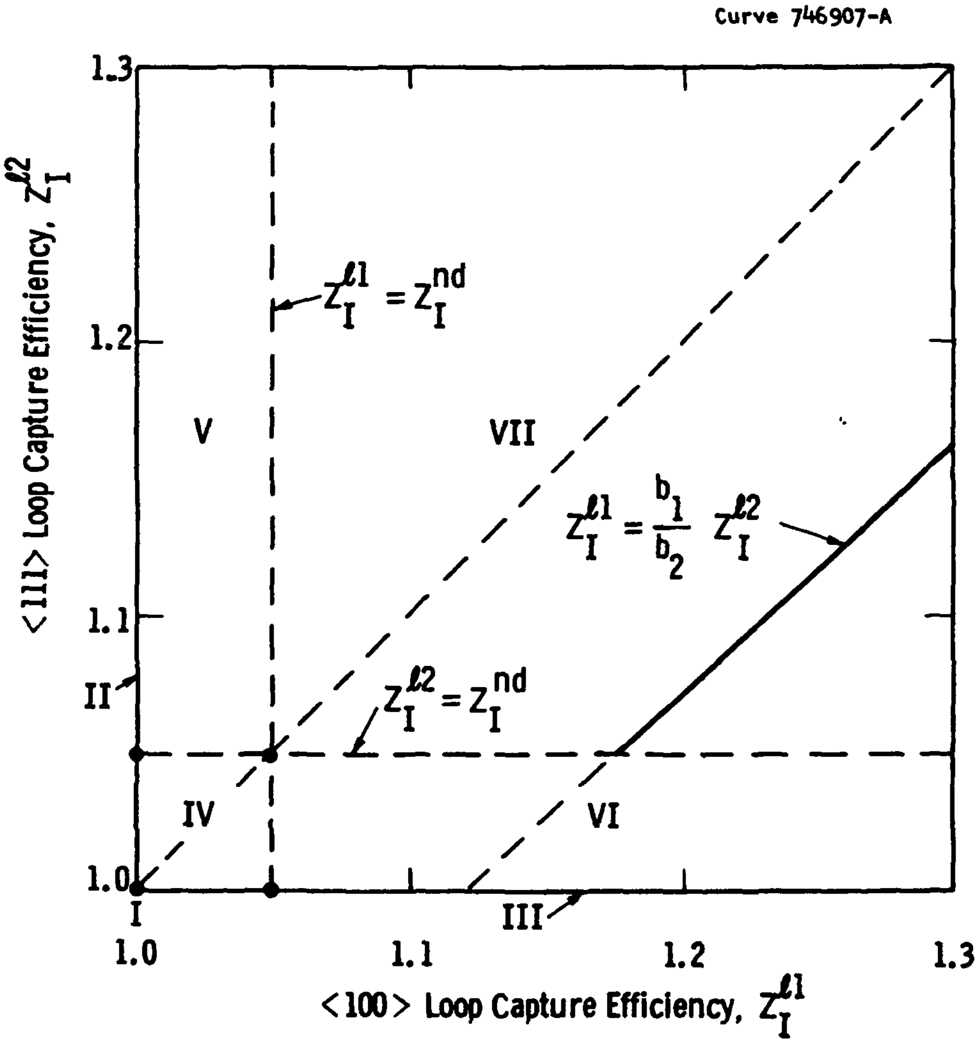

Figure 1. Schematic of Regimes for Loop Capture Efficiencies $Z_I^{\ell 2}$ and $Z_I^{\ell 2}$. Solid Line Indicates Values Consistent With Current Theories.

It should be noted that calculations of capture efficiencies for loops have been done using approaches and approximations that are subject to criticism. Nichols(57), in a recent review of bias factor calculations, concluded that "bias factor estimates are quantitatively unreliable" and that "bias factors used in swelling analyses must be considered empirical." In light of this conclusion, it is useful to view the bias factor as a model parameter and to determine the range of values that is required to reproduce experimental results -- specifically, the necessary conditions for obtaining growth of <100> loops and shrinkage of <111> loops, as seen in FV 448 steel with a high network dislocation density(85).

According to Eq. (22), the growth rate of an interstitial loop when bias effects dominate depends on the difference between two terms, which represent the two defect fluxes:

$$\frac{dr_{\ell i}}{dt} = a\,(Z_I^{\ell i} D_I C_I - D_v C_v) \tag{35}$$

where $r_{\ell i}$ is the loop radius, $Z_I^{\ell i}$ is the capture efficiency, D is a defect diffusion coefficient, and C is a defect concentration. In a system with four types of sink -- network dislocations, <100> loops, <111> loops, and cavities -- a positive growth rate for a loop requires

$$Z_I^{\ell i} > \frac{S_I}{S_v}\,, \tag{36}$$

where S is a defect sink strength. Equation (36) is obtained from Eq. (35) above and Eqs. (10), (11), (13) and (14).

As defined in Section 7.1.1.1:

$$S_I = LZ_I^{nd} + 4\pi r_{\ell 1}^{*} N_{\ell 1} Z_I^{\ell 1} + 4\pi r_{\ell 2}^{*} N_{\ell 2} Z_I^{\ell 2} + 4\pi r_c N_c \tag{37}$$

and

$$S_v = L + 4\pi r_{\ell 1}^{*} N_{\ell 1} + 4\pi r_{\ell 2}^{*} N_{\ell 2} + 4\pi r_c N_c \tag{38}$$

where capture efficiencies for vacancies have been taken as 1 for all sink types, as has the capture efficiency for interstitials at cavities. The notation in Eqs. (37) and (38) is that used before, L is the network density, N is a microstructural defect density, $r_{\ell 1}^{*}$ is an effective capture radius for loops, and r_c is the cavity radius.

When bias effects dominate, the change in cavity radius r_c with time is given by

$$\frac{dr_c}{dt} = \frac{\Omega}{r_c}\left(D_v C_v - D_I C_I\right), \tag{39}$$

and a positive growth rate requires that

$$1 < \frac{S_I}{S_v} \, . \tag{40}$$

This condition is obtained in a straightforward manner from Eq. (39) above and Eqs. (10), (11), (13) and (14).

Bias effects determine the cavity growth rate when the thermal vacancy term in Eq. (34) is small and can be neglected. A comparison of the total vacancy concentration with the thermal vacancy concentration is shown as a function of temperature in Fig. 2 for three values of the defect production rate and two values of the network dislocation density. Other parameters that were used: $\dot{n}_{He} = 0$, $N_c = 10^{14}/\text{cm}^3$, $N_{\ell 1} = 10^{10}/\text{cm}^3$, $N_{\ell 2} = 10^{15}/\text{cm}^3$, $Z_I^{nd} = 1.05$, $Z_I^{\ell 1} = 1.176$, $Z_I^{\ell 2} = 1.05$, $r_c = 10^{-7}$ cm, $r_{\ell 1} = 10^{-7}$ cm, and $r_{\ell 2} = 10^{-7}$ cm. From the figure, it is apparent that the bias-dominated growth regime occurs at low temperatures, and extends toward higher temperatures as either network density decreases or defect production rate increases.

The growth and shrinkage regimes defined by Eqs. (36) and (40) are illustrated schematically in Fig. 3. It is apparent that the sink strength ratio S_I/S_v must lie between $Z_I^{\ell 2}$ and $Z_I^{\ell 1}$ for <111> loops to shrink and <100> loops to grow. In this region, voids grow.

Curve 746905-A

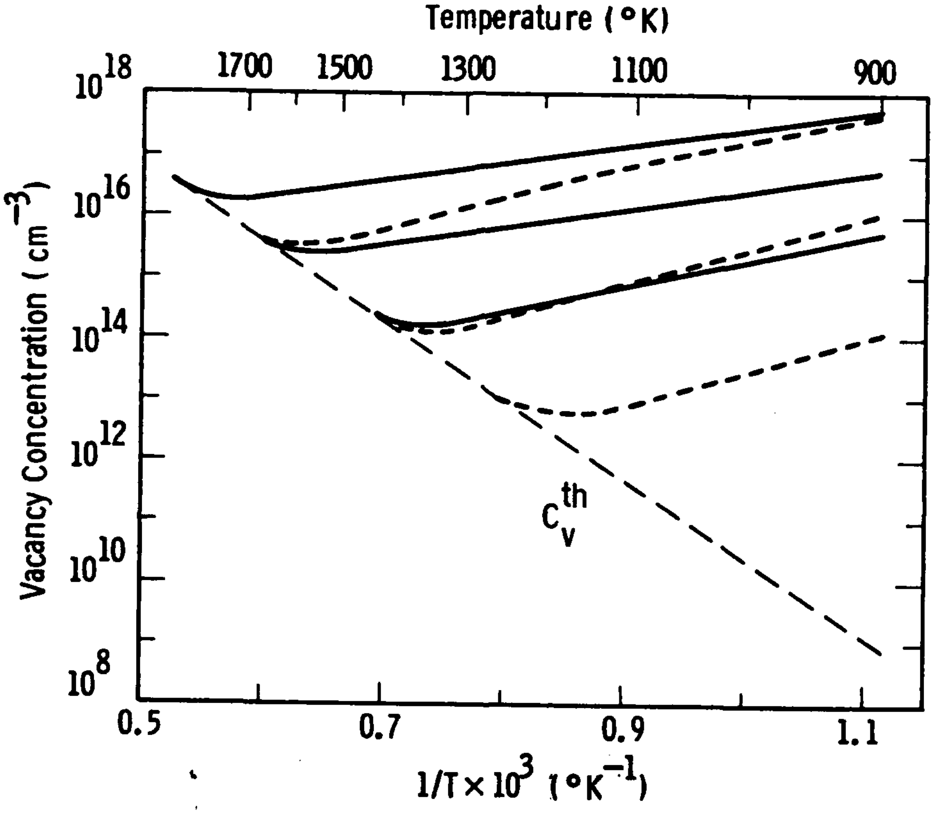

Figure 2. Vacancy Concentration as a Function of Temperature for Production Rates G of 10^{20}, 10^{18}, and 10^{16} cm^3-s, in Descending Order. Solid Curves are for Network Density L = 10^6/cm^2, Dashed Curves for L = 10^{11}/cm^2.

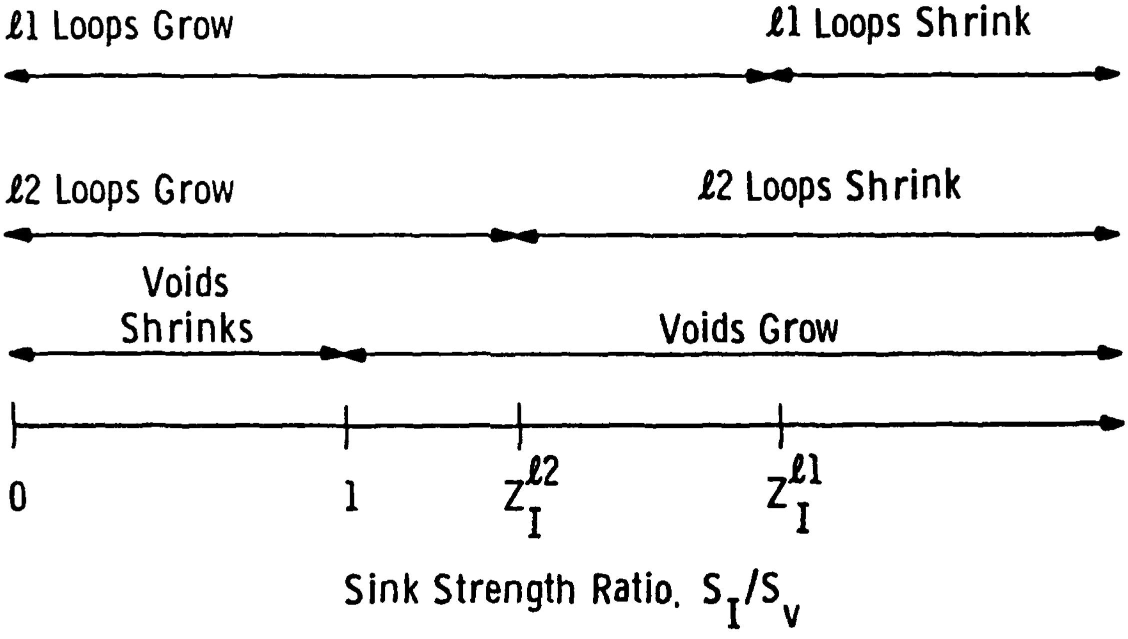

Figure 3. Schematic of Growth and Shrinkage Regimes for Loops and Voids as a Function of Sink Strength Ratio S_I/S_V.

Equations (36), (37), (38), and (39) can be used to evaluate the values of capture efficiencies necessary for growth, stability, or shrinkage of the various microstructural components for a given microstructure. Conversely, for fixed values of the capture efficiencies, the microstructural conditions, parameterized by L, $r^*_{\ell 1}$, $r^*_{\ell 2}$, r_c, $N_{\ell 1}$, $N_{\ell 2}$, and N_c, can be varied in order to investigate the possible values of the sink strength ratio, S_I/S_V.

The latter was done for the ranges of microstructural parameters given in Table V. $Z_I^{\ell 1}$ was assumed equal to $b_1 Z_I^{\ell 2}/b_2$ and Z_I^{nd} to 1.05.

TABLE V

Microstructural Parameters Used for Calculations of

Sink Strength Ratio S_I/S_V

Network Density, L	10^8-10^{12}/cm^2
Cavity Density, N_c	10^{13}-10^{18}/cm^3
<100> Loop Density, $N_{\ell 1}$	$10^{-5} N_{\ell 2}$
<111> Loop Density, $N_{\ell 2}$	10^{13}-10^{18}/cm^3
Capture areas, $4\pi r$	10^{-6}cm

The results for S_I/S_V are plotted in Figs. 4 through 6, for $Z_I^{\ell 1}$ equal to 1.02, 1.05, and 1.1 respectively. Although much detail can be extracted from these figures, several general features are important for this analysis. First, since the ranges of microstructural parameters were selected so that all physically observed microstructural densities are included, the results in Figs. 4 through 6 establish the values of the sink strength ratio that are obtainable in practice. These lie, in the three cases considered, between 1.0 and either Z_I^{nd} or $Z_I^{\ell 2}$, whichever is larger. The former is obtained when the network dislocation density and the <111> loop density are relatively low, and the cavity density is high. The upper limit value, if Z_I^{nd} , occurs when the network density is high and the <111> loop and cavity densities are relatively low. In the case where $Z_I^{\ell 2} > Z_I^{nd}$ (see Fig. 6), S_I/S_V approaches $Z_I^{\ell 2}$ when the network and cavity densities are low, and the <111> loop density is high.

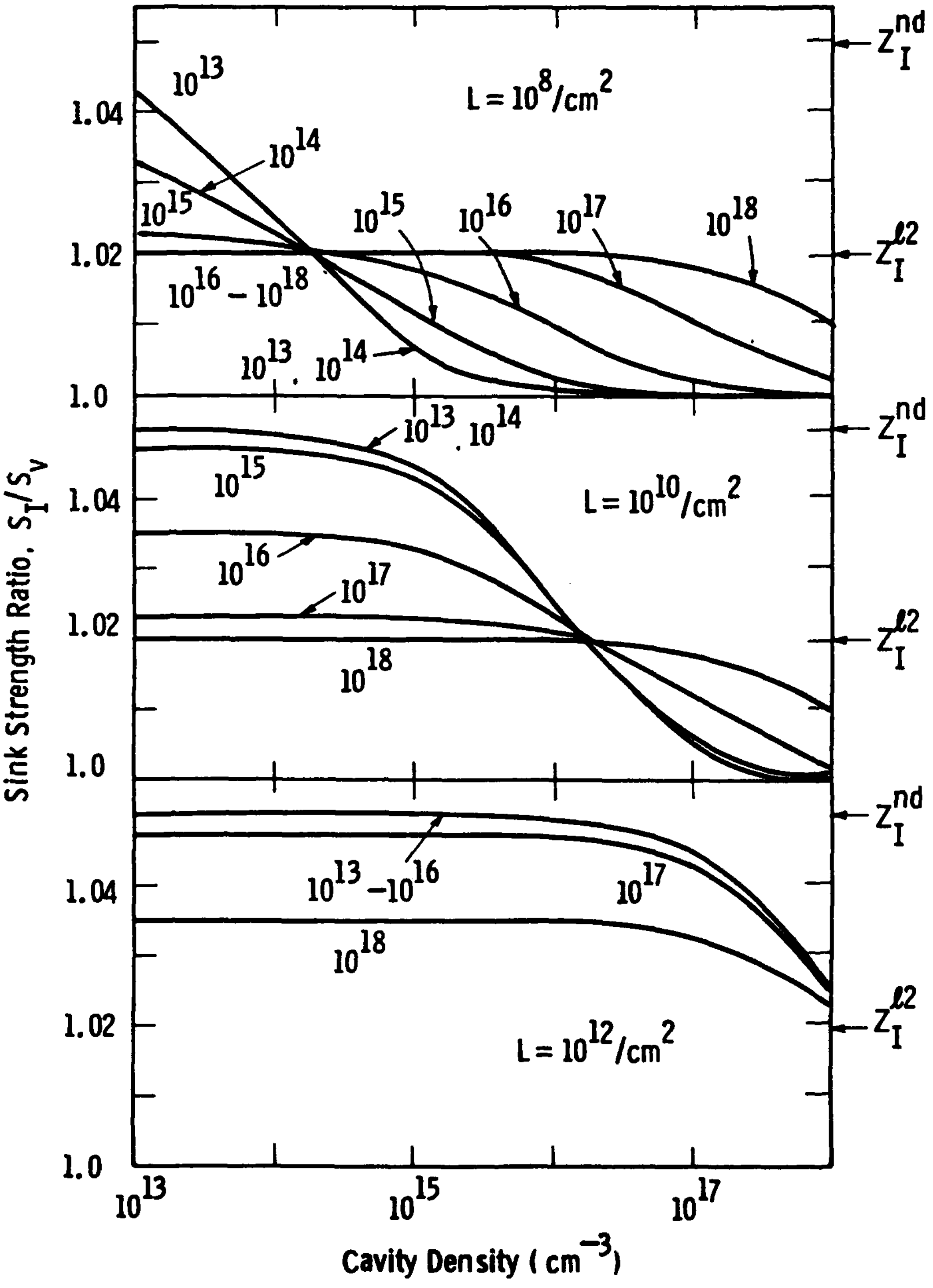

Figure 4. Sink Strength Ratio S_I/S_v as a Function of Cavity Density N_c for $Z_I^{\ell 2} = 1.02$, $Z_I^{\ell 1} = b_1 Z_1^{\ell 2}/b_2$, and $Z_I^{nd} = 1.05$. Panels are Labeled by Network Density L, and Individual Curves by the Value of $N_{\ell 2}$. $N_{\ell 1} = 10^{-5}\ N_{\ell 2}$.

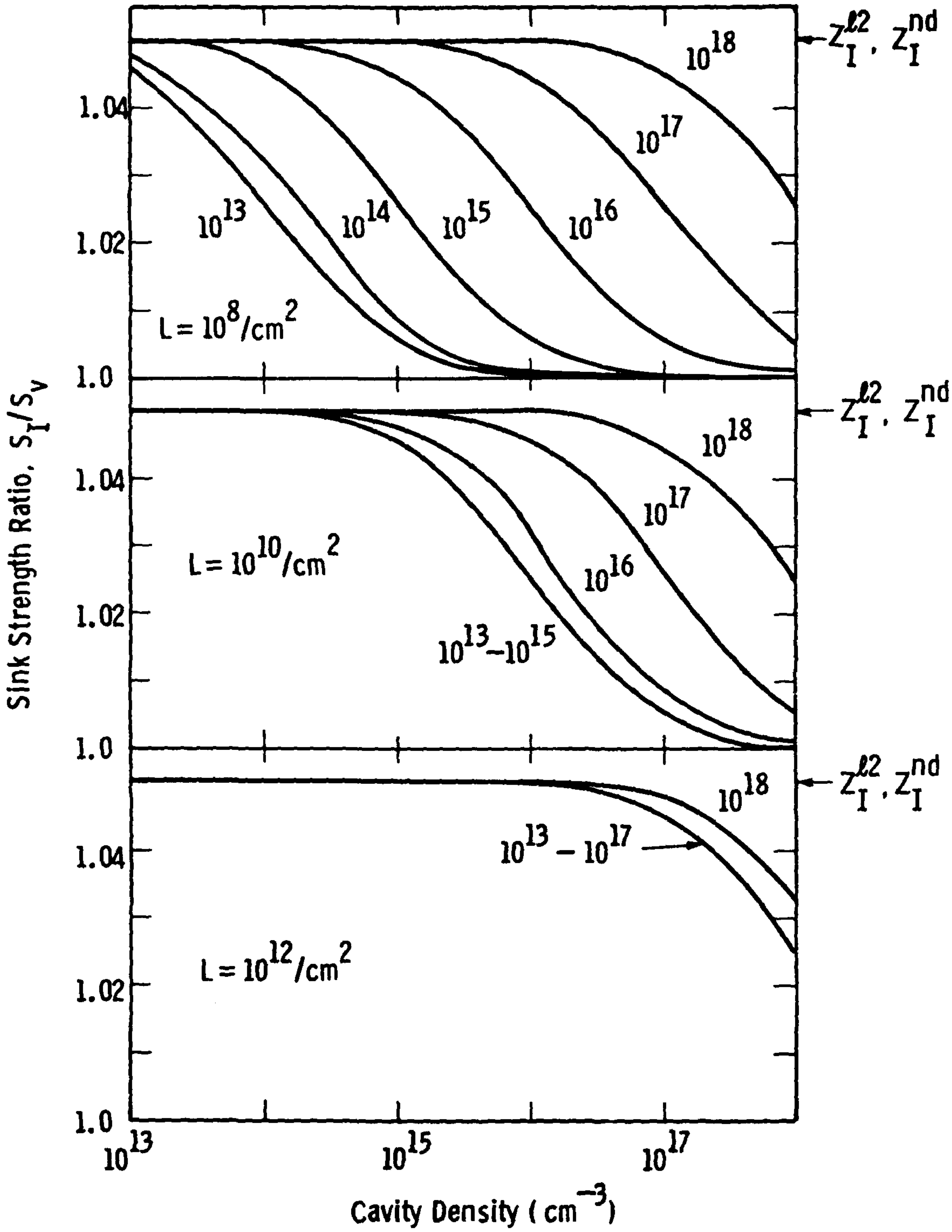

Figure 5. Sink Strength Ratio S_I/S_v as a Function of Cavity Density N_c for $Z_I^{\ell 2} = 1.05$, $Z_I^{\ell 1} = b_1 Z_I^{\ell 2}/b_2$, and $Z_I^{nd} = 1.05$. Panels are Labeled by Network Density L, and Individual Curves by the Value of $N_{\ell 2}$. $N_{\ell 1} = 10^{-5}\ N\ell_2$.

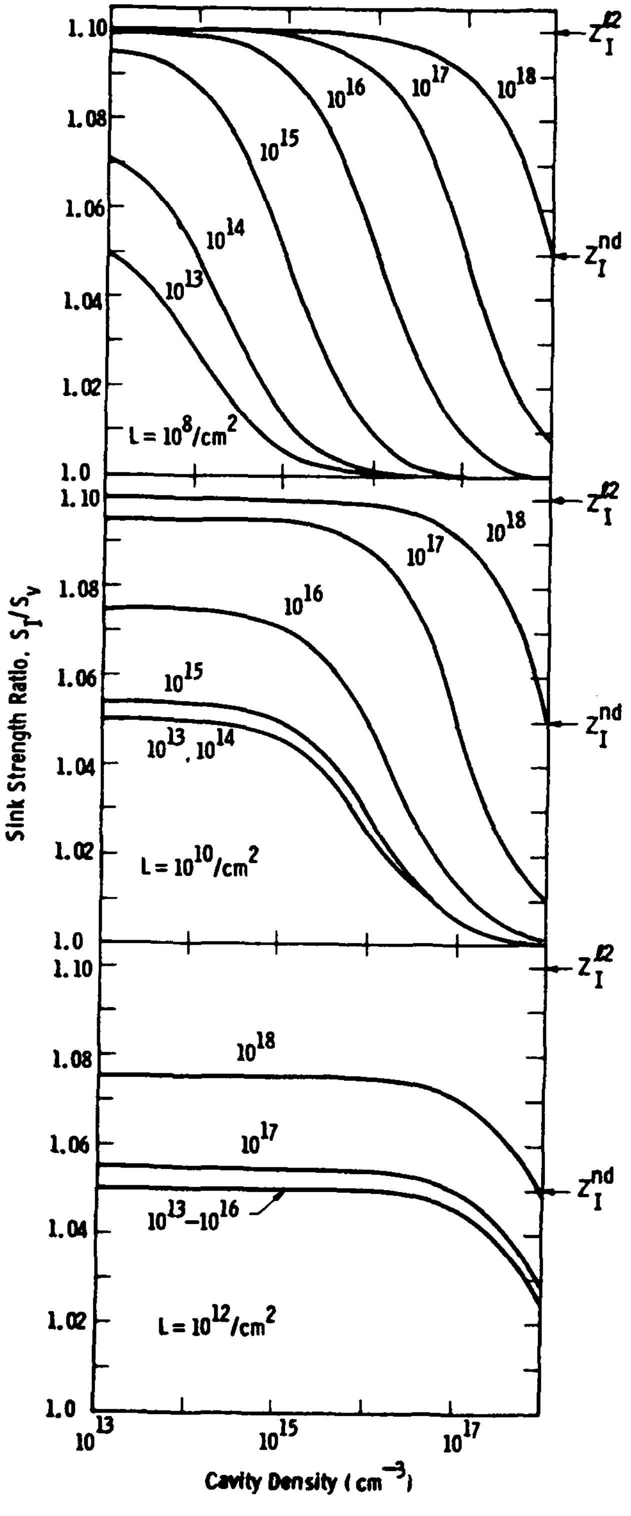

Figure 6. Sink Strength Ratio S_I/S_v as a Function of Cavity Density N_c for $Z_I^{\ell 2} = 1.10$, $Z_I^{\ell 1} = b_1 Z_I^{\ell 2}/b_2$, and $Z_I^{nd} = 1.05$. Panels are Labeled by Network Density L, and Individual Curves by the Value of $N_{\ell 2}$. $N_{\ell 1} = 10^{-5} N_{\ell 2}$.

The second point to be made regarding the results in Figs. 4 through 6 is that they establish the microstructural conditions under which <111> loops shrink, while <100> loops grow. As was stated previously, this requires that $Z_I^{\ell 2} < S_I/S_v < Z_I^{\ell 1}$ in the bias-driven growth regime. The condition is satisfied if $Z_I^{\ell 2} < Z_I^{nd}$ and if the network dislocation density dominates the sink strength ratio. Figure 4 shows that for a network density of $10^8/cm^2$, S_I/S_V is in the appropriate range if the cavity density is less than $\approx 10^{14}/cm^3$ and the <111> loop density is $\approx 10^{15}/cm^3$ or lower. When the network density is $10^{10}/cm^2$, cavity densities of $\approx 10^{16}/cm^3$ or lower and <111> loop densities of $10^{17}/cm^3$ or lower will satisfy the requirement. Finally, if the network density is high, i.e., $10^{12}/cm^2$, $S_I/S_v > Z_I^{\ell 2}$ for all cavity and loop densities considered. This is consistent with experimental observations in FV 448(63,85), but requires a value for the bias factor $Z_I^{\ell 2}$ of <111> loops that is not in accord with current theoretical arguments.

In addition to Nichols' critique of theoretical calculations of bias factors, it should also be noted that these calculations treat a single sink that is isolated in a medium that possesses some averaged properties, which are assumed to account for the multiple-sink nature of the material. This approach may not give the appropriate bias factor for a sink whose absorption of defects is strongly influenced by the surrounding sink structure. In the calculations of void and cavity growth rates, therefore, values of $Z_I^{\ell 2}$ were not restricted to those greater than or equal to the network bias Z_I^{nd}.

7.1.7.2 Loop and Void Growth Rates

Growth rates for loops and voids were calculated as a function of temperature for network dislocation densities of 10^8 and $10^{11}/cm^2$ and bias factors $Z_I^{\ell 2}$ of 1.0, 1.02, 1.05, and 1.1. Values assumed for the microstructural parameters were $N_c = 10^{14}/cm^3$, $N_{\ell 1} = 10^{10}/cm^3$, $N_{\ell 2} = 10^{15}/cm^3$, $r_c = 10^{-7}$ cm, $r_{\ell 1} = 10^{-7}$ cm, and $r_{\ell 2} = 10^{-7}$cm. $Z_I^{\ell 2}$ was equal to $b_1 Z_I / b_2$, the network bias factor Z_I^{nd} equaled 1.05, and the displacement rate G was $10^{20}/cm^3$. The results are given in Figs. 7 through 9.

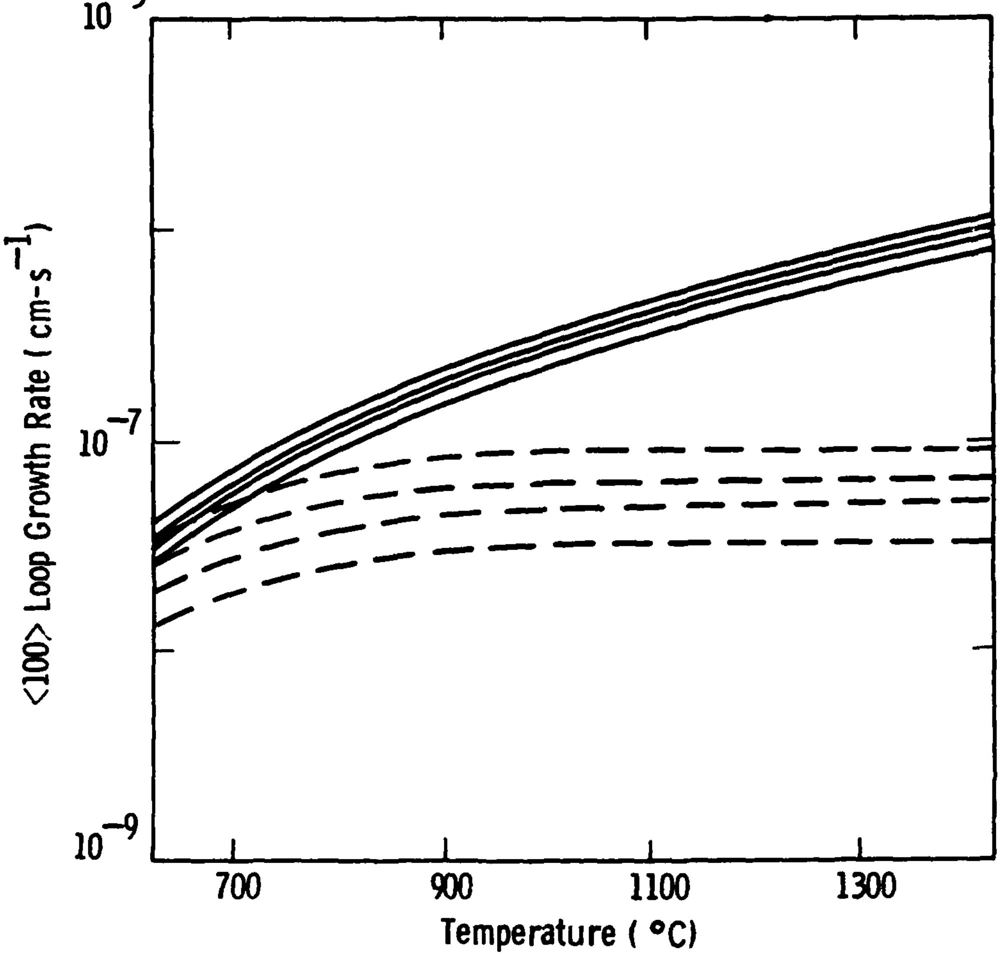

Figure 7. Growth Rate for <100> Loops as a Function of Temperature. Solid Curves are for a Network Disclocation Density L of $10^8/cm^2$; Dashed Curves are for L = $10^{11}cm^2$. Curves in Each Set are for Bias Factors $Z_I^{\ell 2}$ = 1.0, 1.02, 1.05, and 1.1 in an Ascending Sequence, with $Z_I^{\ell 1} = b_1 Z_1^{\ell 2}/b_2$. Irradiation and Microstructure Parameters are Given in the Text.

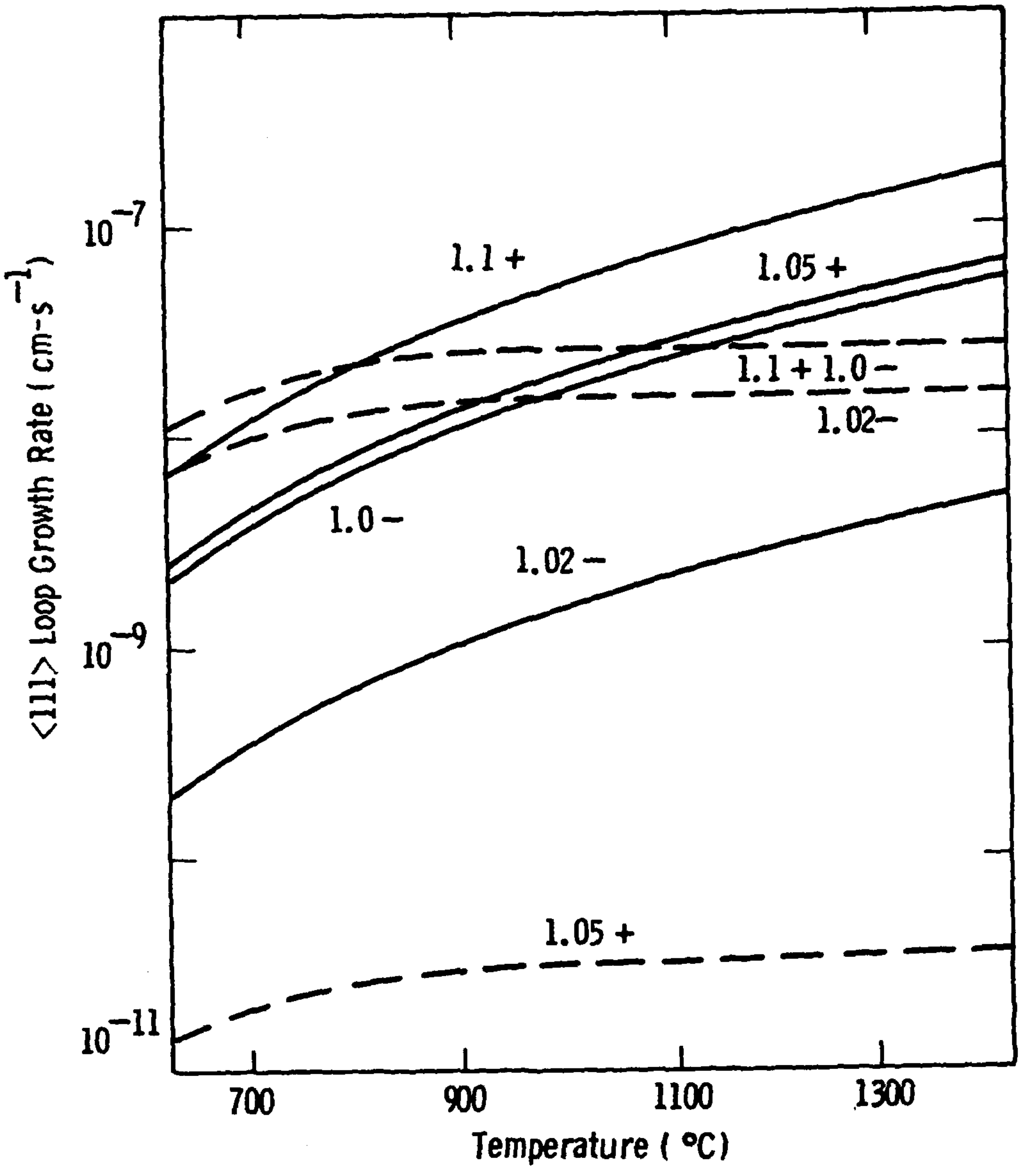

Figure 8. Growth Rate for <111> Loops as a Function of Temperature. Solid Curves are for a Network Dislocation Density L of $10^8/cm^2$; Dashed Curves are for L = $10^{11}/cm^2$. Curves in Each Set are for Bias Factors $Z_I^{\ell 2}$ Values with the Sign Indicating Growth (+) or Shrinkage (-). Irradiation and Microstructural Parameters are Given in the Text.

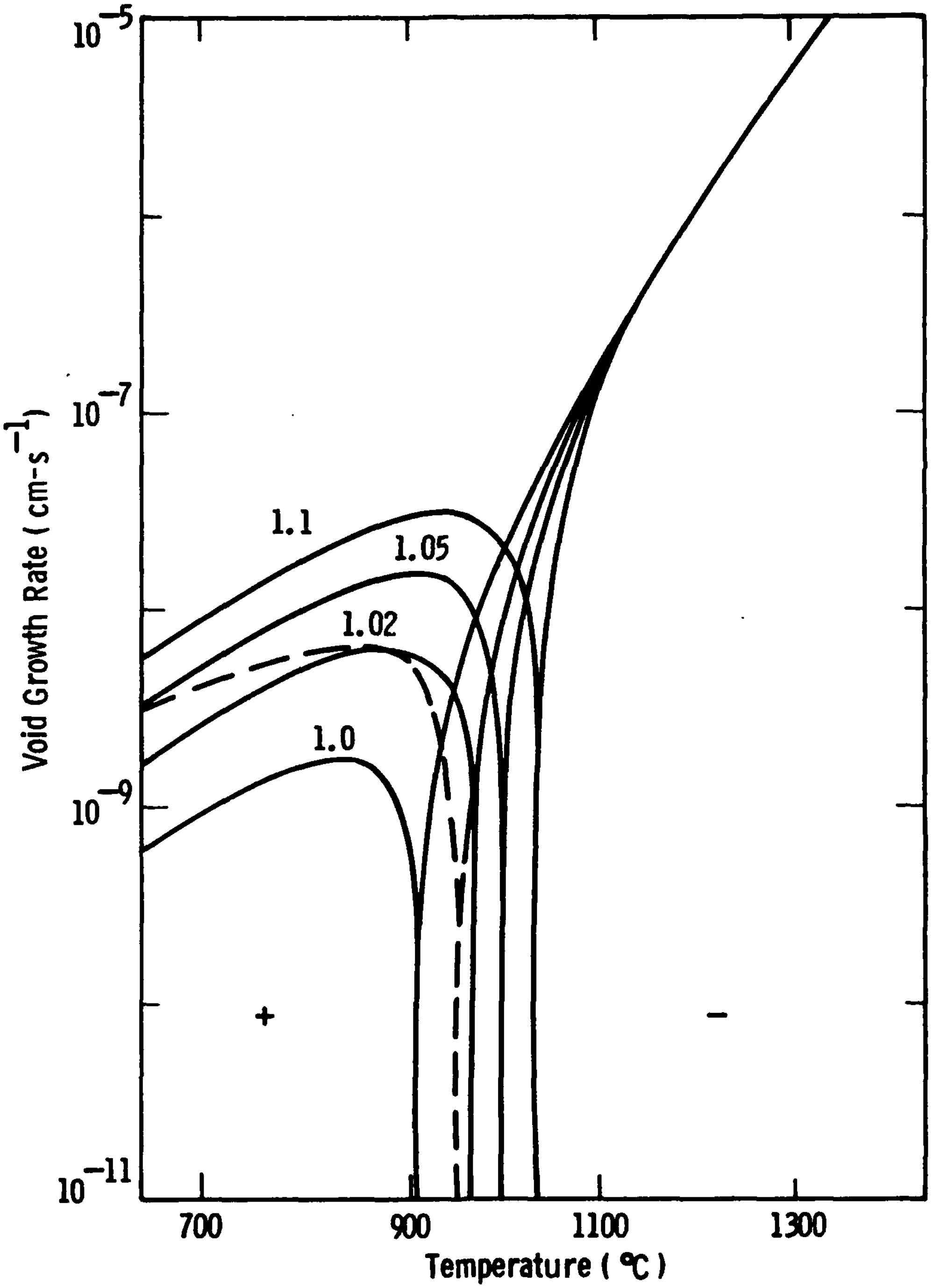

Figure 9. Growth Rate for Voids as a Function of Temperature. Solid Curves are for a Network Dislocation Density L of 10^8/cm^2 and are Labeled by Assumed $Z_I^{\ell 2}$ values. Dashed Curve is for a Network Density L = 10^{11}/cm^2, and for all Values of $Z_I^{\ell 2}$ Investigated. (+) Sign Indicates Growth Regime; (-) Sign Indicates Shrinkage Regime.

For the low network density, the growth rate of <100> loops increases monotonically with temperature as shown in Fig. 7, and, at a given temperature, increases slightly as $Z_I^{\ell 2}$ increases from 1.0 to 1.1.

When the network density is high, the growth rate increases with temperature from 625° to ≈925°C; at higher temperatures it maintains a constant value. The dependence of the growth rate on $Z_I^{\ell 2}$ is stronger, again increasing as $Z_I^{\ell 2}$ increases from 1.0 to 1.1.

As shown in Fig. 8, the temperature dependence of the <111> loop growth rate at low and high network dislocation densities is similar to that of the <100> loop growth rate. The magnitude and sign, however, depend on the choice of loop bias factor, as discussed in the previous section. When $L = 10^8/cm^2$ and $Z_I^{\ell 2} = 1.0$, the <111> loop shrinks at a rate of $\approx 2 \times 10^{-9}$ cm/s at 625°C and $\approx 6 \times 10^{-8}$cm/s at 1425°C. For $Z_I^{\ell 2} = 1.02$, the shrinkage rate is an order of magnitude less at all temperatures. When $Z_I^{\ell 2} = 1.05$, <111> loops grow at rates which are comparable in magnitude to the shrinkage rates for $Z_I^{\ell 2} = 1.0$. An increase of the bias factor to 1.1 leads to roughly a factor of two increase in the growth rate over the $Z_I^{\ell 2} = 1.05$ values.

At the high network density, the growth rate is negative for $Z_I^{\ell 2} = 1.0$ and 1.02, with a decrease in magnitude for the latter values of less than a factor of two. The growth rate for $Z_I^{\ell 2} = 1.05$ is positive, but small -- three orders of magnitude lower than that for $Z_I^{\ell 2} = 1.1$.

The effects of network dislocation density and loop bias factors on the growth rate of voids are illustrated in Fig. 9. All of the curves are qualitatively similar: at low temperatures the growth rate is positive, increases with increasing temperature, then peaks and decreases rapidly to zero, at a temperature which will be henceforth referred to as the critical temperature, T_c. At a temperature above T_c, the growth rate is negative and the void shrinks at an increasing rate. Above ≈1100°C, the shrinkage rate is independent of both dislocation density and the values of $Z_I^{\ell 1}$ and $Z_I^{\ell 2}$ since in this regime, the thermal emission term in Eq. (34) is dominant. For a network density of $10^8/\mathrm{cm}^2$, the void growth rate depends on the values of the loop bias factors, increasing by roughly an order of magnitude at low temperatures as $Z_I^{\ell 2}$ increases from 1.0 to 1.1. The peak temperature, T_p, increases as $Z_I^{\ell 2}$ increases, having values of 850°C, 875°C, 910°C and 935°C for $Z_I^{\ell 2}$ values of 1.0, 1.02, 1.05, and 1.1, respectively. T_c also increases with increasing bias factor, with values of 900°, 950°, 990°, and 1025°C. For the assumed microstructural conditions, the <111> loops are the dominant sink for interstitials and increasing bias on the loops means increasing absorption of interstitials. The vacancy supersaturation and void growth rate therefore increase.

For a network density of $10^{11}/\mathrm{cm}^2$, the void growth rate is controlled by the absorption of interstitials at network dislocations and is independent of the loop bias factors. The peak temperature is ≈860° and T_c is ≈950°C.

7.1.7.3 **Helium**

The effect of helium on the cavity growth rate is illustrated in Fig. 10. The curves were obtained for an assumed bias factor $Z_I^{\ell 2}$ of 1.02, although the results are qualitatively similar for other values as well. The microstructural parameters and irradiation conditions used for the calculations were identical to those for Figs. 7 through 9, with network density $L = 10^8/\mathrm{cm}^2$. Each of the curves in Fig. 10 is labeled by the ratio of the gas pressure P_g in the cavity to the equilibrium pressure given by $P_g^{eq} = 2T/r_c$. The helium was treated as an ideal gas.

Three trends are immediately evident as the gas pressure in the cavity increases: the peak temperature T_p increases, the maximum growth rate

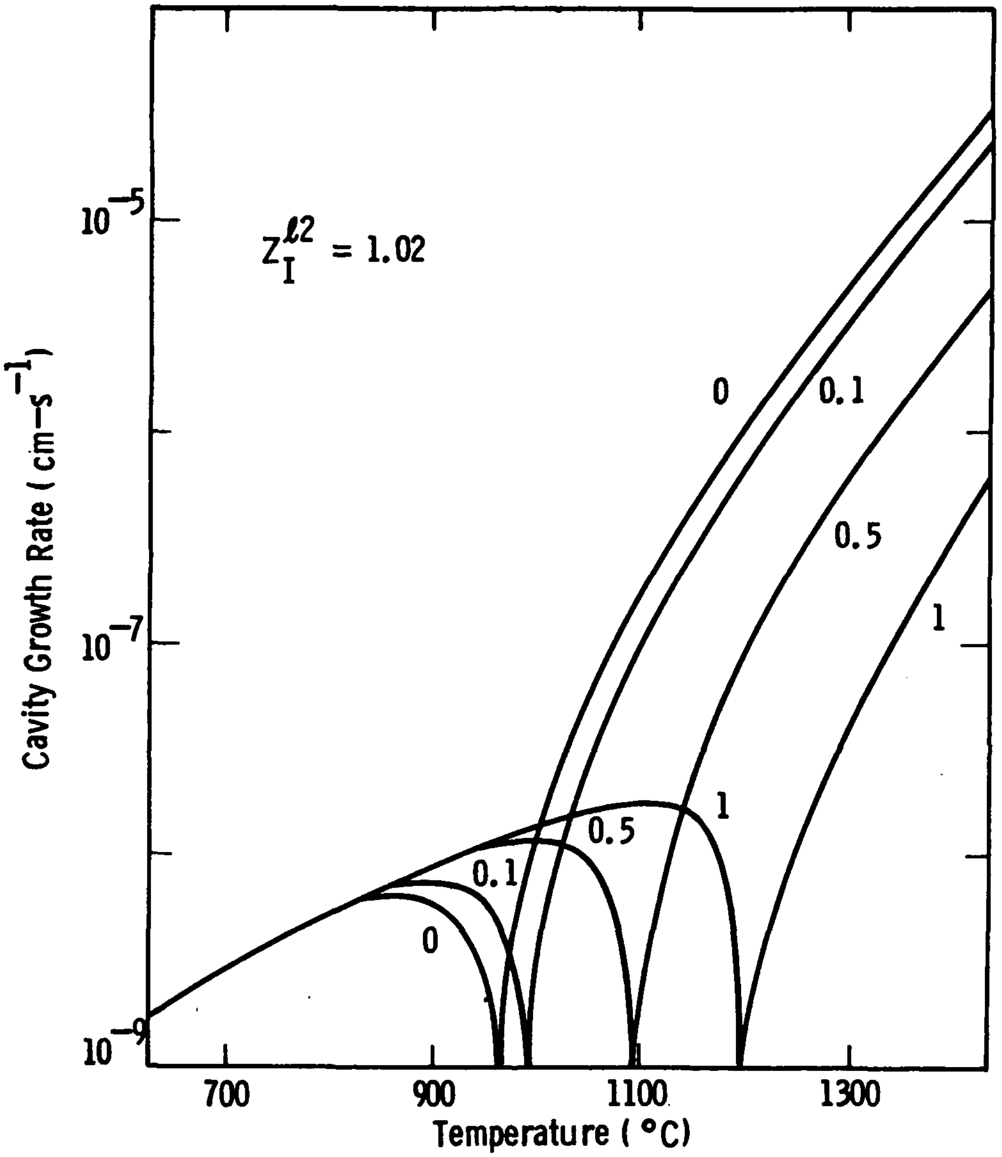

Figure 10. Cavity Growth Rate as a Function of Temperature for L = $10^8/\text{cm}^2$, $Z_I^{\ell 2}$ = 1.02, and Other Parameters as Given in Text. Curves are Labeled by Ratio P_g/P_g^{eg}.

increases, and the critical temperature T_c increases. In Fig. 11, T_c and T_p are plotted as a function of the ratio P_g / P_g^{eg}. Both increase linearly, with T_c having a greater slope.

Swelling vs temperature or S(T) plots for various helium injection rates can only be obtained from a full model calculation, where the size distribution functions for cavities are calculated as a function of irradiation time at various temperatures. Figures 10 and 11, however, can be used to predict several qualitative features of these plots. First, for temperatures between 625°C and 825°C, Fig. 10 shows that the cavity growth rate does not depend on gas pressure, for the range of pressures considered. In this temperature regime, the rate of vacancy emission from cavities is small, cavity growth is determined by the bias, and S(T) plots will be insensitive to the helium injection rate.

Second, since the peak cavity growth rate increases in magnitude and occurs at higher temperatures as gas pressure increases, a temperature shift will be observed for the peak swelling temperature as helium injection rate increases. Third, since T_c increases more rapidly with gas pressure than T_p, the high temperature end of the S(T) plot will broaden as helium injection rate increases.

7.1.8 Summary of Results of Calculations

When microstructural evolution in body-centered cubic metals is described using the formalism of the chemical reaction rate theory, the details of dislocation loop and void or cavity growth depend strongly on the interstitial preference or bias factors of the dislocations in the system. Whether loops of <100> type grow or shrink, the magnitude of loop and cavity growth rates, and the temperature dependence of the cavity growth rate are determined by the (relative) values assumed for these factors, when they are treated as size-independent model parameters. Over the range of microstructural and irradiation conditions investigated, however, shrinkage of cavities in the bias-driven regime (i.e., at low and moderate temperatures) was not observed. For this to occur with the model presented here, a low dislocation density, a high <111> loop density, and a bias factor for <111> loops less than 1 would be required.

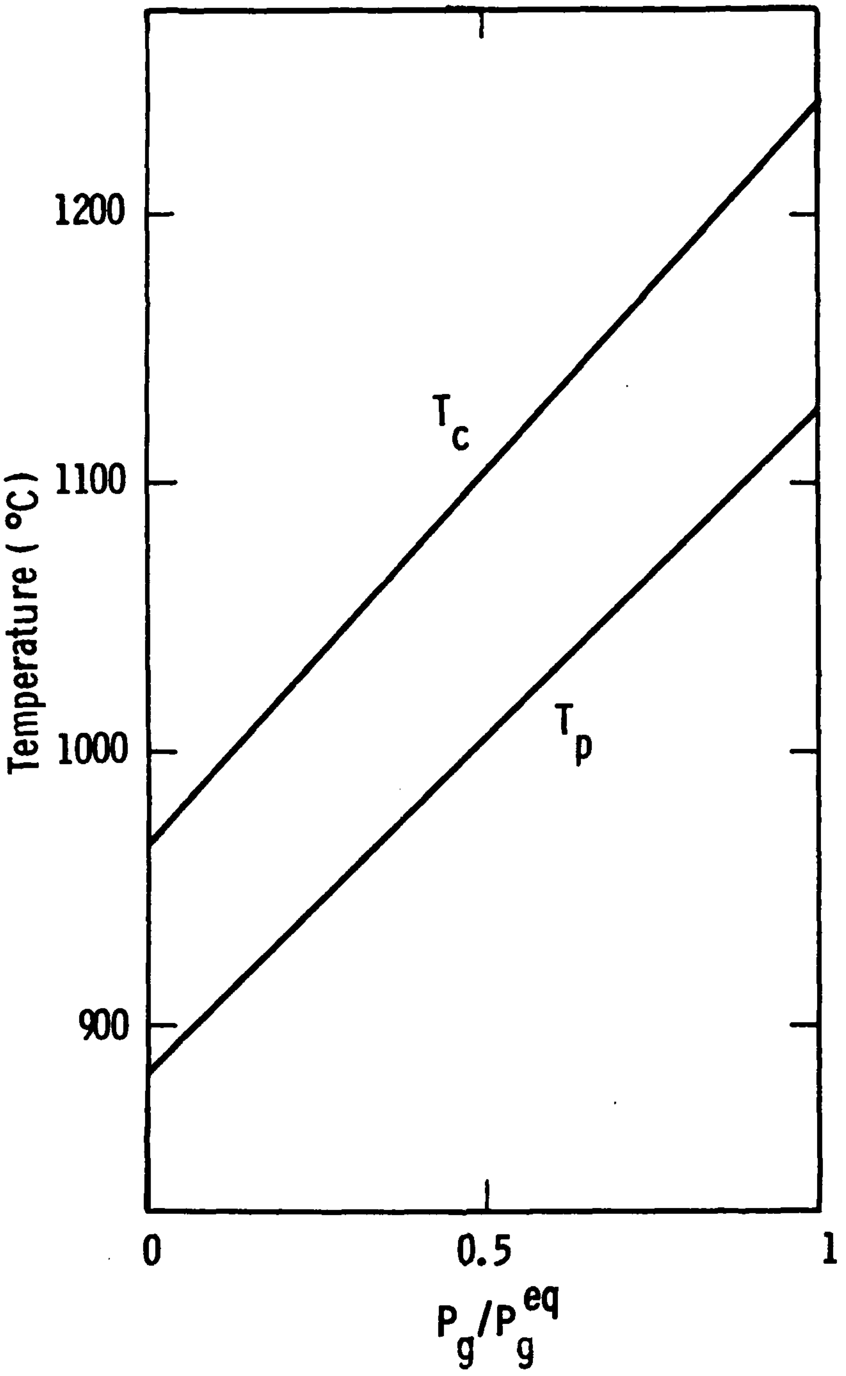

Figure 11. Critical Temperature T_c and Peak Growth Temperature T_p as a Function of Ratio P_g/P_g^{eg}.

The sensitivity of microstructural evolution to the dislocation bias factors in the body-centered cubic metals over the midrange of temperatures suggests that this would be a fruitful regime for experimentation. In this regime, critical tests of theories on bias factors, which provide the fundamental basis for current models of cavity swelling, may be possible.

The model calculations presented here predict that, when helium is present, the temperature range for swelling is increased at the high temperature end and the peak temperature shifts to a higher temperature. These effects of helium in body-centered cubic metals are qualitatively similar to those observed in face-centered cubic metals.

7.2 Experimental

7.2.1 Irradiation Facility

The investigation of high temperature swelling in refractory metals requires a facility capable of providing high current beams of heavy ions and helium, which can simultaneously bombard a specimen heated to a high temperature ($0.6T_m$, approximately 1375°C for Nb). Experimental facilities capable of meeting these stringent requirements, together with high vacuum capability, high isotopic purity of incoming ions, and diagnostics ability, are limited in number. A survey of existing accelerator facilities was therefore conducted to evaluate the best facility for this work. The evaluation also included turnaround times, schedular availability, and unit costs. The following four facilities were considered as candidates:

1. Dual-ion irradiation facility at the Oak Ridge National Laboratory
2. HVEM Tandem Facility at the Argonne National Laboratory (ANL)
3. Irradiation Facility at the Pacific Northwest Laboratory
4. High Energy Ion Bombardment Studies (HEIBS) Facility at the University of Pittsburgh.

Of these four facilities only the HVEM Tandem facility at ANL satisfied all of the program requirements and therefore was contracted to perform the irradiations. A brief description of the facility is provided.

The HVEM Tandem facility consists of a Kratos 1.2 MV high voltage transmission electron microscope, a National Electrostatics 2-MV Tandem type universal ion accelerator, and a Texas Nuclear 300 KV ion accelerator. The two accelerators together provide ion beams of essentially all elements with energies from approximately 10 KeV to 8 MeV. The facility is located in the Materials Science and Technology Division at Argonne National Laboratory.

7.2.1.1 2-MV Tandem Accelerator

The National Electrostatics Type 2 UDHS 2.0-MV Tandem accelerator is equipped with one internal and two external negative ion sources for helium and metal ions, respectively. The specifications are given in Table VI.

Table VI. Specifications of Tandem Accelerator

Terminal Voltage	180-2000 kV
Charging System	1 pelletron chain
Energy Stability	±250 eV
Internal Ion Sources	Danfysik Models 910 & 911 Duoplasmatron
External Ion Sources	
He^-	NEC Alphatros
metal Ions	Wisconsin SNICS Type
Ion Beams	All stable isotopes in the periodic table
UHV Beam Transport System	
Target Room Beam Lines	
West Lines	45° (220)*, 30° (480),
East Lines	8° (6560), 10° (4200), 20° (1060), 30° (480), 45° (220)

* Numbers in parentheses indicate mass energy products (amu·MeV).

The accelerator may be operated in conjunction with the HVEM or separately for ion implantation/bombardment and ion beam analysis studies. Independently powered internal positive ion and external negative ion sources are provided both to obtain all ion species in the periodic table and to minimize downtime caused by ion source malfunction. Available positive ion sources are Danfysik models 910 and 911, a duoplasmatron, a sputter source, and an rf source. Negative ion sources presently available are an NEC Alphatros rf source for He^- ions and a Wisconsin type SNICS source for producing negative ions of selected metals. All ion sources are controlled by fiber-optic telemetry, which also provides direct readout of source parameters at the control console. Access to the internal source may be gained within one hour with use of the high-throughput gas recovery system which serves both the HVEM and the accelerator. Typical ion beam currents will range from ≈10 μA for protons to 0.1 μA for $^{204}Pb^{\pm}$. The mass energy product of the East and West 30° beam lines provides for singly charged ions with an atomic mass of 240 at an energy of 2 MeV.

The 300-KV ion accelerator is a modified Texas Nuclear high current unit that has been equipped with sources for metal and gaseous positive ions. This accelerator will be used to provide helium ion beam for the present program.

The NEC/University of Wisconsin SNICS (Source of Negative Ions through Cesium Sputtering) and negative ion source, with ANL modifications to facilitate target mounting and to provide target cooling, was used to perform the experiments. The source yielded a ion current of ≈40 nA with a metallic Nb target. The flux of ions was too low to perform high fluence (≈60 dpa) irradiations in a reasonable amount of time. Therefore, a novel approach was required to achieve a higher ion output. After a considerable effort, a procedure analogous to the production of titanium ions was successful in achieving high ion currents of niobium. This procedure requires a hydride target material. A special hydriding method was developed at ANL to obtain Nb-hydride. The process involves heating the Nb sample to high temperature under vacuum, backfilling the vacuum chamber with high purity hydrogen at room temperature to absorb the hydrogen and form a Nb-hydride compound. Use of Nb-hydride target improved the output of the SNICS source from ≈40 nA of Nb^- with a metallic source to ≈5-10 μA of Nb ions (Nb^-, NbH^-, NbH_2^-, NbH_3^-, etc.) with a hydrided target.

7.2.1.2 **Material Procurement and Specimen Preparation**

Niobium used in this investigation was Marz-grade foil (0.5 mm thick) obtained from the Materials Research Corporation. The material was received in an annealed condition, (1150°-1200°C for 0.5 h). The chemical composition of the material, as certified by the vendor is shown in Table VII. Overcheck analysis was conducted for the interstitial elements C, O, and N, with results also shown in Table VII. A substantial disagreement is apparent between the vendors analysis and the overcheck analysis.

The preparation of the specimen surfaces to be used for ion irradiations is a delicate and painstaking operation consisting of a number of polishing steps and optical examinations. This process was made more difficult in the case of high purity niobium because of its low hardness, and therefore, susceptibility to surface smearing and cold work. The cold work of the surface was manifested by "mounds" on the specimens. These "mounds" were more numerous near the specimen edges than towards the center, and were always found whenever diamond abrasives were used. The polishing procedure had to be modified to avoid use of high hardness abrasives, and the material removal from the surface to be irradiated was minimized to 50 μm (0.002 in).

Disc specimens, 3 mm (0.12 in) in diameter, were punched from the foil, deburred and mounted with crystal bond wax and cold mounted in a stainless steel holder with a 0.38 mm (0.015 in) recess and polished using a 600 grit paper to a thickness of 0.23 mm (0.009 in) with a final polish with 1 μm alumina. The specimens were then demounted and remounted with the flat 1 μm polished surface facing down, onto a stainless steel holder with 0.18 mm (0.007 in) recess. Two adhesives were then used to mount the specimens flat on the holder. First, specimens were placed on the holder in molten crystal bond wax. Each specimen was pressed to assure that the flat side was against the holder as the wax cooled. The wax from around the specimens was then removed and replaced with epoxy. This procedure assured a good and flat bonding of the specimens.

The specimens were then polished on 400 grit paper until they were flat and then gently polished with 6 μm and 1 μm alumina abrasive. During and after

TABLE VII

Chemical Analysis of Niobium Foil*

Element	Wt. ppm	
	Vendor Analysis**	Overcheck Analysis
H	<1	
C	25	33^{+}
N	<5	
O	15	120^{***}
Na	0.07	
Mg	0.45	
Si	17.0	
P	<0.1	
Al	3.6	
S	1.4	
Cl	0.7	
K	0.2	
Ca	0.1	
Ti	<0.1	
Cr	1.8	
Fe	3.4	
Ni	1.0	
Cu	<0.1	
Zn	0.5	
Ga	<0.1	
Zr	<0.1	
Mo	<0.1	
Pd	<0.1	
Ag	5.9	
In	<0.1	
Sn	<0.1	
Sb	<0.1	
Ta	200	
W	<0.1	
Pt	<0.1	
Au	<0.1	
Pb	<0.1	

* Marz Grade, Lot No. 41/2064, Foil 0.508 cm thick x 2.54 cm wide x 21.24 cm long

** Analysis by mass spectrography.

*** Analyzed by vacuum fusion analysis, average of two analyses.

\+ Leco method.

each polishing step, specimens were examined for flatness, scratches, and cold work. The final polishing step consisted of 12-15 h polishing with 0.05 μm alumina in a vibratory polisher. No cold work was observed on any specimens following the above procedure. Following the polishing, the specimens were demounted and cleaned ultrasonically in multiple baths of acetone and methanol.

The cleaned specimens were lacquered on one side and then electropolished for 20 s in a solution containing 12% HF and 88% HNO_3 maintained at 0^o- 5^oC. This step removed approximately 6 μm from the polished surface and produced a clean surface free of nearly all embedded abrasive. An additional 6-10 μm of material was removed from this surface by ion milling to assure a scratch and deformation-free surface.

Prior to irradiation each specimen was annealed at 1200^oC for 0.5 h in the vacuum chamber of the accelerator. This further assured that the irradiated surface was in the fully annealed condition, devoid of any deformation due to specimen preparation. The temperature was monitored by an infrared temperature monitor (IRCON 300 HCS). After cleaning the specimens, they were stored in 200 proof ethanol to avoid oxidation.

7.2.2 Irradiation Procedure

The specimens were loaded into a tantalum holder. The holder consists of a tantalum strip with 5 holes approximately 2.3 mm in diameter and with a 3 mm recess on one side. The specimens were secured by four tantalum tabs spot welded to the specimen holder. The tabs held the specimen by friction, therefore the specimen was free to move in all directions during annealing and irradiation. This avoided any deformation due to clamping. Four specimens were loaded at one time into the holder (the fifth hole was used to align the beams). The specimen holder had freedom in the x and y directions to enable accurate alignment with the beams. A photograph of the specimen holder and the electron gun heater is shown in Fig. 12.

The specimens were irradiated with 5.3 ± 0.1 MeV Nb^{++} ions at a nominal maximum displacement rate of approximately 6×10^{-3} dpa/s (displacements per atom per second). The target peak dose was approximately 60 dpa. The energy

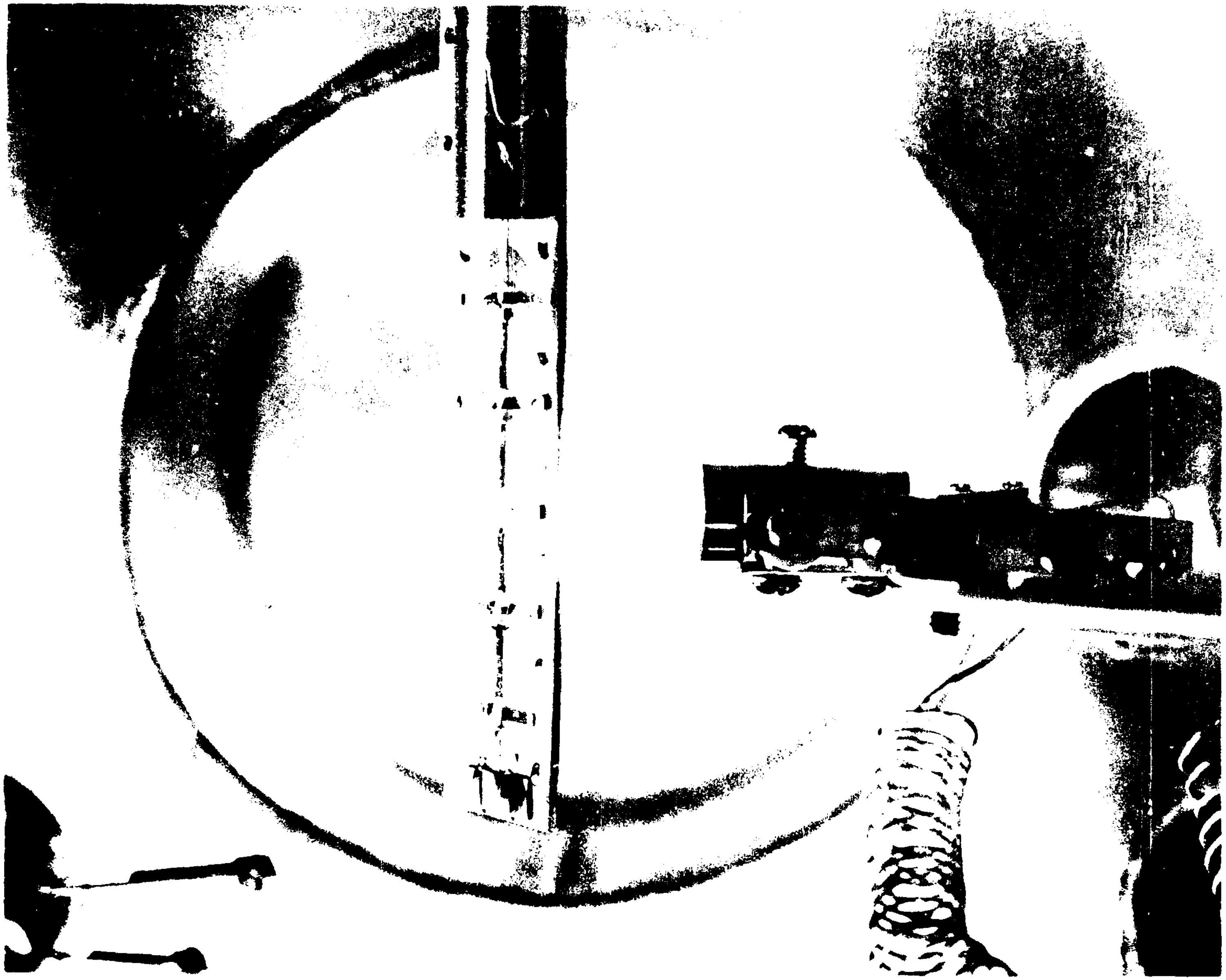

Figure 12. A Photographic View of the Target Holder and Electr[illegible] Arrangement.

deposition profile for Nb was calculated using Biersack's TRIM Monte Carlo program. Figure 13 shows the energy deposition and projected range probabilities for Nb in Nb at an incidence angle of 10^{o}. The maximum energy deposition for 5.3 MeV Nb^{+++} bombardment was computed to occur at a depth of ≈900 nm. The calculated dpa values have an accuracy of ± 10%. In calculation of dpa, a displacement energy of 40 eV and an atomic density of 5.6 x 10^{22} atoms/cm^3 were assumed for Nb.

The implantations were performed at target temperatures ranging from 700^{o} to $1300^{o}C$. The samples were individually heated to the desired temperatures using an electron beam heating system designed at ANL. The temperature was controlled using a feedback signal from an infrared pyrometer (IRCON 300 HCS) to the electron beam heater. The surface emissivity was assumed to be 0.19 independent of temperature and direction. The temperatures were controlled to within ± $5^{o}C$.

Prior to the irradiation and with the sample at room temperature, the all-metal vacuum sorption pumped system was evacuated to a base pressure of ≈2-5 x 10^{-9} torr. Typical vacuum levels achieved during annealing and irradiation are shown in Table VIII. Residual gas analysis of the chamber gases was performed during the annealing and irradiation stages using a Micromass QX200 quadrapole mass spectrometer. The major peaks during the irradiations were identified as being associated with nitrogen, water, and hydrogen.

Table VIII

Vacuum Conditions During Annealing and Irradiation

Irradiation Temperature (^{o}C)	Vacuum During Annealing (torr)	Vacuum During Irradiation (torr)
700	5.0×10^{-8}	4.0×10^{-8}
800	1.0×10^{-7}	4.0×10^{-8}
900	2.0×10^{-7}	2.0×10^{-8}
1000	4.0×10^{-8}	2.0×10^{-8}
1100	6.0×10^{-8}	6.0×10^{-8}
1200	6.0×10^{-8}	7.0×10^{-8}
1300	4.5×10^{-8}	5.0×10^{-8}
700 (10 dpa)	3.0×10^{-8}	3.0×10^{-8}

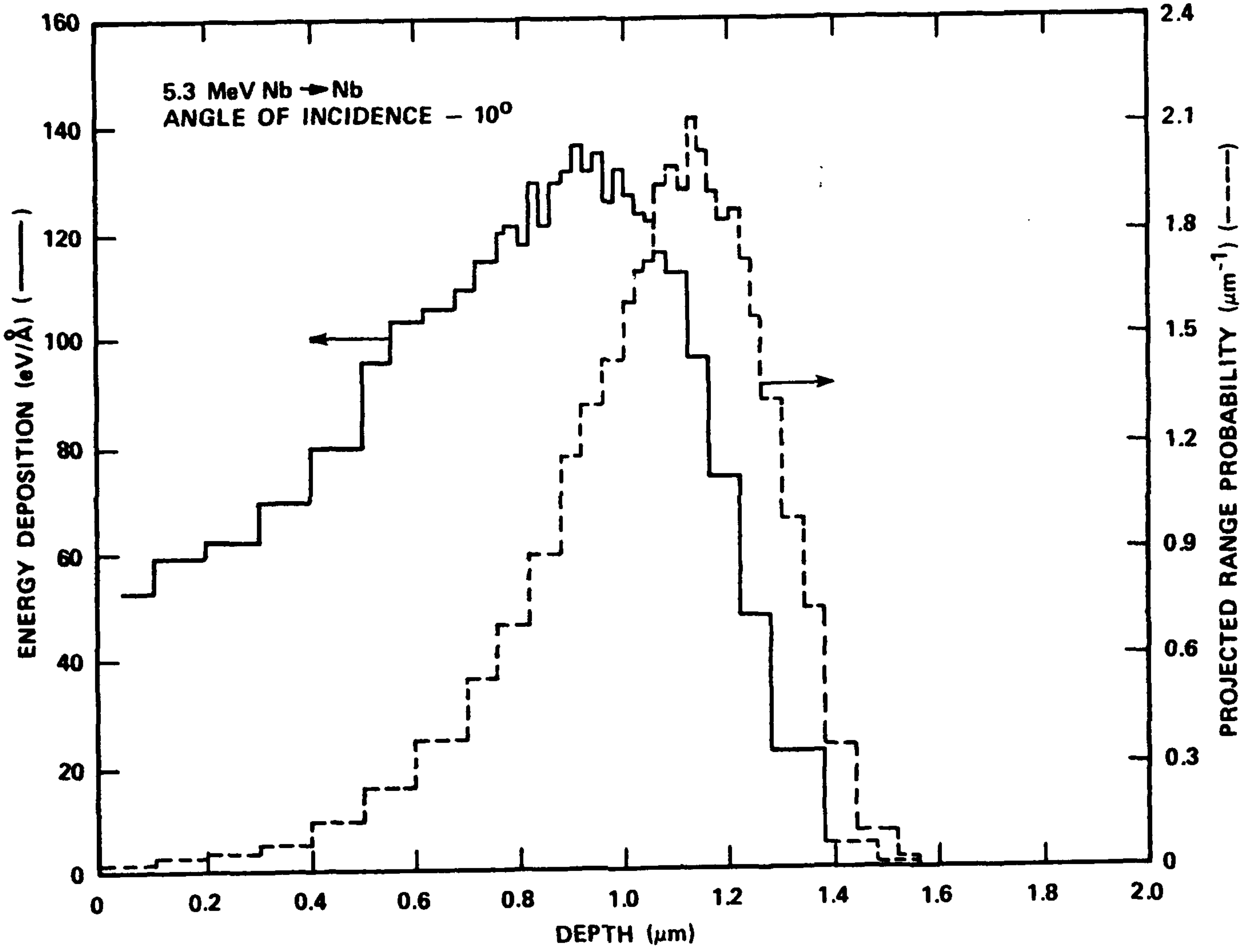

Figure 13. Energy Deposition and Projected Range Probability for Niobium Irradiated with 5.3 MeV Nb^{++} at an Incidence Angle of 10°.

The first 700°C specimen irradiation was performed at incidence angles of 10° and 45° to the specimen normal for equal times to spread the damage zone. However, it was realized that gradient effects may introduce microstructural changes which may be difficult to interpret; therefore, in subsequent experiments the irradiations were conducted at a single incidence angle of 10°.

7.2.3 Post-Irradiation Specimen Preparation and TEM Observations

Post-irradiation specimen preparation involved removal of a controlled amount of material from the front surface (sectioning) so that the peak or near peak region of the damage could be examined in the transmission electron microscope (TEM). This method yielded data in the region of high damage away from the region most susceptible to surface effects. A Siemens Elmiskop 101 TEM operating at 100 kV was used in this work.

The sectioning was accomplished using an ion-milling technique. Ion milling involves removal of material by ion sputtering using inert gas ions, such as argon or krypton, accelerated to approximately 1 KeV. In our experiments, ion milling was accomplished using argon gas accelerated to 800 eV. The specimens were rotated and tilted continuously during milling to achieve a uniform milling of surfaces. Prior to sectioning of irradiated specimens, the ion-milling rate was calibrated using the same surface finish as the pre-irradiated specimens. Figure 14 shows a plot of ion-milling depth as a function of milling time. This master plot was used to determine the time required for sectioning. All specimens except one were sectioned to remove 750 nm.

The irradiated surfaces of the ion-milled specimens were protected by stop-off lacquer and the specimen was back-thinned using a modified Fischione Jet Polisher. One jet of the twin-jet polisher was removed to enable polishing from only the back side of the specimen. Considerable effort was expended in arriving at an appropriate thinning method for the specimens. A number of chemical solutions and conditions were investigated before a satisfactory polish was obtained. A solution of approximately 10% saturated NH_4F in 90% methanol at -30°C was found to produce a good polish in a reasonable time. A current of 12 mA at 100 V was required to polish a 1 mm diameter area in the modified

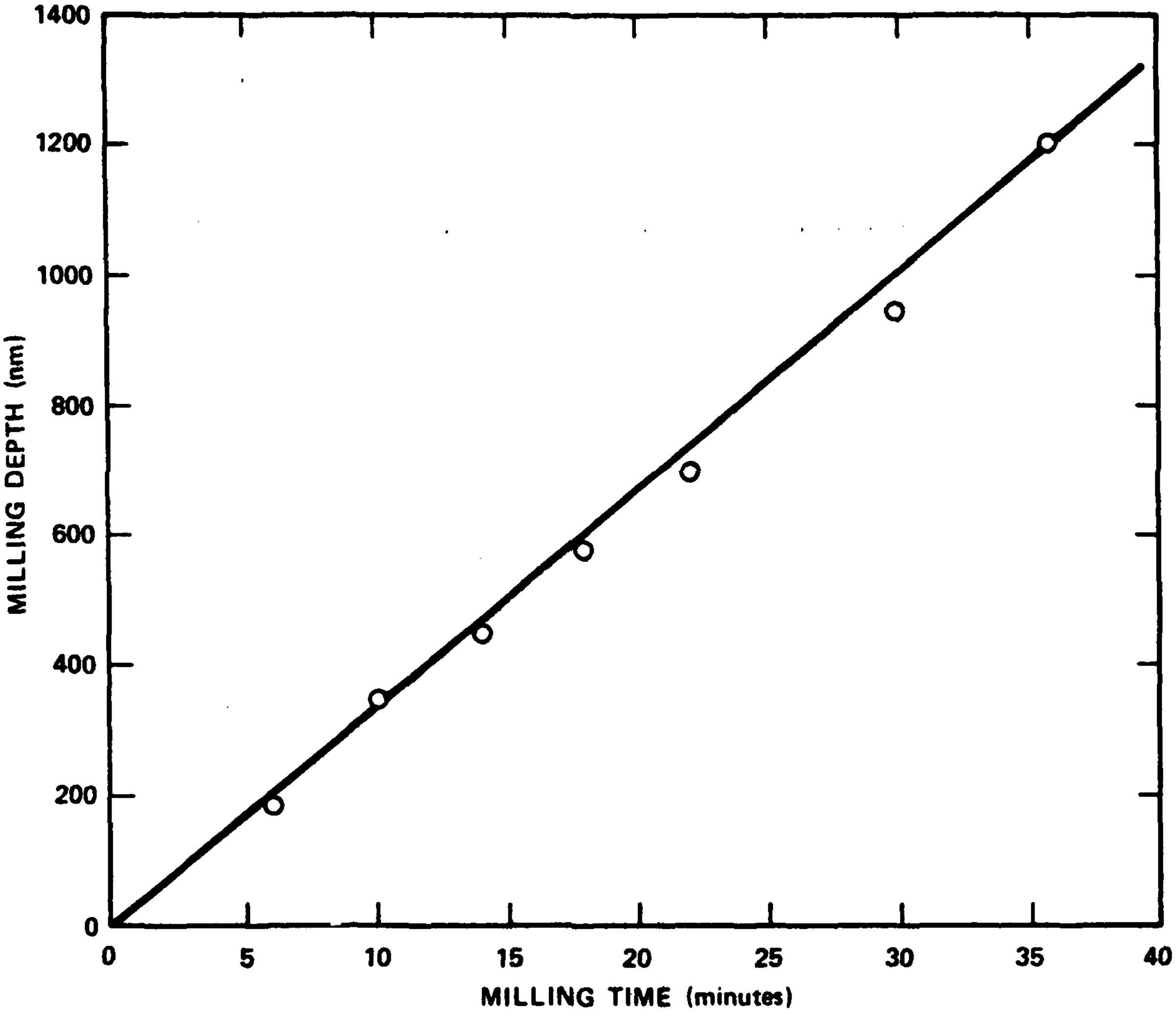

Figure 14. Ion Milling Calibration Curve for Niobium.

Fischione holder. The latter modification was deemed necessary to insure that the perforation and therefore the TEM observation was made in the area of the specimen where the ion beam was most uniform in intensity.

After removal of the specimen from the polishing holder, a gentle concave bowing of the top surface was observed. This may be indicative of some deformation of the specimen due to its softness. The bow was not considered to be a major problem.

TEM observation of an as-prepared specimen showed a thin oxide layer on the surface. This oxide layer was effectively removed by ion milling both surfaces for a duration of 5 minutes each at a low glancing angle of approximately 10^{o} in a Gatan ion miller. It was estimated that this process removed ≈10-20 nm from each surface.

7.2.4 Analysis of Data Obtained from TEM

TEM micrographs were taken at typical magnifications of 40,000X and 75,000X. The voids were imaged in kinematic diffraction conditions in a slightly out-of-focus condition to obtain the true size of the voids. The dislocations and loops were imaged in two beam (dynamical diffraction) conditions. The voids were imaged in stereopairs to enable the determination of foil thickness. The dislocation and loops were imaged in the same areas as the voids to enable the determination of their densities.

The photographic plates were enlarged to a final magnification of 100,000X to 500,000X. Foil thickness was determined by using the following formula:

$$t = \frac{P}{2\ M \sin \theta/_2},$$

where P is the parallax between surface features in a stereopair, M is the magnification, θ is the tilt angle, and t is the foil thickness.

The size and number of microstructural features were analyzed using a Zeiss particle size analyzer.

From the micrographs, the following parameters were evaluated.

(1) Diameter of the voids, d_i, in a size classification.

(2) Number of voids per cm^3, n_i, in a size classification.

(3) Void density $\rho_v = \Sigma F_{ti} \cdot n_i$/foil volume, where F_{ti} is the correction factor for surface intersection.

(4) Number of loops per cm^3.

(5) Average swelling defined by $\frac{\pi}{6} \sum_i F_{ti} n_i d_i^3$

(6) Weighted average diameter, d_v, of void, defined as

$$= \left(\frac{\sum_i F_{ti} n_i d_i^3}{\sum_i F_{ti} n_i} \right)^{\frac{1}{3}}$$

The void parameters were calculated from the void diameters measured on the micrographs. Most of the foils were oriented with the normal in a <111> direction. The diameter of the void was taken as the diameter of a circle inscribed within the black fringe around the void. This void dimension gives an upper bound estimate of swelling, especially at high temperatures (>1000°C) where voids showed less truncation of the cuboidal shape. Assuming a perfect cube projected on a (111) plane, the measured equivalent sphere diameter is $a\sqrt{2}$ (where a is the cube edge). The corresponding swelling is therefore overestimated by 32%. In reality, however, not all voids showed perfect cuboidal shapes and therefore the errors are estimated to be less than 30% in swelling and less than 10% in weighted average diameter. At low temperatures, where voids were truncated in the <100> and <111> directions, the errors are even less since they can be more closely approximated as spheres.

For each specimen (except for those irradiated at 700°C) at least four micrographs were analyzed for void swelling to obtain a statistical estimate of the swelling parameters.

7.2.4.1 Correction Factor F_t for Surface Intersections

Voids exposed at the foil surface during electropolishing quickly erode to larger sizes and more irregular shapes, and may lose observable contrast. This occurrence was quite common in the niobium specimens examined, especially those with large voids. ASTM(86) has recommended corrections for obtaining bulk representative void densities from TEM micrographs. This correction involves exclusion of the voids whose centers lie within 0.5 d_i (d_i = void diameter) of each foil surface. This approach is not practical in many cases where a large number of measurements are required from many areas of foils at different magnification, and where a non-homogeneous distribution of cavities occurs or where thin areas of foils are examined. A correction factor suggested by Spitznagel et al.,(87) which avoids many of the problems, was therefore used here. The correction factor, F_t, is defined such that

$$F_t = n_i = U_c \cdot A_A = \frac{2D_i}{2D_i + 3t} A_A$$

where n_i =number of cavities in size class i

U_c =Underwood correction factor to the specific projected area of the particle per unit test area, A_A

D_i =diameter of cavities in size class i

t =foil thickness

it can be shown(88) that

$$F_t = \frac{3t}{2D_i} \quad \frac{2D_i}{2D_i + 3t}$$

If the number of cavities in each size class is multiplied by F_t, a volume fraction corrected for truncation of cavities, with centers either inside or outside of the foil volume imaged, is obtained. Every feature thought to be an image of a cavity, regardless of its proximity to the foil surface, can thus be counted and sized on the projected image. A numerical exclusion at void size of $D^i > t$ further ensures that an unrealistically large reduction in cavity volume fraction is not introduced. The factor, F_t, was included in all calculations of parameters defined in section 7.1.4.

7.3 Results

The results from the transmission electron microscopy (TEM) of the Nb specimens irradiated from 700°C (0.35 T_m) to 1300°C (0.57 T_m) are presented in Table IX. This table lists the damage levels, swelling, void number density, void size and dislocation density for each of the specimens examined. Additionally, ranges in swelling, void number densities, and void sizes are included. These ranges were obtained from the analysis of multiple areas of a specimen.

Figure 15 shows swelling as a function of irradiation temperature. Swelling was observed at temperatures from 700° to 1200°C. No voids were observed in the specimen irradiated at 1300°C. As seen in Fig. 15, the swelling increased from 700° to 900°C, reached a peak of 7% at 900°C and decreased slowly there- after, with increasing temperature, to zero at 1300°C.

The void number density, expressed as voids per cm^3, is plotted as a function of irradiation temperature, in Fig. 16. The maximum void density was observed at the lowest irradiation temperature of 700°C, where the density was 1×10^{16} cm^{-3}. The void density decreased gradually, to 1×10^{15} cm^{-3}, over a temperature range of 700°-900°C. From 900° to 1000°C the void density decreased rapidly to 5×10^{13} cm^{-3} and then decreased gradually from 1000° to 1200°C.

The decrease in void density was accompanied by an increase in the average void size as shown in Fig. 17. At 700°C, the average diameter of voids was 10 nm. The void diameter increased to ≈45 nm at 900°C and then increased to 110 nm

Table IX

Summary of Swelling Data

Irradiation Temperature (^oC)	Dose dpa	Swelling Range, %	Swelling Avg., %	Number Density Range, cm^{-3}	Number Density Avg., cm^{-3}	Diameter Range, nm	Diameter Avg., nm	Dislocation Density, Avg., cm^{-2}
700	10 ± 2	-	0.5	-	4.8×10^{16}	-	6	-
700*	32 ± 4	0.6-0.8	0.7	$1\text{-}1.2 \times 10^{16}$	1.1×10^{16}	10.5-10.8	10.7	-
800	54 ± 9	2.3-2.9	2.6	$4.1\text{-}6.9 \times 10^{15}$	5.9×10^{15}	19.3-22.5	20.7	6×10^{10}
900	50 ± 9	5.8-7.9	7.0	$1\text{-}1.8 \times 10^{15}$	1.4×10^{15}	44.1-49.9	47.0	4×10^{10}
1000	57 ± 10	3.6-4.9	4.3	$4.1\text{-}6.3 \times 10^{13}$	5.52×10^{13}	107.5-118.3	115.9	3×10^{10}
1100	53 ± 9	2.4-3.2	2.7	$2\text{-}3.4 \times 10^{13}$	2.8×10^{13}	118.2-135.4	125.5	3×10^{10}
1200	52 ± 9	1.24-2.74	2.15	$1.9\text{-}3.1 \times 10^{13}$	2.75×10^{13}	92.7-140.8	116.5	2×10^{10}
1300	54 ± 9	-	-	-	-	-	-	-

---

*Specimen irradiated at incidence angles of 10° and 45° for equal times.

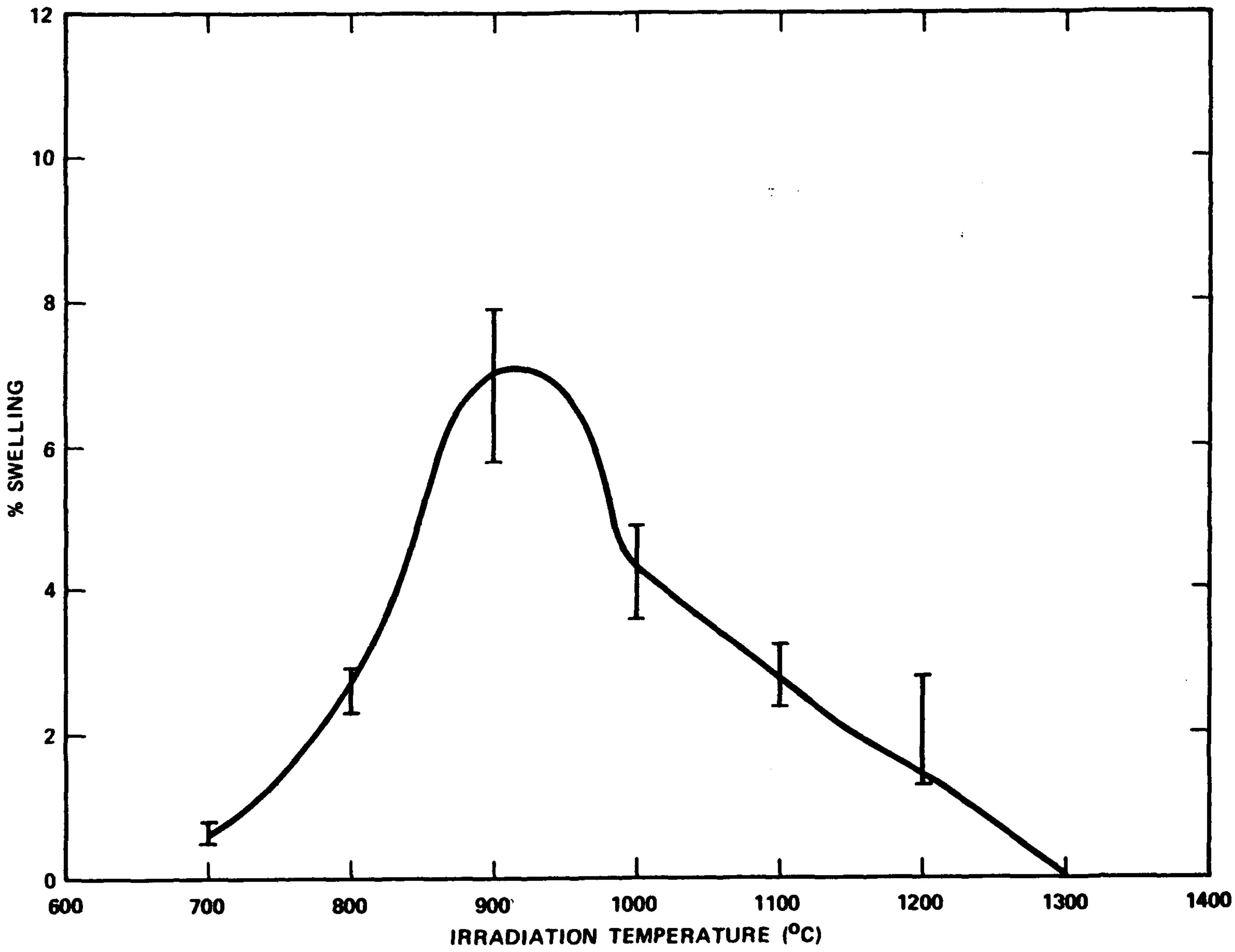

Figure 15. Swelling as a Function of Irradiation Temperature for Self-Ion Irradiated Niobium.

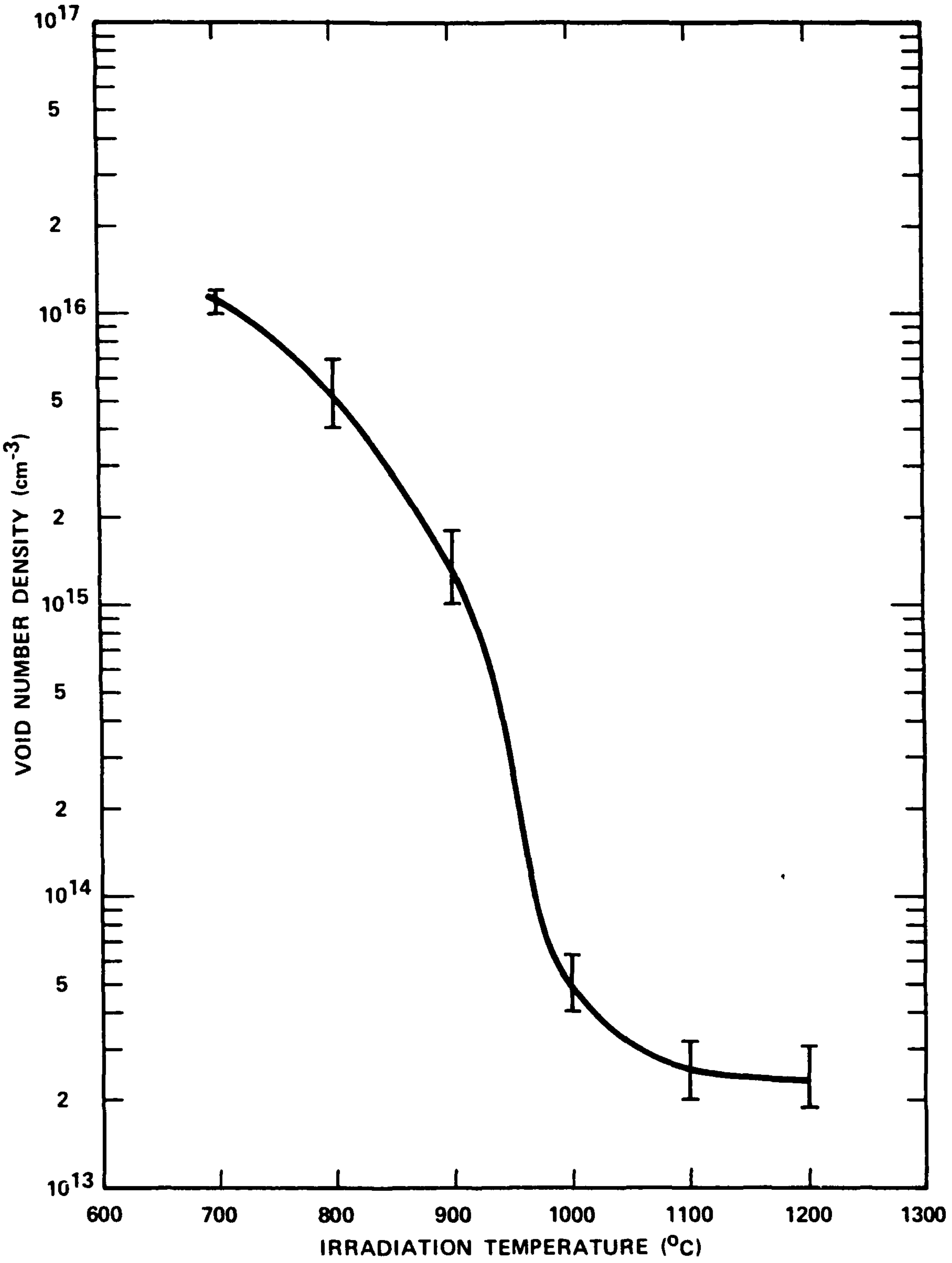

Figure 16. Void Number Density as a Function of Irradiation Temperature for Self-Ion Irradiated Niobium.

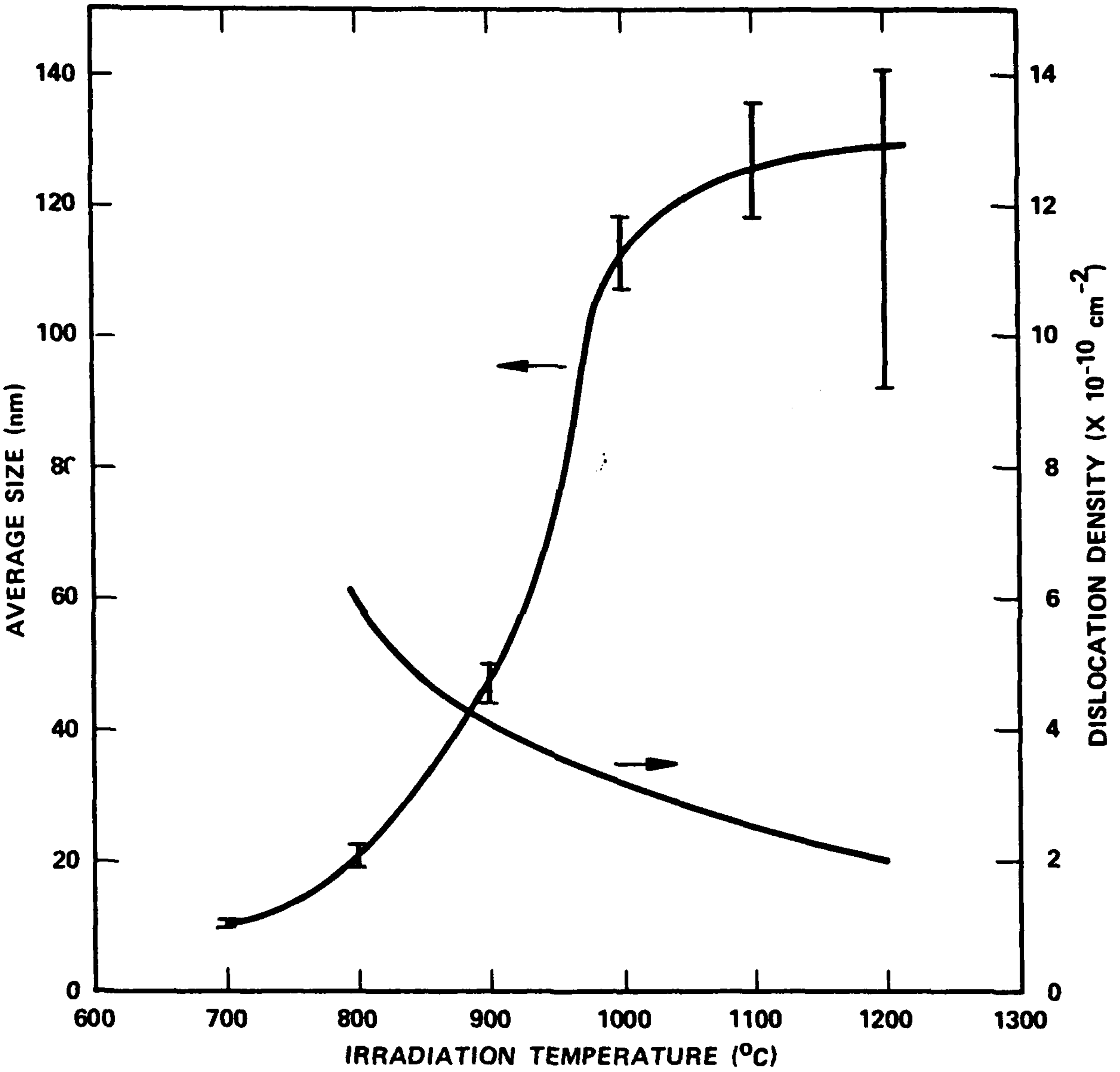

Figure 17. Average Void Size and Dislocation Density as a Function of Irradiation Temperature for Self-Ion Irradiated Niobium.

at 1000°C. Thereafter, the diameter increased slowly with increasing temperature. At 1200°C, a large scatter in void diameter was obtained from area to area in the specimen. A part of this scatter is attributed to enlargements of surface voids due to attack of the electropolishing agent on the large voids. The dislocation densities are also shown in Fig. 17. The dislocation densities varied from 6 x 10^{10} to 2 x 10^{10} cm^{-2} for irradiation temperatures of 800° to 1200°C.

Figures 18-23 show typical photomicrographs of voids in Nb irradiated from 700° to 1200°C. Dislocations are also shown in the insets in these figures. The dislocations were imaged in a two beam condition, mostly with a diffraction vector $\vec{g}$ = <110>. Note the differences in magnifications of the micrographs.

The void size distributions are shown in Figs. 24-29. At low temperatures, the distributions showed single, relatively sharp peaks at 10 nm, 20 nm, and 30 nm for 700°, 800° and 900°C. With increasing temperatures the void distribution shifted to larger sizes and broadened considerably. At the highest temperature (1200°C), the size distribution showed multiple small peaks which are again attributed to the attack on the voids by the electropolishing solution.

Micrographs from specimens irradiated at 700°, 800°, and 900°C were carefully examined under a stereoscope for void ordering (void lattice formation) in all the three directions. No ordering was observed in any of the specimens. Void ordering was also absent in specimens irradiated at higher temperatures.

The loop size and density determinations were hampered by the presence of a high density (>10^{16} cm^{-3}) of small (<10 nm) size loops produced by ion milling(89). These loop sizes and densities were comparable to those expected at irradiation temperatures <800°C. At temperatures of 900°C, the density of loops >30 nm in diameter was estimated to be 5 x 10^{14} cm^{-3}. At temperatures of 1000°-1200°C they were 2-3 x 10^{14} cm^{-3}.

Figure 18. Voids and Dislocations (inset) in Niobium Irradiated to 32 ± 4 dpa at 700°C. For Voids $\vec{Z} = [113]$, for Dislocations $\vec{g} = [110]$, $\vec{Z} = [113]$.

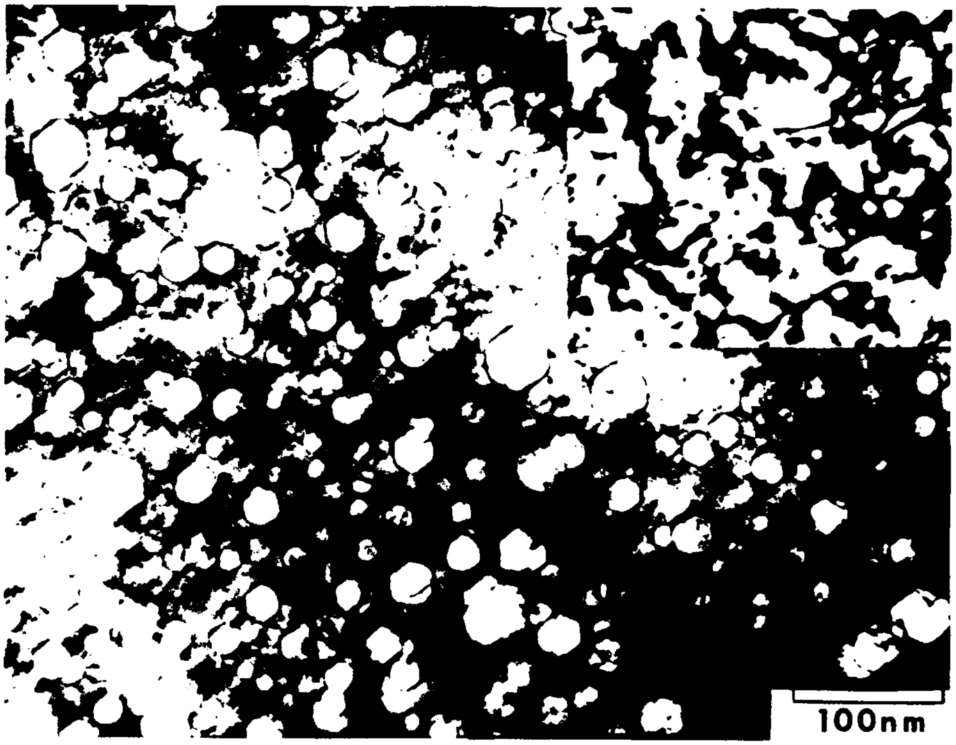

Figure 19. Voids and Dislocations (inset) in Niobium Irradiated to 54 ± 9 dpa at 800°C. For Voids $\vec{Z} \sim [111]$, for Dislocations $\vec{g} = [110]$, $\vec{Z} \sim [111]$.

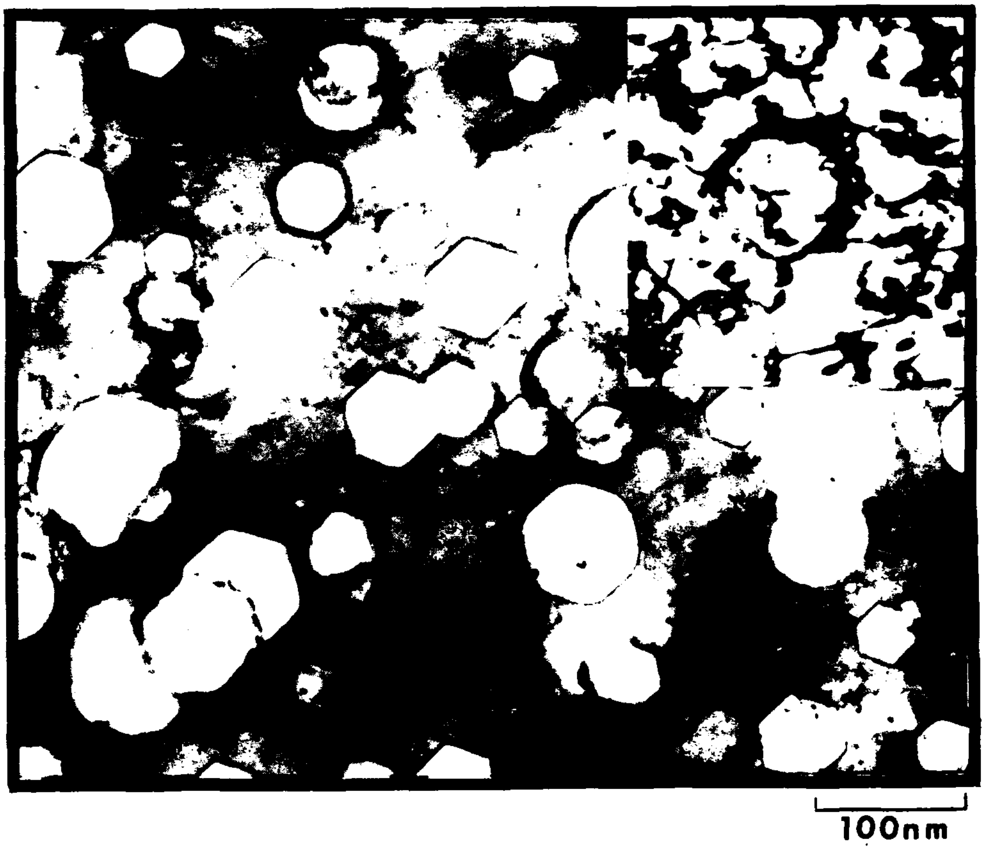

Voids and dislocations (inset) in niobium irradiated to 50 ±9 dpa at 900°C. For voids $\vec{z}$ ~ [111], for dislocations $\vec{g}$ = [110], $\vec{z}$ ~ [111].

Figure 20. Voids and Dislocations (inset) in Niobium Irradiated to 50 ± 9 dpa at 900°C. For Voids $\vec{z}$ ∿ [111], for Dislocations $\vec{g}$ = [100], $\vec{z}$ ∿ [111].

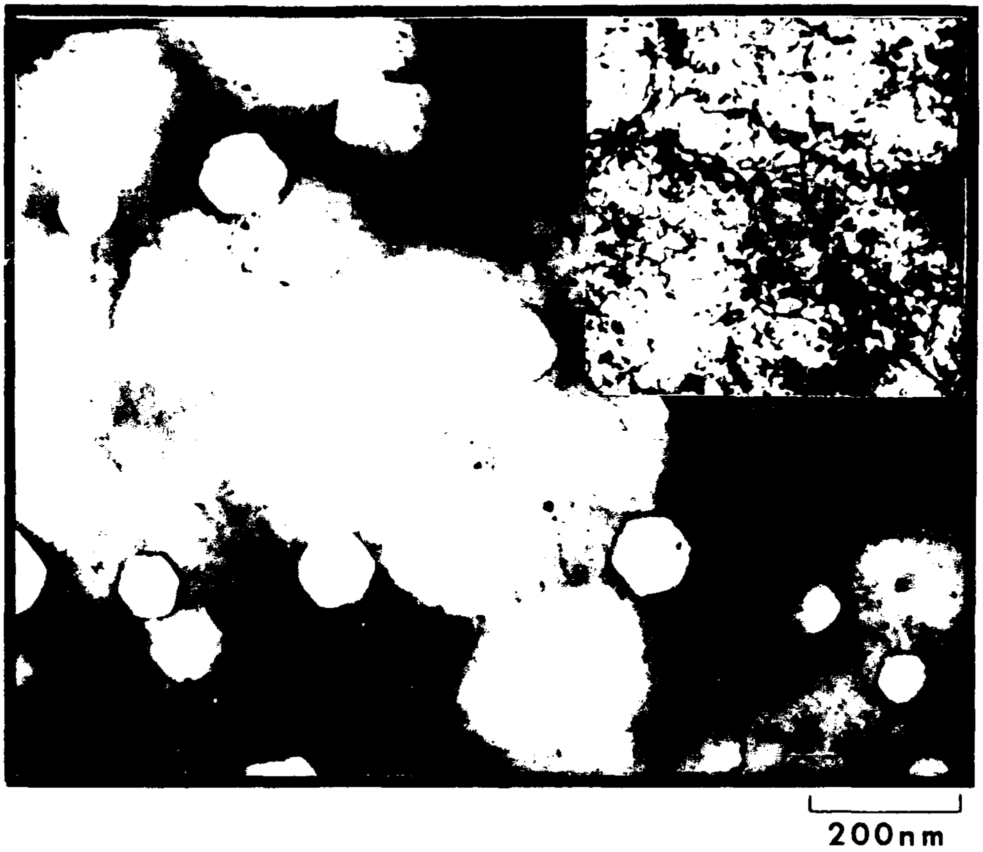

Figure 21. Voids and Dislocations (inset) in Niobium Irradiated to 57 ± 10 dpa at 1000°C. For Voids $\vec{Z} \sim [111]$, for Dislocations $\vec{g} = [110]$, $Z \sim [111]$.

Figure 22. Voids and Dislocations (inset) in Niobium Irradiated to 53 ± 9 dpa at 1100°C. For Voids $\vec{Z} \sim [111]$, for Dislocations $\vec{g} = [110]$, $\vec{Z} \sim [111]$.

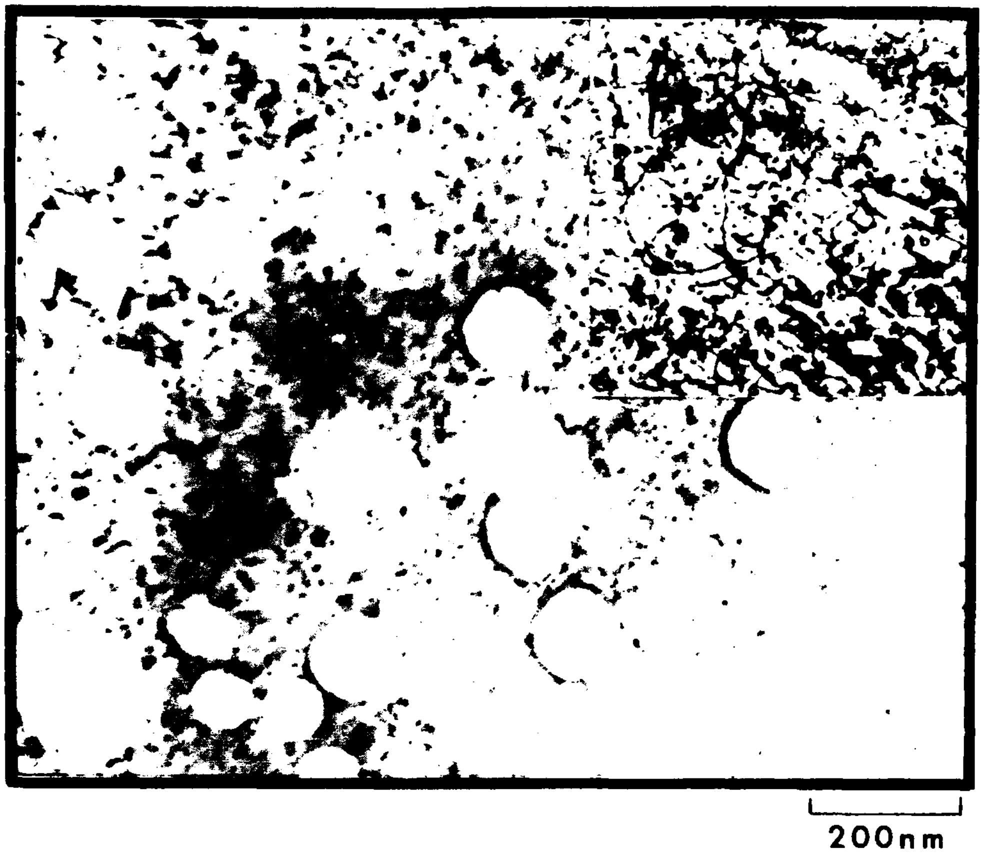

Figure 23. Voids and Dislocations (inset) in Niobium Irradiated to 52 + 9 dpa at 1200°C. For Voids $\vec{Z} \approx [111]$, for Dislocations $\vec{g} = [110]$, $\vec{Z} \approx [111]$.

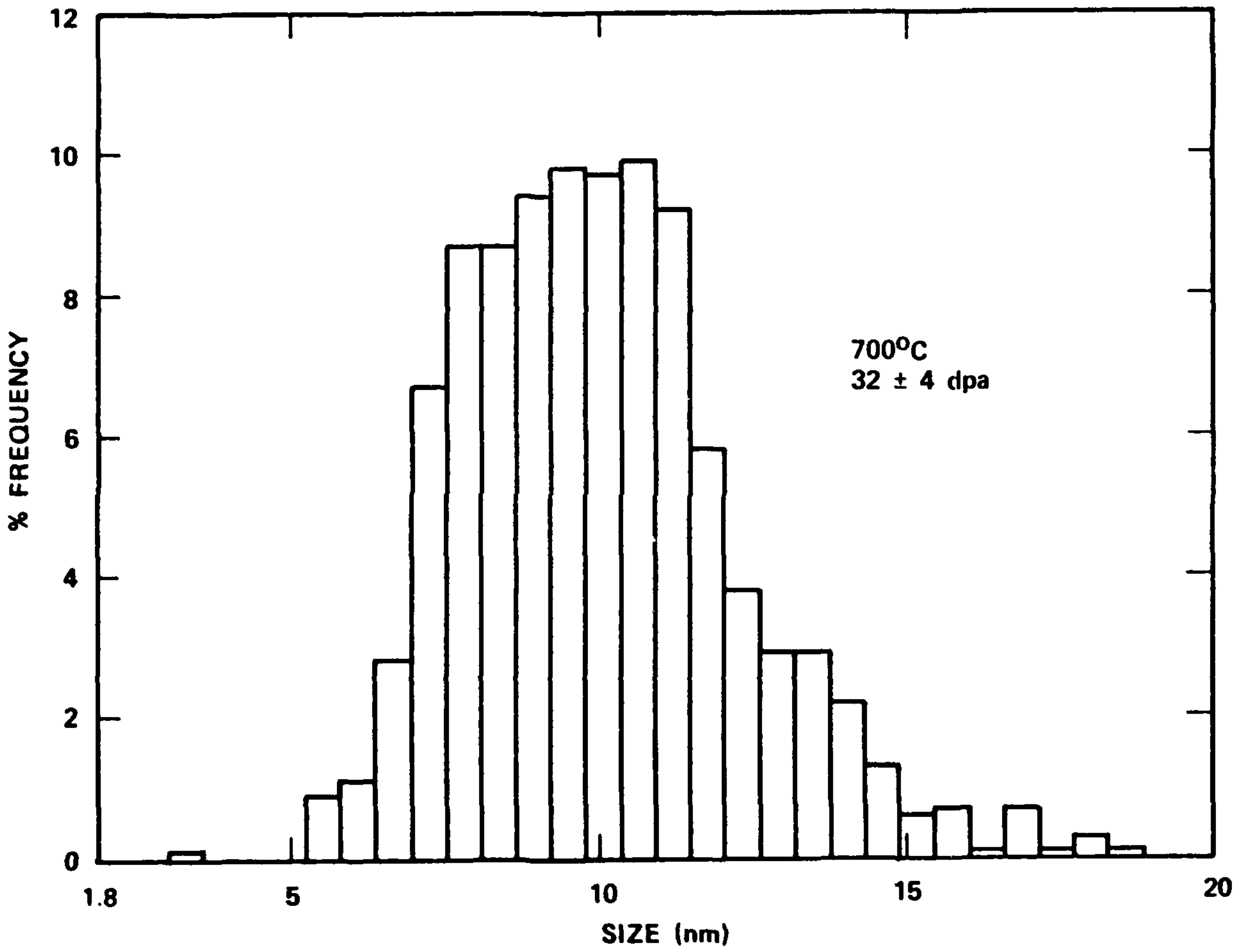

Figure 24. Void Size Distribution in Niobium Irradiated at 700°C to 32 ± 4 dpa.
NOTE: Incidence Angles Were 10° and 45° for Equal Times.

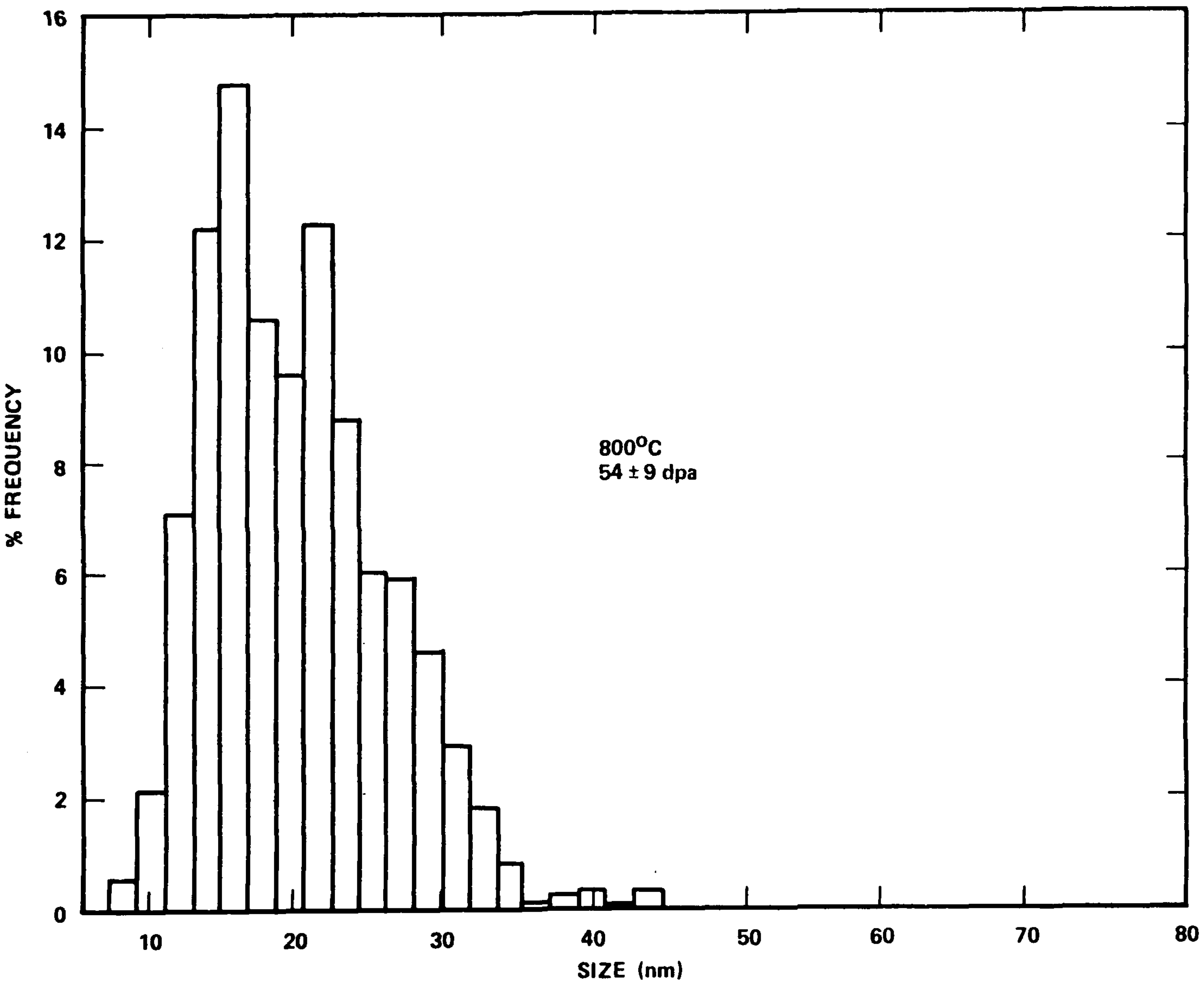

Figure 25. Void Size Distribution in Niobium Irradiated at 800°C.

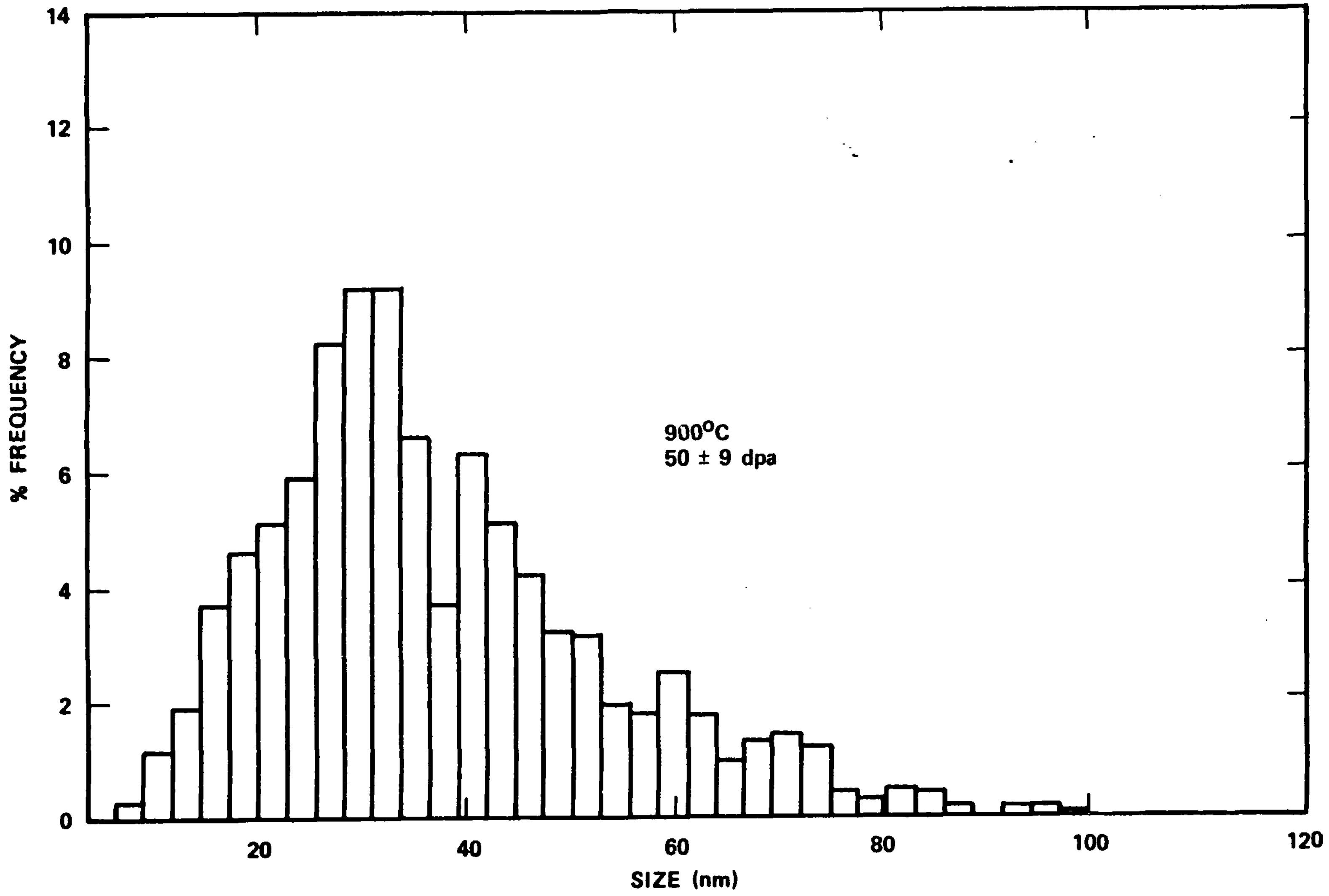

Figure 26. Void Size Distribution in Niobium Irradiated at 900°C.

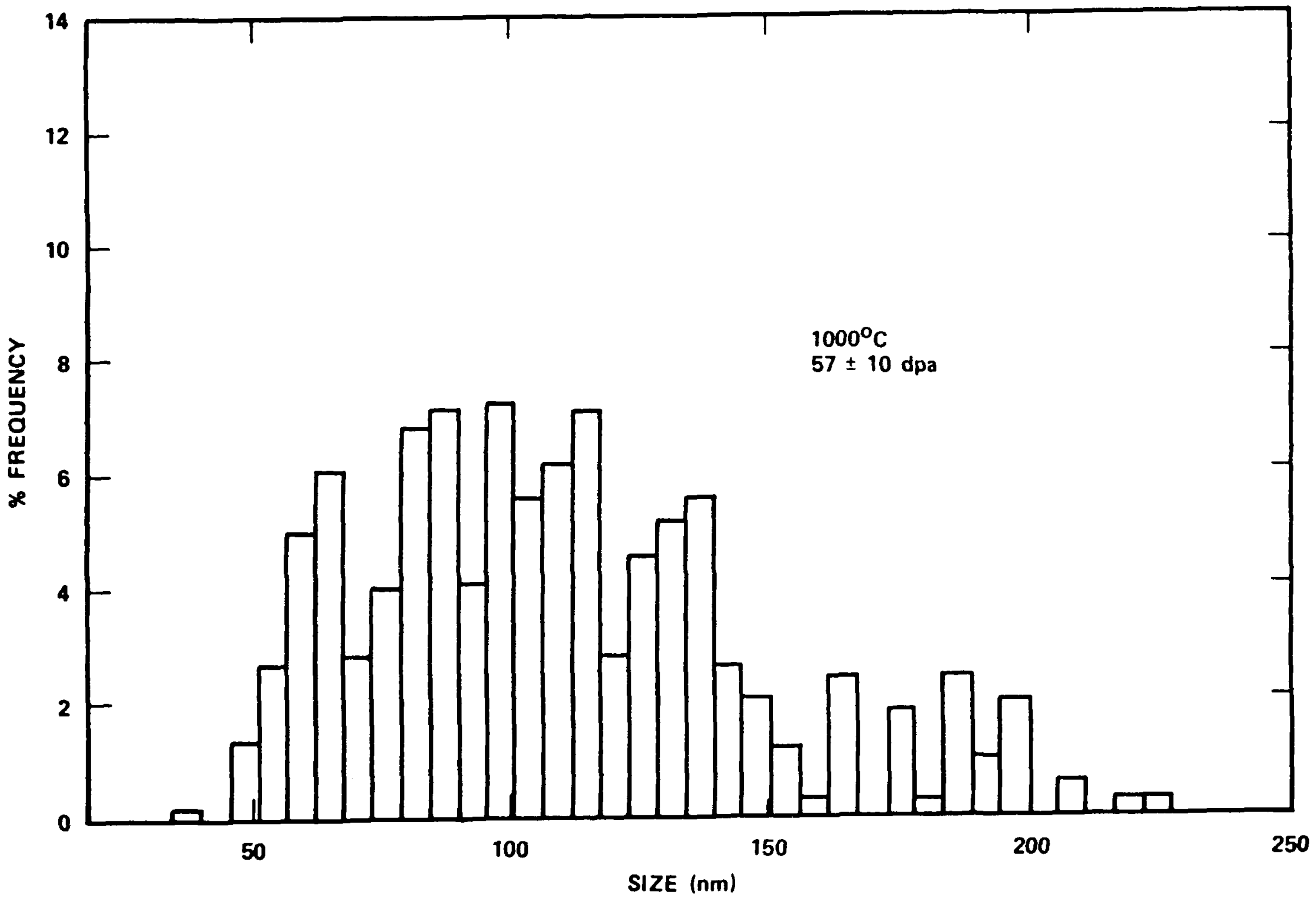

Figure 27. Void Size Distribution in Niobium Irradiated at 1000°C.

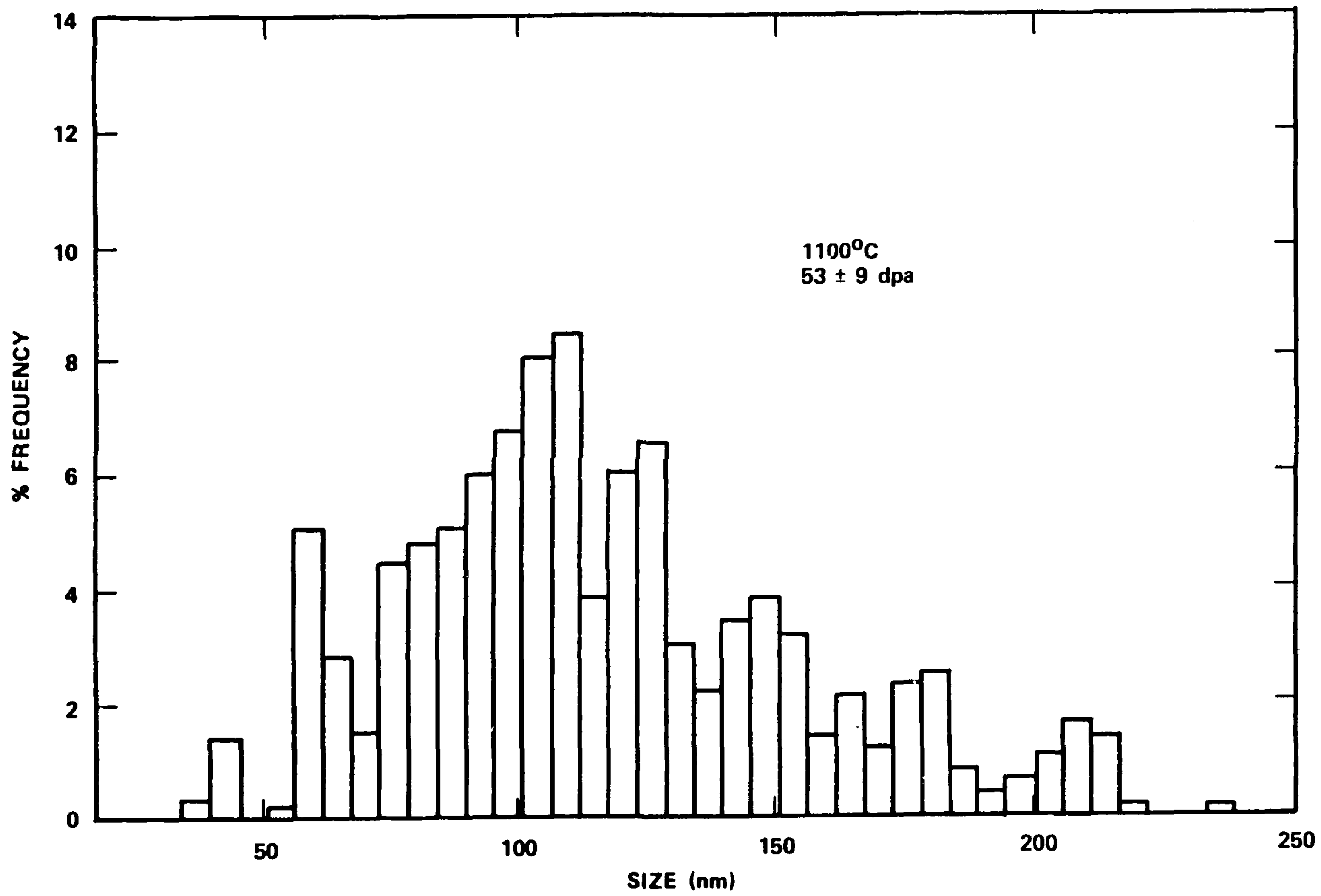

Figure 28. Void Size Distribution in Niobium Irradiated at 1100°C.

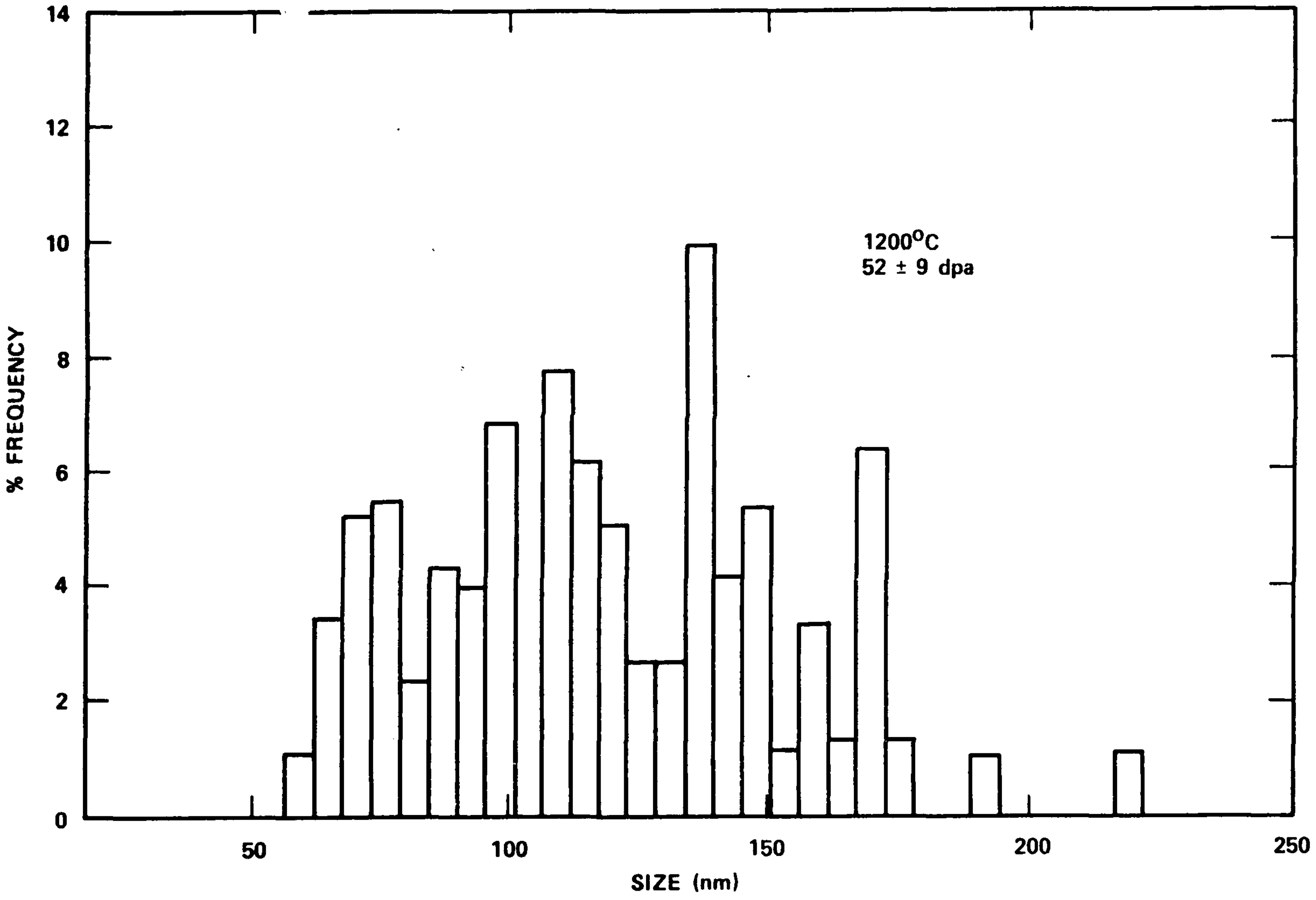

Figure 29. Void Size Distribution in Niobium Irradiated at 1200°C.

Table IX lists data for a specimen irradiated at 700°C to 10 dpa. The purpose of this experiment was to analyze the characteristics of dislocation loops (vacancy vs interstitials) produced at this temperature. The dose was reduced to obtain a small density of loops. However, as seen in Fig. 30 a high density (1.2 x 10^{17} cm^{-3}) of small loops (40 nm) was observed which was very difficult to analyze. It appears that the damage level of 10 dpa was too high to permit loop analysis. Although a lower damage level may increase the probability of this analysis, the small loop size will still pose a problem.

In the specimen irradiated to 10 dpa at 700°C, voids were also observed. Figure 31 shows the micrograph of voids in this specimen. The density of voids was estimated to be 6 x 10^{16} cm^{-3} and the average void size was 6 nm. The size and density of voids observed indicates that at 700°C the swelling incubation dose has been exceeded.

7.4 Discussion

7.4.1 Comparison of Results of Present Study with Existing Data

As stated in section 4.0, no data exist on the swelling of self-ion irradiated Nb; therefore, a comparison can only be made with Nb irradiated with ions other than self-ions. Loomis and Gerber(21,22) have irradiated Nb over comparable temperature and dose ranges with Ni ions. They have also studied the influence of oxygen on the swelling in Nb. These data are compared with the present work. In this comparison, the data of Loomis and Gerber corresponding to an oxygen content of 0.07 a/o were utilized, since vacuum fusion analysis of our material indicated an oxygen concentration of 115 wppm (660 appm, 0.066 a/o).

Figure 32 shows a comparison of swelling data obtained in the two studies. Although the peak swelling values were comparable, significant differences occur in the temperature dependence of swelling. In this study, maximum swelling occurred at 925°C whereas Loomis and Gerber saw a swelling peak at

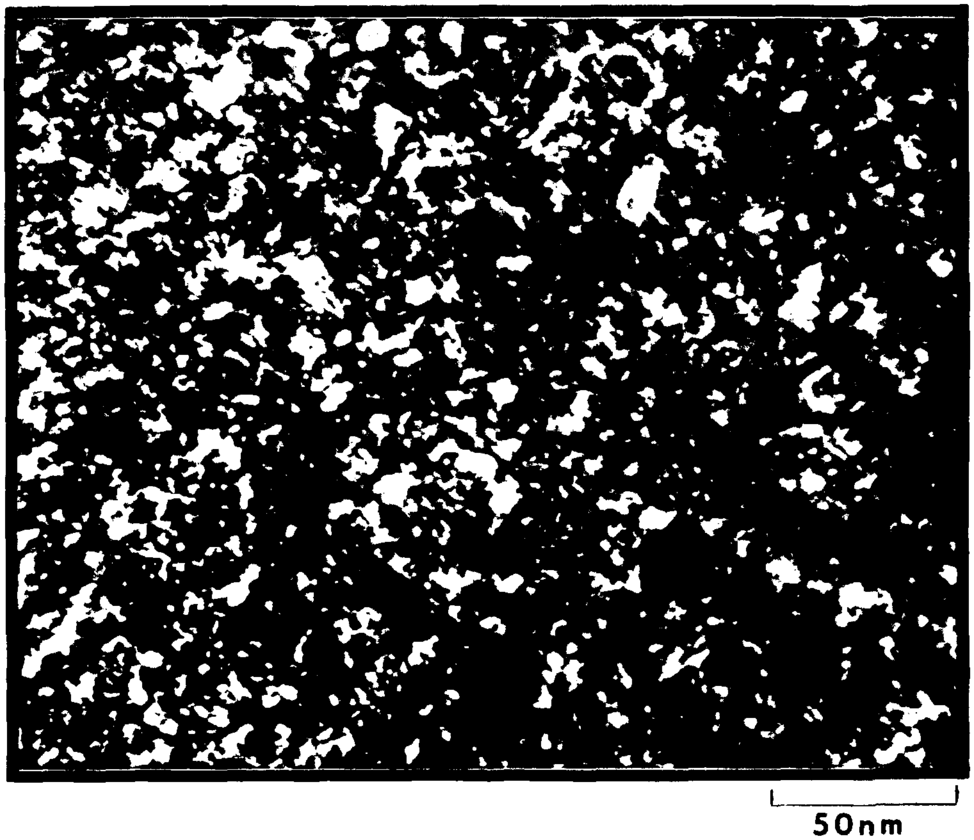

Figure 30. Loops in Weak Beam Dark Field $\vec{g}/3\vec{g}$ Condition in Niobium Irradiated to 10 ± 2 dpa at 700°C $\vec{g}$ = [220].

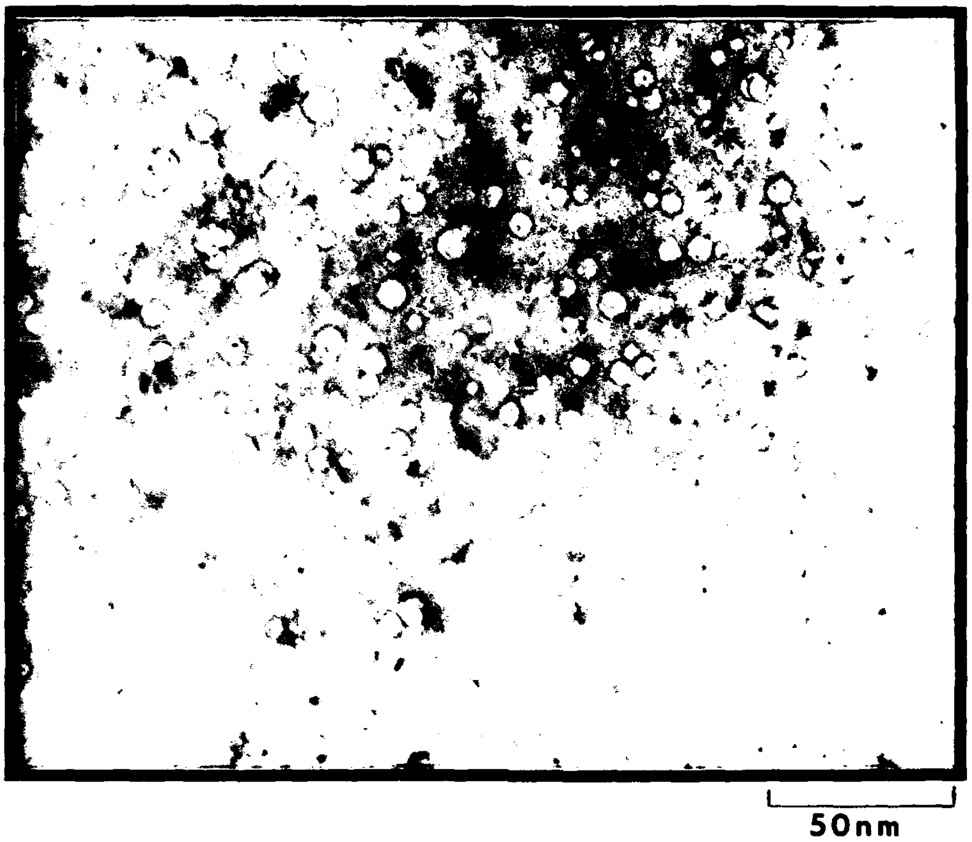

Figure 31. Voids in Niobium Irradiated to 10 ± 2 dpa at 700°C, $\vec{Z} \sim [100]$.

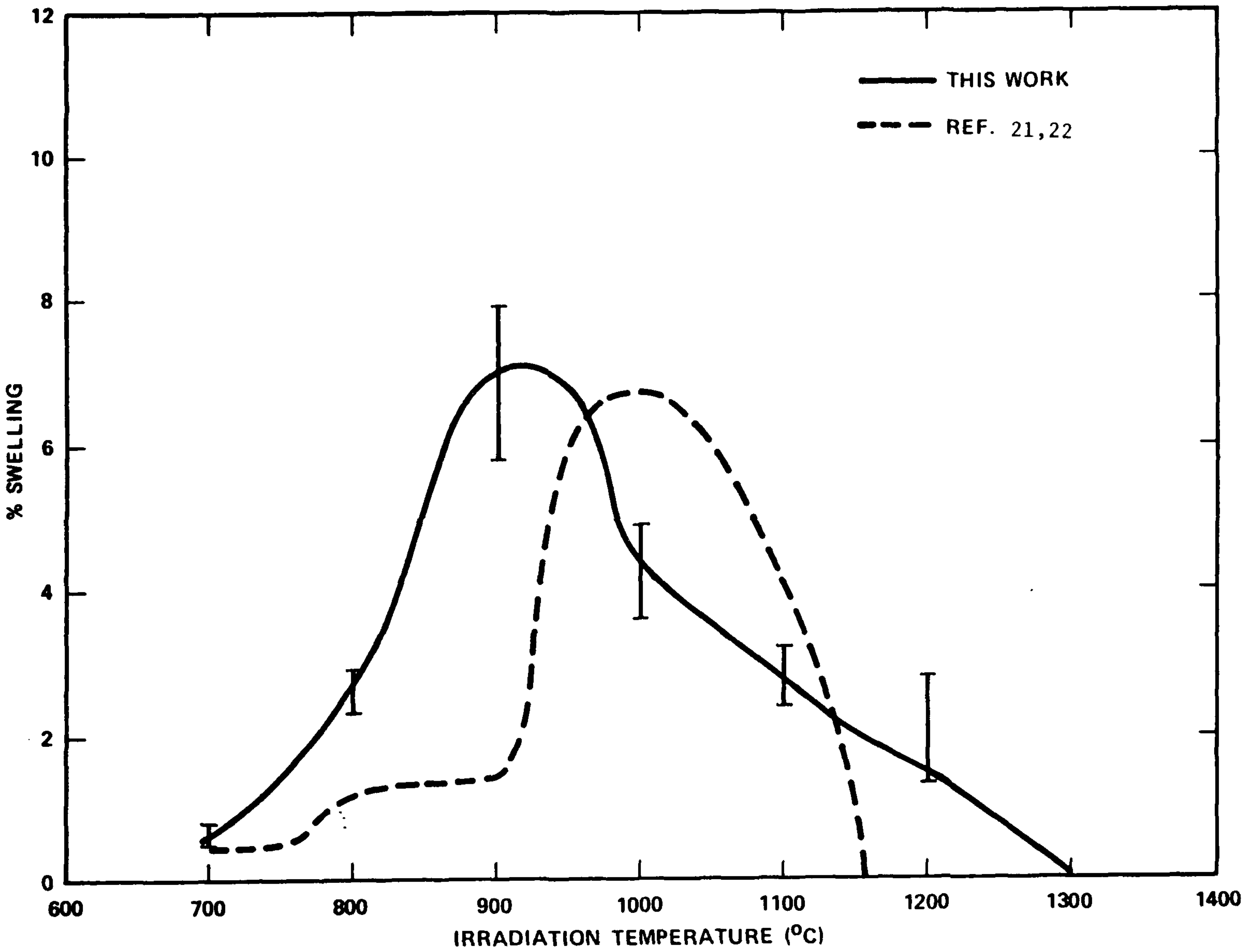

Figure 32. A Comparison of Swelling Data Obtained in this Work with Those of Loomis and Gerber.(21,22)

1000°C. Also, in their study, swelling occurred over a temperature range of 700° to 1150°C; whereas in this work, swelling occurred over a broader temperature range (700°-1300°C). Loomis and Gerber observed no voids at 1150°C, whereas voids were observed at temperatures as high as 1200°C in this work (see Fig. 22). The swelling at 800° and 900°C was also significantly higher.

A comparison of void number densities obtained in the two studies is shown as a function of irradiation temperature, in Fig. 33. A sharp decrease in void number densities as a function of temperature was observed in both studies, although the magnitudes and temperature dependences were different. In this study, the density decreased by a factor of 220 over a temperature range of 700°-1000°C, whereas Loomis and Gerber observed a decrease by a factor of 500. The absolute values of the void number densities are significantly different in the two studies. For example, at irradiation temperatures of 800° and 1000°C, the void densities reported here are a factor of 6 lower than those of Loomis and Gerber.

The average void diameters as a function of temperature from the two studies are plotted in Fig. 34. Rapid size increases are observed from 900° to 1000°C in both studies, but the void diameters are significantly higher in the work reported here.

Loomis and Gerber also observed void ordering in niobium containing oxygen in excess of 0.04 a/o and irradiated at 775°C. No void ordering was observed in specimens irradiated at 700° or 800°C in this study.

In an earlier study, Loomis et al.(90) observed a double peak in the temperature dependence of swelling in niobium containing 0.006 a/o oxygen, irradiated to 50 dpa with Ni^+ ions. The peaks occurred at ≈825°C and 1025°C. The maximum void swelling was 12%. The void number densities showed dips at the peak swelling temperatures. At 1100°C, the void density increased by an order of magnitude over that at 1000°C. The void diameters also showed two peaks occurring at the peak swelling temperatures. The dislocation densities were of the order of 10^9 cm^{-2} and average dislocation loop and spot diameters varied from 10 nm to 98 nm between 800° and 1100°C.

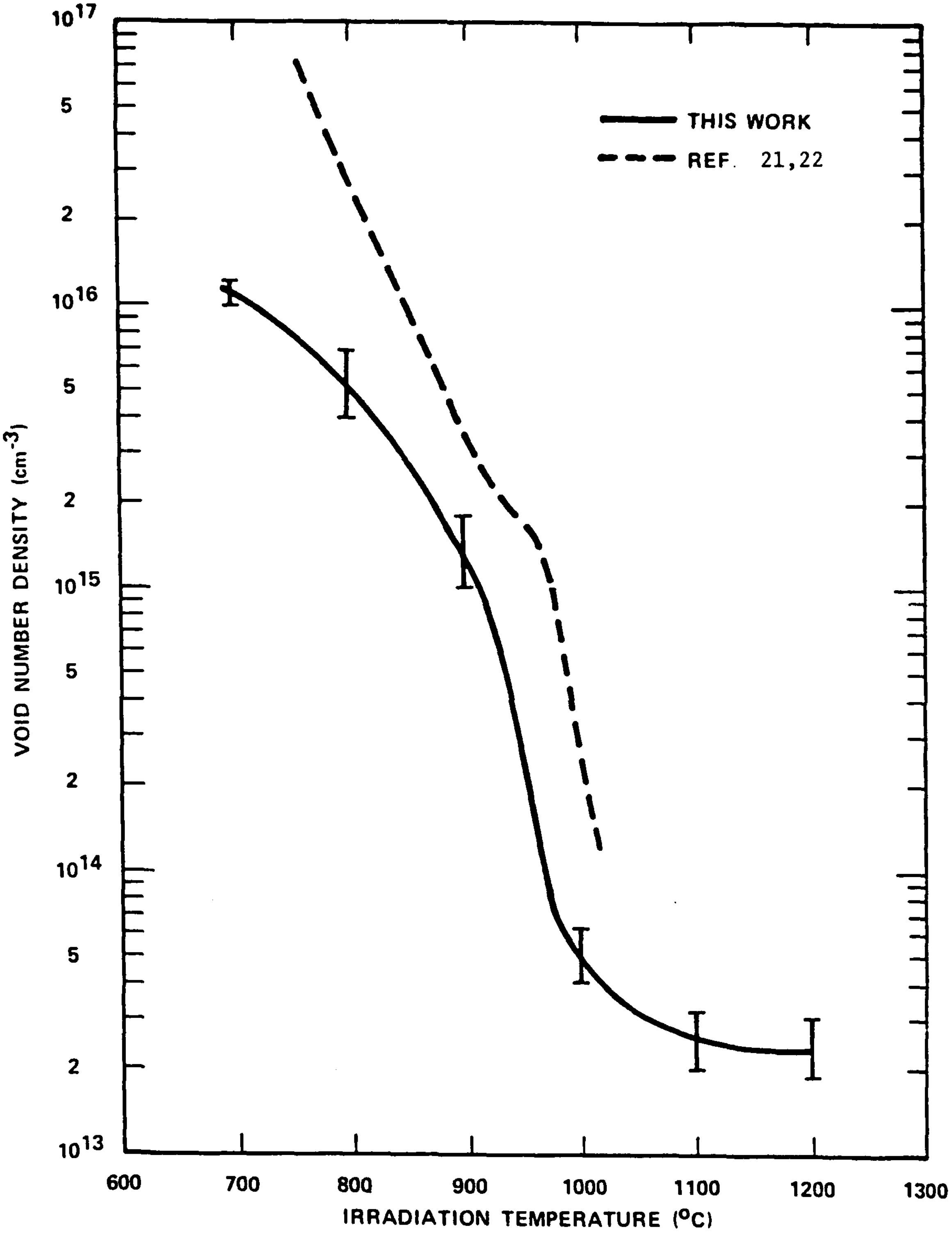

Figure 33. A Comparison of Void Number Densities in this Work with Those of Loomis and Gerber.(21,22) Solid Line Represents Data Obtained in this Work and Dotted Line Shows Data of Loomis and Gerber.(21,22)

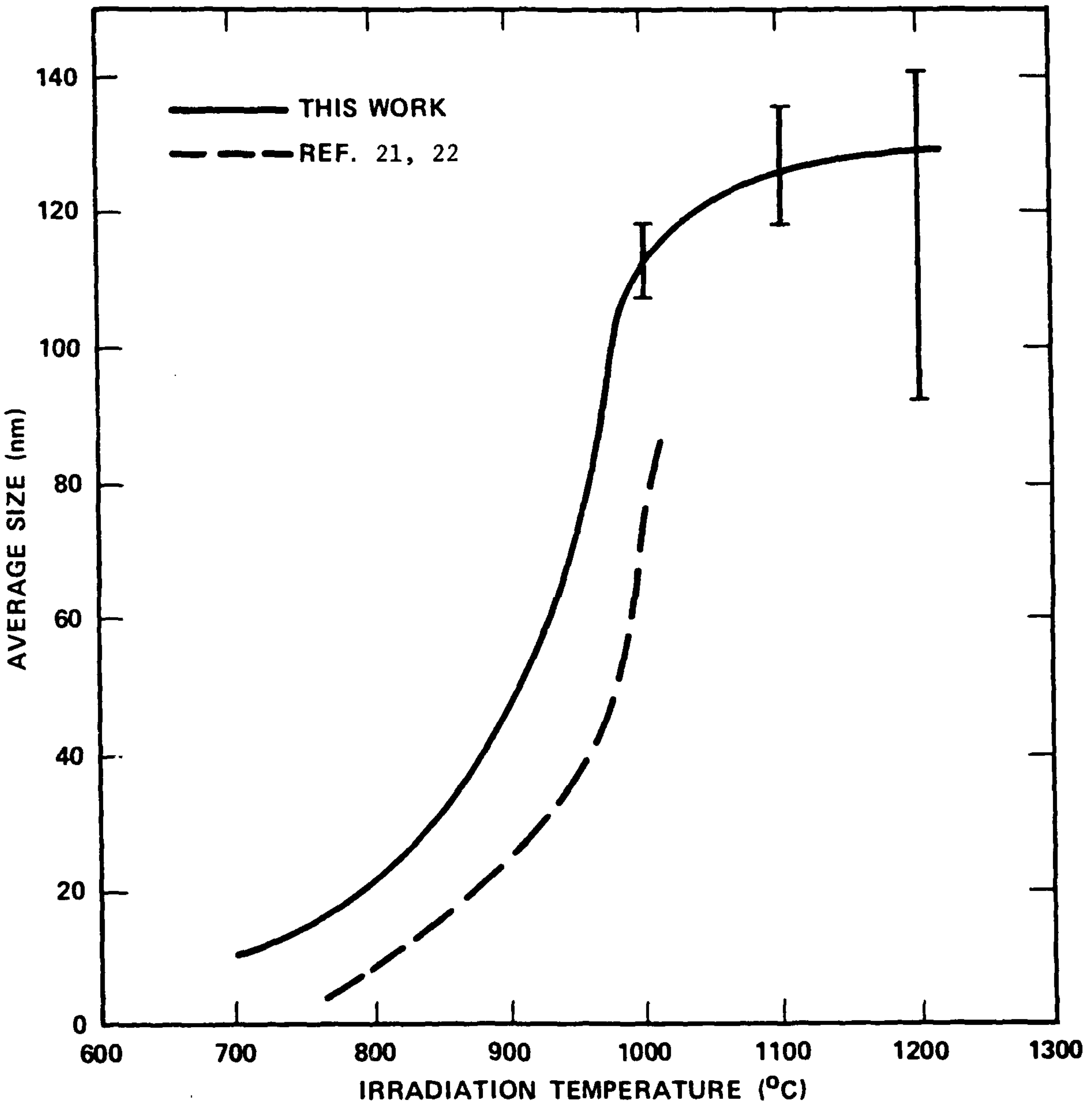

Figure 34. A Comparison of Average Void Sizes in Irradiated Niobium Between this Study and that of Loomis and Gerber.(21,22)

No swelling was observed at temperatures above 1150°C. These data cannot be compared to the data of the present study because of an order of magnitude difference in starting oxygen content and possible continuous oxygen pickup during irradiation as suggested by the authors.

The difference in the results of this study and that of Loomis and Gerber(21,22), especially with regard to the temperature dependence of swelling, void number densities, and average void sizes, cannot be accounted for by the differences in pre-irradiation oxygen levels and oxygen pickup during the irradiation. This is because, at oxygen levels of 0.08 a/o, saturations in void number densities and average void sizes were observed by Loomis and Gerber(21,22). Also, the temperature dependence of swelling was reported to be nearly independent of oxygen content.

The only major difference between the two studies is the ion species used to irradiate the niobium specimens. Loomis and Gerber(21,22) used $^{58}Ni^+$ ions whereas in this study self-ions were used. Chemical effects between the nickel ions and either niobium or oxygen or both cannot be ruled out at this time. Injected interstitials are known to influence swelling and microstructure; the examination of the impact of this effect on the results of this work has not yet been completed.

7.4.2 Comparison of Experimental Data and Model Calcualtions

A major objective of this program is development of a model for swelling in body-centered cubic metals based on the formalism of chemical reaction rate theory. The basic equations of the model and preliminary calculations for niobium were presented in Section 7.1. The results of the calculations were used to determine conditions for the first set of experiments. In this section, the experimental results are compared with model calculations in order to test the validity of the theoretical assumptions that have been made, to evaluate values of critical model parameters, and to determine areas where experiments that lead to refinement of the model can be performed.

The results of three sets of calculations are presented. The first set, which is a determination of the critical cavity size required for growth as a function of temperature, provides an explanation for the high temperature cutoff observed for swelling. Results of the second set, evaluation of sink strength ratios from the experimental data, have implications with respect to the values of the loop bias factors and the temperature dependence of loop growth kinetics. Finally, calculations of swelling as a function of temperature show that swelling depends strongly on interactions of impurities with point defects and development of the dislocation structure before the onset of swelling.

7.4.2.1 Critical Size for Cavity Growth

The differential equation that describes the rate of change of the cavity radius with time [Eq. (34)] contains two terms which are respectively the rate at which the cavity radius increases due to net vacancy absorption and the rate at which the radius decreases due to interstitial absorption per unit time increment. The magnitudes of these terms depend on the cavity radius; appearing directly in the conversion of defect volume to change in radius and in the thermal vacancy emission term [Eq. (25)] and indirectly because of the dependence of the steady state point defect concentrations on the total sink strength [Eq. (10)], which includes a term for the cavity sink strength [Eq.(7)].

In order for a cavity to grow, the cavity radius must be greater than the "critical radius" r_v^{crit}, which will be defined here as the radius at which the vacancy and interstitial absorption terms balance. An expression for r_v^{crit} can be obtained from Eq. (34) by setting the derivative to zero and solving:

$$r_v^{crit} = \left[\frac{kT}{2\,\gamma\Omega} \ln\left(\frac{Z_v^c D_v C_v - Z_I^c D_I C_I}{Z_v^c D_v C_{vc}^{th}} \right) \right]^{-1} \qquad (41)$$

The terms in Eq. (41) have been defined previously in Section 7.1.

The value of the critical radius depends on the sink structure, the bias parameters, dose rate, and temperature. Using the average void densities and dislocation densities given in Table IX, and the experimental temperatures and dose rate, the critical radius was calculated as a function of temperature. The results are shown in Fig. 35 (Curve labeled 0). Bias parameters Z_v^c, Z_I^c were assumed to be one, and Z_I^{nd} to be 1.05. Loop density was taken as zero, since the network is established at doses of the order of 10-20 dpa.

Evaluation of the critical radius is important for analysis of the swelling data for several reasons. First, it establishes the end of the nucleation process for a given set of experimental conditions. Once a cavity has attained this size, it is assumed to continue growing at a rate defined by Eq. (34). In a practical sense, this means that the value of r_v^{crit} is used as the initial cavity radius when the swelling equation is solved. Second, an estimate of the incubation period for swelling at each temperature can be obtained if the measured swelling values are fit to those calculated using the model equations. The difference between the actual irradiation times and the times at which the model calculations reach the measured values provide these data. Finally, the rapid increase in the critical radius at high temperatures explains the observed absence of cavities and the lack of swelling at 1300°C. No cavity embryo can reach the critical radius at this temperature in the absence of a large quantity of gas acting to stabilize the cavity by reducing thermal emission of vacancies. The cavity nucleation rate therefore drops to zero.

7.4.2.2 Sink Strength Ratios

The data given in Table IX can be used to estimate sink strength ratios for the microstructure observed in the implanted niobium specimens. Since experimental data for the dislocation loops are not available, values for the loop densities, bias factors, and sizes must be assumed in order to perform the calculations. $Z_I^{\ell 2}$,the bias factor of <111> loops for interstitials, was assumed to lie between 1.0 and 1.1 and $Z_I^{\ell 1}$ was taken to be equal to $b_1 Z_I^{\ell 2}/b_2$. The <111>

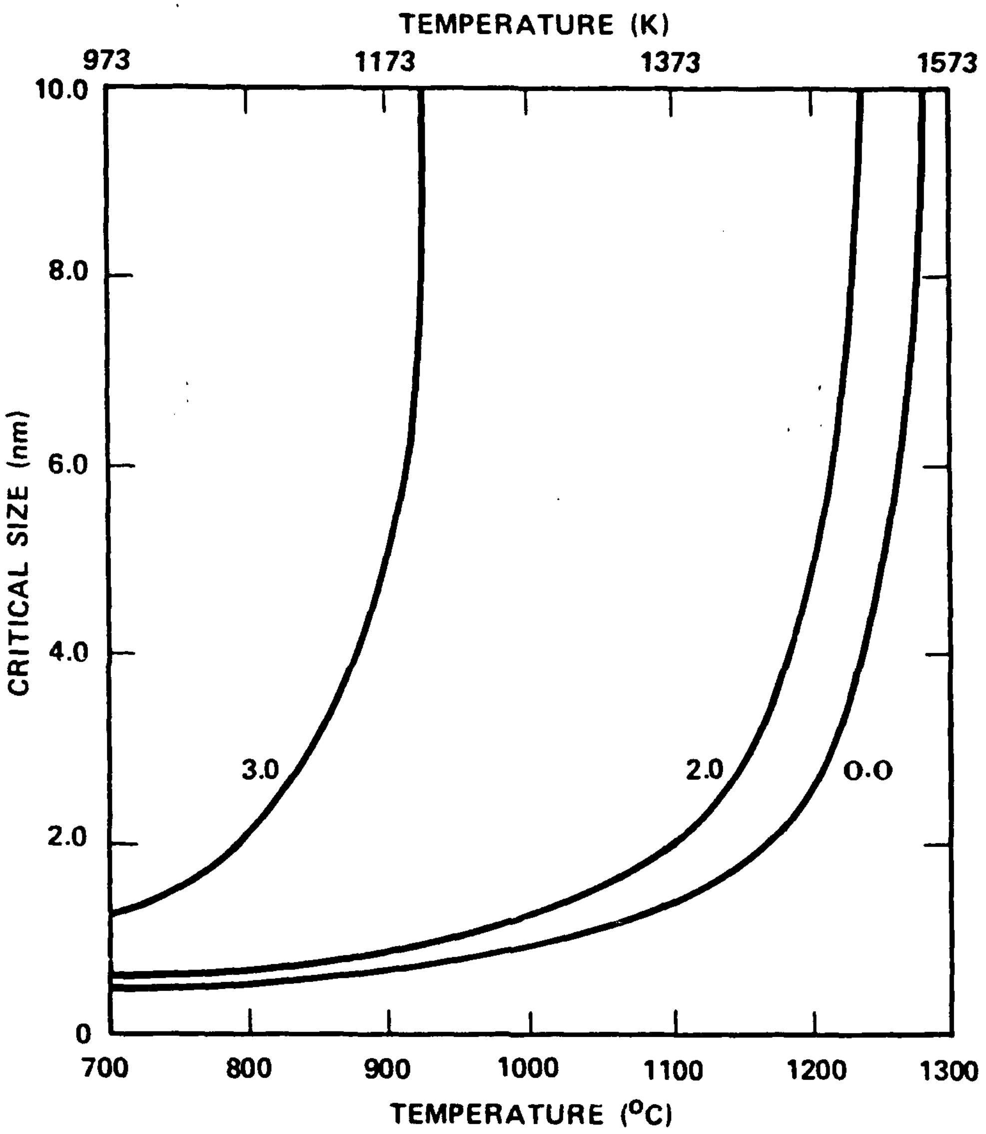

Figure 35. Critical Radius as a Function of Temperature for Three Values of the Interstitial-Oxygen Binding Energy, E_B. Curves are Labeled by E_b in eV.

loop density was assumed to be between 10^{11} and 10^{16} cm^{-3}; the <100> loop density was assumed to be a factor of 10^{-5} lower. The capture area factors, $4\pi r^*$, for both types of loops were taken as 10^{-6} cm.

Results of the calculations are summarized in Table X. Specimens are identified by the irradiation temperature, given in the first column. The range of values of the sink strength ratio, S_I/S_V, obtained for the range of parameters given above are listed in the second column. The final column contains a bounding value Z_{max} for $Z_I^{\ell 2}$. If $Z_I^{\ell 2}$ is less than Z_{max}, then S_I/S_V is greater than $Z_I^{\ell 2}$ and the condition for shrinkage of <111> loops is met. The value of Z_{max} is independent of the assumed <111> loop density for densities from 10^{11} to 10^{16} cm^{-3}.

Table X

Calculated Sink Strength Ratios*

Temperature (°C)	S_I/S_V	Z_{max}
700	1.017-1.021	1.018
700	1.027-1.033	1.029
800	1.020-1.027	1.022
900	1.022-1.033	1.025
1000	1.034-1.057	1.044
1100	1.036-1.059	1.046
1200	1.031-1.062	1.044

---

*See Table IX for swelling data.

A rough estimate of loop densities was made using the micrographs given in Figs. 18-23 and a value of approximately 10^{14} cm^{-3} was obtained. For this density, the calculated sink strength ratio is independent of $Z_I^{\ell 2}$, for $Z_I^{\ell 2}$ between 1.0 and 1.1, at all temperatures, and is given by Z_{max}. In addition, it depends only slightly on temperature, with an average value of 1.023 between 700° and 900°C and 1.045 between 1000° and 1200°C. One implication of this result is immediately apparent; if $Z_I^{\ell 2}$ lies between 1.023 and 1.045, <111> loops will grow at low temperatures and shrink at high temperatures.

7.4.2.3 Calculated Swelling Curves

Theoretical swelling curves were obtained from the model equations for three different sets of assumptions. Each will be discussed in turn, to indicate how the analysis developed.

For the first calculation, the experimental dislocation density was taken as the value for the network density with bias equal to 1.05. The average cavity density was used for N_c, and loop densities were assumed to be zero. (This set of assumptions is equivalent to assuming that the swelling model used for face-centered cubic metals is valid.) The total swelling time was taken equal to the irradiation time; nucleation is thus assumed to occur at $t = 0$. The results of this calculation are given in Fig. 36 (curve labeled 0). The experimental results are indicated in Fig. 36 by the dashed curve, with the measured points and error bars shown. It is apparent that the calculation does not reproduce the data, overpredicting the low temperature results by an order of magnitude, and the high temperature results by roughly a factor of three.

The first modification of the initial assumptions was the inclusion of an incubation time for swelling. At the onset of irradiation, a sequence of events occurs to set the stage for the swelling phenomenon. This sequence includes establishment of steady state point defect concentrations, loop nucleation, loop growth, and cavity nucleation. Loop growth and network formation may be completed within the initial transient period, or may extend into the cavity growth regime. (We have assumed that the former is the case, since the network density is equal to the measured dislocation density.) Cavity growth is significant only after this sequence is completed. The extent of the initial transient period depends on temperature, dose rate, and impurity concentrations and requires on the order of 1-10 dpa. A theoretical estimate can be obtained if a fullscale nucleation calculation is performed.

To examine the effect of an incubation period on the calculated swelling, four incubation times, corresponding to doses of 1, 5, 10, and 15 dpa, were assumed, and the calculations redone. The results are shown in Fig. 36, where the curves are labeled by the incubation dose. As can be seen from the curves,

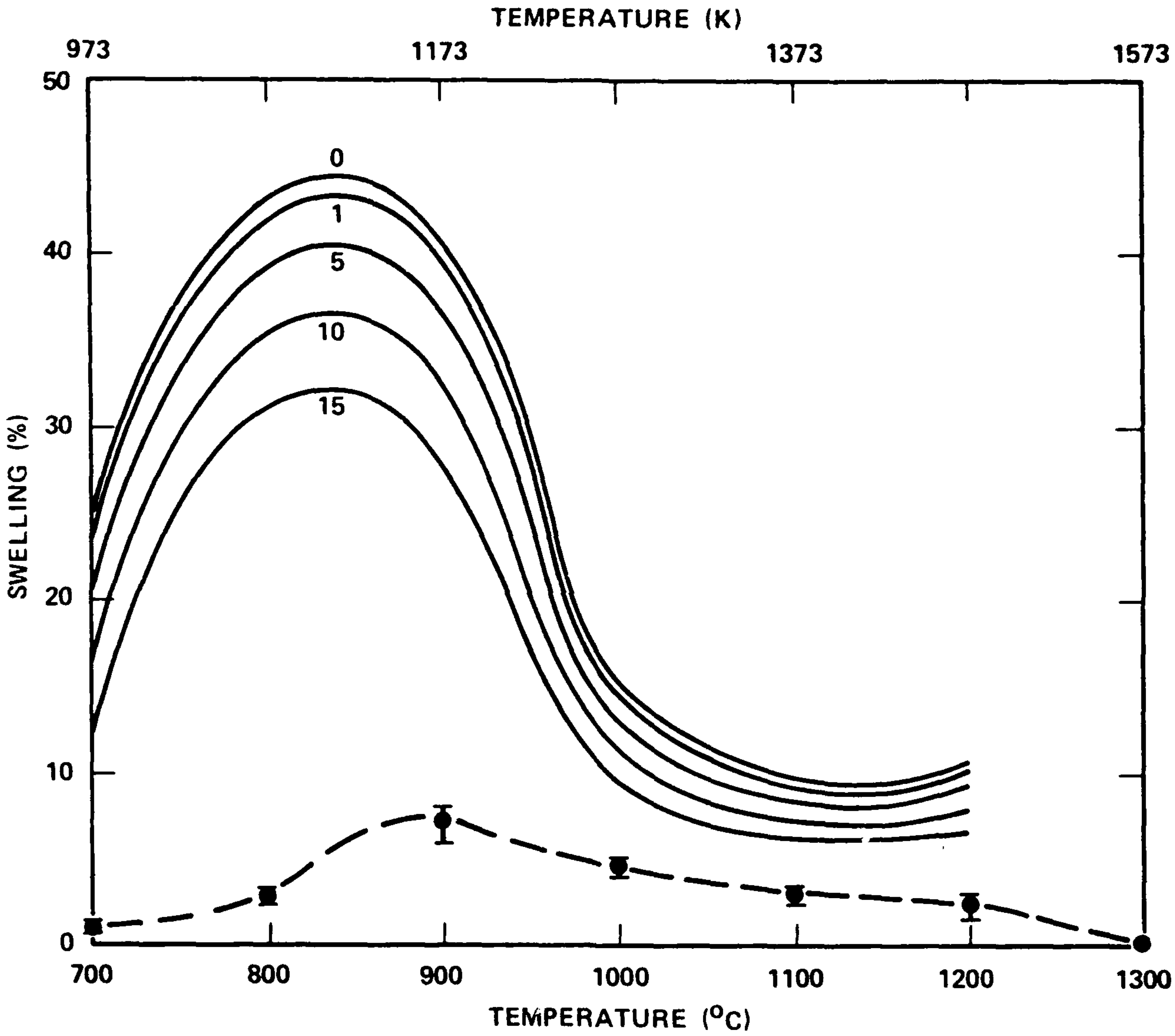

Figure 36. Calculated Swelling as a Function of Temperature. Curves are Labeled by the assumed Value of the Incubation Dose in dpa. Experimental Data are Given by the Dashed Curve.

inclusion of an incubation period does reduce the calculated swelling, but the reduction is not large enough to cause agreement between the calculations and the data. For example, with an incubation dose of 10 dpa, the calculated swelling is reduced by roughly 25 to 30 percent over the entire temperature range.

At this point, two major effects remained to be considered within the context of the model as it has been developed to date: those due to the two types of loops and their differing biases for interstitials, and those due to impurities. At the doses examined, it is apparent from the micrographs that the evolution of the dislocation structure has advanced into the stage where the network dominates the microstructure, and data on loop types, densities, and sizes cannot be obtained. Calculation of the impact of loop properties on swelling is therefore difficult and will be deferred until low dose data is available. The third set of swelling calculations focused on impurity effects.

As mentioned previously in Section 7.1.4, trapping of point defects by impurities can have a significant effect on the cavity growth rate and hence the swelling rate. Measured oxygen concentrations in the material used in this work are roughly 0.07 appm. Work by Loomis and Gerber(21,22) has shown that concentrations of this order are sufficient to affect swelling, leading to a reduction in swelling relative to that in low oxygen material. If we assume that the mechanism involved is trapping of niobium interstitials by oxygen, the diffusion coefficient D_I appearing in the model equations must be replaced by the effective diffusion coefficient given in Eq. (40). This introduces the interstitial-oxygen binding energy E_B as a parameter in the model, since its value has not been measured.

Preliminary calculations showed that binding energies of the order of 2 eV are needed to produce calculated swelling curves that correspond to the experimental curves. A series of calculations was then made with the binding energy ranging between 1.75 and 2.1 eV. Two incubation doses were used: 0 and 10 dpa. The results are shown in Figs. 37 through 40 where the calculated swelling is plotted as a function of binding energy for the six experimental temperatures. Each experimental point was then used, along with its error bar, to determine the range of E_B values that would produce a fit. The procedure

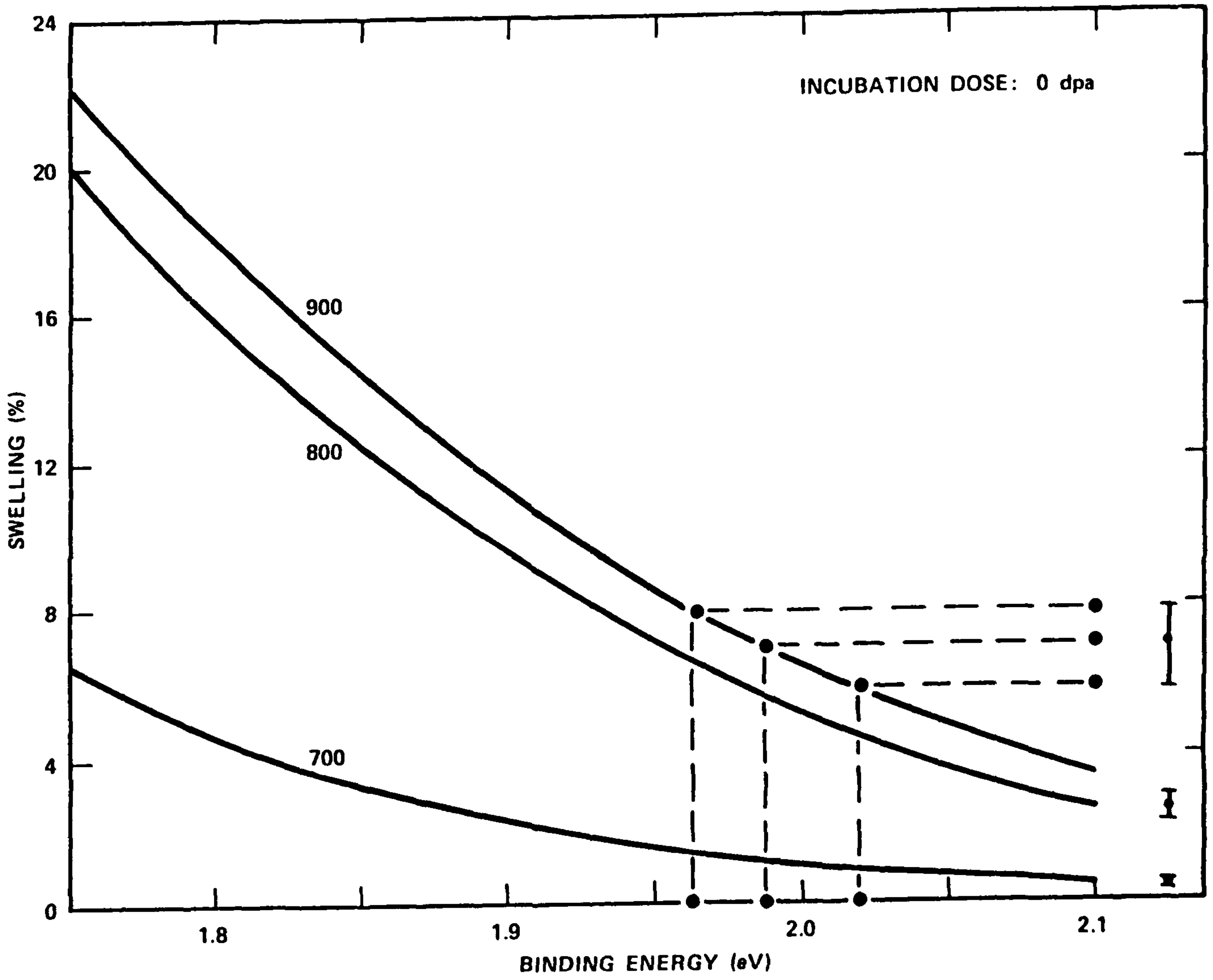

Figure 37. Calculated Swelling as a Function of Interstitial-Oxygen Binding Energy for an Incubation Dose of 0 dpa. Curves are Labeled by Temperature in °C. Experimental Points are Shown Near the Right Margin, for 700°, 800°, and 900°C in Ascending Order.

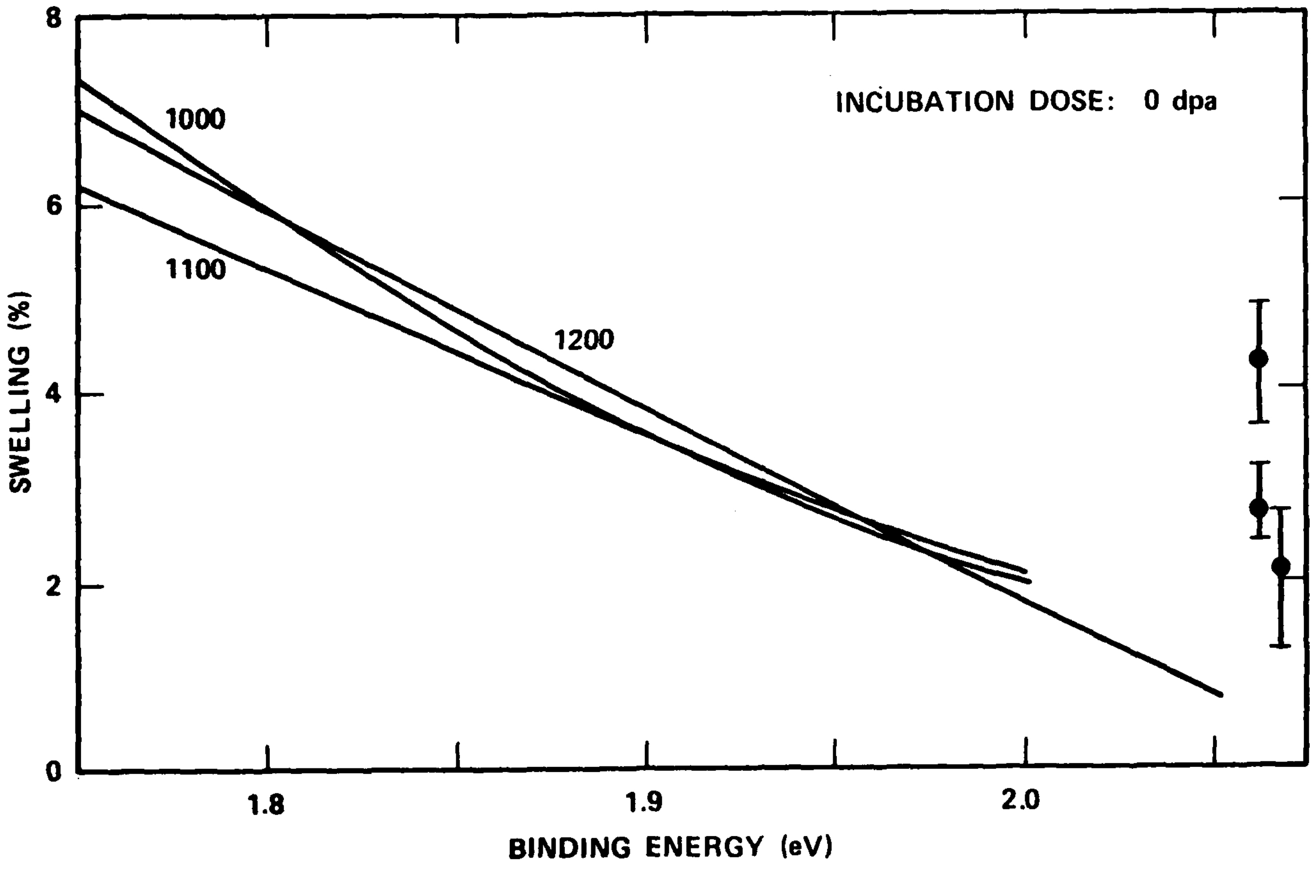

Figure 38. Calculated Swelling as a Function of Interstitial-Oxygen Binding Energy for an Incubation Dose of 0 dpa. Curves are Labeled by Temperature in °C. Experimental Points are Shown Near the Right Margin, for 1000°C, 1100°C, and 1200°C in Descending Order.

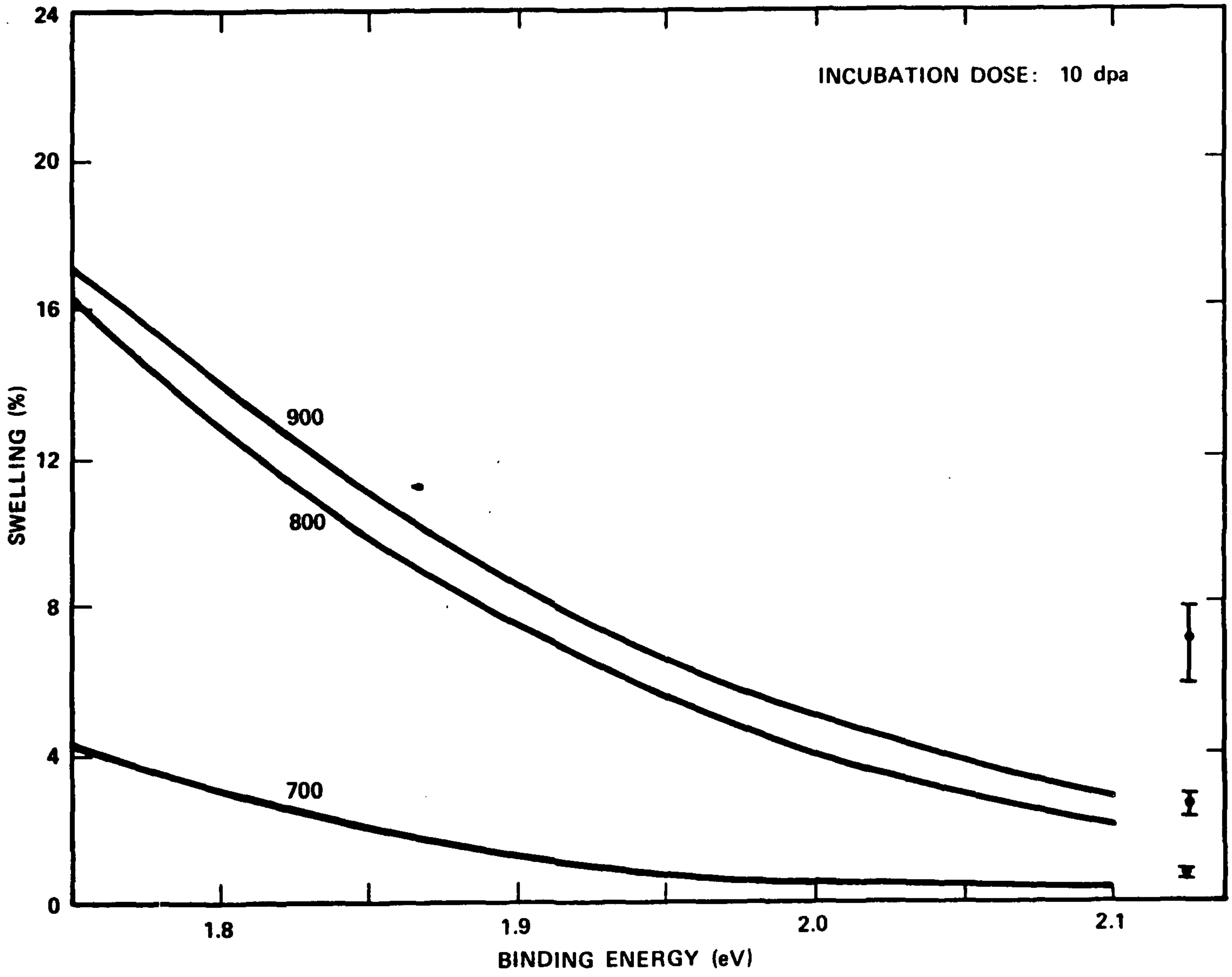

Figure 39. Calculated Swelling as a Function of Interstitial-Oxygen Binding Energy for an Incubation Dose of 10 dpa. Curves are Labeled as in Figure 37.

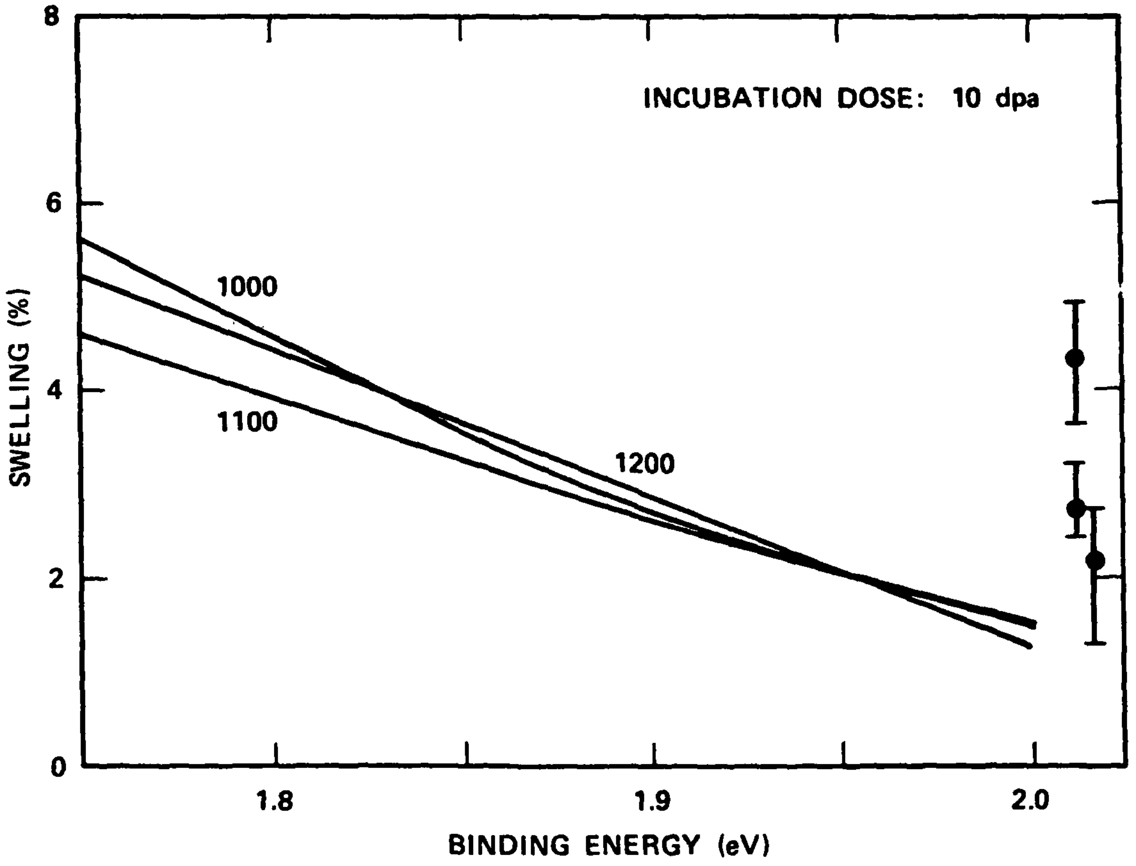

Figure 40. Calculated Swelling as a Function of Interstitial-Oxygen Binding Energy for an Incubation Dose of 10 dpa. Curves are Labeled as in Figure 38.

is illustrated in Fig. 37 for 900°C. Results for all temperatures are given in Table XI for zero incubation dose, and in Table XII for an incubation dose of 10 dpa. As can be seen from the tables, there is some scatter in the results, with an average value of 1.995 eV for 0 dpa and 1.943 eV for 10 dpa. These average values were used in the model equations and swelling calculated as a function of temperature, as shown in Fig. 41. Triangles are for an incubation dose of 0 dpa, and circles for 10 dpa.

Table XI
Fit of Binding Energies to Swelling Data
Incubation Dose: 0 dpa

Temperature (°C)	Range E_B (eV)	Mean Fit
700	2.088-2.049	2.068
800	2.130-2.094	2.111
900	2.021-1.966	1.987
1000	1.898-1.840	1.866
1100	1.976-1.921	1.954
1200	-1.952	1.982
	Average	1.995

Table XII
Fit of Binding Energies to Swelling Data
Incubation Dose: 10 dpa

Temperature (°C)	Range E_B (eV)	Mean Fit
700	2.026-1.986	2.004
800	2.092-2.055	2.073
900	1.972-1.917	1.939
1000	1.846-1.781	1.810
1100	1.917-1.853	1.892
1200	-1.904	1.942
	Average	1.943

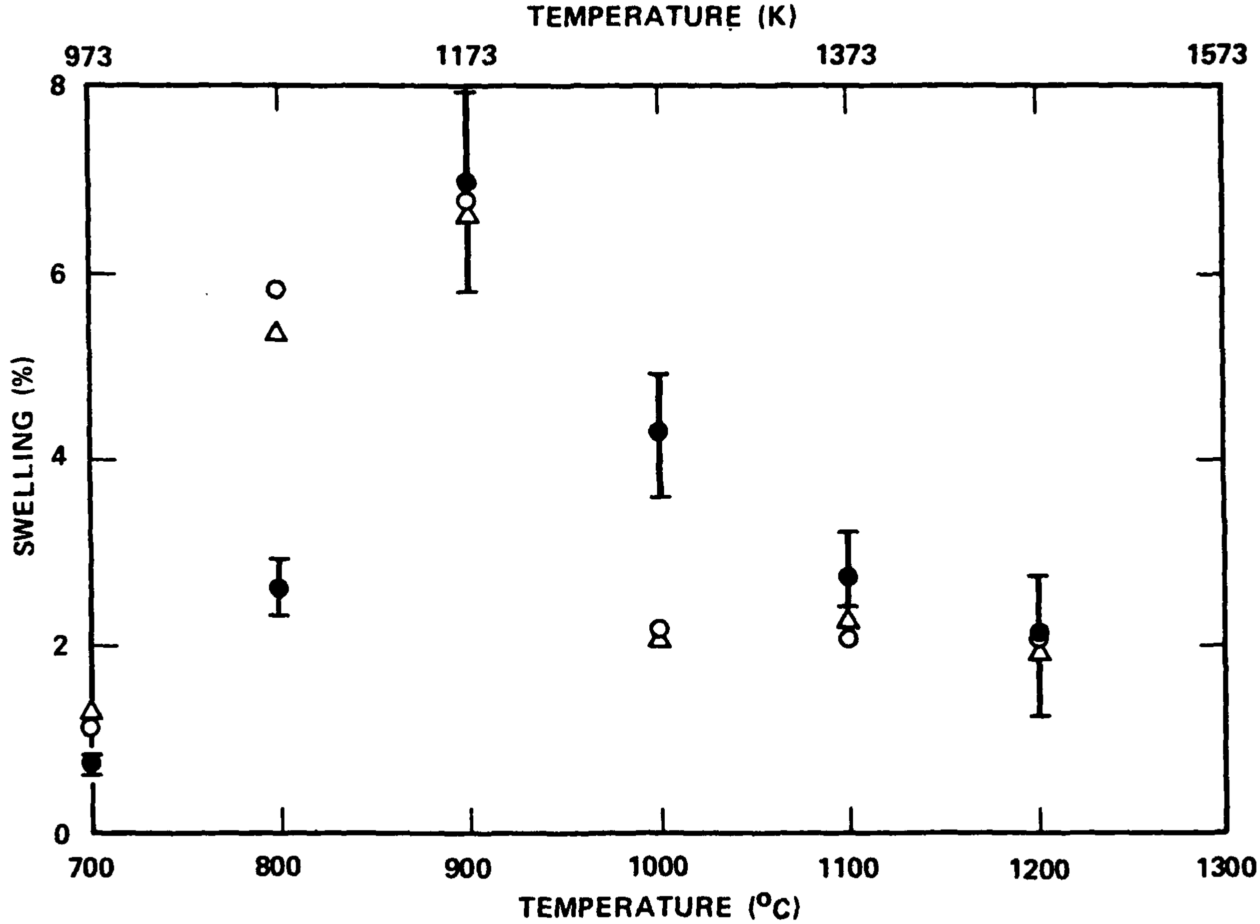

Figure 41. Calculated Swelling as a Function of Temperature for Two Combinations of Incubation Dose and Interstitial-Oxygen Binding Energy: Δ (0 dpa, 1.995 ev); 0 (10 dpa, 1.943 eV). Experimental Points are Shown with Error Bars.

The two combinations of incubation dose and binding energy give approximately the same fit to the data. Significant discrepancies occur at two temperatures, 800° and 1000°C. At the former temperature, the swelling is overpredicted by roughly a factor of two; at the latter, underpredicted by the same factor.

Whether the values obtained for E_B are reasonable can be tested to a limited extent by looking at the effect of the binding energy on the critical radius. Trapping of interstitials by oxygen reduces the diffusivity of interstitials and changes r_v^{crit} [see Eq. (41)]. Calculations of r_v^{crit} as a function of temperature were done for a range of assumed binding energies, and r_v^{crit} increases as binding energy increases for a fixed temperature. Values of r_v^{crit} are plotted in Fig. 35 as a function of temperature for binding energies of 2 and 3 eV. As can be seen from the figure, there is a large shift of the high temperature portion of the curve toward lower temperatures as the binding energy increases from 2 to 3 eV. The shift when E_B changes from 0 to 2 eV is relatively small in comparison. Any increase in assumed binding energy, which would result in a better fit to the 800°C data point, for example, would result in critical radii at high temperatures that would be unacceptably large. Since cavities are observed at 1200°C, r_v^{crit} must remain relatively small until this temperature is exceeded. For binding energies near 2 eV, r_v^{crit} is 5 nm, a value that is somewhat high. A reduced binding energy is therefore more reasonable than an increased one.

By examination of the cavity distribution after implantation, Horton (91) has recently determined the critical cavity radius in Fe-10% Cr irradiated at 577°C ($0.5T_m$) with 4 MeV Fe^{++} ions to a damage level of 30 dpa. The value obtained was 2.5 nm, a result that is of the same order as those calculated in the present work for temperatures near 1200°C with binding energies between 0 and 2 eV.

As indicated in the discussions of experimental results, measured dislocation densities in Ni-implanted niobium are roughly an order of magnitude lower than those measured in the present work. Because of possible deformation during sample preparation, the densities given in Table IX may be high. A series of swelling calculations was performed in order to determine the effect of the dislocation density. Reduction of measured values of dislocation density by an order of magnitude led to a significant reduction in the calculated swelling relative to the first series of calculations (see Fig. 36, curve labeled 0). At 700°C, swelling was reduced by a factor of 5, and at 900°C by a factor of 4. For the three high temperature points, there was only a small reduction, of the order of 10%. If warranted by measurements of deformation induced during sample preparation, modification of the experimental dislocation densities and refitting of the swelling data to the model calculations would give oxygen-interstitial binding energies that are lower than those determined for the conditions as given.

7.4.3 Suggested Areas of Experimental and Theoretical Investigation

The combination of experimental data and calculational results indicate several areas that can be investigated both theoretically and experimentally to aid in the development of the theory for swelling in body-centered cubic metals. These include:

- Low-dose microstructural evolution
- Cavity growth kinetics
- Loop and cavity nucleation
- Oxygen trapping

The first two would require experimental work, the second two, primarily theoretical effort.

A series of experiments at low doses could provide data on the development of the conditions that prevail at the onset of swelling. For example, the data for 10 and 32 dpa at 700°C indicate that coalescence of small cavities may occur, since the cavity number density at the lower dose is greater than that at the higher. The swelling model does not currently include coalescence as a possible growth mechanism. In addition, data on the dislocation loops, including types, densities, and sizes, is needed in order to evaluate the possible effects of the presence of both <100> and <111> loops on swelling.

Data on the growth rate of cavities at moderate doses (between 10 and 50 dpa), obtained from experiments with total dose as a variable, could be directly compared with predicted growth rates. An outcome of this would be an experimental determination of the incubation dose, which in the present analysis was used as a parameter, independent of temperature.

A theoretical estimate of the incubation dose can also be obtained from a three-component nucleation calculation. Nucleation models based on the chemical reaction rate formalism are available, and a calculation that includes <100> and <111> loops as well as cavities is relatively straightforward. Predictions of low dose loop growth kinetics would be automatically a part of the output of this type of computation. As can be seen from the data, the cavity density drops significantly between 900° and 1000°C, and the dislocation density flattens out as a function of temperature. As a result, the calculated sink strength also changes. The key to understanding the temperature dependence of the densities lies in understanding what controls cavity nucleation.

From the swelling calculations, it is clear that any impurity trapping (in this case oxygen) could be significant in determining swelling behavior. An investigation of oxygen effects in niobium would require extensive experimental and analytical work, and is currently not a major focus of the program. Loomis, however, has done extensive work on oxygen in niobium, and his published data provide a test for any swelling model that includes oxygen as a critical component. As a preliminary to performing experiments involving variable oxygen concentrations, it would be useful to analyze Loomis' data with our model.

8.0 PHASE II PROGRAM

8.1 Theoretical Program on Low Dose Microstructural Evolution

8.1.1 Model Development

The theoretical effort was focused on developing the dislocation microstructure at low doses (<5 dpa). This work is intended to complement the experimental effort on dislocation loop and network development at doses ≤ 5 dpa. The conditions for loop growth/shrinkage were refined using the growth equations applicable to small loops. In order to remove the constraint of loop-size independent bias factors, which were used in the previous model, the theoretical bias factors developed by Wolfer and Ashkin(92,93) for interstitial dislocation loops were included in the growth and sink strength equations. Then the conditions for loop growth and shrinkage were reformulated. In this formulation, the loop growth and shrinkage regimes can be expressed in terms of a single materials parameter, the density of the microstructural components, and the loop radii. Boundaries of growth and shrinkage regimes were calculated as a function of the materials parameter for a variety of microstructural conditions with the assumed vacancy bias factor equal to 1. Initial conditions for the growth equations were chosen, and the equations were solved numerically for a variety of temperatures, loop densities, and network dislocation densities. The last were assumed to be constant or to be decreasing with time according to a thermal annealing equation. Examination of the results indicates that, contrary to the model proposed by Little, Bullough, and Wood(63) for bcc metals, the difference in bias of <100> and <111> loops, and a high initial dislocation density that decreases with time, are not sufficient to explain <111> loop shrinkage in body-centered cubic metals.

8.1.2 Conditions for Loop Growth

In the standard rate theory formulation,(49,50,94) growth rate of small interstitial loops, treated as spherical sinks(95,96), is described by the differential equation(94)

$$\frac{\partial r_{\ell i}}{\partial t} = \frac{2}{r_{\ell i} b_i} [r_I^{\ell i} D_I C_I - r_V^{\ell i} D_V (C_V - C_{V\ell i}^{th})] \tag{42}$$

where $r_{\ell i}$ is the mean radius of the loops of type i, b_i is the magnitude of the Burgers vector, $r_I^{\ell i}$ is the effective capture radius of the loop of type ℓi for interstitials, $r_V^{\ell i}$ is the effective capture radius for vacancies, C_V and C_I are fractional point defect concentrations, and $C_{V\ell i}^{th}$ is the thermal vacancy concentration at the loop. The effective capture radii $r_I^{\ell i}$ and $r_V^{\ell i}$ are$^{(54)}$

$$r_{I,V}^{\ell i} = \bar{r}_{\ell i} \left[(1 + \pi \bar{r}_{\ell i}^{3} N_{\ell i})^{1/2} + (\pi \bar{r}_{\ell i} N_{\ell i})^{1/2} \bar{r}_{\ell i} \right]^2 (1 + \delta_{I,V}^{\ell i})$$

$$= r_c^{\ell i} (1 + \delta_{I,V}^{\ell i}) \tag{43}$$

where

$$\bar{r}_{\ell i} = \frac{\pi (r_{\ell i}^2 - r_d^2)^{1/2}}{\ell n \, (8 r_{\ell i} / r_d)} \tag{44}$$

with $N_{\ell i}$ the density of loops of type ℓi, and r_d the dislocation core radius. The preference factors $\delta_I^{\ell i}$ and $\delta_V^{\ell i}$ for interstitials and vacancies respectively can be considered either as model parameters$^{(82)}$ or can be calculated using the infinitesimal loop approximation$^{(92,93)}$.

When bias effects dominate, the thermal vacancy emission term in Eq. (42) can be neglected, and the growth rate of an interstitial loop is given by the difference between the first two terms, which represent the two defect fluxes. When a quasi-steady state condition has been attained, the defect concentrations can be written as

$$C_V = \frac{K_I}{2R} \left[\left(1 + \frac{4RG}{K_I K_V}\right)^{1/2} - 1 \right] \tag{45}$$

$$C_I = \frac{K_V}{2R}\left[\left(1 + \frac{4RG}{K_I K_V}\right)^{1/2} - 1\right] \tag{46}$$

where G is the point defect production rate per unit volume, and R is the recombination coefficient. The rate constants K_I and K_V are given by the product of the point defect diffusion coefficient and the total sink strength

$$K_\alpha = D_\alpha S_\alpha \tag{47}$$

where α is either I or V. Using Eqs. (42) through (47) we obtain the condition that must be met for a positive loop growth rate:

$$\frac{(1 + \delta_I^{\ell i})}{(1 + \delta_V^{\ell i})} > \frac{S_I}{S_V} \tag{48}$$

Equation (48) is formally identical to the equation obtained previously, with the ratio on the left-hand side replacing $Z_I^{\ell i}$.

Wolfer and Ashkin(92) have evaluated the factors $\delta_I^{\ell i}$ and $\delta_V^{\ell i}$ for small loops in the infinitesimal loop approximation using a perturbation technique. If one neglects a strain dependent term, which is negligible for small loops ($r_{\ell i}$ <100 b_i), one obtains

$$\delta_\alpha = \delta \left[\frac{b_i}{r_{\ell i}}\right]^2 \tag{49}$$

for α equal to I or V. The expression that defines the proportionality constant δ_α in Eq. (49) [see Eq. (16.6) of ref. 92] depends on properties of the material, i.e., the bulk modulus and Poisson's ratio; temperature; and defect properties, i.e., elastic polarizabilities and relaxation volumes, but is independent of loop type for edge loops. Thus, for loops of the same size, the magnitude of the preference factors for loops of <100> type are larger than those for <111> loops, the ratio being $\delta_\alpha^{<100>}/\delta_\alpha^{<111>} \approx (b_{<100>}/b_{<111>})^2 \approx 4/3$.

The model system that we assume for low doses contains three types of sink; network dislocations, <111> loops, and <100> loops. The sink strength S_I for interstitials is given by

$$S_I = L\, Z_I^n + 4\pi\, r_c^{\ell 1}\, N_{\ell 1}\,(1 + \delta_I^{\ell 1}) + 4\pi\, r_c^{\ell 2}\, N_{\ell 2}\,(1 + \delta_I^{\ell 2}) \qquad (50)$$

and that for vacancies by

$$S_V = L Z_V^n + 4\pi r_c^{\ell 1}\, N_{\ell 1}(1 + \delta_V^{\ell 1}) + 4\,\pi r_c^{\ell 2}\, N_{\ell 2}\,(1 + \delta_V^{\ell 2}) \qquad (51)$$

where L is the network density, and Z_I^n and Z_V^n are bias factors for the network. Superscripts n, $\ell 1$, and $\ell 2$ are used respectively for parameters referring to network dislocations, <111> loops, and <100> loops. The preference factors $\delta_V^{\ell i}$ are generally small and will be neglected in the subsequent development. The proportionality constant δ_I is redefined as δ.

The boundary between growth and shrinkage regimes is determined by

$$\frac{S_I}{S_V} = 1 + \delta \left[\frac{b_i}{r_{\ell i}}\right]^2 \qquad (52)$$

for i = 1 or 2, and therefore, the condition for shrinkage of <111> loops and growth of <100> loops is

$$1 + \delta \left[\frac{b_1}{r_{\ell 1}}\right]^2 < \frac{S_I}{V^S} < 1 + \delta \left[\frac{b_2}{r_{\ell 2}}\right]^2 \qquad (53)$$

8.1.3 Calculations

Sink strength ratios were calculated as a function of the materials parameter δ for network densities, L, of 10^8 and 10^{12}, <111> loop densities of 10^{14} and 10^{16} cm^{-3}, and loop radii multiples of 2.5, 10, 25, and 50 of their Burgers vector b. Radii of <111> and <100> loops were assumed equal, the vacancy preference factors were assumed to be zero, and the ratio of <100> loop density to <111> loop density was taken as 10^{-5}. Results are plotted in Figs. 42 through 45 for $N_{\ell 1} = 10^{14}$ cm^{-3}. Solid curves are labeled by values of L. The dashed lines define the boundaries of the various regimes. For sink strength ratios to the left of both lines, both types of loop shrink; for those between the lines, <111> loops shrink and <100> loops grow; and for those to the right of both lines, both types of loop grow.

Several trends can be noted in the figures. In the growth/growth regime at higher values of δ in Figs. 42 through 45, S_I/S_V decreases as L increases for constant δ with a limiting value of 1.05, the assumed network bias. In the shrinkage/growth and shrinkage/shrinkage regimes, the situation is reversed with S_I/S_V increasing as L increases. The curves for differing L cross when S_I/S_V equals 1.05; as loop radius increases, the value of δ, defined as δ_c, at which this occurs, increases. In Fig. 46, δ_c is plotted as a function of normalized loop radius. A necessary but not sufficient condition for shrinkage/growth of loops of a given size is that δ be less than the critical value δ_c.

The calculated shrinkage/growth regimes for the set of 16 different conditions considered are summarized graphically in Fig. 47. The filled-in bars indicate the range of δ for which this condition holds.

The parameter δ is fixed by the material and the loop type for small loops. Wolfer and Ashkin(92) calculated δ for edge loops in nickel and obtained a value of 27.4. If we assume a comparable value for niobium, then from Figs. 46 and 47 we find that the loop radii must be of the order of 25 b_1 or approximately 7 nanometers for the shrinkage/growth condition to be realized. These are fairly large loops, well beyond the nucleation stage. Consideration of the experimental results, i.e., <111> loop shrinkage and <100> loop growth in ferritic steels, and the results of these calculations then suggests that <111> and <100> loops nucleate and grow until the critical size is reached, after which shrinkage of <111> loops occurs with continued growth of <100> loops. The loop growth equations were solved for a variety of conditions in order to see if this behavior is predicted by the model.

Curve 750508-A

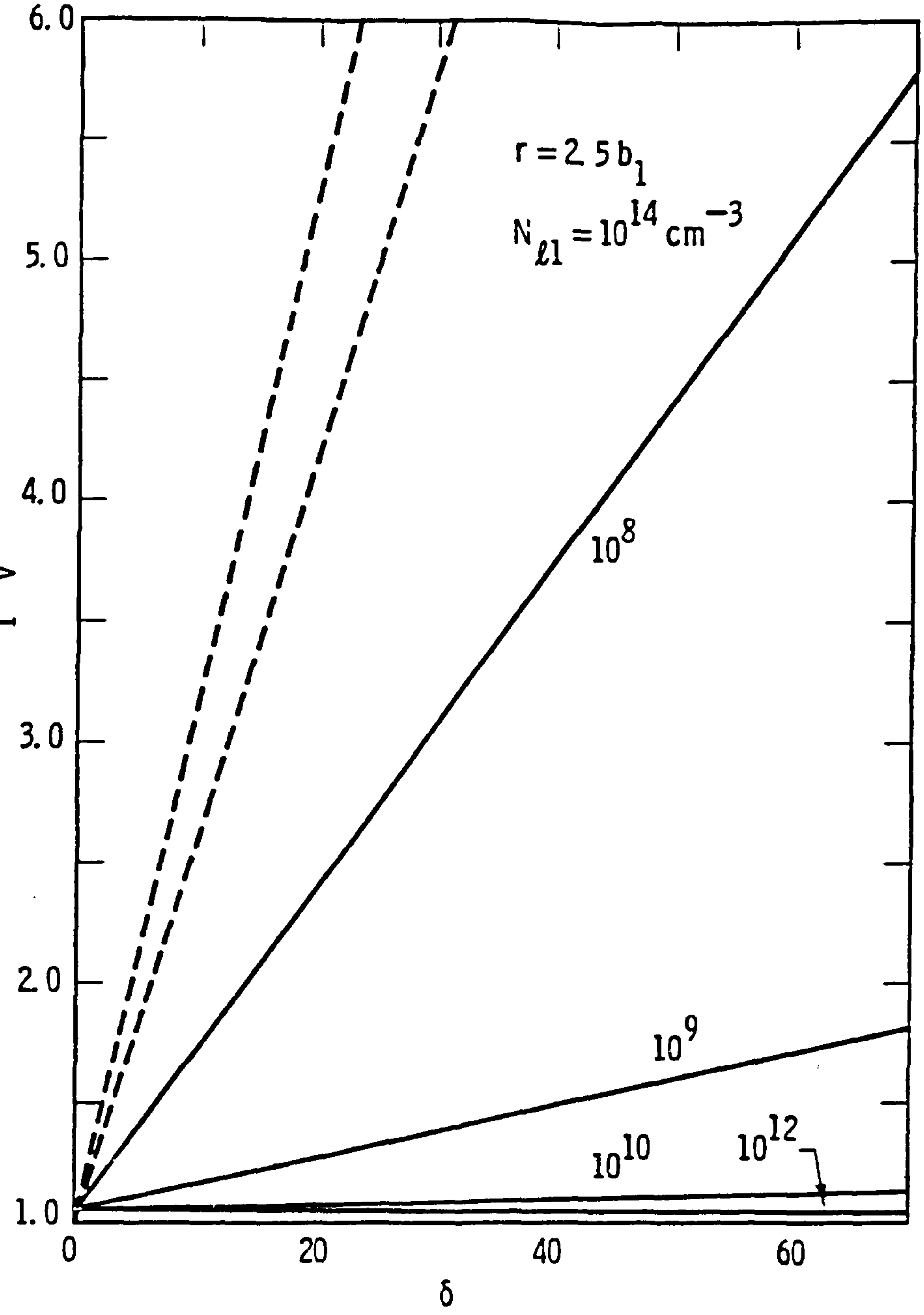

Figure 42. Sink Strength Ratio as a Function of Parameter δ for Several Network Dislocation Densities. Curves are Labeled by Value of L. Dashed Curves Define Zero Growth Conditions for <100> (Upper) and <111> (Lower) Loops. $N_{\ell 1} = 10^{14}$ cm^{-3}, $N_{\ell 2} = 10^9$ cm^{-3}, $Z_I^n = 1.05$, and $r_{\ell 1} = r_{\ell 2} = 2.5\ b_1$.

Curve 750509-A

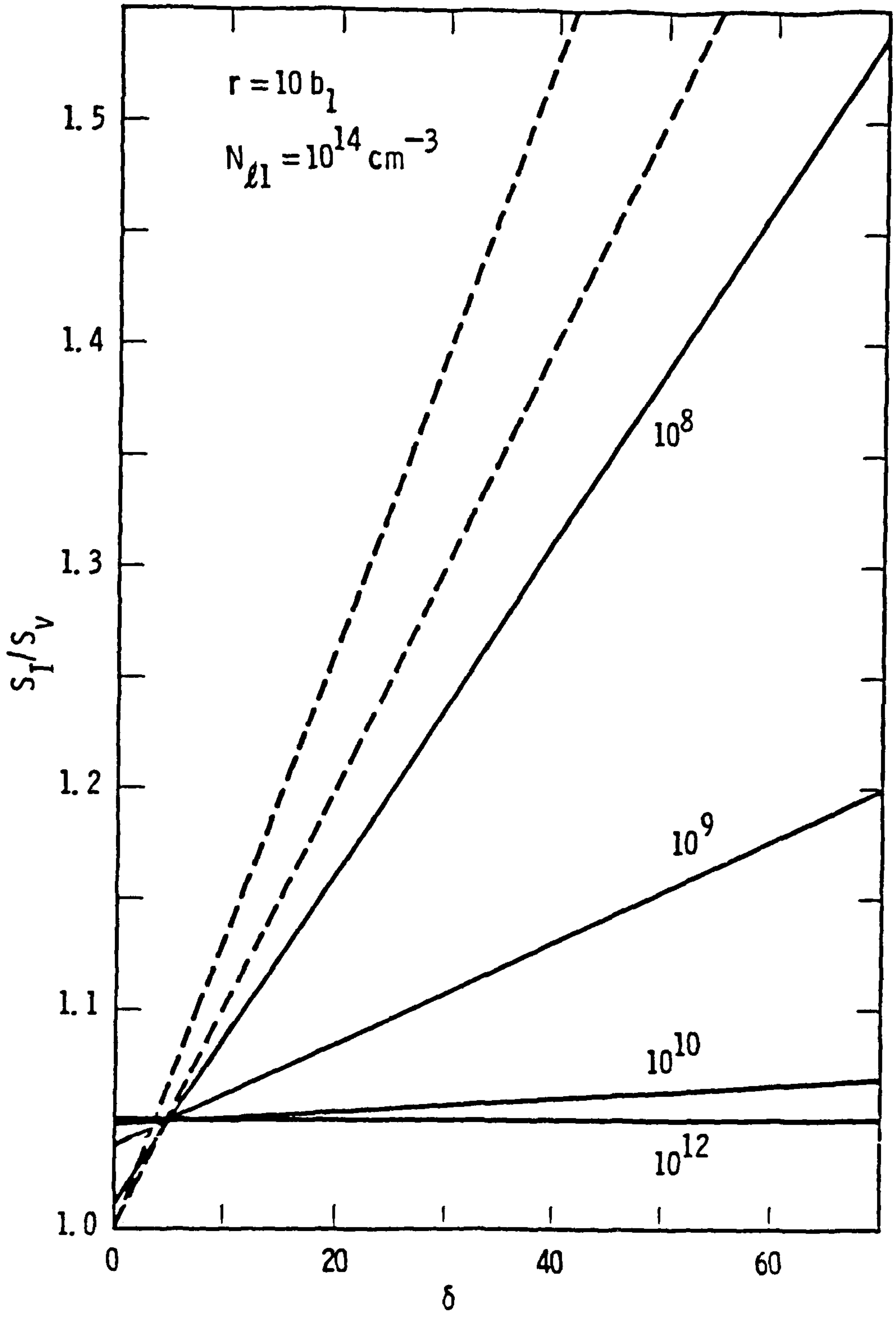

Figure 43. Sink Strength Ratio as a Function of Parameter δ for Several Network Dislocation Densities. Same Labeling as Fig. 42. $r_{\ell 1} = r_{\ell 2} = 10\ b_1$.

Curve 750507-A

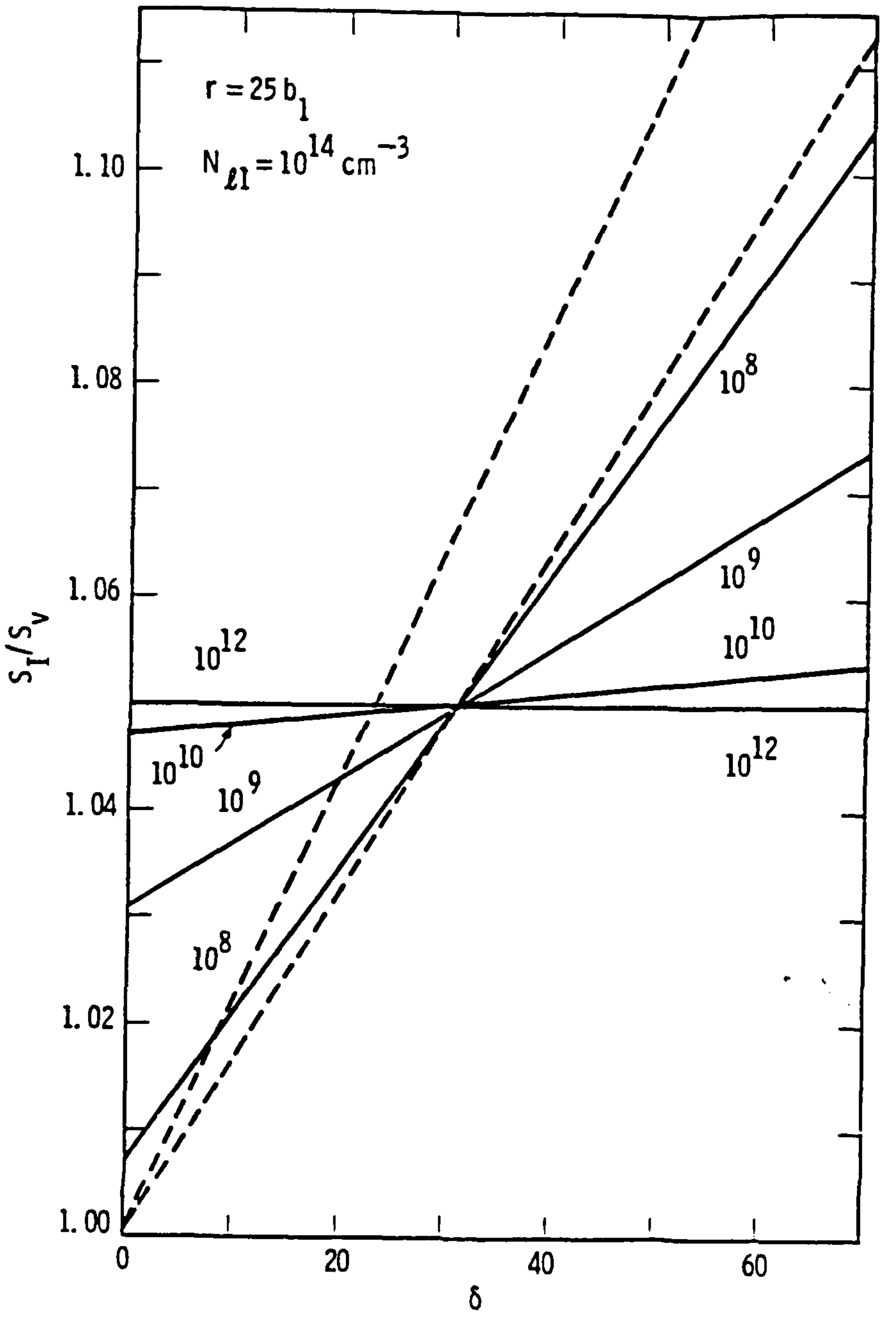

Figure 44. Sink Strength Ratio as a Function of Parameter δ for Several Network Dislocation Densities. Same Labeling as Fig. 42. $r_{\ell 1} = r_{\ell 2} = 25\ b_1$.

Curve 750511-A

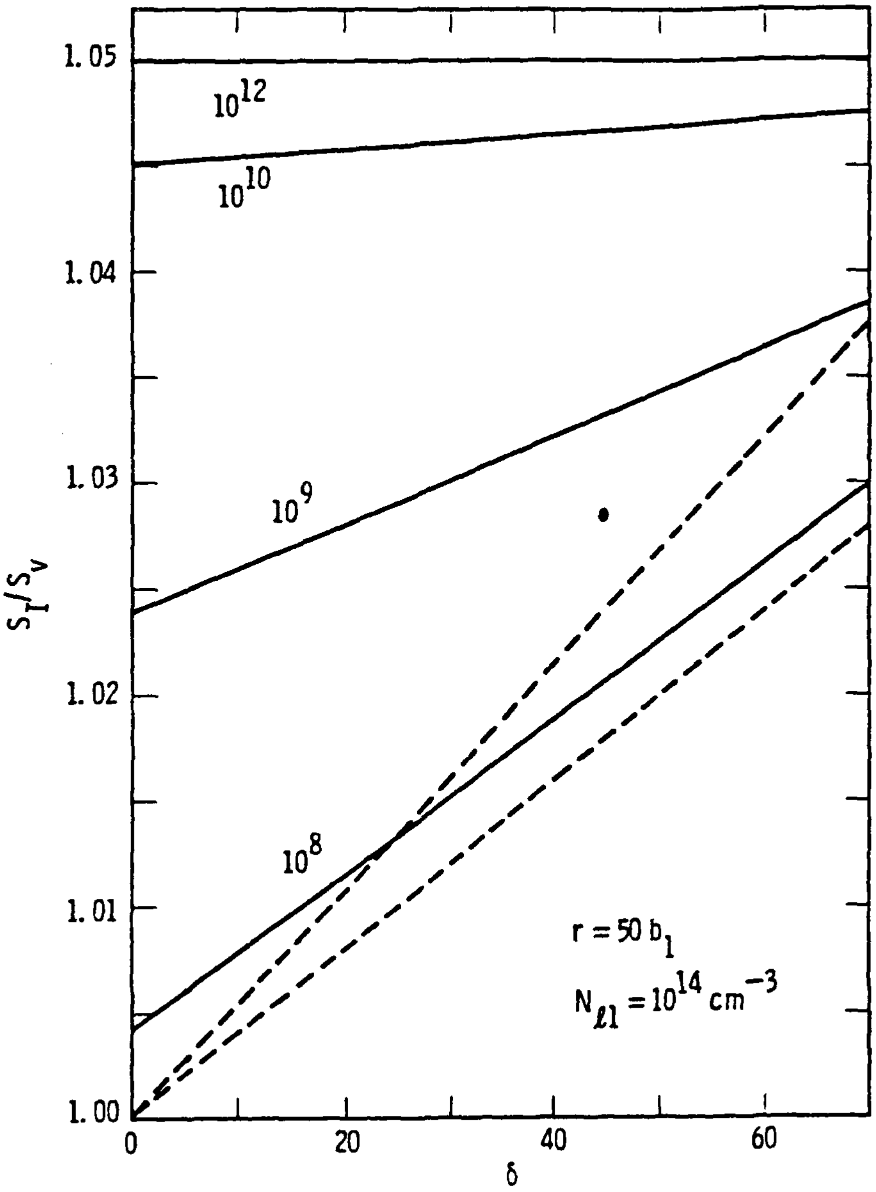

Figure 45. Sink Strength Ratio as a Function of Parameter δ for Several Network Dislocation Densities. Same Labeling as Fig. 42. $r_{\ell 1} = r_{\ell 2} = 50\ b_1$.

Curve 750510-A

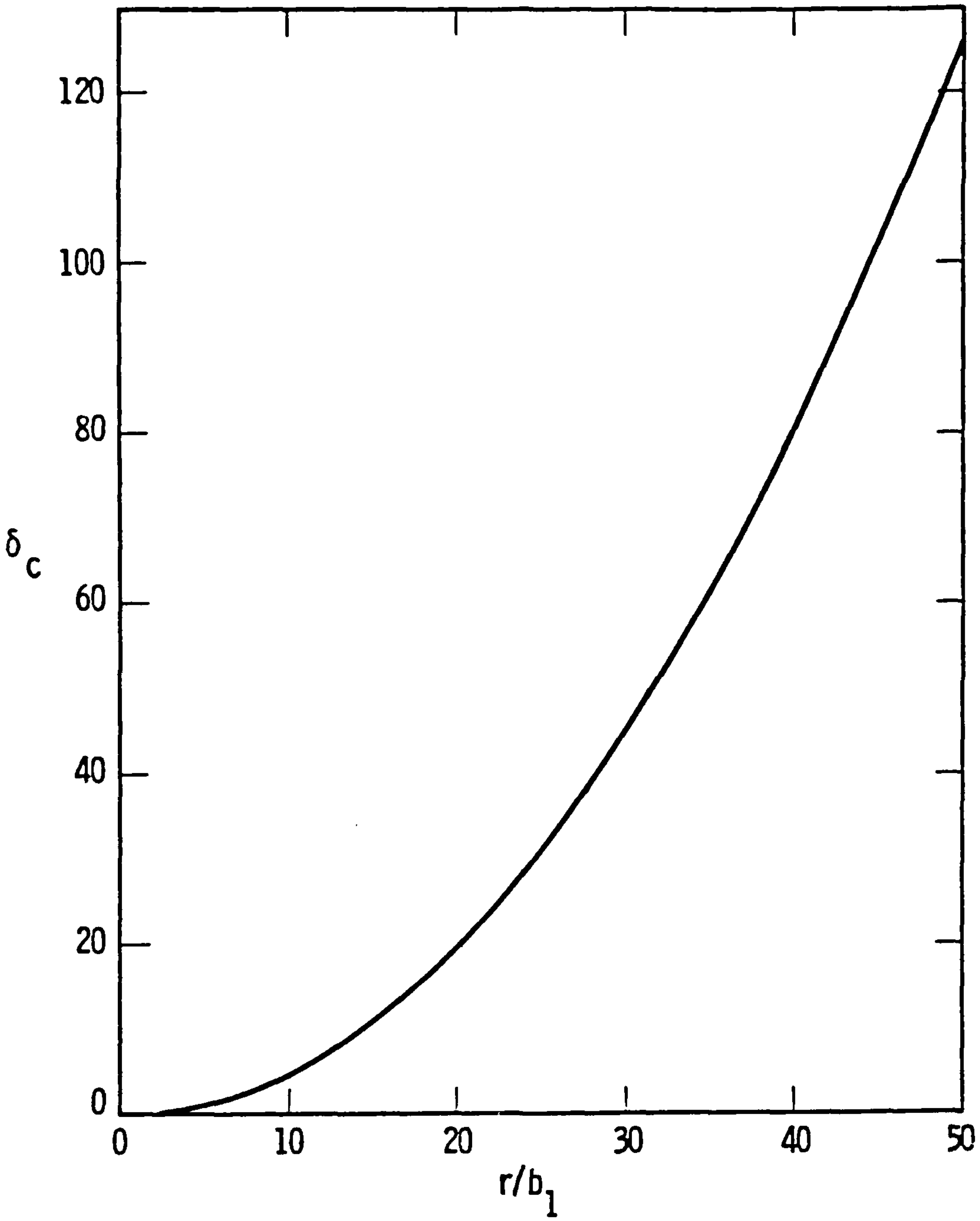

Figure 46. Critical δ as a Function of Normalized Loop Radius. $N_{\ell 1} = 10^{14}$ cm^{-3}, $N_{\ell 2} = 10^{9}$ cm^{-3}, $Z_I^n = 1.05$.

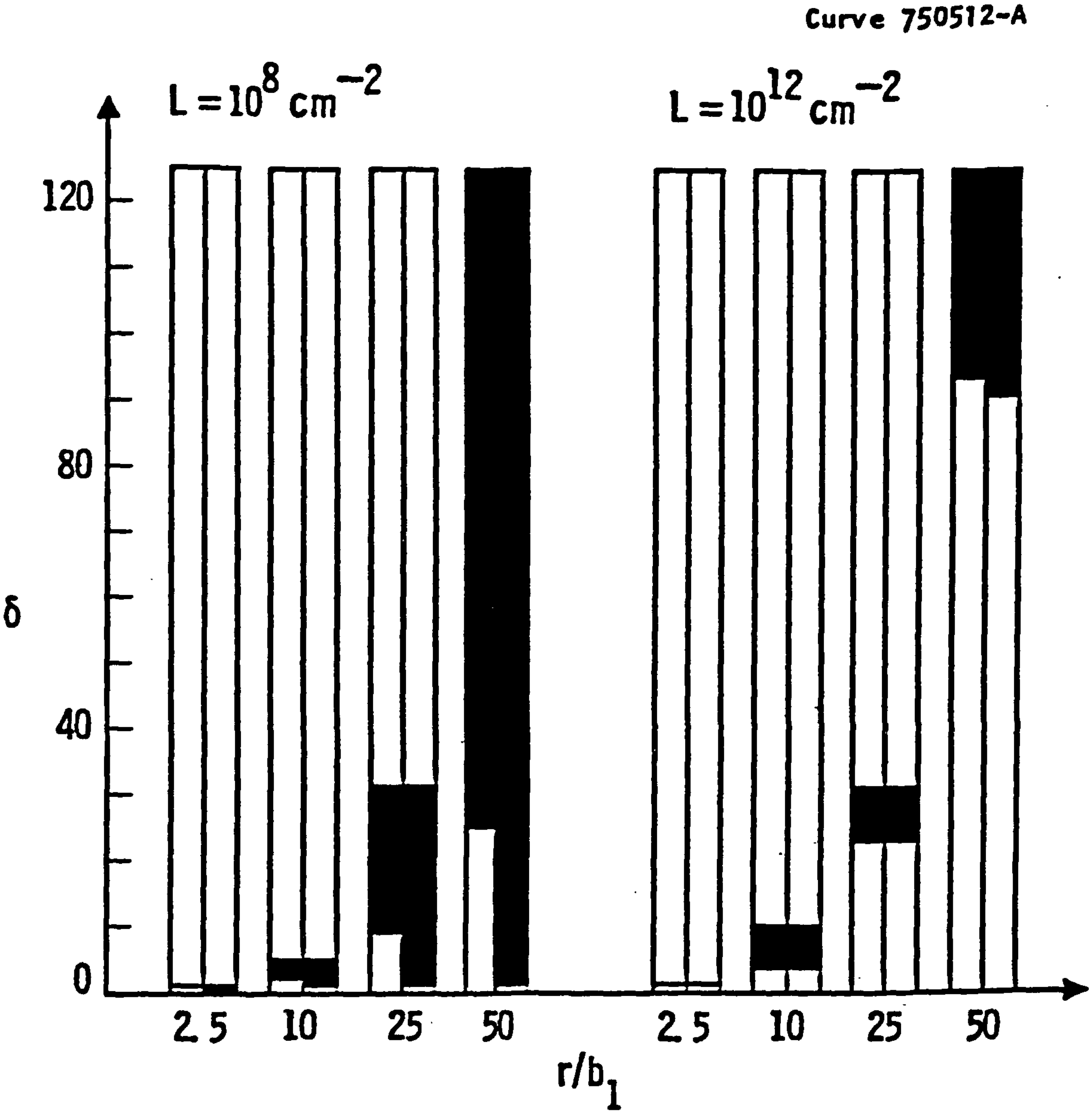

Figure 47. Summary of Growth/Shrinkage Regimes for Four Loop Radii. Sets are Labeled by Network Density L; Left Bar in Each Pair is for $N_{\ell 1} - 10^{14}\ cm^{-3}$ and $N_{\ell 2} - 10^9\ cm^{-3}$, and Right Bar for $N_{\ell 1} - 10^{16}\ cm^{-3}$ and $N_{\ell 2} - 10^{11}\ cm^{-3}$. Solid Region Indicates Range in which <111> Loops Shrink and <100> Loops Grow.

8.1.4 Loop Growth

Equations (42) through (47) define the model. The <111> and <100> loop radii at $t = 0$ were assumed to be equal with a value of 2.5 b_1, since calculations with unequal initial values showed that the final results were unaffected by the initial conditions. Parameters for niobium were used, and are given in Table XIII. Solutions to the system of equations were obtained for temperatures between 700 K (0.26 T_m) and 1100 K (0.40 T_m), with <111> loop densities of 10^{14} and 10^{16} cm^{-3}, and constant network densities of 10^8 and 10^{12}. <100> loop densities were given by

$$N_{\ell 2} = N_{\ell 1} \exp\left(\frac{-6.97 \times 10^3}{kT}\right) \qquad (54)$$

In addition, the network bias Z_I^n was varied.

The calculations showed that:

(1) both types of loops grow as expected when the initial radii are 2.5 b_1;

(2) the growth rate of <100> loops is greater than that of <111> loops due to the larger preference factor of the former;

(3) the initial sink strength of the system is high because of the large values of the loop preference factors at small sizes, but falls rapidly as the loops grow;

(4) the loops grow until the radii reach steady state values given by

$$1 + \delta \left[\frac{b_1}{r_{\ell 1}}\right]^2 = 1 + \delta \left[\frac{b_2}{r_{\ell}}\right]^2 = Z_I^n \qquad (55)$$

after which no further growth (or shrinkage) occurs;

(5) the steady state radii are independent of the assumed values of L, $N_{\ell 1}$, $N_{\ell 2}$, and temperature;

(6) higher temperatures reduce the time required to reach steady state.

TABLE XIII

Parameters for Niobium

Lattice parameter, α	3.29×10^{-8} cm
Atomic volume, Ω	1.78×10^{-23}cm
Nearest neighbor distance, d	2.85×10^{-8} cm
Vacancy migration energy, E_V^m	1.09 eV
Vacancy diffusion prefactor, D_{Vo}	0.008 cm^2/s
Interstitial migration energy, E_I^m	0.115 eV
Interstitial diffusion prefactor, D_{Io}	10^{13} $d^2/6$ cm^2/s

The key to what is happening physically is given in Eq. (54). The bias of network dislocations, <111> loops, and <100> loops are identical. With no differential bias in the system, all of the microstructural elements act as recombination centers, absorbing equal numbers of interstitials and vacancies. No growth or shrinkage is possible in this situation.

The question then arises -- what is necessary to produce <111> loop shrinkage and <100> loop growth? Little, Bullough, and Wood assume a decreasing network density in their model, consistent with experimental observations. Based on a phenomenological model for the change in network density during irradiation(97), a time dependent network density was incorporated in our model. The instantaneous density at time t was assumed to be

$$L = L_o/(ALt + 1) \tag{56}$$

Consistent with result (5) above, the new set of calculations showed that the steady state radii are unaffected, and therefore the decreasing network density does not lead to <111> loop shrinkage. Its primary effect is on the instantaneous sink strength, which is larger at a given time than for a constant network density. The major conclusion to be drawn is that a chemical reaction rate formulation of the model proposed by Little, Bullough, and Wood does not predict <111> loop shrinkage.

Three other possible mechanisms for change from the growth/growth to the shrinkage/growth regime are currently being explored. The first is relatively subtle. The derivation of the preference factor using the infinitesimal loop approximation leads to an expression with a limit of 0 as the loop radius goes to infinity, implying a network bias of 1. In fact, the correct limit should yield a network bias greater than 1. The effect of an appropriately modified preference factor on loop growth kinetics is being examined.

The second mechanism is the introduction of void embryos at some finite time after loop growth is underway. The third is a relatively abrupt change in the network bias, possibly associated with the formation of domains or walls. Both of these processes can be simulated with minor changes in the model equations.

8.2 Experimental Program on Low Dose Microstructural Evolution

As described in ref. 1, bcc metals exhibit low swelling because of the presence of <100> type interstitial dislocation loops. Two types of interstitial loops are observed in bcc metals after irradiations. The type most frequently observed is a perfect loop with $\frac{a}{2}$<111> Burgers vector and a {111} habit plane(58-61).

After ion or neutron irradiation at high temperatures, however, perfect loops with a <100> Burgers vector and {100} habit planes are seen in α-iron(62) and ferritic alloys(63). According to Eyre and Bullough(64), the <100> loops are formed by aggregation of <110> split dumbbell interstitials on {110} planes to form faulted loop nuclei with $\frac{a}{2}$ <110> Burgers vector. These loops undergo unfaulting due to the high stacking fault energies of bcc metals. The two unfaulting reactions are as follows:

$$\frac{a}{2}\,[110] + \frac{a}{2}\,[1\bar{1}0] \rightarrow a[100]$$

or

$$\frac{a}{2}[110] + \frac{a}{2}[001] \rightarrow \frac{a}{2}[111]$$

The mechanism of swelling suppression in bcc metals is based on theoretical considerations of bias factors for interstitial dislocation loops(52-55). Theoretical calculations indicate that the bias of a dislocation depends on the magnitude of its Burgers vector. Hence, the bias of <100> dislocations can act to absorb the excess vacancies that would be available for void formation in their absence.

According to the theory of Eyre and Bullough(64), the necessary conditions for swelling suppression are (1) the presence of a high initial dislocation density and (2) a sufficiently high probability for a <100> loop formation. In this investigation, attention was focused on the latter consideration. As shown in Table XIV, niobium and vanadium have the highest probability of formation of <100> type loops of all the pure bcc refractory metals.

TABLE XIV

Lattice Parameters, Shear Moduli, and Calculated Relative Probabilities for <100> Loop Formation in a Range of BCC Metals

Metal	Parameter a (nm)	Lattice Shear Modulus μ (x 10 GPa)	Relative Probability P
Nb	0.330	39.6	4.3×10^{-5}
V	0.304	4.73	5.5×10^{-5}
Fe	0.287	8.60	5.7×10^{-9}
Ta	0.330	7.07	7.9×10^{-11}
Mo	0.315	12.3	1.9×10^{-19}
W	0.317	16.0	1.4×10^{-27}

These theoretical considerations were paramount in designing the experimental matrix.

8.2.1 Test Matrix

Table XV shows the experimental matrix for the investigation of low dose microstructural evolution.

TABLE XV

Irradiation Test Matrix for the Low Dose Experiment

Irradiation Temperature (°C)	Dose (dpa)					
1000	0.05	0.1	0.5	1	3	5
800	0.05	0.1	0.5	1	3	5

Two temperatures, 800° and 1000°C, were chosen for irradiation. These temperatures, which lie on either side of the swelling peak, were chosen as representative temperatures for the two groups of sink strength ratios, S_I/S_V, i.e., 1.017-1.033 and 1.034-1.062, as shown in Table X of ref. 1. Since the sink strength ratios are directly correlatable to growth and shrinkage of the two types of loops and growth, and concomitant shrinkage of voids, as shown in ref. 1, the microstructural evaluation of specimens irradiated to a fixed dose at two different temperatures should provide data which can be directly compared to the theoretical predictions.

The irradiation dose was varied over two orders of magnitude, from 0.05 dpa to 5 dpa, to provide data on the microstructural evolution including the nucleation and incubation stages on the low dose side and network formation and loop-network coupling on the high dose side of the matrix. The high dose irradiations may also provide useful information on the incubation dose for cavity formation.

The data obtained from the examination of these specimens will afford a systematic description of loop characteristics ($\frac{a}{2}$ <111> vs a <100>), loop density, loop size distribution, network development, network dislocation densities, and cavity and loop incubation parameters.

8.2.2 Material Procurement and Specimen Preparation

Niobium used in this investigation was Marz-grade rod (3.2 mm dia.) obtained from the Materials Research Corporation. The material was received in the as-worked condition. The vendor supplied chemical analysis indicated oxygen, carbon, and nitrogen contents of 15, 25, and <5 wppm, respectively.

The rod was machined to ≈3 mm in diameter, cut into ≈0.6 mm thick discs and mechanically polished using procedures outlined in ref. 1. The disc specimens were cleaned and annealed under vacuum of $\leq 2 \times 10^{-8}$ torr at 1200°C for 30 min. in a closed tantalum box. Titanium and tantalum blocks were placed in the hot zone of the furnace as trapping agents for gases.

The annealed specimens were cleaned, examined, and immediately stored in 200 proof ethanol to avoid oxidation of the annealed and polished surfaces. The hardness of these specimens was the same as specimens irradiated in the Phase I study; i.e., 70-74 VHN. This indicates that the two materials, obtained from the same vendor, have similar impurity contents. The measured values of O and C impurities in the Phase I material were 700 and 255 appm, respectively.

8.2.3 Irradiation Procedure

The specimens were loaded into a tantalum holder consisting of a 5 x 6 array of holes approximately 2.3 mm in diameter with a 3 mm recess on the back side. They were secured by four tantalum tabs spot-welded to the specimen holder. The tabs held the specimens so that they were free to move in all directions during annealing and irradiation. This avoided any deformation due to clamping. Although 20 specimens were loaded into the holder at one time, all specimens could not be brought into line with the beam because of the limited travel of the loading system.

The specimens were irradiated with 5.3 ± 0.1 MeV Nb^{++} ions at a displacement rate of 5 to 6 x 10^{-3} dpa/s (displacement per atom per second) to various peak doses ranging from 0.05 to 5 dpa.

Prior to irradiation, each specimen was annealed at 1200°C for 1/2 h. The base vacuum prior to annealing was 5 x 10^{-9} torr. After outgassing of hydrogen, detected by a residual gas analyzer, the pressure decreased to $\leq 8 \times 10^{-8}$ torr. The vacuum was kept at $\leq 4 \times 10^{-8}$ torr during irradiation. Immediately after removal from the irradiation chamber, the specimens were stored in 200 proof ethanol.

Sectioning was accomplished by ion milling with 800 eV argon for 20-25 minutes to remove ≈700 nm from the front surface. The sectioning depths were determined by profilometer of control specimens ion-milled along with the irradiated specimens. The section depths varied from 60-67 nm.

The TEM specimen preparation of the sectioned specimens was accomplished by electropolishing in a solution of NH_4F in methanol at -30°C. This method of electropolishing resulted in good polished specimens however, a thin layer of oxide was invariably formed on the foil which made the TEM examination difficult, especially when imaging in $g = [200]$ diffraction condition. In this condition, Moire' fringes, due to the oxide, were observed superimposed on the image of the specimen. Removal of oxide by ion milling with 5 KeV was possible, but this resulted in buckling of the foil due to removal of the high strength oxide and low inherent strength of the material. Upon examination of the ion-milled foils, however, fine scale damage, manifested as dislocations and small loops, was observed on the milled surfaces. This damage was limited to <25 nm from the surface, however, it made the analysis of loops difficult. It was therefore necessary to selectively remove this damage without affecting the microstructure underneath. A number of methods were examined to accomplish this, including electropolishing and chemical polishing. After many attempts, a solution consisting of 15 ml HNO_3+ 5 ml HF in 50 ml glycerine was found to be successful in controlled removal of small amounts of material. A dip in this solution for 2-3 min. removed all the fine milling damage, however, some of the dislocation segment damage persisted. This was confirmed on a control specimen milled for 22.5 min. prior to acid dip.

8.2.4 Results of TEM Examinations

All specimens were examined in a Philips EM-400 microscope operating at 120 KeV. The specimens had a large grain size and were preferentially oriented such that the foil normal was in the [011] direction. Images were obtained by tilting the specimen to obtain diffraction, $g = \pm [011]$. To determine the density and characteristics of the loops, it is necessary to know the conditions for their visibility with operating g.

Table XVI lists $g \cdot b$ for g^s in <100>, <110>, and <112> for all possible combinations of loop orientations. A $g \cdot b = 0$ indicates that under these conditions, loops will not be visible (except for residual contrast) whereas $g \cdot b > 0$ indicates visibility.

Examination of the micrographs, taken in stereopairs, showed that the loops were uniformly distributed, but the dislocation segments were located predominately near one surface. These segments were the result of remnant ion-milling damage. The dislocations produced by self-ion damage appeared different and were distributed throughout the foil. These dislocations were often pinned at the loops.

Figures 48a and 48b show TEM micrographs of specimens irradiated at 1000°C to 0.05 and 0.1 dpa, respectively. The diffraction conditions for these and other loops were described above. The loops can be easily resolved at a magnification of 440,000. The fine mottling in the background results from ion-milling damage and some evidence of Moire' fringes due to surface oxide can also be seen. The Moire' fringes were not observed on all specimens examined. Figures 49a and 49b show TEM micrographs of specimens irradiated at 1000°C to 0.5 and 2.9 dpa, respectively, and Fig. 50 shows loops produced at 4.3 dpa. The dislocation segments referred to above can be easily seen in these figures and pinning of these segments is clear in Figs. 49b and 50 (see segments A and B).

TABLE XVI

Results of g·b Analysis for $\frac{a}{2}$ <111> and a <100> Loops

g·b

b

g	$\frac{a}{2}[111]$	$\frac{a}{2}[\bar{1}\bar{1}\bar{1}]$	$\frac{a}{2}[\bar{1}11]$	$\frac{a}{2}[1\bar{1}1]$	$\frac{a}{2}[11\bar{1}]$	$\frac{a}{2}[\bar{1}\bar{1}1]$	$\frac{a}{2}[1\bar{1}\bar{1}]$	$\frac{a}{2}[\bar{1}1\bar{1}]$	a[100]	a[$\bar{1}$00]	a[010]	a[0$\bar{1}$0]	a[001]	a[00$\bar{1}$]
200	1	-1	1	1	1	-1	1	-1	2	-2	0	0	0	0
$\bar{2}00$	-1	1	1	-1	-1	1	-1	1	-2	2	0	0	0	0
020	1	-1	1	-1	1	-1	-1	1	0	0	2	-2	0	0
$0\bar{2}0$	-1	1	-1	1	-1	1	1	-1	0	0	-2	2	0	0
002	1	-1	1	1	-1	1	-1	-1	0	0	0	0	2	-2
$00\bar{2}$	-1	1	-1	-1	1	-1	1	1	0	0	0	0	-2	2
$01\bar{1}$	0	0	0	-1	1	-1	0	1	0	0	1	-1	-1	1
$0\bar{1}1$	0	0	0	1	-1	1	0	-1	0	0	-1	1	1	-1
$\bar{1}10$	0	0	1	-1	0	0	-1	1	-1	1	1	-1	0	0
$1\bar{1}0$	0	0	-1	1	0	0	1	-1	1	-1	-1	+1	0	0
$10\bar{1}$	0	0	-1	0	1	-1	1	0	1	-1	0	0	-1	1
$\bar{1}01$	0	0	1	0	-1	+1	-1	0	-1	1	0	0	1	-1
$11\bar{2}$	0	0	-1	-1	2	-2	2	2	1	-1	1	-1	-2	2
$\bar{1}\bar{1}2$	0	0	1	1	-2	2	-2	-2	-1	1	-1	1	2	-2
$1\bar{2}1$	0	0	-1	2	-1	1	1	-2	1	-1	-2	2	1	-1
$\bar{1}2\bar{1}$	0	0	+1	-2	1	-1	-1	2	-1	1	2	−2	-1	1
$\bar{2}11$	0	0	2	-1	-1	1	-2	1	-2	2	1	-1	1	-1
$2\bar{1}\bar{1}$	0	0	-2	1	1	-1	2	-1	2	-2	-1	1	-1	1
$2\bar{1}1$	1	-1	-1	2	0	0	1	-2	2	-2	-1	1	1	1
$\bar{2}1\bar{1}$	-1	1	1	-2	0	0	-1	2	-2	2	1	-1	-1	1
$21\bar{1}$	1	-1	-1	0	2	-2	1	0	2	-2	1	-1	-1	1
$\bar{2}\bar{1}1$	-1	1	1	0	-2	2	-1	0	-2	2	-1	1	1	-1
$1\bar{1}2$	1	-1	0	2	-1	1	0	-2	1	-1	-1	1	2	-2
$\bar{1}1\bar{2}$	-1	1	0	-2	1	-1	0	2	-1	1	1	1	-2	2
$12\bar{1}$	1	-1	0	-1	2	-2	0	1	1	-1	2	-2	-1	1
$\bar{1}\bar{2}1$	-1	1	0	1	-2	2	0	-1	-1	1	-2	2	1	-1

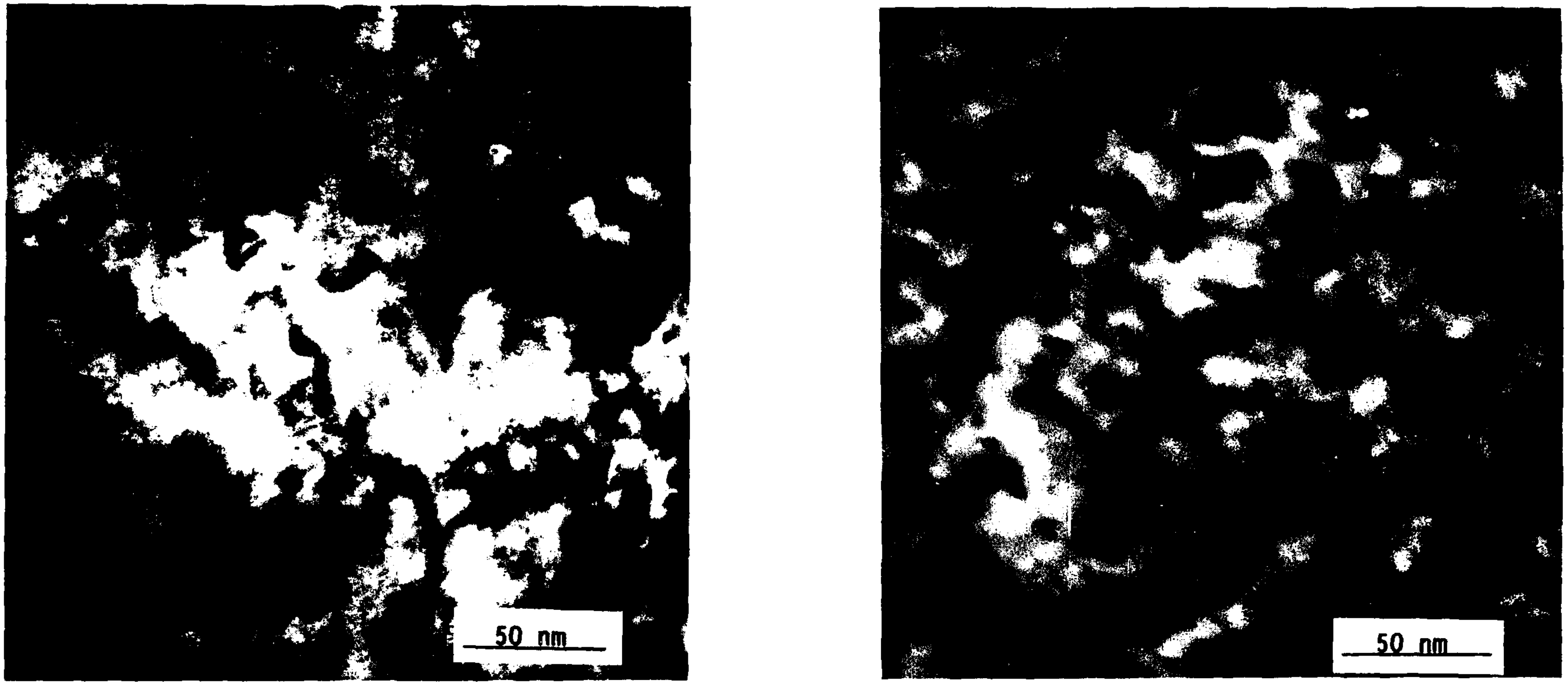

(a)

(b)

Figure 48. Loops in Niobium Irradiated at 1000°C to (a) 0.05 dpa and (b) 0.1 dpa. $g = [011]$, $Z \sim [011]$.

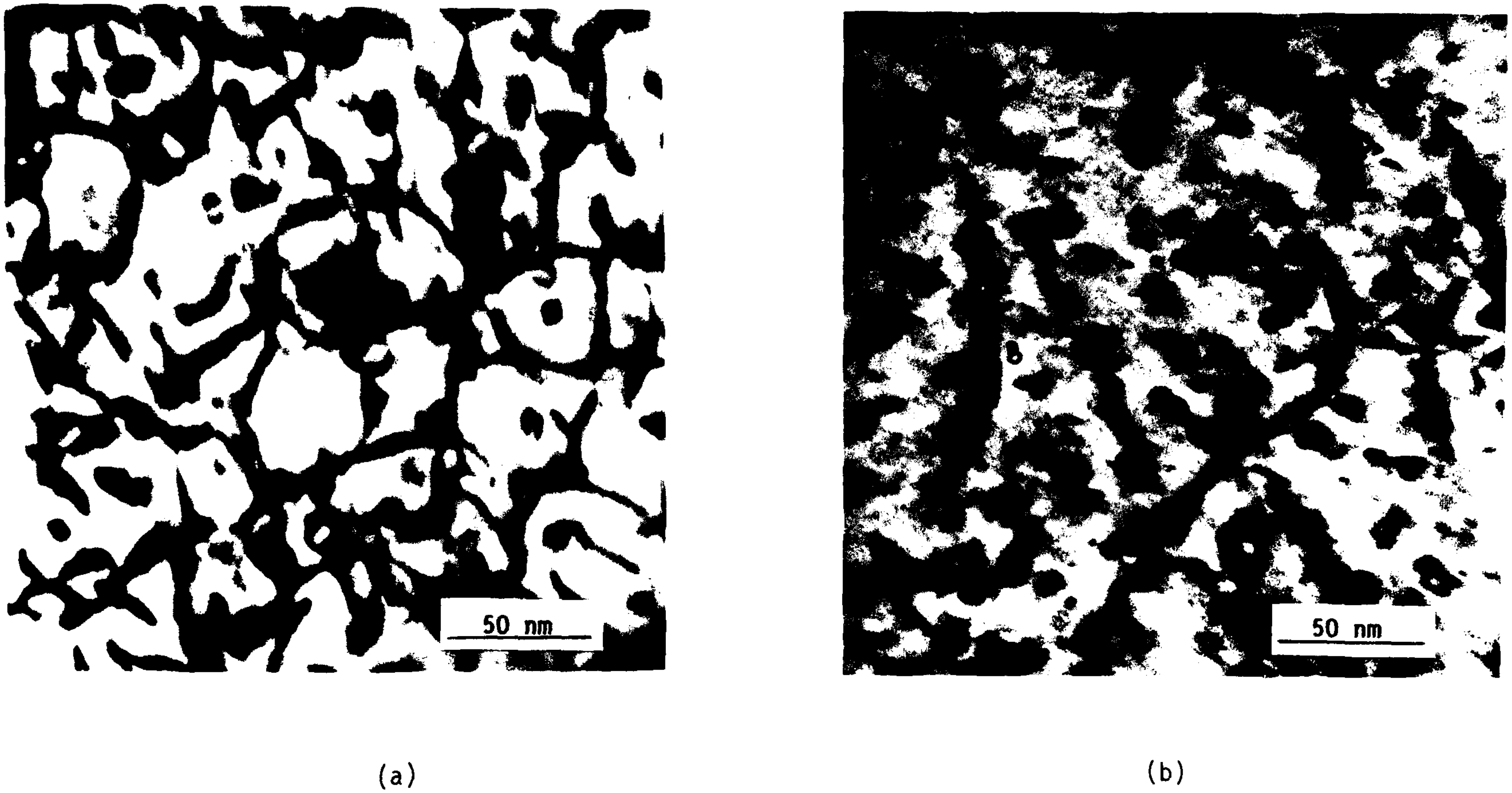

(a)

(b)

Figure 49. *Loops in Niobium Irradiated at 1000°C to (a) 0.5 dpa and (b) 2.9 dpa.* $g = [011]$, $Z \sim [011]$.

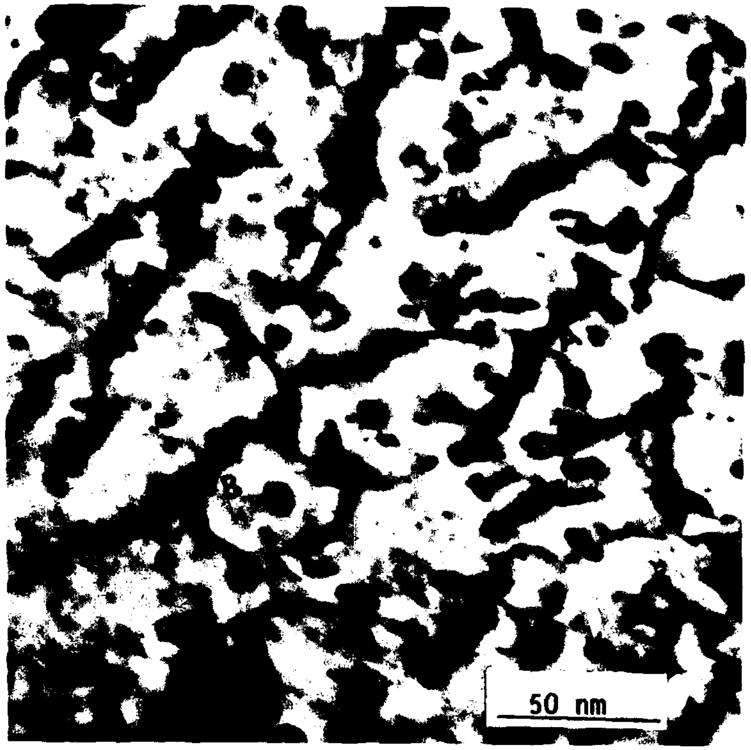

Figure 50. Loops in Niobium Irradiated at 1000°C to 4.3 dpa.
g = [011], Z ~ [011].

The loops produced at 800°C in specimens irradiated to 0.09 and 0.5 are shown in Fig. 51a and 51b, respectively, and those produced at doses of 2.5 and 3.8, respectively, are shown in Fig. 52a and 52b.

At the irradiation temperature of 800°C, voids were also found at doses above 0.5 dpa. TEM micrographs of voids at 0.5, 1.0, 2.7 and 4.1 dpa are shown in Fig. 53a and 53b, and Fig. 54a and 54b, respectively. The voids were imaged in the kinematic diffraction condition, with slight defocusing, to obtain the true size of the voids.

Table XVII summarizes the result of the analysis of loops and voids and lists average loop size, loop size range, average loop density and average void size and percent swelling for specimens. In Table XVII, the doses correspond to the dose at the section of foil examined, and are correct to within ± 10%. The number density of loops in Table XVII was obtained by multiplying the observed density by a factor of 2 since only half of the loops will be visible in g = [011] diffraction condition as shown in Table XVI.

Table XVII shows that at 1000°C the loop size is small and remains relatively constant over a wide range of doses. The loop density decreases with increasing dose and the loops are small. At 800°C, the loop size is small and the loop densities are comparable to those at 1000°C.

The density and size of loops at 800°C are consistent with the results of the only other study on niobium ion-irradiated at elevated temperatures conducted by Loomis et al.(90) They irradiated niobium with nickel ions to 34-44 dpa at 828°-875°C. The loop size ranged from 10-12 nm and densities were 9-4 x 10^{15} cm^{-3} over this temperature range. Their results would indicate that the equilibrium loop size over this temperature range is ≈10 nm because of their high doses.

The constant small size of loops at 1000°C is surprising since, with increasing temperature, the loop size is expected to increase. Loomis et al. showed an average loop size of 98 nm, which are an order of magnitude larger

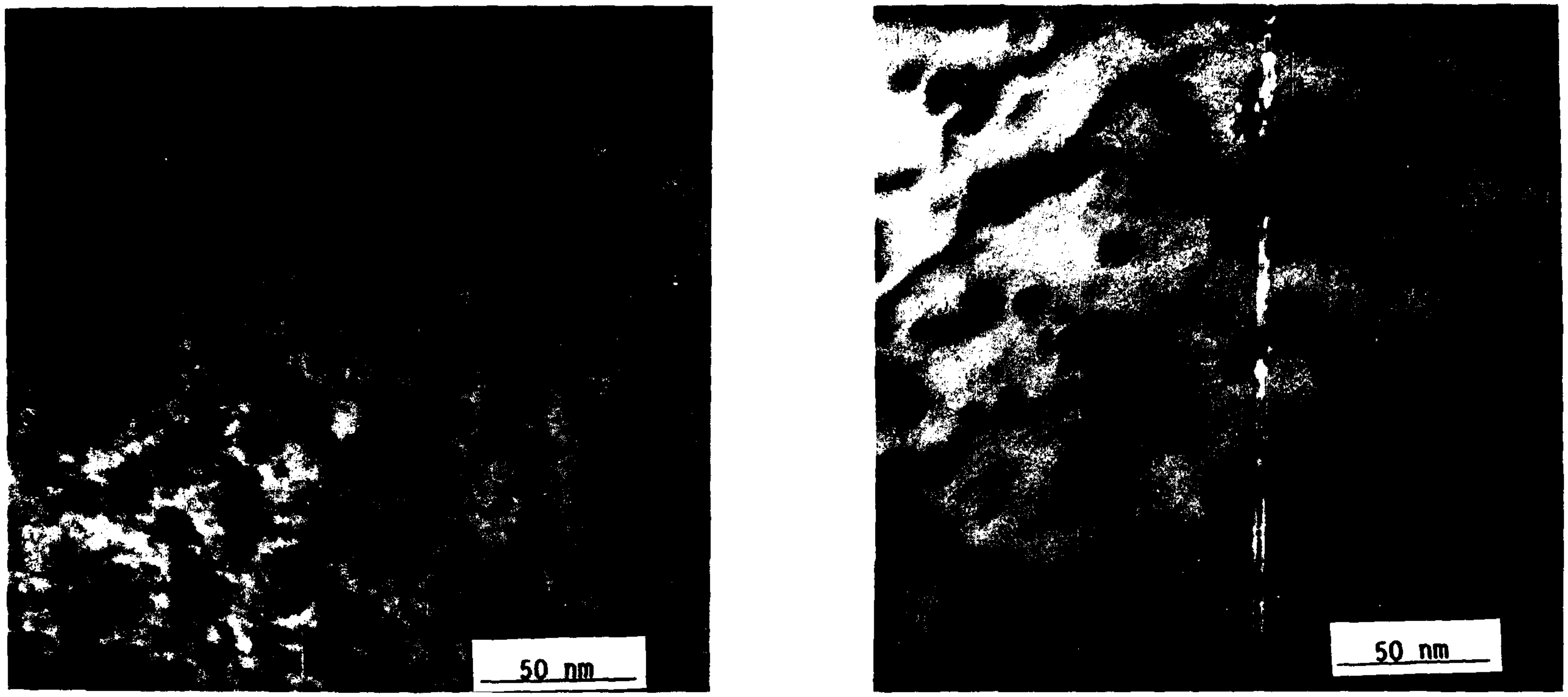

(a)

(b)

Figure 51. Loops in Niobium Irradiated at $800^{o}C$ to (a) 0.09 dpa and (b) 0.5 dpa. g = [011], Z ~ [011].

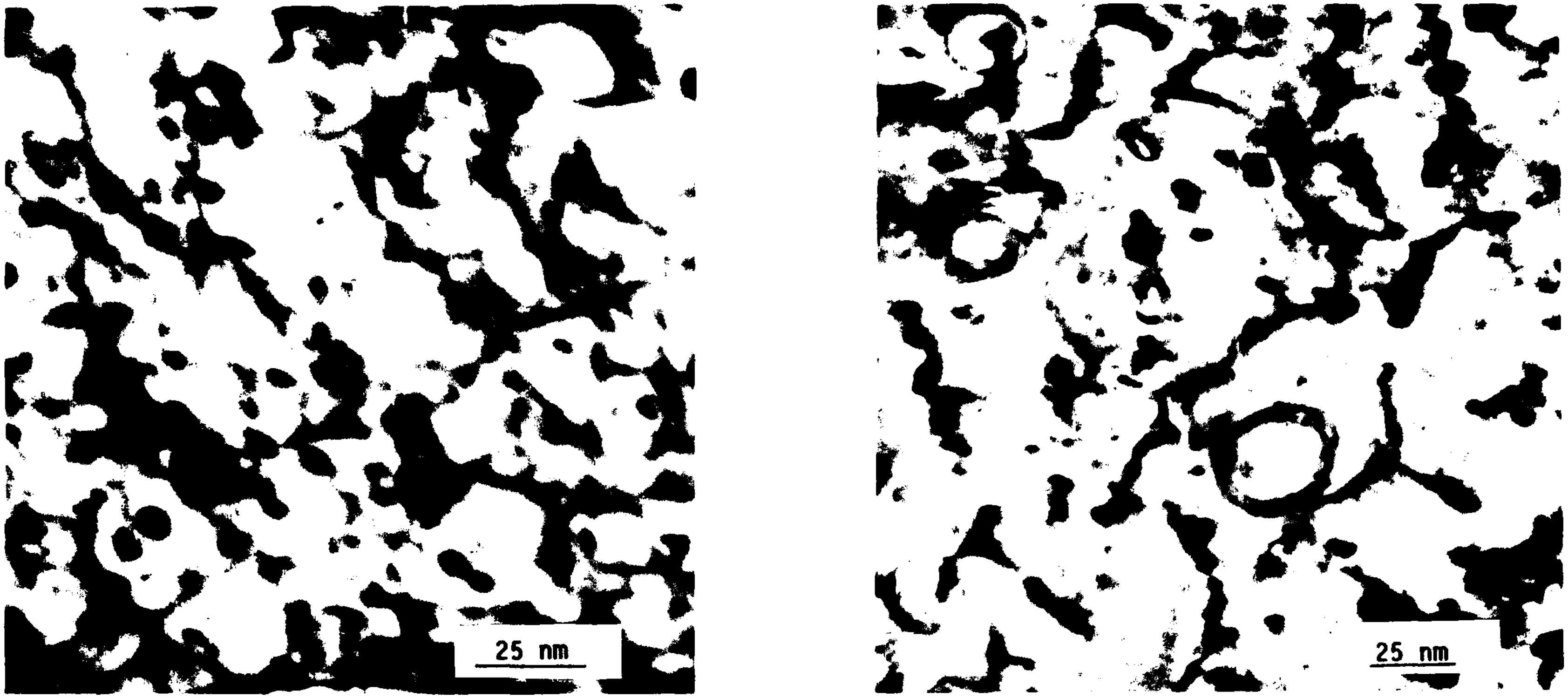

(a) (b)

Figure 52. Loops in Niobium Irradiated at 800^{o}C to (a) 2.7 dpa and (b) 4.1 dpa. g = [011], Z ~ [011].

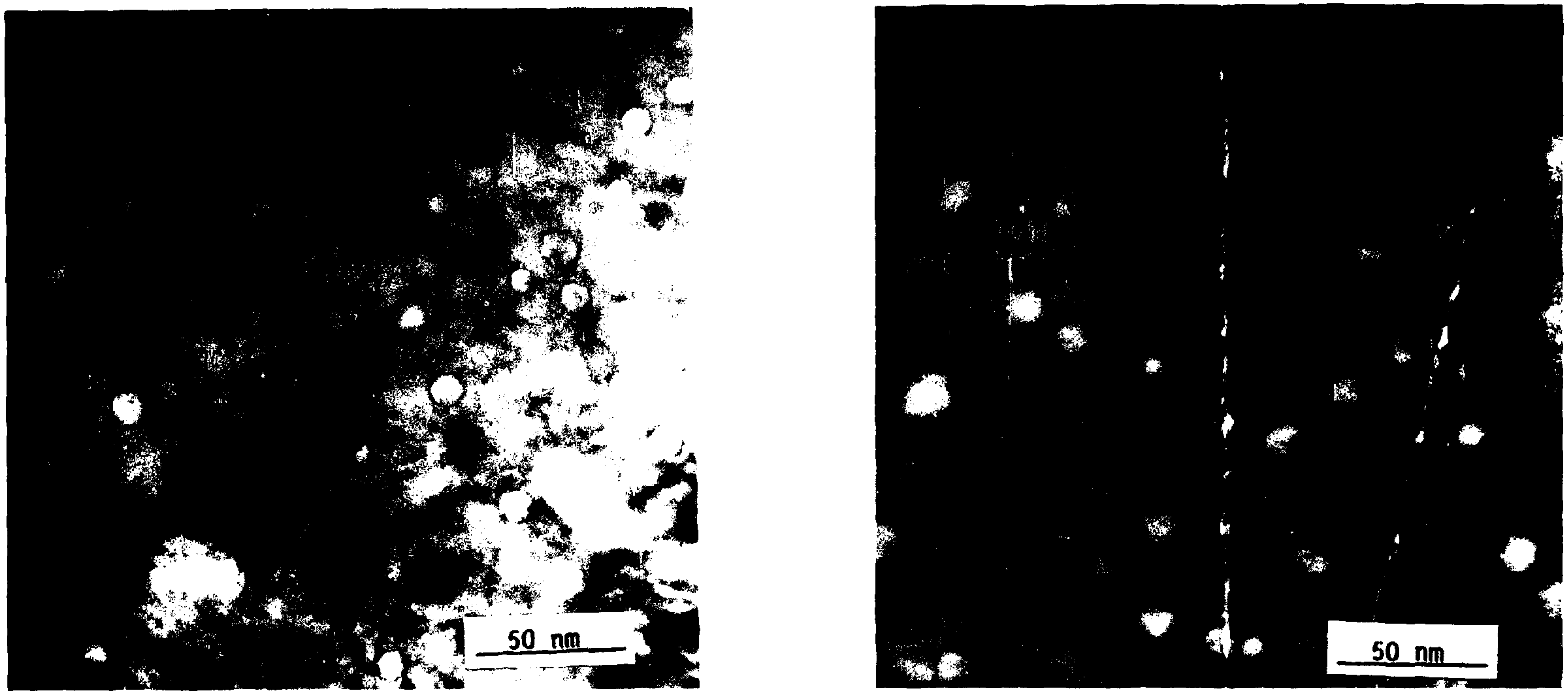

Figure 53. Voids in Niobium Irradiated at 800^{o}C to (a) 0.5 dpa and (b) 1.0 dpa. g = [200], Z ~ [011].

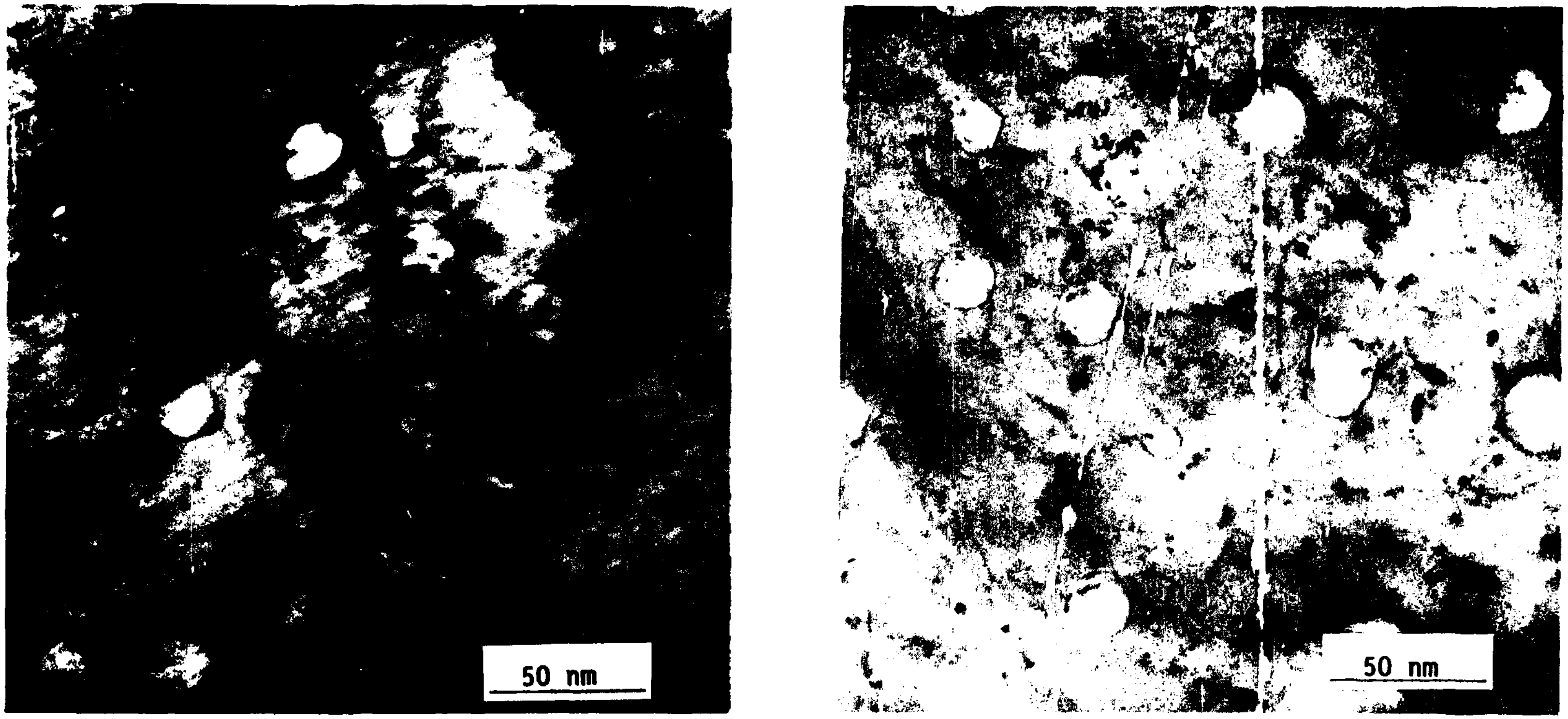

(a)

(b)

Figure 54. *Voids in Niobium Irradiated at 800°C to (a) 2.7 and (b) 4.1 dpa.*

TABLE XVII

Loop and Void Analysis for Irradiated Niobium

Dose*	Temperature (^oC)	Average Loop Size (nm)	Loop Size Range (nm)	Average** Loop Density (cm^{-3})	Average Void Size (nm)	Void** Density (cm^{-3})	Swelling** (%)
0.05	1000	9.7	4.5-20	2.1×10^{16}	-	-	-
0.1	1000	10.2	4.5-20	2.0×10^{16}	-	-	-
0.5	1000	10.0	4.5-20	2.1×10^{16}	-	-	-
2.9	1000	10.0	4.0-20	1.3×10^{16}	-	-	-
4.3	1000	8.6	4.0-20	1.5×10^{16}	-	-	-
0.5	800	9.6	4.0-18	2.7×10^{16}	9.9	4.1×10^{15}	0.2
1.0	800	6.0	4.0-20	4.5×10^{16}	17.5	3.5×10^{15}	1.0
2.7	800	9.4	4.0-18	1.9×10^{16}	21.4	1.1×10^{15}	0.8
4.1	800	9.1	3.0-20	2×10^{16}	23.1	1.5×10^{15}	1.0

*Error of estimation = ± 10%.

**Foil thickness estimated. Error of estimation = ± 25%.

than loops observed in this study and the density was 2×10^{13} cm^{-3} at 1010°C. These loops can be much more easily resolved than those reported here. No such loops were observed as can be seen from Figs. 48-50.

The major discrepancy between the results of this present study and that of Loomis et al. may be due to (a) differences in impurity content and (b) the difference in irradiating ion species.

Loomis et al.(90) used niobium containing 58 and 108 appm of O and C, respectively. However, an undetermined amount of oxygen and nitrogen was introduced during irradiation. Our niobium may have contained up to ≈700 appm O and 255 appm C (based on phase I analyses), and was irradiated under high vacuum. It is entirely possible that the higher initial oxygen and carbon contents in our material caused the high loop densities, since oxygen is known to affect nucleation of defect clusters in vanadium(98) and niobium(99) at low temperatures (50°-100°C). However, the variation in cluster density with oxygen content was much shallower than observed here. The observation of loop interaction with dislocations (i.e., pinning) also agrees with the association of impurities with the loops. The difference in loop densities and size caused by different irradiating ions, Nb vs. Ni may also have contributed to these discrepancies.

It is worth noting that, at 800°C, void nucleation occurred early. Voids were observed at doses of 0.5 dpa and above. At 1000°C, voids were not resolvable even after 4.3 dpa. These observations are being examined in light of the theoretical model developed.(1)

It can be argued that the damage observed is ion-milling damage and not niobium ion damage. This was ruled out by a careful and thorough examination of micrographs and the techniques used.

First consideration was given to the possibility that ion milling and a subsequent acid dip removed all the damage produced by Nb^{++} ions. This cannot be true since voids were observed in specimens irradiated at 800°C after ion milling and an acid dip as shown in Figs. 53 and 54 (the 1000°C specimens were prepared in identical fashion along with 800°C specimens). This categorically proves that the damage Nb^{++} produced is still present. The ion-milled damage produced by 800 eV argon ions, if present, will be located on the milled surface and penetrate <25 nm. Observations of stereopairs revealed that the loop damage was uniformly distributed throughout the thin foil. This again proves that the damage being observed is real damage; i.e., produced by the Nb^{++} ions. An example of a uniform distribution of loops is shown in Fig. 55, a stereopair from a specimen irradiated at 1000°C to 4 dpa.

8.2.5 Loop Characterization

Dislocation loops were characterized by determining the Burgers vectors of the loops and whether they are vacancy or interstitial in nature. The analysis of the Burgers vectors of loops is carried out by $g \cdot b$ analysis knowing that dislocations will be invisible when $g \cdot b = 0$ and visible when $g \cdot b$ is non-zero. $g \cdot b = 1$ images can be mistaken for $g \cdot b = 0$ invisibility in the presence of $g \cdot b = 2$ images if W, the product of deviation vector S and the extinction distance ζ_g, is large. Therefore the diffraction vectors should be chosen carefully to eliminate ambiguities.

Dislocation loops generally lie on inclined planes and frequently appear to be elliptical. Edge dislocation loops may be either interstitial (extra plane) or vacancy (one plane missing), Fig. 56a. There are two possible senses of inclinations of the loop, but an edge dislocation loop may have four possible configurations as shown in Fig. 56b. The nature of a loop is determined by imaging the loop at the proper diffraction conditions and observing whether the image of the loop is inside or outside the dislocation core. This is determined by the sense of rotation of reflecting planes around the dislocation. For diffraction conditions shown in Fig. 56c, i.e., S, the deviation vector is positive, the strain field of the edge dislocation is as shown in Fig. 56d. The reflecting plane XX is rotated clockwise; i.e., away from $s = 0$. Now referring to Fig. 56a, position A corresponds to rotation towards $s = 0$ and position B to rotation away from $s = 0$. The loop image, therefore occurs near A relative to the dislocation core, and images

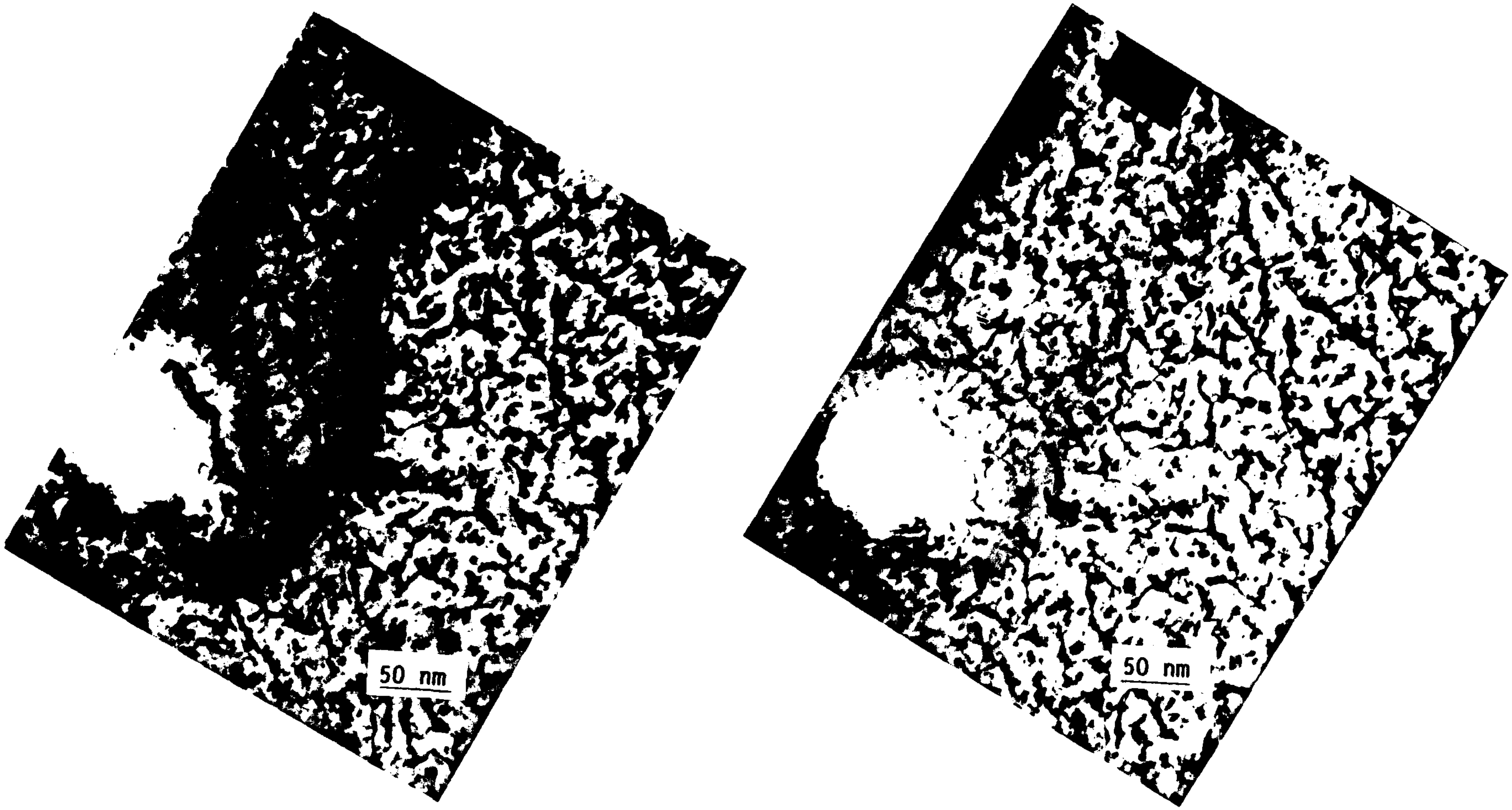

(a)

(b)

Figure 55. A Stereopair of Loops in Niobium Irradiated at 1000°C to 4.3 dpa. (The Pair is Oriented for Easy Viewing with a Stereoviewer.)

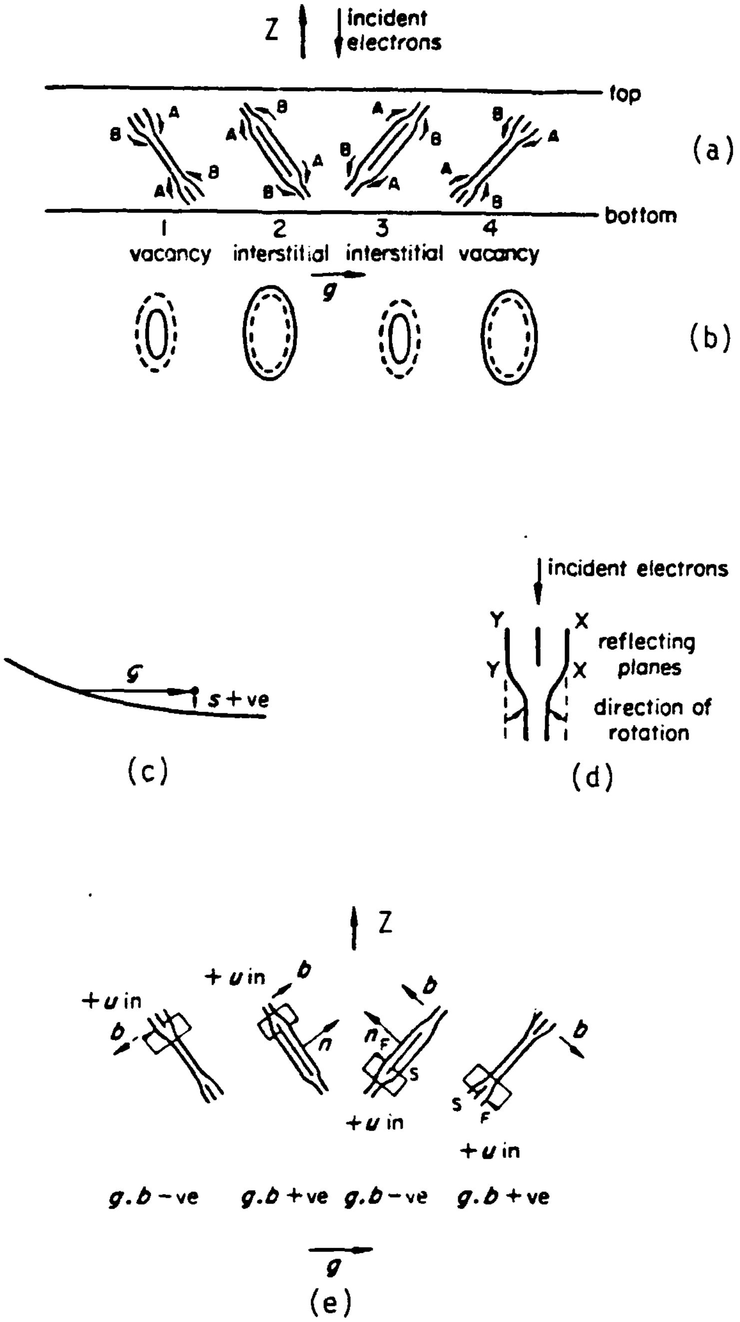

Figure 56. Dislocation Loop Characteristics and Contrast.

(a) The Four Possible Configurations of Inclined Vacancy or Interstitial Loops; (b) the Position of Image (Heavy Line) Relative to the Core (Dashed Line); (c) S Positive for the Operating Reflection; (d) the Rotation of the Reflecting Planes at an Edge Dislocation; (e) the Direction of b for Each Loop, the Upward Drawn Plane Normal n, and the Sign of g·b are Shown in Each Case.

are formed as shown in Fig. 56b. The dashed lines in Fig. 56b indicate the position of the dislocation core. Loops 2 and 4 show images outside the core (outside contrast) and for loops 1 and 3 the images are inside the core (inside contrast). This means that the sign of g·b is the same for loops 1 and 3 and opposite of 2 and 4.

Figure 56e shows the position of an upward drawn normal n, Burgers vector, b, for the four loop configurations for positive and negative g·b but for the same g. In practice, to analyze the loop characteristics, images are taken in positive and negative g conditions and the direction of upward drawn normal (i.e. habit plane) is determined by noting the direction of rotation of the loop upon tilting or by tilting to the edge on position. These two conditions represent positive and negative g·b comparable to Fig. 56e.

This procedure was used to analyze loops in neutron-irradiated and annealed molybdenum.(59) The loops in this condition were larger, ranging from 10 nm to 90 nm.

The analysis briefly described above is relatively straight forward, although not easy, for large loops (diameter >50 nm). However, for medium loops (10-50 nm) the analysis is much more difficult because of a variety of factors such as elastic anisotropy, presence of loops with $g \cdot b = \pm 2$, the image visibility only as two arcs or a single dot, difficulty in assigning outside/inside contrast and trace direction. In these situations, inconsistencies arise experimentally and it becomes impossible, except in a few cases to unambiguously assign vacancy or interstitial characteristics to the observed loops(100).

In the present work, the loops are small, ranging from ≈4 to 20 nm, and therefore are difficult to analyze. Further complications arise from the relatively high density of loops and the presence of voids (in specimens irradiated at 800°C) and dislocations. Because of these factors, only the larger loops can be analyzed and even for these loops, ambiguities cannot be totally eliminated.

The following procedure was used to image and analyze the loops in ion-irradiated niobium. The analysis is described for one specimen irradiated at 1000°C to 2.9 dpa. Identical procedures were used for other specimens. The micrographs for specimens irradiated at 1000°C to 0.05 dpa and 800°C to 2.7 dpa are shown in Appendix A.

The specimen was loaded in the double-tilt goniometer stage and surveyed to find the best area for examination. Because of the large grain size of the material,only a few grain orientations were available. The foil oriented in the zone axis Z ~ [011] showed the best image. The loops were imaged in the same area with g = $[01\bar{1}]$ in +g and -g diffraction condition with $S > 0$. The specimen was then tilted towards [111] and $[\bar{1}11]$ with images recorded at six intermediate tilt positions: Z ~ [011] on [111] side, near [122] and near [111], ~[011] on $[\bar{1}11]$ side, $[\bar{1}22]$ and near $[\bar{1}11]$ side. At each of these tilt position loops, images were recorded in +g and -g diffraction conditions in the same area. Diffraction patterns were also recorded to enable assignment of a trace direction (the direction of a long axis of a loop imaged as ellipse) and the diffraction of g for the micrographs. The procedure was repeated for at least one more area in the specimen. The images were recorded at a high magnification, 220,000X, because of the small loop size.

A procedure was developed to analyze the loop character for a set of imaging conditions. This consists of determining possible loop traces for $\frac{a}{2}$<111> and a<100> type pure edge loops on a (110) plane and the resulting contrast for the diffraction conditions used.

Table XVIII lists the Burgers vectors for $\frac{a}{2}$ <111> and a<100> type loops, g·b for these loops for g = $[01\bar{1}]$, and intersection of loop planes with the (011) plane. The intersections of the loop plane with (011) indicate the directions of elongation of the circular loops imaged as ellipses. As can be seen from the table, one-half of the $\frac{a}{2}$ <111> type loops and one-third of the a<100> type will be invisible with g = $[01\bar{1}]$ because g·b for these loops is zero. Also, the visible loops should have their elongated directions oriented in <211> and <100> directions.

TABLE XVIII

Visibility and Loop Intersections for $\frac{a}{2}$ <111> and a <100> Loops

Loop Burgers Vector	g·b for g = $[01\bar{1}]$	Intersection of Loop Plane with (011)
± 1/2 $[111]$	0	$[011]$
± 1/2 $[\bar{1}11]$	0	$[0\bar{1}1]$
± 1/2 $[1\bar{1}1]$	± 1	$[21\bar{1}]$
± 1/2 $[11\bar{1}]$	± 1	$[\bar{2}11]$
± $[100]$	0	$[011]$
± $[010]$	± 1	$[100]$
± $[001]$	± 1	$[100]$

Table XIX describes the contrast produced by the two types of loops upon tilting the foil to [111] or $[\bar{1}11]$ for all possible trace directions for $\frac{a}{2}\langle 111\rangle$ type pure edge loops. Note that the $\pm g$ contrast reverses on either side of the [011] zone axis for a given loop type because the upward drawn normal reverses direction.

Figure 57 (a through f) shows a full set of micrographs taken in various diffraction conditions of a specimen irradiated to ≈3 dpa at 1000°C. Fifteen common loops, numbered 1-15, are shown on the micrographs. Each loop was analyzed individually to ascertain its nature. Table XX lists the contrast for each of the loops in the various micrographs.

A close comparison of the contrast for loops in the table with the expected contrasts in Table XIX reveals major inconsistencies for a majority of the loops. Although the loops change contrast from the +g to -g condition, the contrast did not reverse upon tilting from [111] to $[\bar{1}11]$. Also, the trace directions were not precise. These inconsistencies were not the result of small loop sizes because even the larger loops exhibited similar behavior. After a thorough examination, the contrast, sense of rotation, and projected size upon tilt, it was concluded that the types of contrasts were the result of loops not lying precisely on {111} planes. In other words, the loops are not pure edge loops and contain some shear component. Because of the deviation from the pure edge configuration, the loops do not reverse in contrast from [111] to $[\bar{1}11]$.

The loops were then re-examined. The loop contrast with tilting was then found to be consistent with the loop rotation and the projected size of the loops.

The results of this analysis for 15 loops are shown in Table XX. The loop characterization for three typical loops, Nos. 1, 6 and 14, can now be discussed.

TABLE XIX
Loop Contrast

<u>Case</u>

I. Tilting from [011] zone to [111] zone

A. Loops on $(11\bar{1})$ and $(\bar{1}\bar{1}\bar{1})$ planes. Trace ~ $[\bar{2}1\bar{1}]$, $[2\bar{1}1]$ upward drawn normal is $[11\bar{1}]$

(1) For g = $[01\bar{1}]$ Outside Contrast
g = $[0\bar{1}1]$ Inside Contrast
} Interstitial

(2) For g = $[01\bar{1}]$ Outside Contrast
g = $[0\bar{1}1]$ Inside Contrast
} Vacancy

B. Loops on $(\bar{1}1\bar{1})$ and $(1\bar{1}1)$ plane. Trace ~ $[\bar{2}\bar{1}1]$, $[21\bar{1}]$ upward drawn normal is $[1\bar{1}1]$

(1) For g = $[01\bar{1}]$ Outside Contrast
g = $[0\bar{1}1]$ Inside Contrast
} Vacancy

(2) For g = $[01\bar{1}]$ Inside Contrast
g = $[0\bar{1}1]$ Outside Contrast
} Interstitial

TABLE XIX

Loop Contrast (Cont.)

<u>Case</u>

II. Tilting from [011] zone to $[\bar{1}11]$ zone (upward normal)

A. Loops on $(11\bar{1})$ and $(\bar{1}\bar{1}1)$ planes. Trace ~ $[\bar{2}1\bar{1}]$, $[2\bar{1}1]$ upward drawn normal is $[\bar{1}\bar{1}1]$

(1)	For g = $[01\bar{1}]$ Outside Contrast	Vacancy
	g = $[0\bar{1}1]$ Inside Contrast	
(2)	For g = $[01\bar{1}]$ Inside Contrast	Interstitial
	g = $[0\bar{1}1]$ Outside Contrast	

B. Loops on $(\bar{1}1\bar{1})$ and $(1\bar{1}1)$ plane. Trace ~ $[\bar{2}\bar{1}1]$, $[21\bar{1}]$ upward drawn normal is $[\bar{1}1\bar{1}]$

(1)	For g = $[01\bar{1}]$ Outside Contrast	Interstitial
	g = $[0\bar{1}1]$ Inside Contrast	
(2)	For g = $[01\bar{1}]$ Inside Contrast	Vacancy
	g = $[0\bar{1}1]$ Outside Contrast	

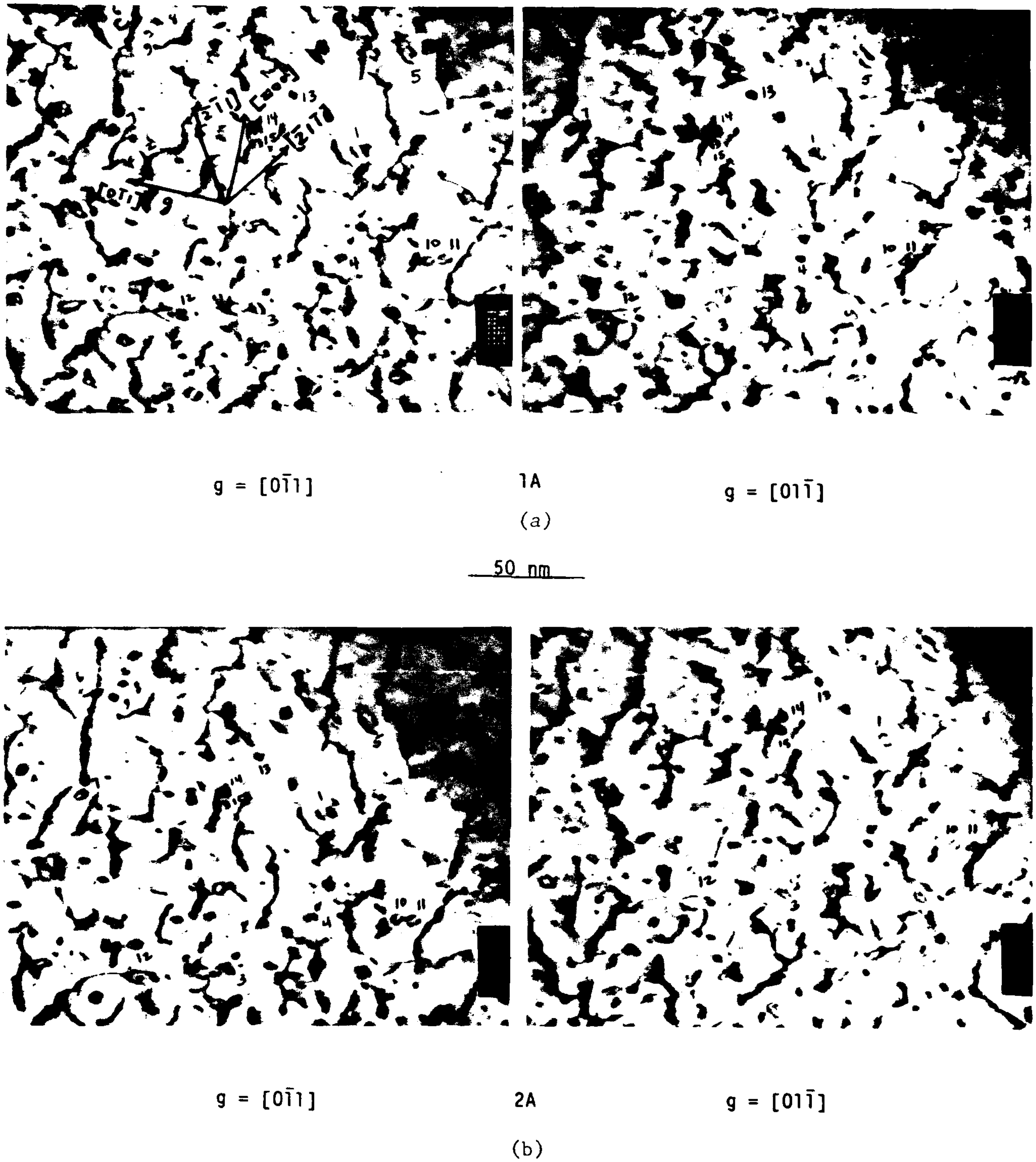

$g = [0\bar{1}1]$ 1A $g = [01\bar{1}]$

(a)

50 nm

$g = [0\bar{1}1]$ 2A $g = [01\bar{1}]$

(b)

Figure 57. Loops in Various Diffraction Conditions in Niobium Irradiated to 2.9 dpa at 1000°C. (a) 1A = Z ~ [011] on [111] Side; (b) 2A = Z near [122].

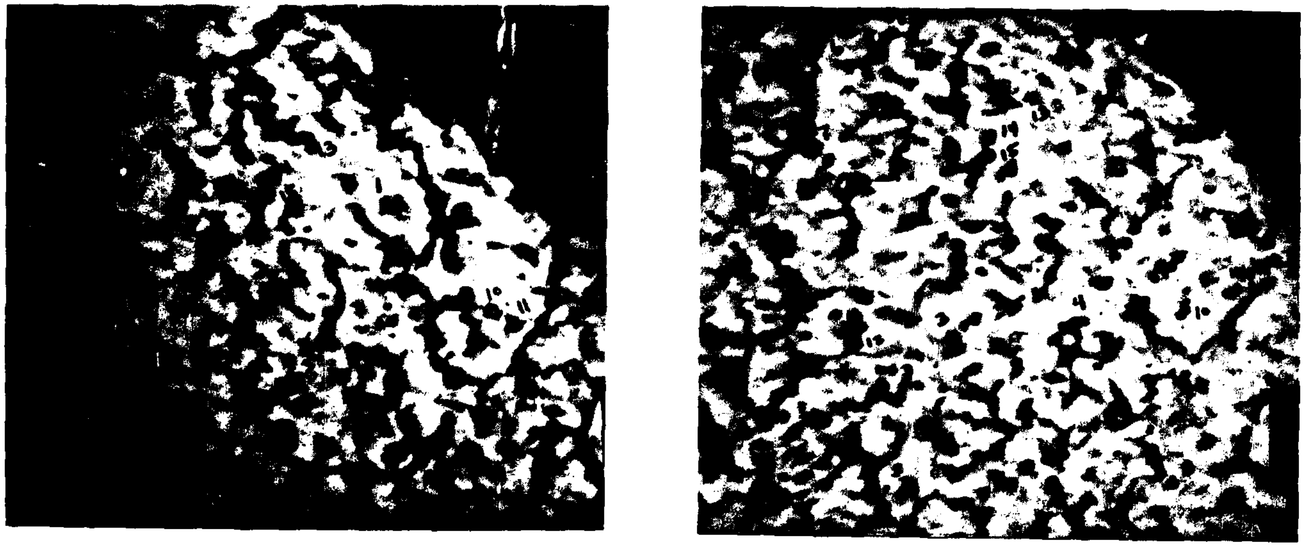

$g = [0\bar{1}1]$ 3A $g = [01\bar{1}]$

(c)

50 nm

Figure 57 (Cont.). Loops in Niobium Irradiated to 2.9 dpa at 1000°C.
(c) 3A – Z near [111] Condition.

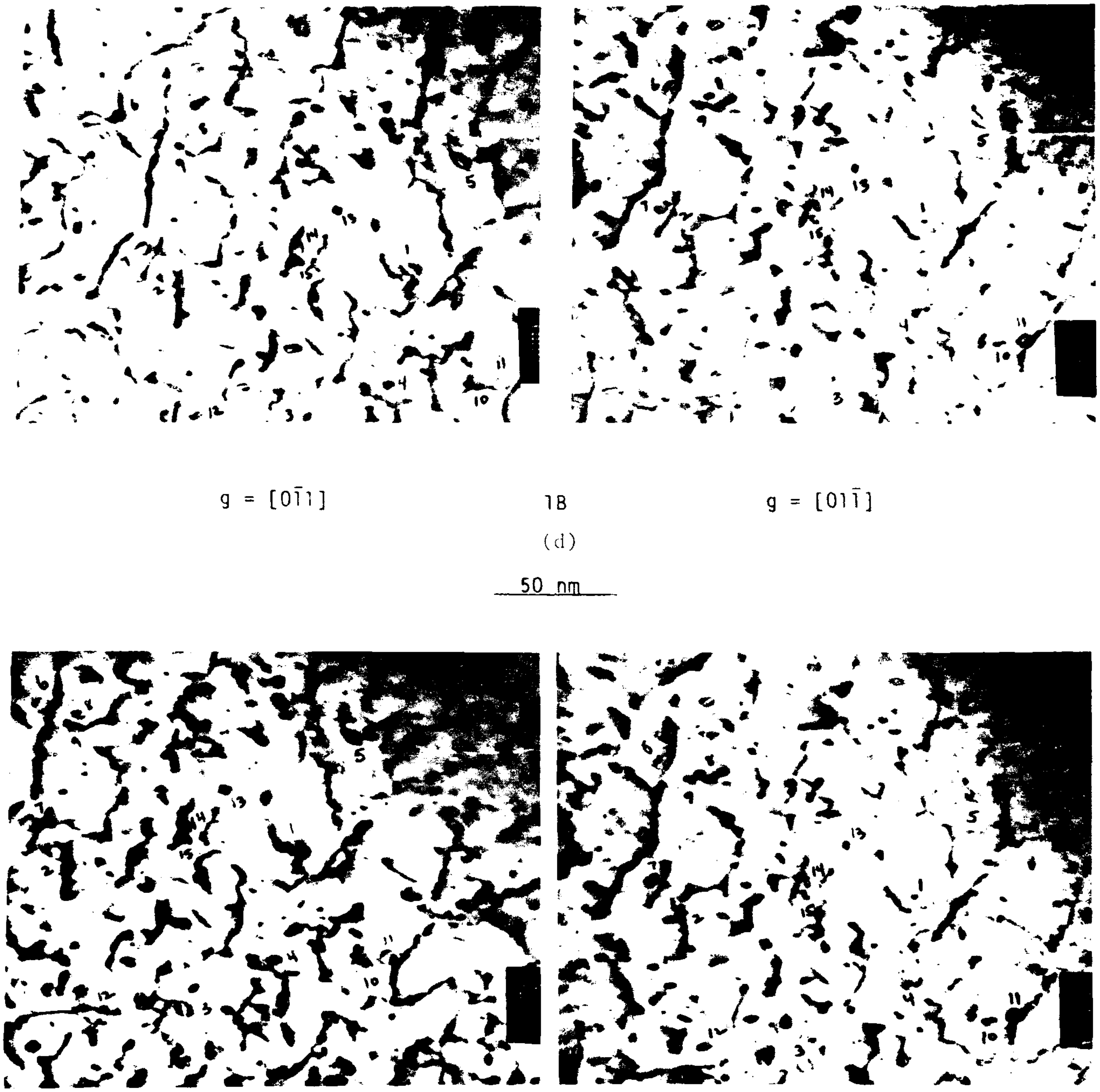

(d)

(e)

Figure 57 (Cont.). Loops in Various Diffraction Conditions in Niobium
Irradiated to 2.9 dpa at 1000°C.
(d) 1B = Z ~ [011] at [$\bar{1}$11] side;
(e) 2B = Z near [$\bar{1}$22].

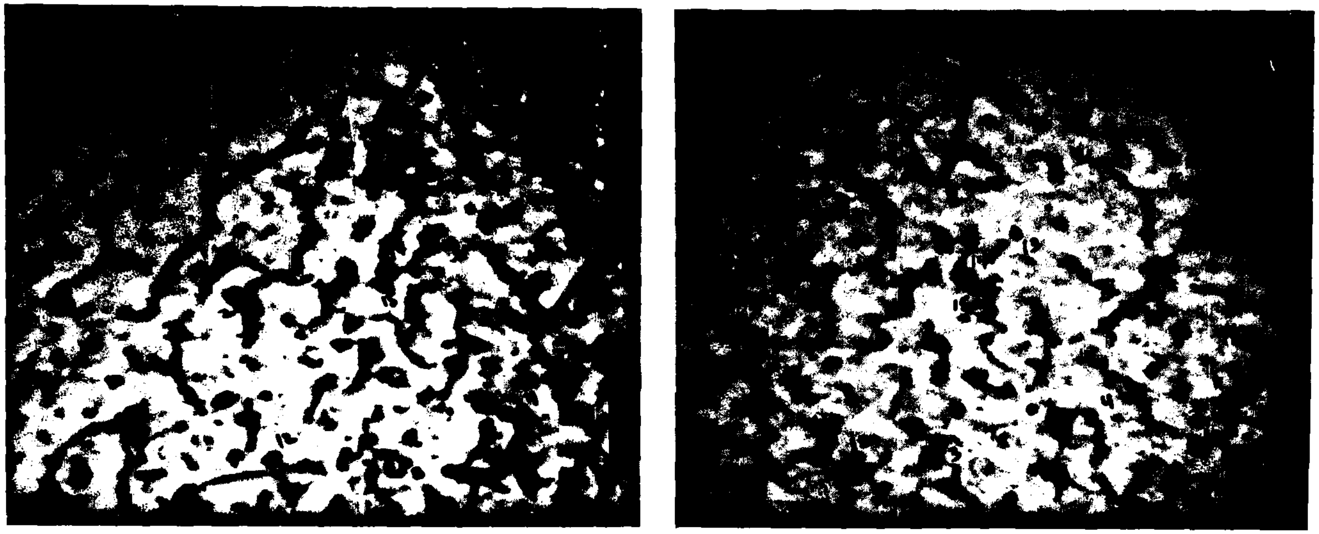

g = $[0\bar{1}1]$ 3B g = $[01\bar{1}]$

(f)

50 nm

Figure 57 (Cont.). *Loops in Niobium Irradiated to 2.9 dpa at 1000°C.*
(f) 3B = Z near $[\bar{1}11]$ Condition.

TABLE XX

Summary of Loop Contrasts Under Various Diffraction Conditions and Loop Characteristics for a Specimen Irradiated to 2.9 dpa at 1000°C

Loop Number	Trace Direction	Contrast												Loop Character
		1A		2A		3A		1B		2B		3B		
		g=[0$\bar{1}$1]	[g=01$\bar{1}$]	g=[0$\bar{1}$1]	g=[01$\bar{1}$]	g=[0$\bar{1}$1]	g=[01$\bar{1}$]	g=[0$\bar{1}$1]	g=[01$\bar{1}$]	g=[0$\bar{1}$1]	g=[01$\bar{1}$]	g=[0$\bar{1}$1]	g=[01$\bar{1}$]	
1	[$\bar{2}\bar{1}$1]	0	I	0	I	0	I	0	I	0	I	-	-	Interstitial
2	[$\bar{2}\bar{1}$1]	0	I	0	I	0	I	0	I	0	I	0	I	Interstitial
3	[$\bar{2}$11]	I	0	I	0	-	-	I	0	I	0	I	0	Interstitial
4	[$\bar{2}\bar{1}$1]	0	I	0	I	0	I	0	I	0	I	0	I	Interstitial
5	[$\bar{2}\bar{1}$1]	0	I	0	I	0	I	0	I	0	I	0	I	Interstitial
6	[$\bar{2}$1$\bar{1}$]	0	I	-	-	0	I	0	I	0	I	0	I	Interstitial
7	[$\bar{2}$1$\bar{1}$]	0	I	0	I	I	0	0	I	0	I	0	I	Interstitial
8	[$\bar{2}$11]	0	I	0	I	-	-	0	I	0	0	0	I	Interstitial
9	[$\bar{2}$1$\bar{1}$]	0	I	0	I	-	-	0	I	I	I	0	I	Interstitial
10	[$\bar{2}$1$\bar{1}$]	I	0	0	0	I	0	0	I	0	I	-	-	Interstitial
11	[$\bar{2}$1$\bar{1}$]	0	I	0	I	0	I	0	I	0	I	-	-	Interstitial
12	[$\bar{2}$1$\bar{1}$]	0	I	0	I	0	I	0	I	0	I	0	I	Vacancy
13	[$\bar{2}$1$\bar{1}$]	0	I	0	I	0	I	0	I	0	I	0	I	Interstitial
14	[200]	0	I	0	I	-	-	0	I	0	I	-	-	Interstitial
15	[$\bar{2}$00]	0	I	0	I	0	I	0	I	0	I	-	-	Interstitial

I: Inside Contrast

0: Outside Contrast

1A: Zone Axis ~[011] on [111] Side

2A: Zone Axis near [122]

3A: Zone Axis near [111]

1B: Zone Axis near [011] on [$\bar{1}$11] side

2B: Zone Axis near [$\bar{1}$22]

3B: Zone Axis near [$\bar{1}$11]

Loop 1 has a ~ $[\bar{2}\bar{1}1]$ trace in direction and contrasts as shown in Table XX. The loop opens up when the specimen is tilted towards [111] and closes when tilted in $[\bar{1}11]$. This indicates that the upward drawn normal for the loop is to the left (see stereogram in Fig. 58) and the loop contrast is outside when $g = [0\bar{1}1]$, therefore the loop is interstitial.

Loop 6 has a trace in ~ $[\bar{2}\bar{1}1]$ direction and contrast as shown in Table XX. The loop opens up when the specimen is tilted towards $[\bar{1}11]$. The upward drawn normal is to the left and the loop is interstitial.

Loop 14 has a trace close to $[\bar{2}00]$. The tendency is therefore to assign this loop a Burgers vector of $a\langle 100\rangle$ consistent with Table XVIII. However, two considerations make that assignment ambiguous. These considerations are first, a deviation of $\approx 20^{\circ}$ from the $[20\bar{0}]$ trace and changes in the projected loop size upon tilting. If the latter is taken into consideration, it can be seen from Fig. 58 that, most likely, the loop is lying on a plane somewhere between $\{111\}$ and $\{112\}$ type planes.

From the analysis of loops in this specimen and others (see Appendix A), it is concluded that the majority of loops in irradiated niobium are interstitial loops with a Burgers vector of $\frac{a}{2}\langle 111\rangle$ type. Also, the loops contain some shear component. Vacancy loops were also found (see Table XX and Appendix A), but their numbers were small. It is also possible that small loops, not thoroughly analyzed, are vacancy type.

Trace Direction for Loops 14 and 15

Trace Direction for Loops 6-13

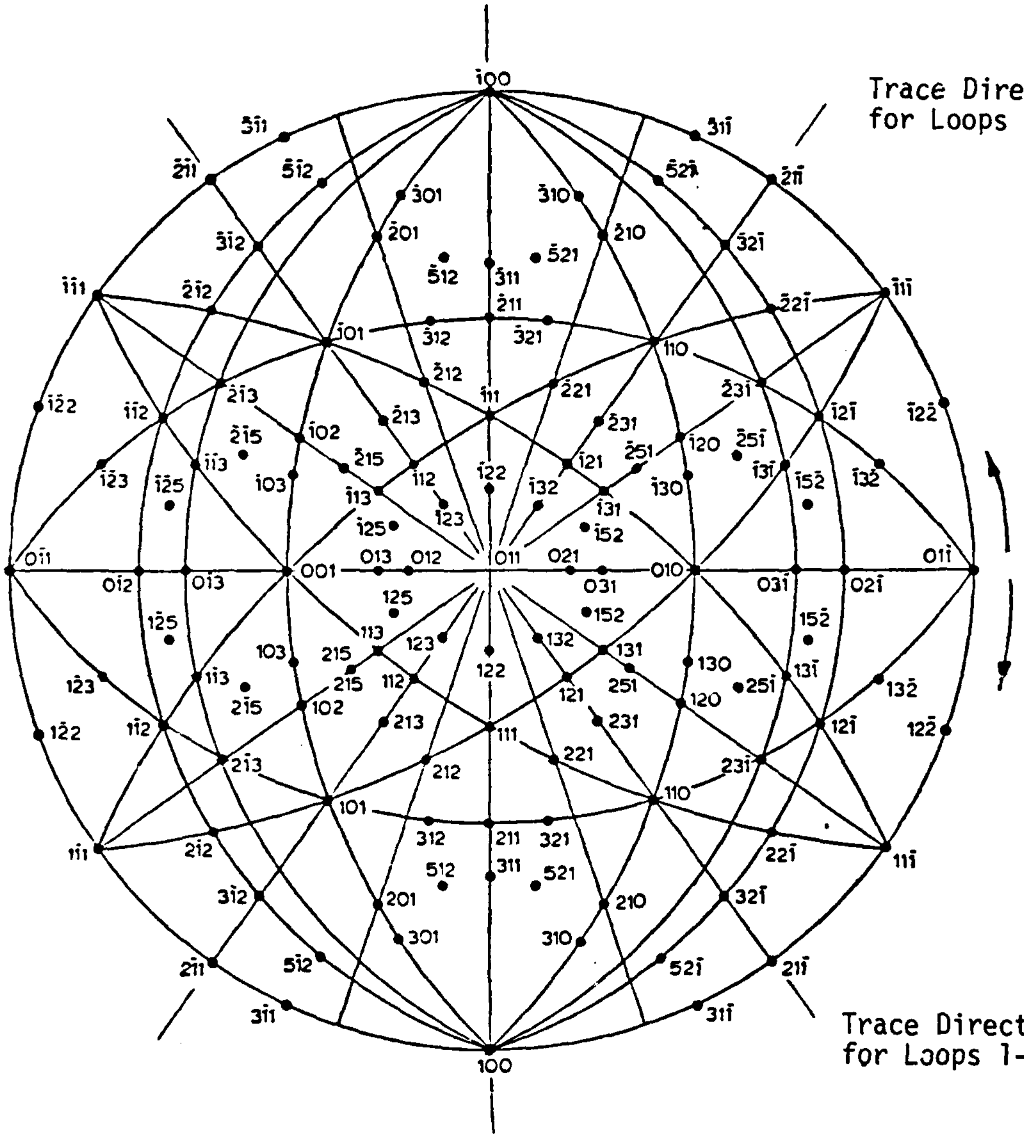

Direction of Tilt

Trace Direction for Loops 1-5

Figure 58. Stereographic Projection for Cubic Crystals on (011) Showing Direction of Rotation (Tilt) and Trace Directions for the Loops.

The presence of <100> type loops is ambiguous. The loop traces along the <200> direction would suggest that these loops are a<100> type, however, these image contrasts can also be explained by assuming a shear component to the $\frac{a}{2}$<111> type loops. Further work is required to remove these ambiguities.

Other authors also have reported interstitial loops in bcc metals irradiated with neutrons or ions. Eyre and Evans(101) observed predominately interstitial loops in high purity molybdenum irradiated to 18 dpa (1.7×10^{22} n/cm^2) at 650°C. A small percentage (≈4%) of the loops were characterized as vacancy loops. The loops had a low density (≈5×10^{14} cm^{-3}) and were easily resolvable.

The loop sizes ranged from 2-150 nm in diameter. All the vacancy loops were <20 nm and difficulties were experienced in analyzing loops at the low end of the size spectrum.

Eyre(102) irradiated molybdenum of various purities to 1×10^{19} n·cm^2 at 200°C and examined the microstructure. A comparison of these materials indicated that impurity trapping of interstitial point defects had a strong influence on the distribution of defect clusters. Annealing these materials at 900°C resulted in loop growth. The percentage of interstitial loops increased with decreasing purity of the material, however, in all cases both loop types were observed.

High temperature irradiations have also been carried out on molybdenum. Meakin and Greenfield(103) irradiated zone-refined molybdenum to 8×10^{17} n·cm^{-2} at 600°C and found large loops (average diameter 110 nm) of low density (≈2×10^{13} cm^{-3}). The loops were analyzed to be interstitial with a Burgers vector of $\frac{a}{2}$ <111>. No vacancy loops were observed. Brimhall et al.(104) found only interstitial loops ≈100 nm in diameter in commercially pure molybdenum irradiated to 6×10^{19} n·cm^{-2} at 600°C.

It is worth noting that the material purity has an insignificant effect on the high temperature void and dislocation microstructure in molybdenum. Eyre and Bartlett(105) made a detailed comparison of both the void distribution and dislocation substructure of a commercial purity and two zone-refined materials irradiated to 640°C to a dose of 3×10^{22} $n \cdot cm^{-2}$. They found little difference in the size distribution of the voids and dislocation structure. The loops were analyzed to be interstitial with Burgers vector of $\frac{a}{2}\langle 111\rangle$.

The studies on other bcc metals, vanadium, niobium, tungsten, and tantalum are either at low temperatures, ≈70°-450°C, or at temperatures where voids are observed. In the void swelling regimes, loop structures were not thoroughly examined.

8.2.6 Theoretical Consequences of Experimental Observations of Loop Characteristics

The theory for loop development in body-centered cubic metals (paper in Appendix B) is based on the following assumptions:

(1) Two types of interstitial loops can exist after irradiation.

(2) The predominant loop type is a perfect loop with $\frac{a}{2}\langle 111\rangle$ Burgers vector and a {111} habit plane. The minority type, which are perfect loops with $a\langle 100\rangle$ Burgers vector and a {111} habit plane, have a low relative probability of formation ($\approx 10^{-5}$ at 420°C in niobium).

(3) The loop bias or preference factors are given by the expression developed by Wolfer and Ashkin.(92,93) For pure edge loops, the interstitial preference factor $\delta_I^{\ell i}$ is

$$\delta_I^{\ell i} = \delta\left[\frac{b_i}{r_{\ell i}}\right]^2$$

I indicates interstitial, ℓi is loop type, δ is a materials constant, b_i is the Burgers vector, and $r_{\ell i}$ is the loop radius.

The results of the loop analysis are inconclusive with respect to the first assumption. No <100> loops were identified because of a limited statistical sampling and low relative probability of <100> loop formation. Assumption (2) was confirmed. The predominant loops observed were perfect interstitial loops of <111> type. However, they did not have {111} habit planes, but had both edge and shear components. Because of the existence of the shear component, assumption (3) is incorrect and must be modified. In particular, the general form(55) for $\delta_I^{\ell i}$ must be used instead of the simplified form for edge loops.

9.0 PHASE III PROGRAM

9.1 Development of Low Swelling Alloys

As described in the program objective (section 3.0), the ultimate technological goal of the program was to demonstrate the practicality of low swelling alloy compositions for elevated temperature service. With the basic model development and experimental work completed for pure niobium, Phase III of the program was devoted to the study of niobium with alloying elements that were expected to significantly affect the microstructural development, and hence the swelling behavior of the alloy. Also, it was the purpose of this phase of the program to study the effects of helium on the high temperature swelling. Therefore, both single and dual-ion irradiations were conducted. Theoretical work for the loop growth model, suggested by the second phase study, was therefore deferred in preference to the study of the alloys.

9.2 Alloy Selection

Comparison of model calculations with the results of experiments for pure niobium showed that the model as originally formulated overpredicts the swelling at all temperatures(106). Loomis and Gerber(21,22) have shown that concentrations of oxygen on the order of 0.07 atomic percent (the level present in the pure niobium specimens) are sufficient to affect swelling, leading to a reduction relative to that in low oxygen material. When an incubation period for swelling and an interstitial-oxygen binding energy of approximately 2 eV were included in the swelling model, the calculated swelling curves had a significantly improved correspondence to the experimental data. Thus, alloying elements that getter oxygen were of interest.

Diffusivity of the alloying element was also expected to be important. Low diffusivity elements can potentially act as binding sites for the point defects. They could serve as void nucleation sites or affect the diffusion kinetics of either point defect types. High diffusivity elements, if they couple with interstitials or vacancies, can segregate to the voids or dislocations.

In addition to oxygen affinity and diffusivity, several other properties of the alloying element were considered in the selection process. First, to avoid complications due to second phases, a solid solution alloy is desirable, and therefore, the alloying element has to have a reasonable range of solid solubility in niobium. Second, the misfit in the matrix must be considered. As a rule of thumb, the coupling between oversized elements and interstitials is weak or nonexistent; that between undersized elements and interstitials is strong. For maximum impact on the interstitial diffusion kinetics, therefore, undersized elements are preferred over oversized elements. Other considerations included elastic modulus difference and technological importance of the resulting alloy.

9.3 Data on Properties

Data on the various properties of alloying elements were collected and are summarized in Tables XXI through XXIII. Table XXI contains experimentally measured diffusion parameters for a number of elements in niobium(107). For each element, the table gives the frequency factor, D_o, and the activation energy, Q, from which the diffusion coefficient D_I can be calculated using the Arrhenius form:

$$D_I = D_o \exp(-Q/RT) \qquad (57)$$

where R is the gas constant, and T is the temperature. The table also gives the temperature range where the parameters are applicable. The last column gives the ratio of the impurity diffusion coefficient to the self-diffusion coefficient at 0.7 T_m, where T_m is the melting temperature. From this column, it can be seen that the elements are listed in order of decreasing diffusivity.

Table XXII contains the atomic radii of the various elements and the ratio of the radii to the radius of niobium. Table XXIII gives the solubility limits for various elements in niobium. These were taken from the compilation of binary phase diagrams by Hansen and Anderko(108). In both tables, the order of the elements is the same as in Table XXI.

TABLE XXI

Diffusion in Niobium

Element	Temperature Range (°C)	Do (cm^2/sec)	Q (kcal/mole)	$D_{I(Nb)}/D_{Nb(Nb)}$ at 0.7 T_m
Ni and ^{63}Ni	1161-1773	0-077	63.1	$4.80 X 10^2$
^{60}Co	1550-2050	0-74	70.5	$6.78 X 10^2$
Co and ^{60}Co	1307-1647	0-11	65.6	3.59×10^2
^{55}Fe	1400-2100	1.5	77.7	2.13×10^2
Fe and ^{59}Fe	1389-1895	0.14	70.3	1.35×10^2
Cu	1556-1636	0.15	≈72.0	1.03×10^2
^{113}Sn	1850-2390	0.14	78.9	1.45×10^1
	953-1435	0.30	83.5	9.45×10^1
^{51}Cr	947-1493	0.13	80.6	8.68×10^1
Zr	1582-2084	0.47	87.0	5.97×10^1
Ti	1625-2075	0.40	88.5	3.45×10^1
V	1625-2075	0.47	90.0	2.74×10^1
	878-2395	1.1	96.0	1.32
^{95}Nb	1148-2236	0.61	94.9	1.00
^{182}Ta	1103-2072	1.0	99.3	5.24×10^{-1}
Mo	1725-2182	92.0	122.0	1.34×10^{-1}
W	1902-2170	7×10^4	156.0	1.51×10^{-2}

TABLE XXII

Atomic Radii of Elements

Element	r (Å)	r_I/r_{Nb}
Ni	1.38	0.847
Co	1.38	0.847
Fe	1.40	0.859
Cu	1.41	0.865
Sn	1.86	1.141
Cr	1.42	1.871
Zr	1.71	1.049
Ti	1.62	0.994
V	1.52	0.933
Nb	1.63	1.000
Ta	1.64	1.006
Mo	1.55	0.951
W	1.56	0.957

TABLE XXIII

Solubility and Elastic Modulus

Element	Solubility in Niobium (a/o)	Elastic Modulus (GPa)
Ni	<7.7	206.8
Co	No data for Nb > 33.3 a/o	206.8
Fe	No data for Nb > 60 a/o	196.5
Cu	No data	110.3
Sn	No data	41.4
Cr	No data	248.2
Zr	< 7	94.4
Hf	Continuous solid solution	136.5
Ti	Solid solution from 40-100 a/o Nb	115.8
V	Continuous solid solution	124.0
Ta	Continuous solid solution	186.1
Mo	Continuous solid solution	310.2
W	Continuous solid solution	358.5
Nb	Continuous solid solution	110.0

9.4 Alloying Element Selection

As indicated in Table XXIII, there is a lack of data on the solubility of Co, Fe, Cu, Sn, and Cr in niobium. With the exception of Ni, the species with the highest diffusivities in niobium were eliminated as candidates for the investigation.

From the standpoint of fabrication and general technological interest, the elements from Zr down were considered the best candidates. Table XXIV summarizes the properties of these elements for purposes of comparison. The symbols > and < are used to indicate the magnitude relative to that of niobium. For example, the atomic radius of Zr is greater than, and the radius of W is less than that of niobium. Continuous solid solution is indicated by ss.

A systematic comparison of the swelling behavior of a series of binary niobium alloys containing these elements would allow investigation of the separate influences of size, diffusivity, oxygen gettering, and elastic distortion on swelling. The present program, however, is more limited in scope. Two alloying elements were therefore chosen: Hf and W. Zr (or equivalently Hf) and W have the greatest difference in properties. Hf was chosen instead of Zr, since a substantial amount of work has already been done on Nb-Zr alloys; its use expands the available data base; and comparison of the swelling behavior of Nb-Hf with the published results on Nb-Zr can potentially yield valuable information.

A 5 a/o addition of alloying element was selected. This assured a complete solid solution and high ductility of the alloys and in the case of niobium-hafnium alloy, a sufficient amount of hafnium to affect oxygen gettering.

9.5 Alloy Melting

The two alloys of niobium, containing 5 w/o hafnium and 5 w/o tungsten, were prepared by melting using a nonconsumable electrode technique in a button melting furnace. The furnace contained six removable hearths mounted on a

TABLE XXIV

Comparative Properties with Respect to Nb

Element	Zr	Hf	Ti	V	Mo	W
Atomic Radius	>	>	≈	<	<	<
Diffusion Coefficient	>>	>>	>	>	<	<<
Oxygen Gettering	Strong	Strong	Strong	Moderate	Weak	Weak
Solubility	<7	ss	ss	ss	ss	ss
Elastic Modulus	≈	≈	≈	≈	>>	>>
Technological Importance	>>	>>	>	>	<	>>

revolving pedestal. The furnace was equipped with a diffusion pump backed by a mechanical pump to facilitate evacuation prior to backfilling with an inert gas. A photograph of the button melter is shown in Fig. 59.

Ultra-high purity niobium obtained from Teledyne Wah Chang, and Marz grade tungsten and hafnium procured from the Materials Research Corporation, were used to prepare the alloys. The chemical composition of these materials is shown in Table XXV. The niobium was in the form of thick plate (≈2.5 cm thick) and the hafnium and tungsten were in the form of 0.635 cm diameter rods.

Pre-weighed quantities of niobium and the alloying elements were loaded into the hearths to make up 50 g total weight. In addition to the alloys, high purity niobium and a titanium button were also loaded in two other hearths. The former was utilized to prepare specimens of pure niobium and to monitor pickup of impurities during the melting and the latter was used to getter the impurities from the atmosphere prior to melting of the alloys.

After loading the melter, it was evacuated to a vacuum of $<10^{-5}$ torr prior to backfilling with an inert atmosphere. High purity helium was then backfilled and the atmosphere was purified by melting the titanium button. The buttons of niobium and the alloys were then melted. After melting, hardness measurements were made. An increase in hardness of niobium was used as an indicator of impurity pickup. To assure homogeneity of the alloys, the buttons were cut into smaller pieces, cleaned, etched and remelted, by the above technique, two additional times. Each time, the titanium button was melted before the alloys and hardness was used as a monitor for impurity pickup. Table XXVI lists the hardness values of Nb and the two alloys, and shows that no significant pickup occurred during the melting operation.

The buttons of niobium, Nb-Hf and Nb-W were then rolled at room temperature to foils approximately 0.051 cm thick. No cracking was observed in any of the three materials indicating high ductility of the materials. The as-rolled foils were cleaned and analyzed for W (or Hf), O, C, and N contents. Table XXVII shows the results of chemical analysis.

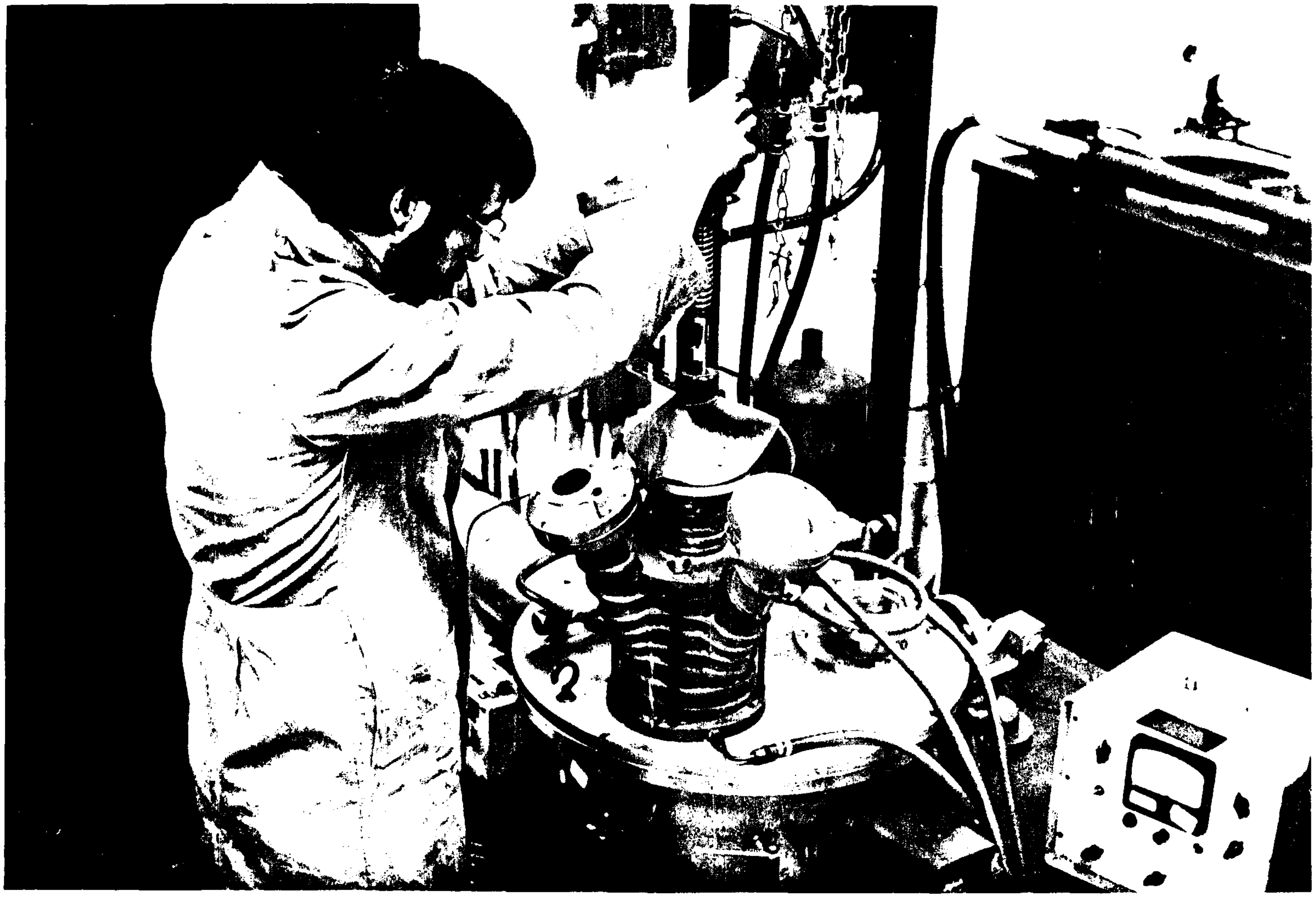

Figure 59. Photograph of Button Melter Used to Melt Nb-5Hf and Nb-5W Alloys.

TABLE XXV

Composition of Starting Materials Used to Prepare Alloys

Impurity Element (ppm)	Niobium* (Wah Chang)	Hafnium** (Marz Grade - MRC)	Tungsten** (Marz Grade - MRC)
Al	< 20	ND	10
B	< 1	-	< 0.1
C	33	30	35
Ca	< 20	15	< 1
Cd	< 5	ND	ND
Co	< 10	< 10	< 3
Cr	< 20	10	< 10
Cu	< 40	< 10	< 1
Fe	< 50	150	30
H	< 5	6	ND
Hf	< 50	Bal	ND
Mg	< 20	< 10	< 1
Mn	< 20	15	10
Mo	< 50	< 10	65
N	< 15	15	25
Ni	< 20	< 10	0.4
O	68	200	40
P	< 25	ND	ND
Pb	< 20	< 10	ND
Si	< 50	< 10	15
Sn	< 10	< 10	< 10
Ta	<200	ND	ND
Ti	< 50	< 10	< 10
V	< 20	< 10	< 30
W	37	ND	Bal
Zr	<100	3 w/o	ND

---

*Average of top, middle, and bottom of ingot.
**Typical Analysis
ND: Not Detected

TABLE XXVI

Hardness of Nb, Nb-Hf, and Nb-W Buttons after Melting

	Hardness, Hv (200 g Load)		
	First Melt	Second Melt	Third Melt
Nb	52	47	51
Nb-5 w/o Hf	93.5	89.8	96.5
Nb-5 w/o W	82.0	84.6	82.6

Hardness of as-received Nb was 45 Hv.

TABLE XXVII

Chemical Analysis of the Alloys After Rolling

Element (ppm)	Nb	Nb-5%Hf	Nb-5%W
C	120	110	130
O	105	40	120
N	< 5	< 5	< 5
H	5	5	5
Hf	-	4.95 w/o	-
W	-	-	4.81 w/o

It can be seen that carbon pickup occurred in all three materials during the melting and rolling operations with the carbon level going up from ≈30 ppm to ≈120 ppm. Oxygen was picked up in pure Nb and Nb-5%W, increasing from ≈70 ppm to 105-120 ppm in Nb and Nb-W, respectively, while Nb-Hf showed a lower level of oxygen than the starting material.

9.6 Specimen Preparation

Disc specimens, 3 mm (0.12 in) in diameter, were punched from the foil, deburred and mounted with crystal bond wax in a stainless steel holder with a 0.38 mm (0.015 in) recess. They were then polished using a 600-grit paper to a thickness of 0.23 mm (0.009 in) with a final polish with 1 μm alumina. The specimens were then demounted and remounted with the flat 1 μm polished surface facing down, onto a stainless steel holder with a 0.18 mm (0.007 in) recess. The specimens were placed on the holder in molten crystal bond wax. Each specimen was pressed to assure that the flat side was against the holder as the wax cooled. This procedure assured a good and flat bonding of the specimens.

The specimens were then polished on 400-grit paper until they were flat and then gently polished with 6 μm and 1 μm alumina abrasive. During and after each polishing step, specimens were examined for flatness and scratches. The final polishing step consisted of 12-15 h polishing with 0.05 μm deagglomerated alumina in a vibratory polisher. Following the polishing, the specimens were demounted and cleaned individually in an ultrasonic cleaner in multiple baths of acetone and methanol. The final thickness of the specimens was $\approx$0.12-0.15 mm (0.005-0.006 in).

The final cleaning procedure consisted of dipping each specimen in a solution of 15 ml HNO_3 + 5 ml HF in 50 ml glycerine for 30-60 s, followed by cleaning in multiple baths of acetone and methanol. After cleaning, each specimen was optically examined at a magnification of 500X in bright and dark fields and only scratch-free and clean specimens were selected for irradiation. These specimens were stored in 200 proof ethanol before loading them into the irradiation chamber.

9 7 Irradiation Test Matrix

As stated before, one of the purposes of this phase of the program was to evaluate the effects of helium on swelling. Theoretical considerations of these effects in niobium(106) indicate that, for temperatures between 625°C and 825°C, the cavity growth rate does not depend on gas pressure for reasonable helium injection (or production in a reactor) rates. In this temperature regime, the rate of vacancy emission from cavities is small and cavity growth is determined by bias. At higher temperatures, the peak cavity growth rate increases in magnitude and occurs at higher temperatures as gas pressure increases. Additionally, since the critical temperature T_c (defined as the temperature at which growth rate starts to decrease) increases more rapidly with gas pressure than the peak swelling temperature (T_p); i.e., swelling occurs over a wider temperature range.

Based on these considerations and the technological consideration of high service temperatures an irradiation test matrix was designed. This matrix is shown in Table XXVIII. It can be seen that the high temperature range of irradiation was expanded to include irradiations at 1350°C even though no swelling was observed at 1300°C in pure niobium. The lowest temperature of irradiation was raised from 700°C to 800°C because of the above considerations. An irradiation temperature of 950°C was added to better define the swelling behavior in the 800°-1000°C range.

The matrix consists of irradiations without helium and a relatively high He/dpa ratio (4) at the peak damage and high dose (50 dpa), so that the helium effects can be clearly delineated.

In the test matrix, specimens with zero He/dpa imply irradiations with Nb^{++} ions alone. The total irradiation dose was to 50 dpa. The temperature range for these specimens is restricted since a limited swelling is expected beyond 1000°C (at least in Nb) in accordance with experimental results of the Phase I study.

9.8 Irradiation Procedure

The Argonne National Laboratory facility, using the 2 MeV Tandem accelerator and a 650 keV helium accelerator which was to be installed, was not available for use in this program for dual ion irradiations because of budgetary and schedular constraints. Therefore, an alternate dual ion accelerator system

TABLE XXVIII

Irradiation Test Matrix for Nb, Nb-5 Hf and Nb-5W

He/dpa	Irradiation Temperatures (^oC)							
4	800	900	950	1000	1100	1200	1300	1350
0	800	900	950	1000	-	-	-	-

at the Radiological Physics Division of Battelle Pacific Northwest Laboratory (PNL) in Richland, WA was utilized to accomplish these irradiations. Parts of this facility had to be extensively modified to suit the requirements of this program. In addition, a new target holder was designed capable of accommodating multiple specimens, maintaining specimens at elevated temperature (up to 1350^oC) during irradiation, monitoring specimen temperature, and maintaining beam characteristics and beam alignment.

The dual ion accelerator facility at PNL consists of a 2 MV National Electrostatic Tandem accelerator equipped with Cs sputter source and a 2 MV Van de Graaf equipped with an rf ion source. For the present program, Nb ions were accelerated to an energy of 5 MeV and the helium ions were at an energy of 425 keV. The angle of incidence of helium ions was 32 degrees and the Nb ions were directed onto the target at normal incidence. Under these conditions, the maximum straggling of the helium implantation was obtained given the restrictions set by the layout of the two accelerators. The selection of the energies and current densities of the Nb and He beams was determined from calculations of the range, range straggling, and damage distribution of the particles using the TRIM88 computer code. The maximum energy of the Nb beam, 5 MeV, corresponds to the maximum particle current of the charge 2 state of the stripped ion, and the terminal voltage at which the accelerator would operate with good stability over long periods of several hours. The helium energy was selected to place the calculated peak in the implant distribution on the leading side of the Nb++ damage curve close to the peak damage depth. Because of uncertainties in the range of the He^+ ion, the energy corresponding to depth of the peak damage was not selected. Figures 60 and 61 show plots of the He profile and damage versus depth due to Nb in an Nb-5%W target obtained from the TRIM88 computer code. The helium and damage profiles in Nb-5Hf are alike because of similar atomic densities. The current of helium ions was set to achieve an implantation to atomic displacement ratio of 4 appm/dpa.

A photograph of the target holder is shown in Fig. 62 which illustrates the details of construction of the holder and its operation. Figure 63 illustrates the path of the ion beam through the system in the beam characterization mode and in the irradiation mode. The location of the beam and the beam profile were monitored outside the target chamber by the slits and the rotating wire beam profile monitor shown to the left in Fig. 63. The mask which is mounted about 2.5 cm (1 in) in front of the specimens, carries three apertures. The smaller inner aperture connected to an electrometer, defines the size of the beam impinging on the target. The two larger apertures maintained at ground potential serve to shield the defining aperture from electrons emitted from the specimen when at elevated temperature.

For beam alignment, the specimen holder plate was moved to its middle position while the electron gun assembly was lowered to provide an unobstructed path to the Faraday cup or window mounted in the back of the chamber. The central aperture, 0.3 mm (0.12 in) in diameter, measured the average current density of the specimen. The spatial profile of the beam in one dimension was assessed by measuring the beam current as a function of the aperture position. Following the characterization of the beam, the specimen holder plate is moved to one of the 18 specimen positions referenced to the vernier readout on the larger "unislide" seen [illegible] right side of the side view in Fig. 62. Note that the mask which was mounted on four insulating rollers supported from the specimen holder assembly remains stationary during this adjustment. The electron gun was moved to the beam axis using the smaller unislide (Fig. 62 lower right detail). The electron beam is then aligned by heating the specimen to a few hundred degrees and maximizing the surface temperature by either translating the gun with the unislide or

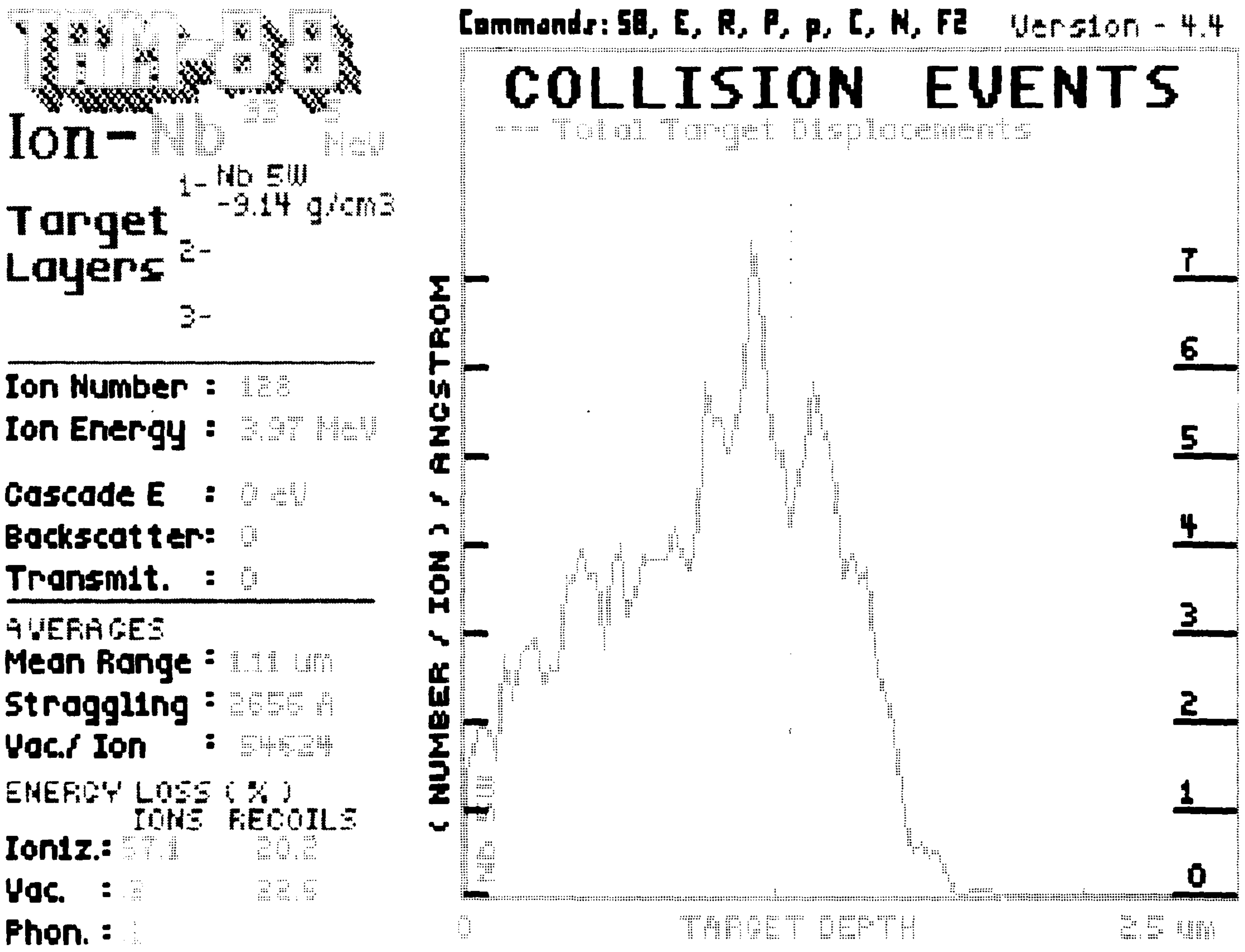

TRIM-88

Ion- Nb 93 5 MeV

Target Layers
1- Nb 5W -9.14 g/cm3
2-
3-

Ion Number : 128
Ion Energy : 3.97 MeV

Cascade E : 0 eV
Backscatter: 0
Transmit. : 0

AVERAGES
Mean Range : 1.11 um
Straggling : 2656 A
Vac./ Ion : 54624

ENERGY LOSS (%)

	IONS	RECOILS
Ioniz.:	57.1	20.2
Vac. :	2	22.6
Phon. :	1	

Figure 60. Damage Profile for Niobium Ions in Nb Target.

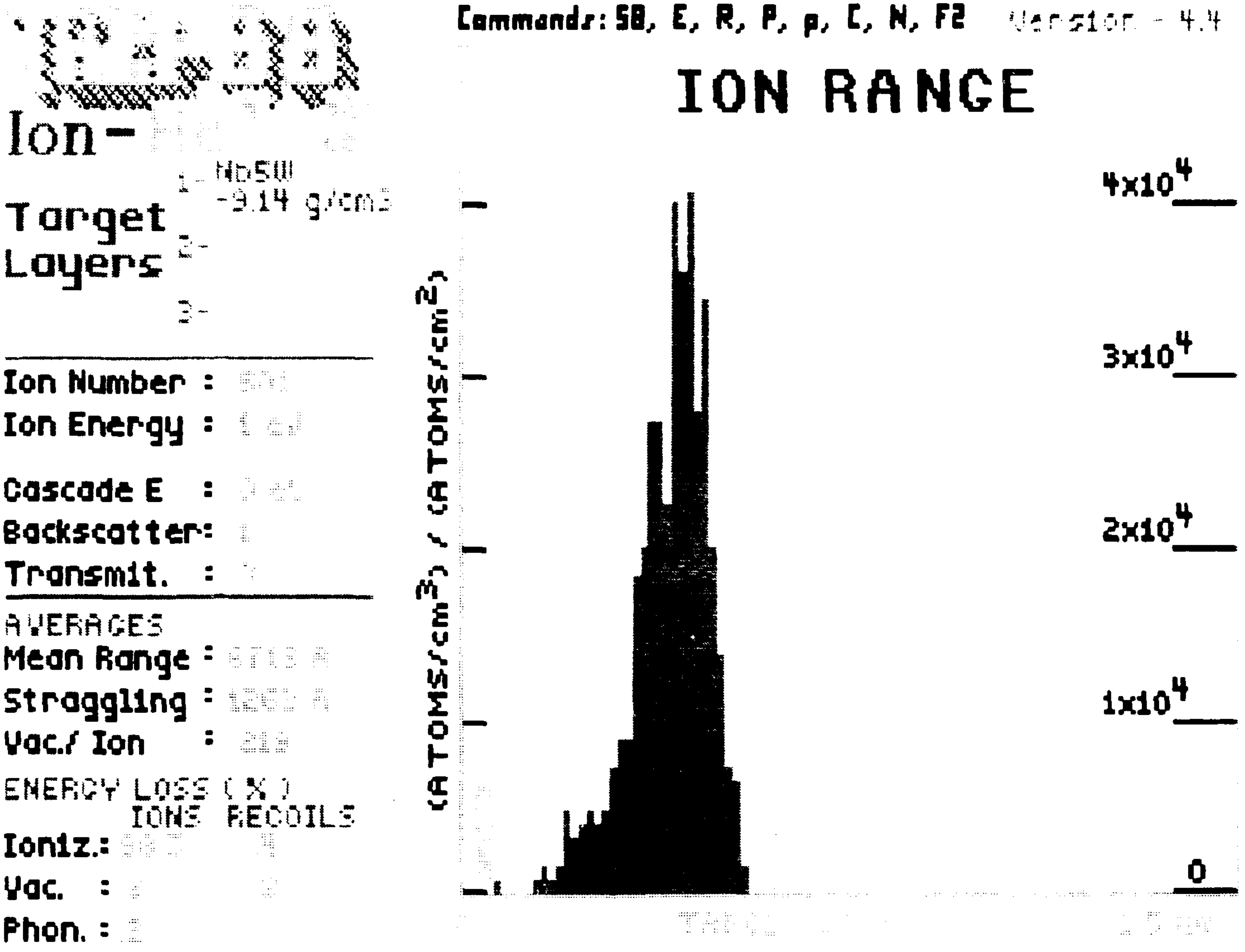

```
Commands: SB, E, R, P, p, C, N, F2    Version - 4.4

Ion-
Target   1- NbSW
Layers      -9.14 g/cm3
         2-
         3-

Ion Number :
Ion Energy :

Cascade E  :
Backscatter:
Transmit.  :

AVERAGES
Mean Range :
Straggling :
Vac./ Ion  :
ENERGY LOSS (%)
      IONS  RECOILS
Ioniz.:
Vac.  :
Phon. :
```

Figure 61. Deposition Profile for He^+ Ions in Nb Target.

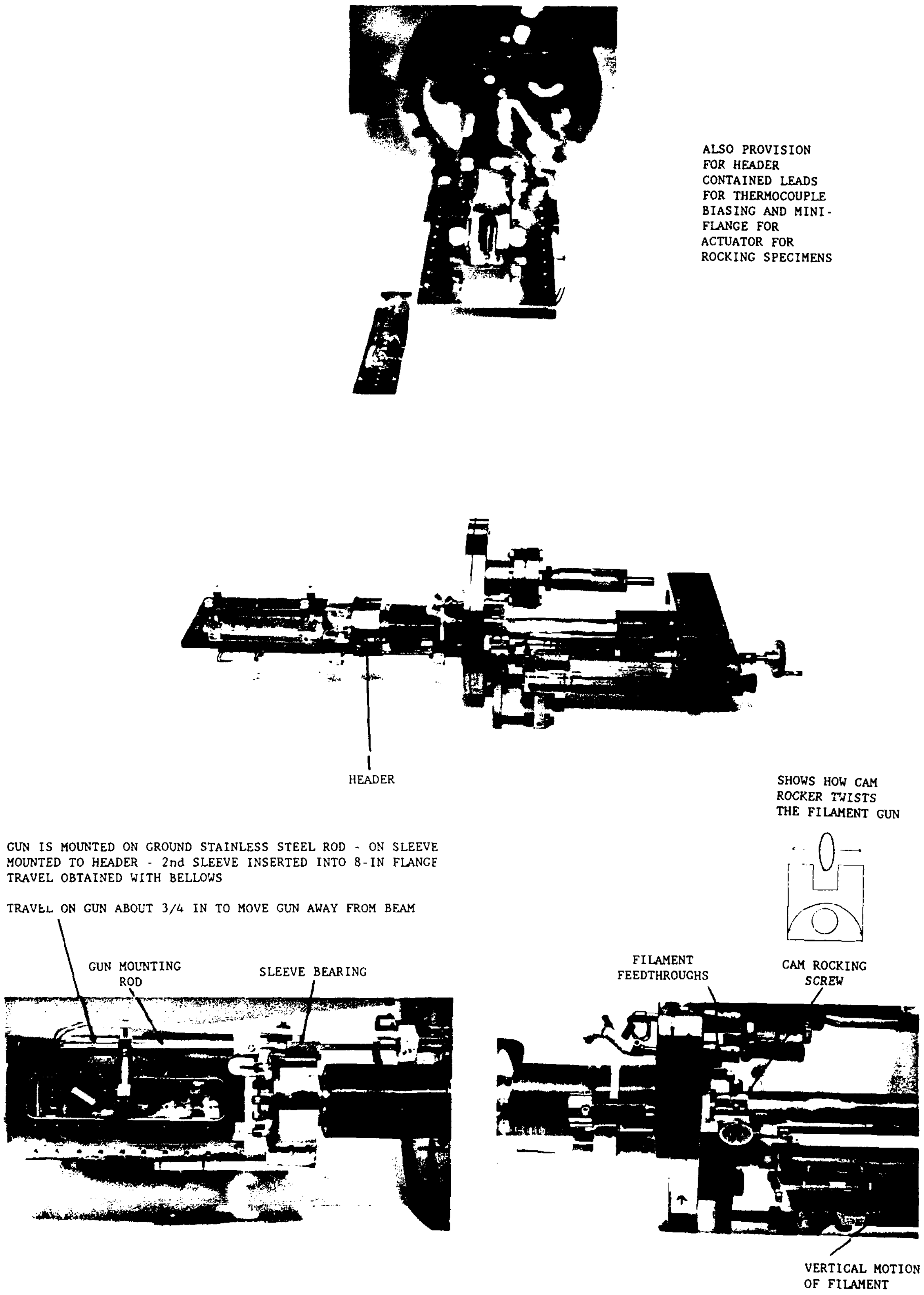

Figure 62. Specimen Holder and Specimen Heating Arrangement for Dual Ion Bombardments.

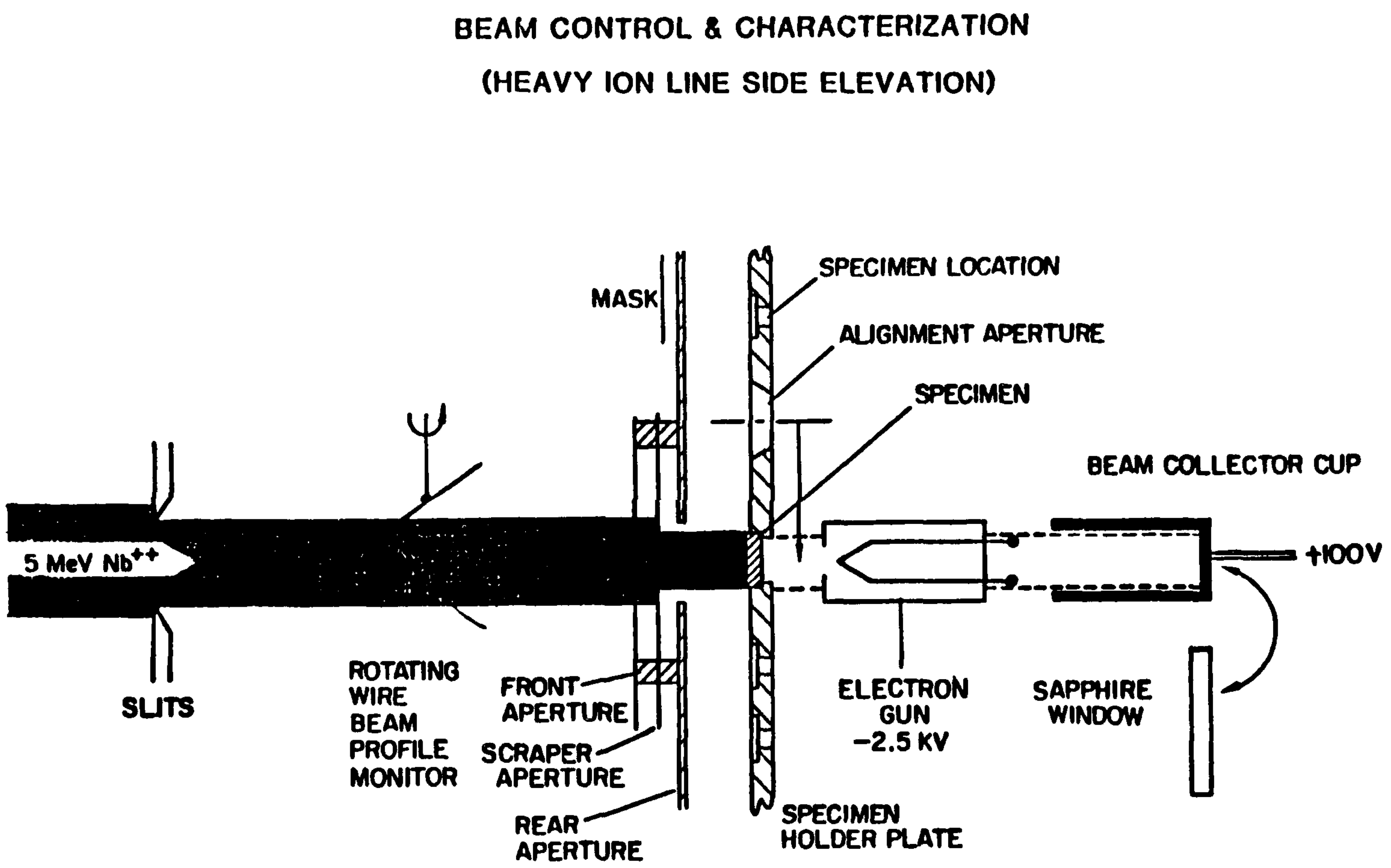

Figure 63. Schematic of Beam Control and Monitoring and Characterization Arrangement for Dual Ion Irradiation.

tilting it by rotating the shaft from which it is mounted by the cam actuator seen in Fig. 62 lower right. Details of the shaft supporting the electron gun and the isolated power leads for the filament of the gun can be seen in the photograph to the lower left.

During the irradiations, the electron gun current was modulated by a control circuit connected to the output of an IRCON Infrared Optical Pyrometer. The temperature was controlled to ± 5°C. The specimens were irradiated in vacuums in the 10^{-8} torr range maintained by a triode ion pump. The spectra of the residual gas were recorded by a Varian RGA unit.

Prior to irradiation, each specimen was annealed at 1200°C for 0.5 h, in the chamber, at a vacuum in the 10^{-8} range. The target dose for the irradiation was 50 dpa at 0 or 4 appm He/dpa at a displacement rate of 1×10^{-2} sec^{-1}.

9.9 Post-Irradiation Specimen Preparation and TEM Observations

Post-irradiation specimen preparation involved removal of a controlled amount of material from the front surface (sectioning) so that the desired peak or near peak region of damage and helium deposition could be examined in the transmission electron microscope (TEM). Generally, the sectioning can be achieved by electrochemical means or by ion milling. The former is preferred because of less damage to the surface. Following sectioning, the specimen is electropolished from the back side to perforation, thus producing a thin foil.

Both techniques of sectioning were attempted in Nb-Hf and Nb-W alloys. In the electrochemical technique, a portion of the specimen was masked using stop-off lacquer and the specimen was held on the side with a pair of tweezers before electropolishing as described in ref. 109. The sectioning thickness was measured by interference microscopy. The sectioning of these alloys by electrochemical means proved to be tedious and produced unpredictable results despite a number of different solutions and polishing conditions attempted. Although some specimens were prepared by electrochemical sectioning, the sectioning depths were variable. Sectioning was also accomplished by an ion-milling technique similar to that described in Phase I of the program, except that a smaller beam angle (75° vs. 90°) was used during the milling operation. The depth of material removal was measured by interference metallography. Another major difference between ion milling done in Phase I and Phase III was that in the latter case, ion milling was accomplished after back-thinning of the specimens as opposed to before back-thinning. The back-thinned specimens had some sectioning on them produced by electrochemical means.

Back-thinning of Nb-5W and Nb-5Hf proved to be a very tedious, time consuming, and frustrating experience due to unpredictability of the electropolishing characteristics and preferential attack of the grain boundaries in these fine-grained materials. A large number of solutions were tried, and for each solution a large number of attempts were made by varying parameters essential to electropolishing; i.e., temperature, current density, type of cathode, jet diameter, distance between cathode and anode, and stirring speed. Most of these attempts were futile. The electropolishing solutions tried were:

- 5.3 g $LiC\ell_2$, 11.2 g $MgC\ell O_4$, 100 mℓ butyl cellusolve, 500 mℓ methanol
- 20% saturated NH_4F in methanol, 80% methanol
- 13% HCl, 10% butyl cellusolve, 77% ethanol
- 88% HNO_3, 12% HF
- 2.5% HF, 5% H_2SO_4, 92.5% methanol
- 0.5 mole/ℓ $Mg(ClO_4)_2$ in methanol
- 0.05 mole/ℓ $Mg(ClO_4)_2$ in methanol

Most of these solutions produced an excellent polish in pure niobium with large grain size; however, the quality of polish in alloys with recrystallized grains was marginal. The solution containing 0.5 mole/ℓ $Mg(ClO_4)_2$ in methanol was used to obtain a dish in the specimens and the final polishing was accomplished in BK-2 solution. In a significant number of specimens, a salt-like deposit [an insoluble Mn, Fe, Cr, $Mg(ClO_4)_2$ complex adhering to the thin areas near the perforation] was seen in the TEM. This was partially removed by cleaning in a mixture of 15 HNO_3 + 5mℓ HF in 50 mℓ glycerine. Ion milling was used to remove the remainder, however, at the expense of loss of depth reference during the TEM examinations.

Table XXIX lists the specimens and their sectioning depths achieved by ion milling along with the irradiation temperatures. It can be seen that despite identical ion-milling conditions, the sectioning depth (and therefore dose) showed a wide variation.

The transmission electron microscope examination of these specimens was carried out in a Phillips 420 STEM microscope at the Argonne National Laboratory. The specimens were imaged to show the voids in contrast by using a slightly out of focus condition. Large voids near the surfaces in the specimens irradiated at high temperatures were often attacked by the electropolishing solution, resulting in a fuzzy image.

9.10 Results

Transmission Electron Microscopy (TEM) examination was carried out on all (a total of 24) irradiated specimens along with two control specimens. The primary purpose of this examination was to determine swelling in these alloys and to see if the effect of helium can be separated from the displacement damage alone (i.e., examine specimens irradiated with Nb^{++} + He^{+} and those irradiated with Nb^{++} alone). The irradiation-produced dislocation and black dot damage was also examined to evaluate the effect of helium on them, however, they were not examined extensively. As described before, the foil preparation was tedious and less than perfect foils had to be examined. The quality of TEM images was sometimes marginal. A few specimens, for

TABLE XXIX

Summary of Sectioning Depth for Nb-5W and Nb-5Hf Specimens

Material	Specimen No.	Irradiation Temp. (^{o}C)	Sectioning Depth (Å)
Nb-5Hf Irradiated with Nb+He	H7	800	6000
	H3	900	6000
	H6	950	8400
	H1	1000	4500
	H4	1100	6000
	H13	1200	6000
	H5	1300	6000
	H14	1350	6000
Nb-5Hf Irradiated with Nb	H8	800	3000
	H10	900	-
	H12	950	-
	H15	1000	6000
	H11	Control	6000
Nb-5W Irradiated with Nb+He	W9	800	4500
	W7	900	-
	W4	950	6000
	W6	1000	1000
	W8	1100	6000
	W14	1200	6000
	W2	1300	6000
	W15	1350	6000
Nb-5W Irradiated with Nb	W10	800	6000
	W5	900	4500
	W12	950	3000
	W13	1000	2300

example, H15, H5, and W13, could not be examined because of poor foil quality and numerous artifacts in the foil. These needed additional ion milling (≈1000 Å) to remove an oxide film from the surface. The results of TEM examination are summarized below.

9.10.1 Niobium-5% Hafnium Alloy

Table XXX summarizes the results of microscopic examination of specimens of this alloy. In the specimen irradiated with Nb^{++} alone (Specimens H8, H10, and H12) voids were observed at 900°C and above. The void distribution was nonuniform and estimated swelling was <<0.1% at 900°, 950°, and 1000°C. Below 900°C, only black dot damage and dislocation loops were present. This damage was very fine (5-10 nm diameter). No attempt was made to characterize this damage. Dislocations were also observed, but their densities appear to be comparable to the density in annealed materials ($\approx 10^9$ cm^{-2}). At 1000°C, only isolated voids were observed along with dislocations. Examples of damage in specimens irradiated at 900°, 950°, and 1000°C are shown in Fig. 64.

The dual-ion irradiated specimen, subjected to irradiations at 800°C, showed behavior similar to the specimen irradiated with Nb^{++} alone. Black dot damage and dislocation damage plus occasional voids were observed. At 900°C, an anamolous behavior was observed. In one area of this specimen a relatively high density of small voids was observed (see Fig. 65). The swelling due to these voids was small (<0.1%). Along with voids, a high density ($\approx 7 \times 10^{16}$ cm^{-3}) of linear features was observed. These features, aligned along certain crystallographic directions, were presumably precipitates of HfO_2 formed during the irradiation and/or heat treatment. In another area of the same specimen, no voids were observed and the damage was characterized by small black dots. In the specimen irradiated at 950°C, isolated voids were observed and no significant swelling was measured.

A comparison of damage (including swelling) characteristics over a temperature range of 800°-950°C, in specimens irradiated with Nb^{++} alone and Nb^{++} + He^{+}, showed insignificant contribution due to helium.

TABLE XXX

Summary of TEM Results of Irradiated Nb-5Hf

Spec. No.	Irradiating Ions	Temp. (^{o}C)	dpa	He/dpa	Microstructural Features Voids	 Dislocations	 Dislocation Loops	Maximum Estimated Swelling
H8	Nb^{++}	800	35	0	Isolated	✓	✓	<<0.1
H10	Nb^{++}	900	-	-	Isolated	✓	✓	<<0.1
H12	Nb^{++}	950	-	-	Isolated	✓	✓	<<0.1
H15	Nb^{++}	1000	35	0	Isolated	✓	✓	<<0.1
H7	$Nb^{++} + He^{+}$	800	35	1.7	Isolated	✓	✓	<0.1
H3	$Nb^{++} + He^{+}$	900	35	1.7	Isolated	✓	✓	<0.1
H6	$Nb^{++} + He^{+}$	950	43	4.4	Isolated	✓	✓	<0.1
H1	$Nb^{++} + He^{+}$	1000	30	1.0	✓	✓	✓	<0.1
H4	$Nb^{++} + He^{+}$	1100	35	1.7	✓	✓	✓	<0.1
H13	$Nb^{++} + He^{+}$	1200	35	1.7	✓	✓	✓	<0.1
H5*	$Nb^{++} + He^{+}$	1300	35	1.7	-	-	-	-
H14	$Nb^{++} + He^{+}$	1350	35	1.7	✓	✓	✓	<10

*Poor foil preparation, no data obtained.

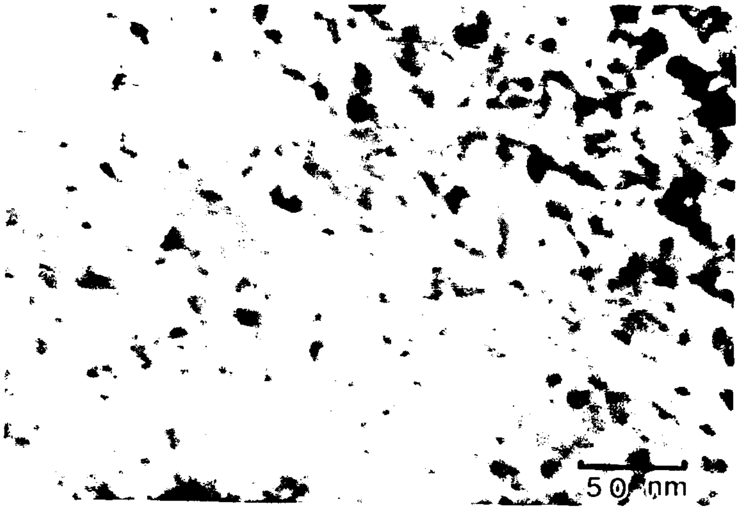

(a)
Irradiated at
900°C

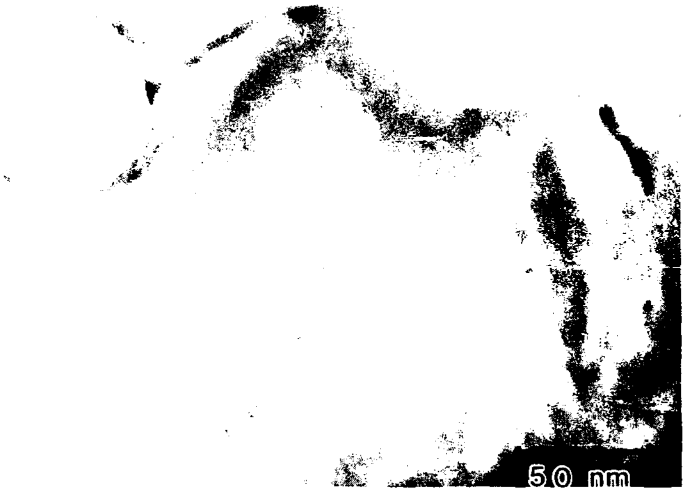

(b)
Irradiated at
950°C

(c)
Irradiated at
1000°C

Figure 64. Irradiation Damage in Specimens of Nb-5Hf Irradiated with Nb^{++} Ions Alone. (Note Differences in Magnifications.)

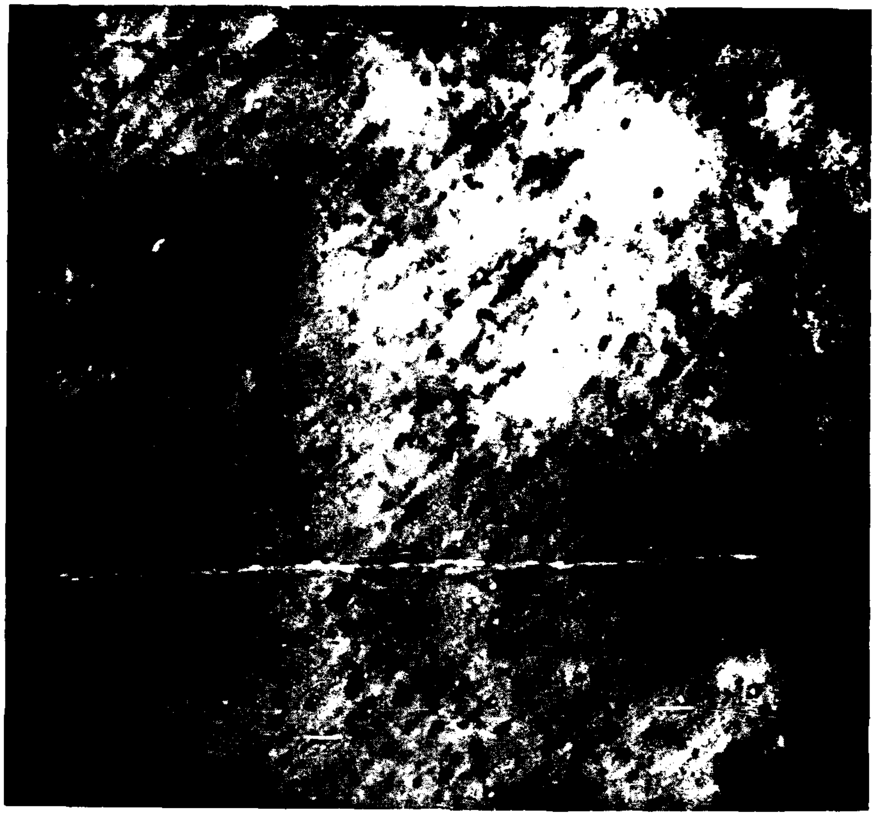

Figure 65. Voids and Linear Features in Nb-5Hf Irradiated at 900°C.

At 1000°, void formation was inhomogeneous. In one region, voids associated with precipitates were observed and in another area, rows of voids appeared to have formed along grain boundaries which had moved during irradiation. The overall swelling was still small. Examples of voids in the 1000°C specimen are shown in Fig. 66. At 1100° and 1200°C, void distribution was inhomogeneous with isolated voids observed in TEM. The overall swelling was small. For examples of voids at 1100° and 1200°C, see Fig. 67.

With increasing irradiation temperature, the void diameter increased. Large voids were observed in specimens irradiated at 1350°C. The voids were so large that some of them intersected the foil surfaces resulting in chemical attack by the polishing electrolyte, thereby enlarging them. This results in a fuzzy void image (see Fig. 68) which makes the estimates of size difficult. The density of voids estimated from three different areas was $\approx 8 \times 10^{13}$ cm^{-3}. Due to the attack of voids with the electrolyte, their size could not be estimated with any degree of confidence. The upper bound of swelling due to large voids was estimated at <10%. An example of voids produced at 1350°C is shown in Fig. 68.

9.10.2 Niobium-5% Tungsten Alloy

Specimens of Nb-5W irradiated with Nb^{++} alone over a temperature range of 800°-1350°C and those irradiated with Nb^{++} + He^{+} ions over 800°-1350°C were examined by TEM. None of these specimens examined exhibited any voids. The damage was characterized by black dot damage, dislocation loops, and some dislocations. Table XXXI summarizes the irradiation conditions of these specimens. The lack of swelling in this material is significant compared with pure niobium (Phase I) and Nb-5Hf alloy. It shows that an addition of a small amount of tungsten can suppress swelling in niobium over a wide temperature range. Damage structure of representative specimens of Nb-5W irradiated at 950°C and 1100°C are shown in Figs. 69 and 70, respectively.

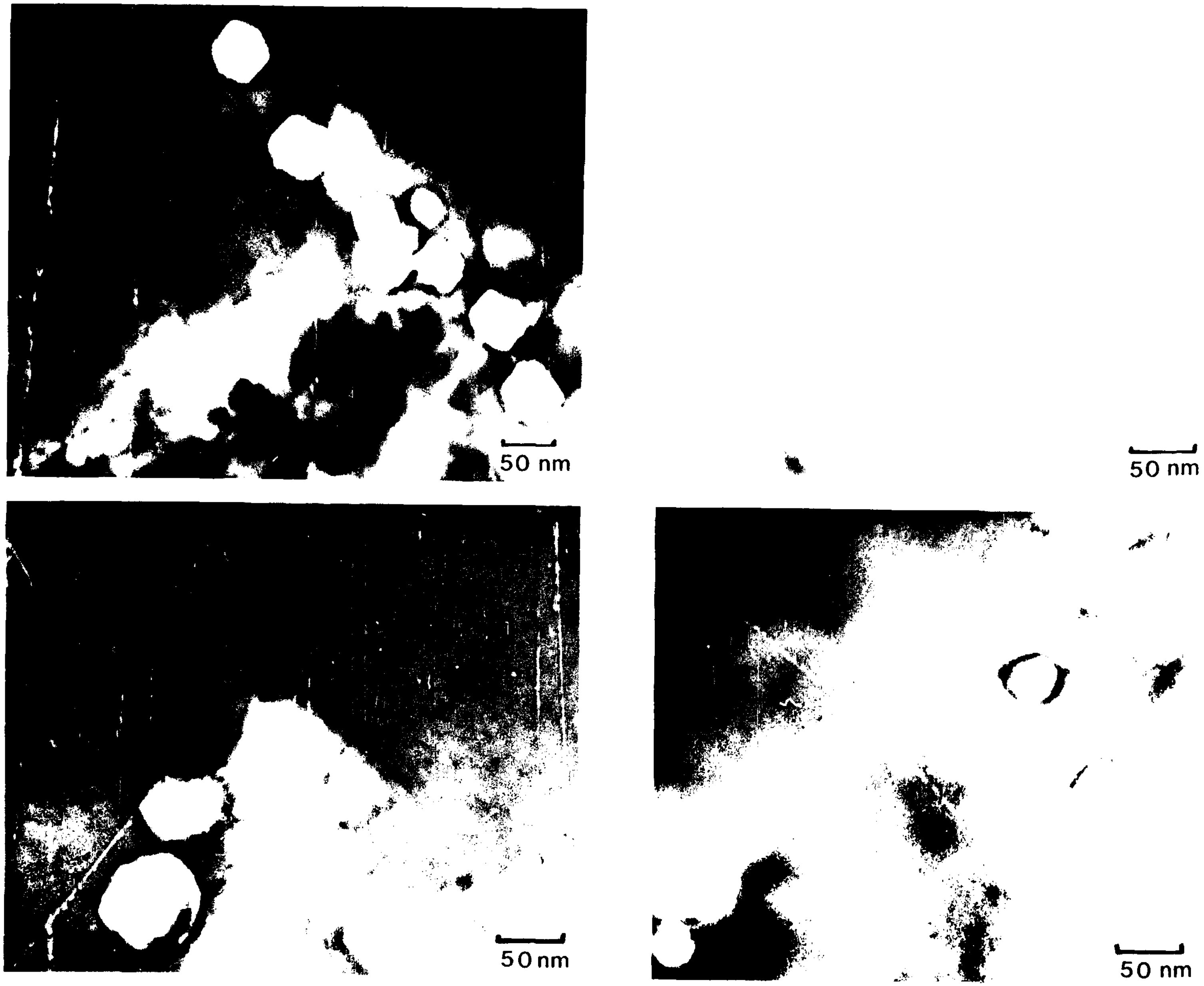

Figure 66. Voids in Nb-5Hf Alloy Irradiated with Nb^{++} + He^{+} Ions at 1000°C.

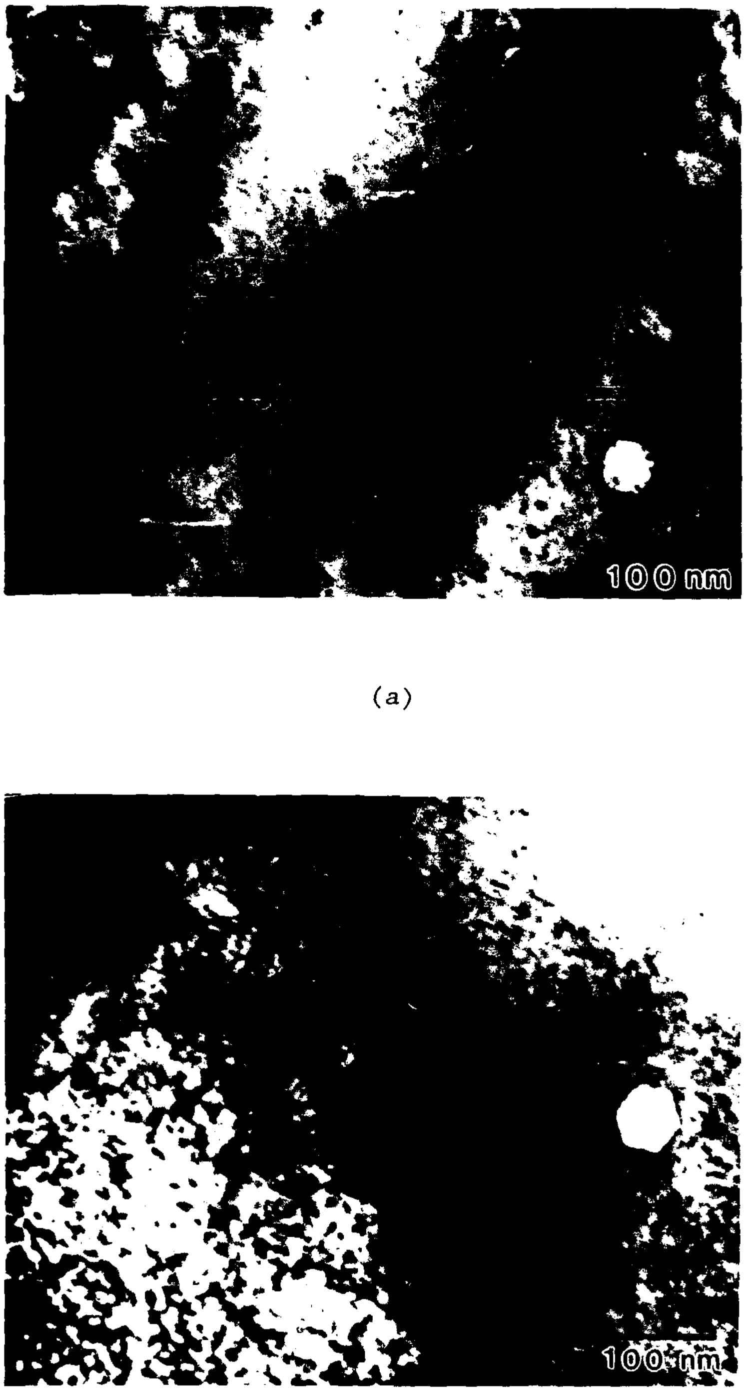

(a)

(b)

Figure 67. Voids in Nb-5Hf Alloy Irradiated with Nb^{++} + He^{+} Ions at (a) 1100°C and (b) 1200°C.

Figure 68. Voids in Nb-5Hf Alloy Irradiated with Nb^{++} + He^{+} Ions at 1350°C.

TABLE XXXI

Summary of TEM Examination of Nb-5W

Specimen No.	Irradiating Ions	Temp. (^{o}C)	dpa	He/dpa	Swelling (%)
W10	Nb^{++}	800	35	0	0
W5	Nb^{++}	900	30	0	0
W12	Nb^{++}	950	25	0	0
W13	Nb^{++}	1000	18	0	0
W9	$Nb^{++} + He^{+}$	800	30	1.0	0
W7	$Nb^{++} + He^{+}$	900	-	-	-
W4	$Nb^{++} + He^{+}$	950	35	1.7	0
W6	$Nb^{++} + He^{+}$	1000	18	0	0
W8	$Nb^{++} + He^{+}$	1100	35	1.7	0
W14	$Nb^{++} + He^{+}$	1200	35	1.7	0
W2	$Nb^{++} + He^{+}$	1300	35	1.7	0
W15	$Nb^{++} + He^{+}$	1350	35	1.7	0

9.11 Discussion

As mentioned before, the post-irradiation specimen preparation of Nb-5Hf and Nb-5W was wrought with numerous problems which resulted in poor quality foils. The variability in the sectioning depths obtained by electrochemical or ion milling resulted in variation in dpa and He/dpa ratios of the specimens examined. For example, as shown in Table XXX for Nb-5Hf irradiated with Nb^{++} + He^{+}, the dpa ranged from 18 to ≈40 dpa and the He/dpa ratio from 0 to ≈4.4. These problems make a quantitative assessment of effects of alloying elements difficult. Despite these problems, important qualitative conclusions can be drawn from these data. The most important of these conclusions is that Nb-5W is a swelling resistant alloy. This alloy did not show any voidage over a wide temperature range from 800°-1350°C, up to a dose of ≈35 dpa.
The subtle differences due to variation in He/dpa ratio from 0 to ≈1.7 and

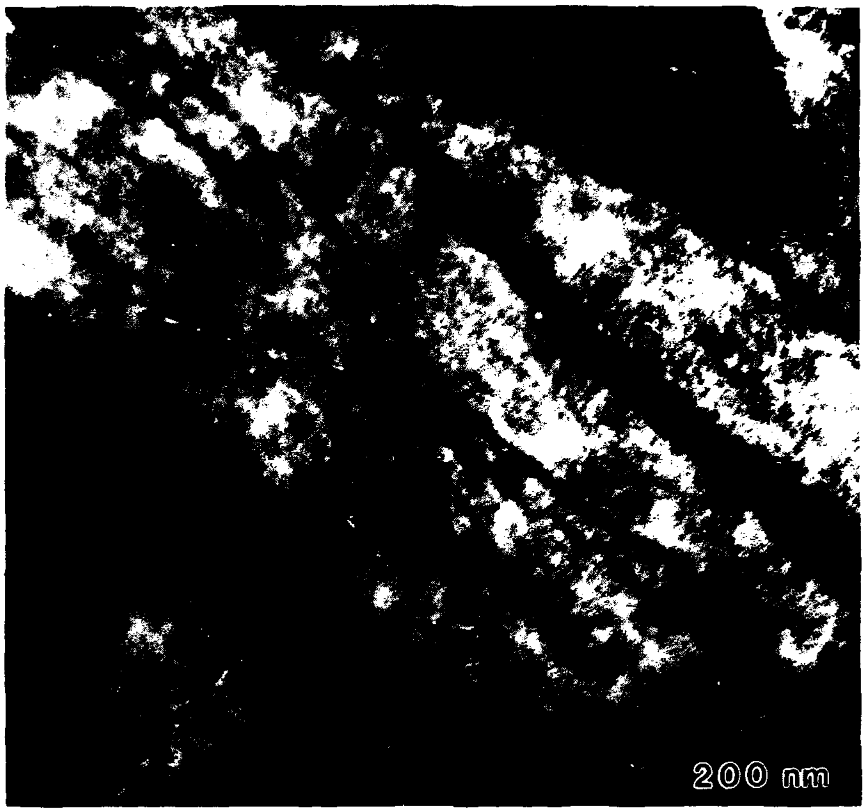

Figure 69. Irradiation Damage in Nb-5W Irradiated with Nb^{++} + He^{+} at 950°C.

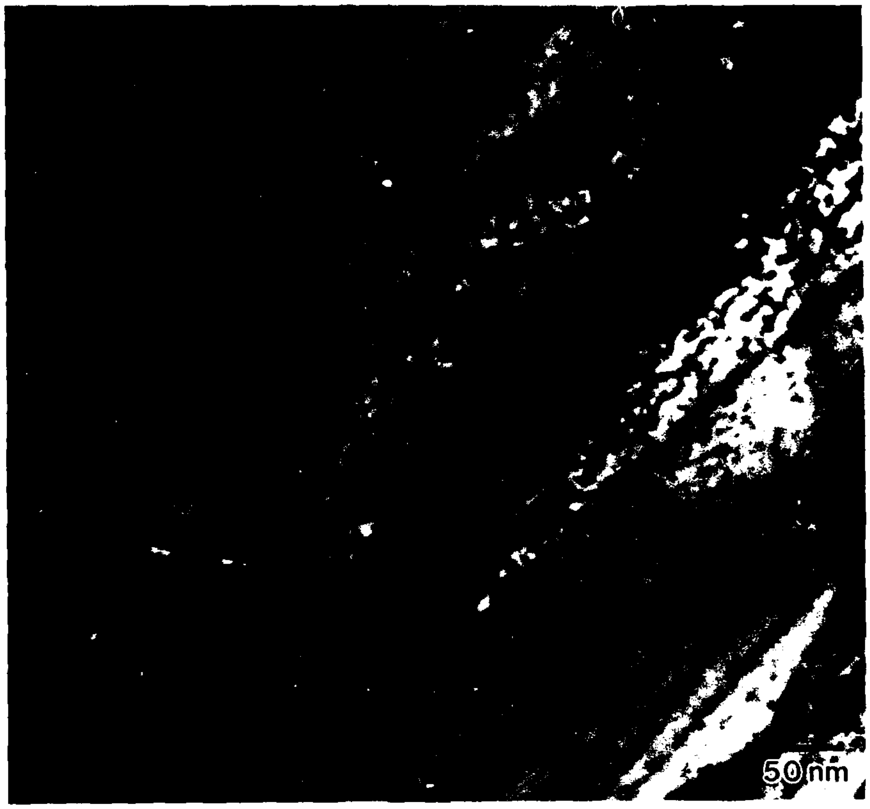

Figure 70. Irradiation Damage in Nb-5W Irradiated with Nb^{++} + He^{+} at 1100°C.

dpa from 18 to 35 cannot be resolved from these data, but they do not compromise the conclusion that this alloy is a potential swelling resistant niobium base material, at least up to 35 dpa. It warrants further investigation to determine if the swelling resistance is continued to higher dpa levels.

The swelling in Nb-5Hf alloy was skewed toward much higher temperatures when compared to pure Nb and other niobium alloys. In the Phase I study, it was shown that the peak swelling occurs at 900°C. In Nb-5Hf, very few voids were observed at this temperature. Instead, major swelling occurred at temperatures >1100°C and voids were observed even at 1350°C ($\approx 0.6\ T_m$). In pure niobium, no swelling was observed at 1300°C ($0.57\ T_m$).

Loomis and Gerber(21) irradiated niobium alloys containing 2.5% Hf + 2.5% Mo with nickel ions and helium. They observed <0.1% swelling at 950°C and suggested that swelling would not occur at temperatures >1175°C ($0.53\ T_m$). Whether the difference observed here is due to the difference in alloying constituents or bombarding species (Ni^+ vs Nb^{++}) is not clear. If simultaneous helium injection has a large influence of shift in the swelling peak then Loomis and Gerber's alloys should have exhibited swelling at even higher temperatures since they used 20 appm He/dpa versus ≈1 in the present work.

Loomis and Gerber(110) irradiated niobium with titanium additions. They irradiated niobium containing 2-25 a/o titanium at 780° and 980°C and saw near zero swelling at 780°C (2.5 a/o Ti) and at 980°C (>15 a/o Ti).

Nb and Nb-1Zr irradiated with nickel ions at temperatures 600°C and 1150°C were studied by Loomis, Taylor, and Gerber(90). They saw double peaks in the temperature dependence of swelling. No swelling was observed at 1150°C ($0.52\ T_m$) and above. No shift in swelling peaks was observed due to the addition of Zr.

The high temperature swelling (at $>0.50\ T_m$) does, however, have an example in another refractory metal; i.e., Mo. Extensive swelling (≈10%) was observed in Mo irradiated with ions over a temperature range of 1250°-1500°C ($0.53\text{-}0.61\ T_m$) as shown by Loomis(111).

No literature data exists on irradiated Nb-Hf alloys or other refractory metals with hafnium addition. Also, no data exist on Nb-W alloys. Loomis(112) has irradiated a number of vanadium alloys containing tungsten and Mo additions. Preliminary results show significant reduction in swelling in vanadium due to W and Mo additions in agreement with the results of this work.

The reduced swelling in Nb-W alloy is of considerable technological importance. It demonstrates, for the first time, that a small addition of tungsten can significantly reduce swelling in niobium making it a candidate material for space nuclear reactor applications where high displacement damage may occur. A further study of this material is warranted to extend these early results to higher doses and He/dpa ratios prototypic of service conditions.

In addition, the basic theoretical model developed during the first two phases of this program should be further developed to include the effects of alloying element additions to thus enable predictions of swelling behavior of these alloys.

10.0 SUMMARY AND CONCLUSIONS

A three phase study was conducted to investigate high temperature irradiation swelling mechanisms in refractory metals. In this study, a basic theoretical model based on the chemical reaction rate formalism was developed for the body-centered cubic (bcc) metals. A material, niobium, was selected and experimental techniques and ion source were developed to irradiate this material, for the first time, with self-ions. Transmission electron microscopy was conducted to characterize the microstructures after irradiation. Ion irradiations to 50 dpa produced a swelling of 7% at a peak temperature of 900°C. No swelling was observed at temperatures $\geq 1300^\circ$C. The experimental results were compared to the theoretical model calculations. A reasonable agreement between the calculated and experimental swelling values was obtained when trapping of interstitials by oxygen was included. An interstitial oxygen binding energy of ≈ 2 eV/atom provided the best fit to the experimental data. Microstructural data were utilized to calculate sink-strength rates whose average values as a function of temperature ranged from 1.018 to 1.046.

A theoretical model for loop growth and shrinkage in bcc metals was developed which showed that contrary to Little, Bullough and Wood(63), the difference in bias of <111> and <100> and high initial dislocation density which decreases with time are not sufficient to explain <111> loop shrinkage. Experimental investigation of low dose microstructural evolution at 800°C and 1000°C at doses ranging from 0.05 to 5 dpa in self-ion irradiated niobium showed high densities, on the order of 10^{16}, of dislocation loops ≈10 nm in diameter at both temperatures.

Careful contrast experiments were conducted to characterize the nature of loops. The loops were predominantly interstitial in nature with a Burgers vector of $\frac{a}{2}\langle 111\rangle$. Vacancy loops were also found but their numbers were small. The $\frac{a}{2}\langle 111\rangle$ loops also contained a shear component. The a<100> type loops were not found, perhaps because of low probability of formation of these loops.

Two alloys of niobium containing 5 w/o hafnium and 5 w/o tungsten were selected based on theoretical, practical, and technological considerations. These alloys were irradiated with Nb^{++} alone over a temperature range of 800°-1000°C and with $Nb^{++} + He^{+}$ over a temperature range of 800°-1350°C. Nb-5Hf showed a shift in peak swelling temperatures compared to pure Nb with swelling observed at temperatures ≥1100°C. Swelling was also observed at 1350°C. Nb-5W alloy showed no swelling in any of the specimens examined. It was concluded that Nb-5W is a swelling resistant alloy at least up to 35 dpa and it needs further investigation to extend the irradiation study to higher doses. Nb-5W appears to be a promising swelling resistant alloy candidate for space reactor applications. It is recommended that theoretical effort be continued to understand swelling in these materials, including the effects of alloying elements.

11.0 RECOMMENDATIONS FOR FUTURE WORK

(1) Develop improved electrochemical/ion-milling specimen preparation techniques for sectioning and thin foil preparation of Nb-W and Nb-Hf and other alloys.

(2) Develop a centralized facility for dual-ion irradiations of refractory metal alloys under ultra-high vacuum conditions (see Appendix C).

(3) Verify swelling resistance of Nb-5W alloy as a function of displacement dose and He/dpa ratio.

(4) Extend the basic model developed in Phases I and II of this program to include the effects of substitutional alloying elements such as tungsten and hafnium.

12.0 REFERENCES

1. R. Bajaj, B. O. Hall, and G. R. Fenske, "An Investigation of the Irradiation Swelling Mechanisms in Refractory Metals at High Temperatures," Phase I Report, WAESD-TR-85-005, February 1985.

2. R. Bajaj, B. O. Hall, and J. C. Greggi, "An Investigation of the Irradiation Swelling Mechanisms in Refractory Metals at High Temperatures," Interim Scientific Report, WAESD-TR-86-0016, June 1986.

3. M. L. Bleiberg and J. W. Bennett, Eds., Proceedings of International Conference on the Radiation Effects in Breeder Reactor Structural Materials, Scottsdale, Arizona, June 19-23, 1977, Metallurgical Society of AIME, 1977.

4. R. Bajaj, S. Diamond, and M. L. Bleiberg, "Optimization of Precipitation Hardened Fe-Cr-Ni Alloys Using Nickel Ion Bombardment Simulation Studies," in Effects of Radiation on Materials, Eleventh Conference, ASTM-STP-782, H. R. Brager and J. S. Perrin, Eds., American Soc. for Testing and Materials, 1982, pp. 856-884 .

5. S. Wood, J. A. Spitznagel, W. J. Choyke, et al., "Microstructural Development in Dual-Ion Bombarded 316 Stainless Steel," in Effects of Radiation on Materials, Tenth Conference, ASTM-STP-725, D. Kramer, H. R. Brager and J. S. Perrin, Eds., American Soc. for Testing and Materials 1981, pp. 455-469.

6. W. G. Johnston, T. Lauritzen, J. H. Rosolowski, et al., "The Effect of Metallurgical Variables on Void Swelling," in Radiation Damage in Metals, Cleveland, OH, ASTM 1976, pp. 227-266.

7. M. L. Bleiberg, R. Bajaj, I. M. Baron, et al., "Swelling and Gamma-Prime Particle Stability of Ion-Bombarded Iron-Chromium Nickel Alloys," in Irradiation Effects on the Microstructure and Properties of Metal, ASTM-STP-611, American Society for Testing and Materials 1976, pp. 315-336.

8. W. J. Weber, G. L. Kulcinski, R. G. Lott, et al., "Ion Simulation Study of Void Formation in High Purity Vanadium," in Radiation Effects and Tritium Technology for Fusion Reactors, CONF-750939, March 1976, pp. I-130-149.

9. S. C. Agarwal and A. Taylor, "Dose Dependence of Void Swelling in Vanadium Irradiated with Self Ions," in Radiation Effects and Tritium Technology for Fusion Reactors, CONF-750989, March 1976, pp. I-150-157,.

10. S. C. Agarwal, D. I. Potter, and A. Taylor, "Effect of Interstitial Solutes on the Microstructures of Self Ion Irradiated Vanadium," in Irradiation Effects on the Microstructure and Properties of Metals, ASTM-STP-611, American Society for Testing and Materials, 1976, pp. 298-311.

11. A. T. Santhanam, A. Taylor, and S. D. Harkness, "Charged Particle Simulation Studies of Vanadium and Vanadium Alloys," in Defects and Defect Cluster in B.C.C. Metals and Their Alloys, R. J. Arsenault, Ed., 1973, pp. 302-320.

12. R. G. Lott, G. L. Kulchisni, P. Wilkes, et al., "Effect of Nickel and Nitrogen on Void Formation in Ion Bombarded Vanadium," J. Nucl. Mat. 85-86, pp. 751-755 (1979).

13. J. Bressers and W. Van Witzenberg, "The Influence of Oxygen on Void Formation in Neutron Irradiated Vanadium," J. Nucl. Mater. 85-86, pp. 757-761 (1979).

14. S. K. Tyler and P. J. Goodhew, "Helium Bubble Growth in Vanadium," in Effects of Radiation on Materials, Tenth Conference, ASTM-STP-725, D. Kramer, M. R. Broger and J. S. Perrin, Eds., American Soc. for Testing and Materials, 1981, pp 654-662.

15. W. Van Witzenberg, A. Mastenbrock, and J. D. Elen, "The Influence of Preimplanted Helium on the Microstructure of Neutron Irradiated Vanadium," J. Nucl. Mater. 103-104, pp. 1187-1192 (1982).

16. R. E. Gold and D. L. Harrod, "Radiation Effects in Vanadium and Vanadium Base Alloys," Int. Met. Rev. 25, Nos. 5 and 6, pp. 232-254 (1980).

17. M. P. Tanaka, E. E. Bloom, and J. A. Horak, "Tensile Properties and Microstructure of Helium Injected and Reactor Irradiated V-20Ti," J. Nucl. Mater. 103-104, pp. 895-900 (1981).

18. B. A. Loomis and G. Ayrault, "Cavity Formation in Single and Dual-Ion Irradiated V-1 5Cr 5Ti Alloy," Oct.-Dec. 1982, Quarterly Progress Report, DOE/ER-0046/12, pp. 194-205, February 1983.

19. B. A. Loomis, A. T. Taylor, T. E. Klippert, et al.,"Effect of Oxygen Impurity on Void Formation in Ion Bombarded Niobium," in Defects and Defect Clusters in B.C.C. Metals and Their Alloys, R. J. Arsenault, Ed., 1973, pp. 332-340.

20. B. A. Loomis, A. T. Taylor, and S. B. Gerber, "Void Swelling of Nb, Nb-1AT%Zr and Nb-0.5At%O Induced by ^{58}Ni^{+} Bombardment," in Radiation Effects and Tritium Technology for Fusion Reactors, CONF-750989-P1, March 1976, pp. I-93-105.

21. B. A. Loomis and S. B. Gerber, "Swelling of ^{58}Ni^{+} and ^{3}He^{+} Ion-Irradiated Nb and Nb Alloys," J. Nucl. Mater. 103-104, pp. 1193-1197 (1982).

22. B. A. Loomis and S. B. Gerber, "Similar Dependence on Dilute O Concentration of Void Formation in Ion-Irradiated Nb and Some Properties of Unirradiated Nb," J. Nucl. Mater. 97, pp. 113-125 (1981).

23. H. Jang and J. Moteff, "The Influence of Neutron Irradiation Temperature on the Void Characteristics of Nb and Nb-1/Zirconium Alloy," in Radiation Effects and Tritium Technology for Fusion Reactors, CONF-750989-P1, March 1976, pp. I-106-121.

24. A. F. Bartlett J. H. Evans, B. L. Eyre, et al. "High Temperature Irradiation Damage Structures in Fast Reactor Irradiated Niobium and Vanadium Alloys," in Radiation Effects and Tritium Technology for Fusion Reactors, CONF-750989-P1, March 1976, pp. I-122-129.

25. F. W. Wiffen, "The Microstructure and Swelling of Neutron Irradiated Tantalum," J. Nucl. Mater. 67, pp. 119-130 (1977).

26. J. F. Bates and A. L. Pitner, "Dimensional Stability of Tantalum Control Rods in LMFBRS," Nucl. Technol. 16, pp. 406-409 (1972).

27. R. A. Murgatroyd, I. P. Bell, and J. T. Bland, "Dimensional Stability of Tantalum During Fast Neutron Irradiation," in Properties of Reactor Structure Alloys After Neutron or Particle Irradiation, ASTM, STP 570, American Soc. for Testing and Materials, 1975, pp. 421-432.

28. F. W. Wiffen, "Swelling of Irradiated Tantalum and Tantalum Alloys," Quarterly Prog. Report Irradiation Effects on Reactor Structural Materials, Aug.-Oct. 1972, HEDL-TME-72-144, Dec. 1972.

29. J. L. Brimhall and E. P. Simonen,"Microstructure of Ion Bombarded Single Crystal Molybdenum," in Defects and Defect Clusters in B.C.C Metals and Their Alloys, R. J. Arsenault, Ed., 1973, pp. 321-331.

30. E. P. Simonen and J. L. Brimhall, "The Dependence of Swelling on Void Surface Reaction Rate Constants," in Fundamental Aspects of Radiation Damage in Metals, CONF-751006-P2 II, 1973, pp. 1196-1202.

31. E. R. Bradley and J. L. Brimhall, "The Effect of the Free Surface on Void Formation in Ion Bombarded Molybdenum," in Radiation Effects and Tritium Technology for Fusion Reactors, CONF-750989-P1, March 1976, pp. I-337-351.

32. J. L. Brimhall, L. A. Charlot, and H. E. Kissinger, "Effect of He on the Swelling/Microstructure Produced in Mo by Ion Bombardment," J. Nucl. Mater. 85-86, pp. 731-734 (1979).

33. K. Y. Liou, P. Wilkes, G. L. Kulcinski, et al., "Void Swelling and Phase In Stability in Heavy Ion Irradiated Mo-Zr Alloy," J. Nucl. Mater. 85-86, pp. 735-738 (1979).

34. J. H. Stubbins and J. Moteff, "Swelling Behavior of Mo-0.5Ti and TZM Bombarded with Heavy Ions at Temperatures Between 750 and $1450^{\circ}C$," J. Nucl. Mater. 103-104, pp. 1163-1168 (1981).

35. J. Bentley, B. L. Eyre and M. H. Loretto, "High Temperature Neutron Irradiation Damage in Molybdenum," in Fundamental Aspects of Radiation Damage in Metals, CONF-751006-P2, 1973, pp. 925-931.

36. J. Bentley, B. L. Eyre, and M. H. Loretto, "Suppression of Void Formation in Neutron Irradiated TZM," in Radiation Effects and Tritium Technology for Fusion Reactors, CONF-750989-P1, pp. I-297-322 (1976) .

37. A. G. Pard and K. R. Garr, "Damage Structure in Neutron Irradiated TZM," in Radiation Effects and Tritium Technology for Fusion Reactors, CONF-750989P1, pp. I-312-322, March 1976.

38. J. A. Sprague, F. A. Smidt, Jr., and J. R. Reed, "The Microstructure of Some Refractory Metals and Alloys Following Neutron Irradiation at 650°C," J. Nucl. Mater. 85-86, pp. 739-743 (1979).

39. D. S. Gelles, D. T. Peterson and J. F. Bates, "Void Swelling in Molybdenum Alloy TZM Irradiated to High Fluence," J. Nucl. Mater. 103-104, pp. 1141-1146 (1981).

40. J. Matolich, H. Nahm, and J. Moteff, "Swelling in Neutron Irradiated Tungsten and Tungsten-25 Percent Rhenium," Scripta Met. 8, pp. 837-842 (1974).

41. R. K. Williams, F. W. Wiffen, J. Bentley, et al., "Irradiation Induced Precipitation in Tungsten Based W-Re Alloys," Met. Trans. 14A, pp. 655-666 (1983).

42. F. W. Wiffen, "Proceedings of the Symposium on Refractory Alloy Technology for Space Nuclear Power Applications," Oak Ridge, TN, Aug. 1983, R. H. Cooper, Jr., and E. E. Hoffman, Eds., Jan. 1984, pp. 252-277.

43. C. Cawthorne and E. J. Fulton, "Voids in Irradiated Metals", Nature 216, pp. 575-576 (1967).

44. J. L. Katz and H. Wiedersich, "Nucleation of Voids in Materials Supersaturated with Vacancies and Interstitials," J. Chem. Phys. 55, pp. 1414-1425 (1971).

45. K. C. Russell, "Nucleation of Voids in Irradiated Metals", Acta Met. 19, pp. 753-758 (1971).

46. J. J. Burton, "Effect of Mobile Interstitials on the Nucleation of Voids," Scripta Met. 5, pp. 449-458 (1971).

47. M. R. Hayns, "The Nucleation and Early Growth of Interstitial Dislocation Loops in Irradiated Materials," J. Nucl. Mater. 56, 267-274 (1975).

48. B. O. Hall, "Point Defect Clustering During Irradiation," J. Nucl. Mater. 91, pp. 63-72 (1980).

49. H. Wiedersich, "On the Theory of Void Formation During Irradiation," Rad. Effects 12, pp. 111-125 (1972).

50. A. D. Brailsford and R. Bullough, "The Rate of Swelling Due to Void Growth In Irradiated Metals," J. Nucl. Mater. 44, pp. 121-135 (1972).

51. B. O. Hall, "Helium Partioning Between Voids and Dislocations," J. Nucl. Mater. 117, pp. 89-95 (1983).

52. W. G. Wolfer and M. Ashkin, "Diffusion, Vacancies and Interstitials to Edge Dislocations," J. Appl. Phys. 47, pp. 791-800 (1976).

53. P. T. Heald, "The Preferential Trapping of Interstitials at Dislocations," Phil. Mag. 31, pp. 551-558 (1975).

54 A. D. Brailsford, R. Bullough and M. R. Hayns, "Point Defect Sink Strengths and Voids Swelling," J. Nucl. Mater. 60, pp. 246-256 (1976).

55. R. Bullough, M. R. Hayns, and C. H. Woo, "The Sink Strengths of Dislocation Loops and Their Growth in Irradiated Materials," J. Nucl. Mater. 84, pp. 93-100 (1979).

56. F. A. Nichols, "Bias Factors for Use in Reaction-Rate-Theory Analysis of Void Swelling and Radiation Creep," Rad. Effects 39, pp. 169-175 (1978).

57. F. A. Nichols, "Bias Factors for Radiation Creep, Growth and Swelling," J. Nucl. Mater. 90, pp. 29-43 (1980).

58. M. E. Downey and B. L. Eyre, "Neutron Irradiation Damage in Molybdenum," Phil. Mag. 11, pp. 53-80 (1965).

59. B. L. Eyre, D. M. Maher, and A. F. Bartlett, "Neutron Irradiation Damage in Molybdenum," Phil. Mag. 23, pp. 439-465 (1971).

60. K. Shiraishi, K. Fukaya, and Y. Katano, "Radiation and Anneal Hardening in Neutron-Irradiated Vanadium," J. Nucl. Mater. 54, pp. 275-285 (1974).

61. J. Narayan and S. M. Ohr, "The Characteristics of 15 MeV and Fission Neutron Damage in Niobium," J. Nucl. Mater. 63, pp. 454-459 (1976).

62. E. A. Little and B. L. Eyre, "The Geometry of Dislocation Loops Generated in Alpha-Iron by 1-MeV Electron Irradiation at 550°C, "J. Microscopy 97, pp. 107-111 (1973).

63. E. A. Little, R. Bullough, and M. H. Wood, "On the Swelling Resistance of Ferritic Steels," Proc Royal Soc. London A 372, pp. 565-579 (1980).

64. B. L. Eyre and R. Bullough, "On the Formation of Interstitial Loops in BCC Metals," Phil. Mag. 8 12, pp. 31-39 (1965).

65. R. Bullough and R. C. Perrin, "The Morphology of Interstitial Aggregates in Iron," Proc. Roy. Soc. London A 305 pp. 541-552 (1968).

66. E. A. Little and D. A. Snow, "Void Swelling in Irons and Ferritic Steels -II An Experimental Survey of Materials Irradiated in a Fast Reactor," Nucl. Mater. 87, pp. 25-39 (1979).

67. D. J. Bacon and A. G. Crocker, "The Elastic Energies of Dislocation Loops," in Lattice Defects in Quenched Metals, R. M. J. Cotterill, M. Koyama, J. J. Jackson, and M. Meshii, Eds., Academic Press, New York, 1965, pp. 667-678.

68. K. C. Russell, "Thermodynamics of Gas Containing Voids in Metals," Acta Met. 20, pp. 899-907 (1972).

69. J. L. Katz and H. Wiedersich, "Effect of Insoluble Gas Molecules on Nucleation of Voids in Materials Supersaturated with Both Vacancies and Interstitials," J. Nucl. Mater. 45, pp. 41-45 (1973).

70. J. A. Spitznagel, S. Wood, and N. J. Doyle, et al., "Helium Partioning to Extended Defects in Dual Ion Bombarded 304 and 316 SS," J. Nucl. Mater. 103-104, pp. 1463-1468 (1981).

71. B. O. Hall, "Trap Theory of Helium Partioning at Low Doses," J. Nucl. Mater. 103-104, pp. 1391-1396 (1981).

72. P. R. Okamoto, N. Q. Lam, and H. Wiedersich, "Effects of Defect Trapping and Radiation-Induced Segregation on Void Swelling," in Proc. of Workshop on Correlation of Neutron and Charged-Particle Damage, CONF-760673, pp. 111-146 (1973).

73. H. Wiedersich, P. R. Okamoto, and N. Q. Lam, "Solute Segregation During Irradiation," in Radiation Effects in Breeder Reactor Structural Materials, M. L. Bleiberg and J. W. Bennett, Eds.,The Metallurgical Society of AIME, pp. 801 (1977).

74. B. O. Hall and D. I. Potter, "Microstructural Development During Low Dose Irradiation," in Effects of Radiation on Structural Materials, ASTM-STP-683, J. A. Sprague and D. Kramer, Eds. pp. 32-45 (1978)

75. A. C. Hindmarsh, "GEAR: Ordinary Differential Equation System Solver," UCID-3001 (Rev. 3), December 1974.

76. C. Kittell, Introduction to Solid State Physics, 3rd Ed., Wiley, London, p. 29 (1968).

77. J. P. Hirth and J. Lothe, Theory of Dislocations, McGraw Hill, New York, p. 762 (1968).

78. R. W. Balluffi, "Vacancy Defect Mobilities and Binding Energies Obtained from Annealing Studies," J. Nucl. Mater. 69-70, pp. 240-263 (1978).

79. N. L. Peterson, "Self Diffusion in Pure Metals," J. Nucl. Mater. 69-70, pp. 3-37 (1978).

80. F. W. Young, Jr., "Interstitial Mobility and Interactions," J. Nucl. Mater. 69-70, pp. 310-330 (1978).

81. D. J. Reed, "A Review of Recent Theoretical Developments in the Understanding of the Migration of Helium in Metals and Its Interaction with Lattice Defects," Rad. Effects 31, pp. 129-147 (1977).

82. M. H. Yoo and J. O. Stiegler, "Growth Kinetics and Preference Factor of Frank Loops in Nickel During Electron Irradiation," Phil. Mag. 36, pp. 1305-1315 (1977).

83. R. Bullough, B. L. Eyre, and R. C. Perrin, "The Growth and Stability of Voids in Irradiated Metals," Nucl. Applic. Technol. 9, pp. 346-355, (1970).

84. W. G. Wolfer, "Correlation of Radiation Creep Theory With Experimental Evidence," J. Nucl. Mater. 90, pp. 175-192 (1979).

85. J. T. Buswell and S. B. Fisher, "Interstitial Loop Growth in Electron Irradiated Vacuum-Remelted FV448," CEGB-RD-B-N-4564, May 1979.

86. ASTM Proposed New Standard Recommended Practice for Neutron Radiation Damage Simulation by Charged Particle Irradiation Part II, Post Irradiation Examination, American Society for Testing and Materials, 1975.

87. J. A. Spitznagel, S. Wood, and W. J. Choyke, "Irradiation Response of Materials," April-June 1980, in Damage Analysis and Fundamental Studies, Quarterly Progress Report, DOE/0046, pp. 103-114, August 1980.

88. J. A. Spitznagel, Westinghouse Research and Development Center, Unpublished Work (1980).

89. J. Greggi, Westinghouse Research and Development Center, Private Communication (1984).

90. B. A. Loomis, A. Taylor, and S. B. Gerber, "Void Swelling of Nb and Nb-1% Zr Induced by $^{58}Ni^{+}$ Bombardment," J. Nucl. Mater. 56, pp. 25-37 (1975).

91. L. L. Horton, "Experimental Determination of the Critical Cavity Radius in Fe-10% Cr For Ion Irradiation," CONF-840848-6, pp. 6-7 (1984).

92. W. G. Wolfer and M. Ashkin, "Stress-Induced Diffusion of Point Defects to Spherical Sinks," J. Appl. Phys. 46, No. 2, p. 547 (1975).

93. W. G. Wolfer and M. Ashkin, "Erratum: Stress-Induced Diffusion of Point Defects to Spherical Sinks," J. Appl. Phys. 46. p. 4108 (1975).

94. L. K.Mansur, "Void Swelling in Metals and Alloys Under Irradiation: An Assessment of the Theory," Nucl. Technol. 40, No. 1, pp. 5-34 (1978).

95. F. Kroupa, "Circular Edge Dislocation Loops," Czech. J. Phys. B10, pp. 284-293 (1960).

96. C. P. Flynn, Point Defects and Diffusion, p. 486, Clarendon Press, Oxford, England (1972).

97. W. G. Wolfer, "Stress-Induced Diffusion of Point Defects to Spherical Sinks," UWFDM-312 (1979).

98. R. Bajaj and M. S. Wechsler, "Defect Clusters in Neutron Irradiated Vanadium Containing Oxygen," Met. Trans. 7A, pp. 351-358 (1976).

99. B. A. Loomis and S. B. Gerber, "Effect of Oxygen Purity on Defect Agglomeration and Hardening of Neutron Irradiated Niobium," Acta Met. 21, pp. 165-172 (1973).

100. J. W. Edington, Practical Electron Microscopy in Material Science, p. 128, Van Nostrand Reinhold Publ. (1976).

101. B. L. Eyre and J. H. Evans, "A Comparison of the High Temperature Damage Structures in Accelerator and Reactor Irradiated Molybdenum," in Effects of Radiation on Substructure and Mechanical Properties of Metals and Alloys, ASTM-STP-529, pp. 184-198, American Soc. for Testing and Materials, Philadelphia, PA (1973).

102. B. L. Eyre, "A Review of the Contribution Made by Microscopy to the Study of Point Defects in BCC Metals," Defects in Refractory Metals, pp. 311-350, Studiecentrum Voor Kernenergie, Centre d'Etude de l'Energie Nucleaire, Mol. (1972).

103. J. D. Meakin and I. G. Greenfield, "Interstitial Loops in Neutron-Irradiated Molybdenum," Philos. Mag. (8), 11, p. 277-290 (1965).

104. J. L. Brimhall, B. Mastel, and T. K. Bierlein, "Thermal Stability of Radiation Produced Defects in Molybdenum," Acta Met. 16, pp. 781-788 (1968).

105. B. L. Eyre and A. F. Bartlett, Unpubished work reported in Reference 102.

106. R. Bajaj, B. O. Hall, G. R. Fenske, and S. A. Shiels, "Proceedings of the 3rd Symposium on Space Nuclear Power Systems," Albuquerque, NM, January 1986.

107. D. Ablitzer, Phil Mag. 35, pp. 1239-1256 (1977).

108. M. Hanson, K. Anderko, "Constitution of Binary Alloys," 2nd Ed., McGraw Hill, NH (1958).

109. B. J. Kestel, Polishing Methods for Metallic and Ceramic Transmission Electron Microscopy Specimens, ANL-80-120, Argonne National Laboratory (1981).

110. B. A. Loomis and S. B. Gerber, "Reduction of Void Volume Fraction in Nb by Ti Alloying," J. of Nucl. Mater., 80, pp. 383-385 (1979).

111. B. A. Loomis, "Comparison of Swelling for Structural Materials on Neutron and Ion Irradiation," J. of Nucl. Mater., 141-143, pp. 690-694 (1986).

112. B. A. Loomis, Private Communication (1988).

13.0 PUBLICATIONS/PRESENTATIONS

The following publications/presentations have resulted from this program:

1. B. O. Hall, "Loop Growth in Body-Centered-Cubic Metals," submitted to Journal of Nuclear Materials for publication. Copy appended in Appendix B.

2. R. Bajaj, B. O. Hall, G. R. Fenske and S. A. Shiels, "Irradiation Swelling in Self-Ion Irradiated Niobium," Proceedings of the 3rd Symposium on Space Nuclear Power Systems, Albuquerque, NM, January 1986. Copy appended in Appendix B.

3. R. Bajaj, B. O. Hall, G. R. Fenske and S. A. Shiels, "Irradiation Swelling in Self-Ion Irradiated Niobium," presented at the 3rd Symposium on Space Nuclear Power Systems, Albuqueque, NM, January 1986.

4. R. Bajaj, B. O. Hall, G. R. Fenske, and S. A. Shiels, "Swelling in Self-Ion Irradiated Niobium," presented at the Symposium on Refractory Metals and Alloys in Nuclear Reactors, AIME Meeting, New Orleans, LA, February 1986.

5. B. O. Hall, "Conditions for Growth/Shrinkage of Interstitial Loops in Body-Centered-Cubic Metals," presented at the Symposium on Refractory Metals and Alloys in Nuclear Reactors, AIME Meeting, New Orleans, LA, February 1986.

14.0 ACKNOWLEGMENTS

The performance of this work involved the efforts of many people at ANL, PNL, and Westinghouse. The following people are gratefully acknowledged for their sincere efforts and cooperation.

Argonne National Laboratory

Jack Wallace and Pete Baldo for their efforts in constructing, testing, and operation of the SNICS source, operation of the Tandem accelerator, and their guidance and assistance in setting up and aligning the beam lines and target chamber.

Pete Billquist and Don Westlake developed, fabricated, and tested the Nb-hydride target for the SNICS source which resulted in approximately three orders of magnitude increase in the niobium ion current. Without this breakthrough, the Nb irradiations would not have been possible.

Bob Ercek is credited for setting up the electron beam heater which permitted heating of individual samples from 600° to 2000° while nearby samples remained unaffected.

Ed Johanson designed and constructed the equipment used to control the target rocking during each irradiation. Jim Emerson is thanked for his effort in the construction, alignment, and vacuum leak checking of beam lines and accelerators.

We are indebted to Ray Kentra for his timely effort in fabricating components for the SNICS source, Tandem and 300 kV accelerators, beam lines, and target chambers.

Ben Loomis and Stu Gerber are thanked for permitting us to utilize their beam line facility, and for their help and guidance in assembling the entire system. Beth Beiersdorf's efforts in performing the Monte Carlo range and energy deposition calculations using the TRIM program and B. Kestal's guidance in post-irradiation specimen preparation are greatly appreciated.

Drs. R. W. Seigel and R. Poeppel are acknowledged for their encouragement and administrative support during all stages of the program.

Battelle Pacific Northwest Laboratory

The staff of Battelle PNL is sincerely thanked for their timely and valuable contribution to the completion of the third phase of the program. Mr. Larry Taburen, Section Chief, kindly arranged for the use of their accelerator. Mark Middendorf and Marvin Lien assisted with the preparation of equipment and operated the accelerator during the holiday weekend. Drs. Ed Simonen and John Brimhall of Materials Sciences are thanked for permitting the use of their irradiation chamber equipment.

Westinghouse

The efforts of Janet Lauer, Wes Hughes, and Jim Haugh in ion milling of specimens, R. Reese for foil thickness measurements, Sam Laciak and Bob Muir for pre-irradiation specimens preparation, are gratefully appreciated. Management support provided by R. W. Buckman, Jr., S. A. Shiels, M. L. Bleiberg, and S. Wood is appreciated. Without the arduous and dedicated efforts of Nora Haines and Bea Chiappetta in compiling and word processing, this report would not have been completed. Their efforts are sincerely appreciated.

APPENDIX A

LOOPS IN IRRADIATED NIOBIUM

APPENDIX A-1

Loops in a Specimen Irradiated to 0.05 dpa at 1000°C

TABLE A-1: Summary of Loop Contrasts Under Various Diffraction Conditions and Loop Characteristics for a Specimen Irradiated to 0.05 dpa at 1000°C

		Contrast												
		1A		2A		3A		1B		2B		3B		
Loop Number	Trace Direction	g=$[0\bar{1}1]$	[g=$01\bar{1}$]	g=$[0\bar{1}1]$	g=$[01\bar{1}]$	g=$[0\bar{1}1]$	g=$[01\bar{1}]$	g=$[0\bar{1}1]$	g=$[01\bar{1}]$	g=$[0\bar{1}1]$	g=$[01\bar{1}]$	g=$[0\bar{1}1]$	g=$[01\bar{1}]$	Loop Character
1	$[\bar{2}00]$	0	I	0	I	0	I	-	-	I	0	-	-	Interstitial
2	U	0	I	I	0	I	0	-	-	I	0	I	0	Interstitial
3	U	I	0	I	0	I	0	I	0	I	0	I	0	Interstitial
4	U	I	0	I	0	I	0	0	I	0	I	0	I	Interstitial
5	U	I	0	I	0	I	0	I	0	0	I	I	0	Vacancy
6	$[\bar{2}00]$	0	I	0	I	I	0	0	I	0	I	0	I	Interstitial
7	$[\bar{2}\bar{1}1]$	0	I	0	I	0	I	0	I	0	I	0	I	Interstitial
8	U	-	-	0	I	0	I	0	I	I	0	I	0	Vacancy
9	$[\bar{2}\bar{1}1]$	I	0	I	0	I	0	I	0	I	0	0	I	Interstitial
10	$[\bar{2}\bar{1}1]$	I	0	I	0	I	0	I	0	I	0	I	0	Interstitial
11	V	I	0	I	0	I	0	0	I	0	I	0	I	Interstitial

I: Inside Contrast
0: Outside Contrast
1A: Zone Axis ~[011] on [111] Side
2A: Zone Axis near [122]
3A: Zone Axis near [111]

1B: Zone Axis near [011] on $[\bar{1}11]$ side

2B: Zone Axis near $[\bar{1}22]$

3B: Zone Axis near $[\bar{1}11]$
U: Traces of these loops were bet . $[\bar{2}00]$ and $[\bar{2}\bar{1}1]$ directions.

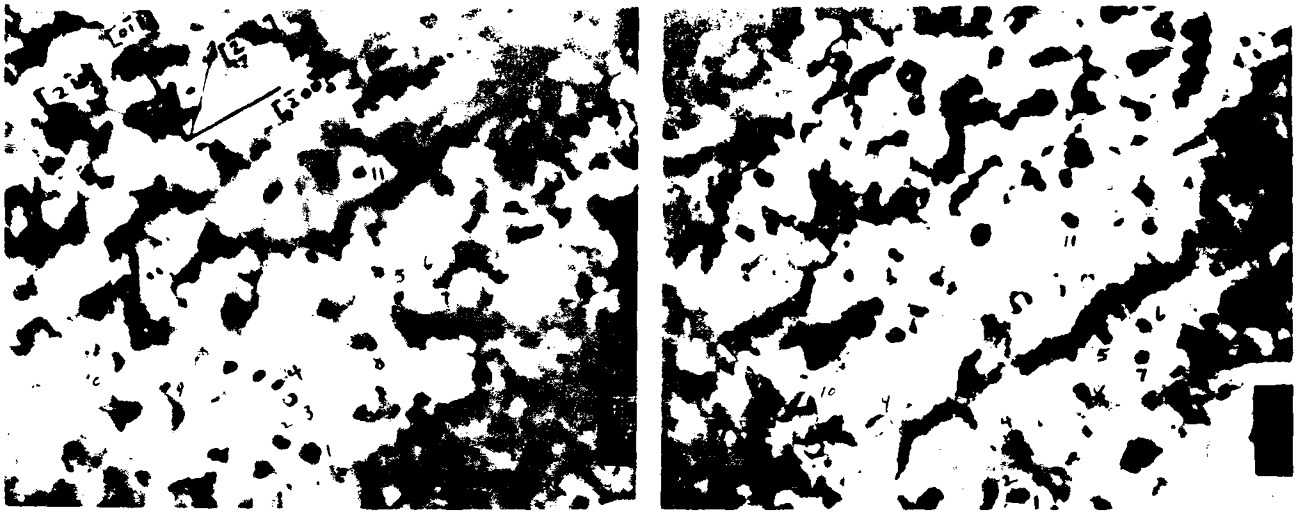

$[01\bar{1}]$

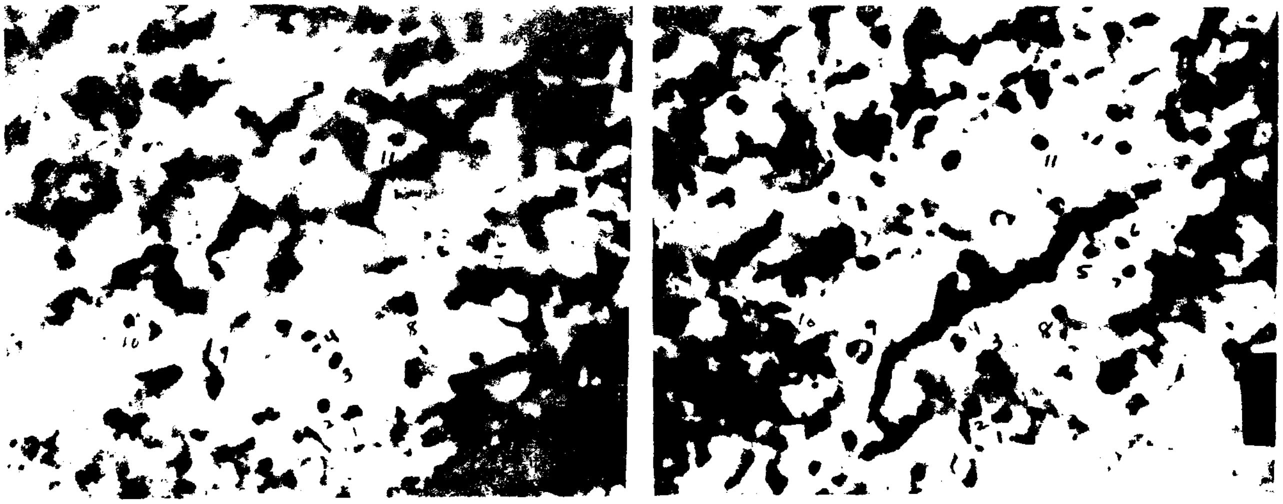

$g = [0\bar{1}1]$ 2A $g = [01\bar{1}]$

Figure · Loops in Various Diffraction Conditions in Niobium Irradiated to 0.05 dpa at 1000°C. (a) 1A = Z [011] on [111] side, (b) 2A = Z near [122].

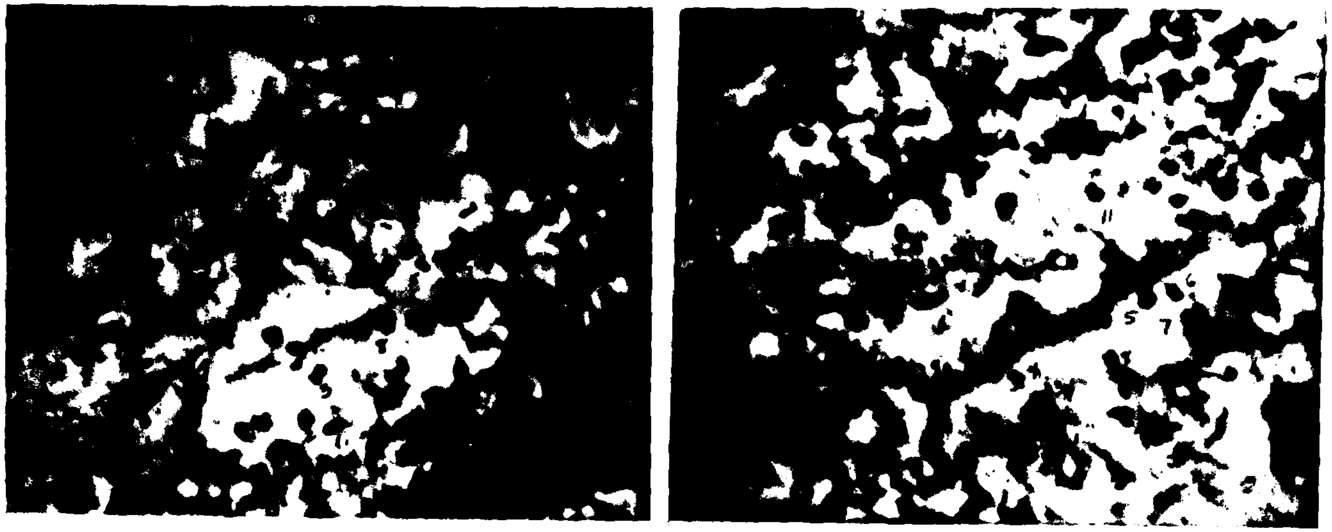

(c)

g = [0$\bar{1}$1] 3A g = [01$\bar{1}$]

50 nm

Figure A-1 (Cont.). Loops in Various Diffraction Conditions in Niobium Irradiated to 0.05 dpa at 1000°. (c) 3A - Z near [111] Condition.

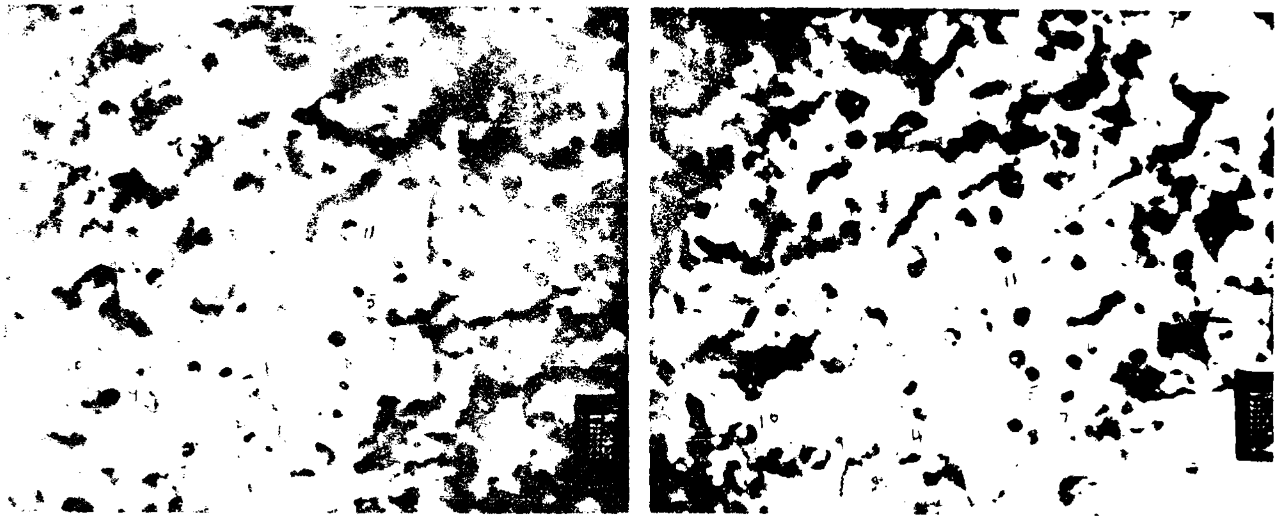
11
5
7
11
10
4
7

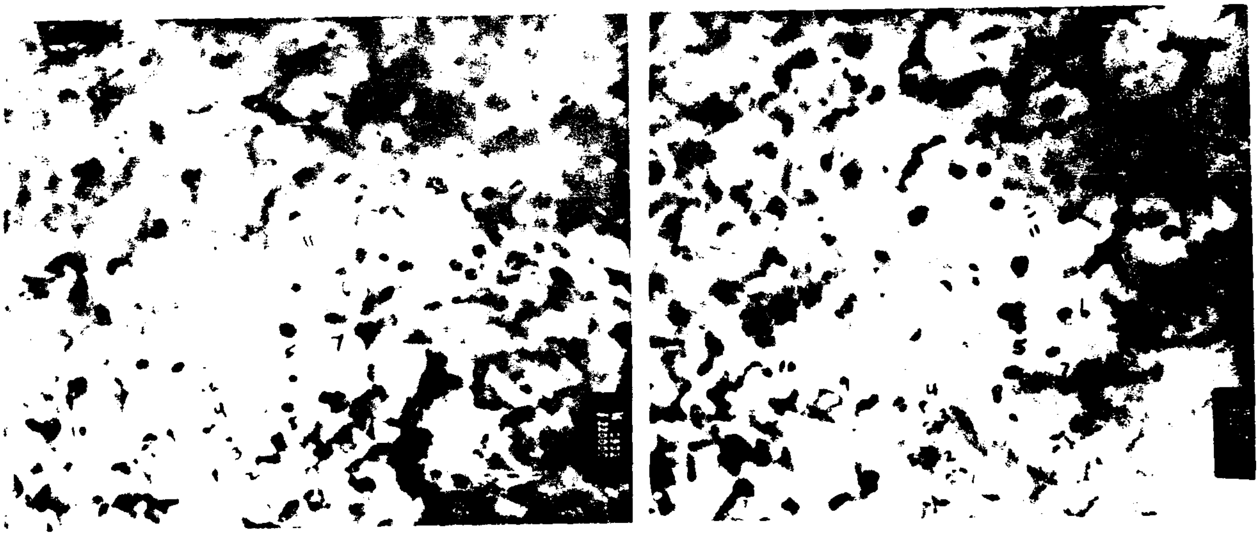
11
7
4
11
6
5
4
2

[illegible]

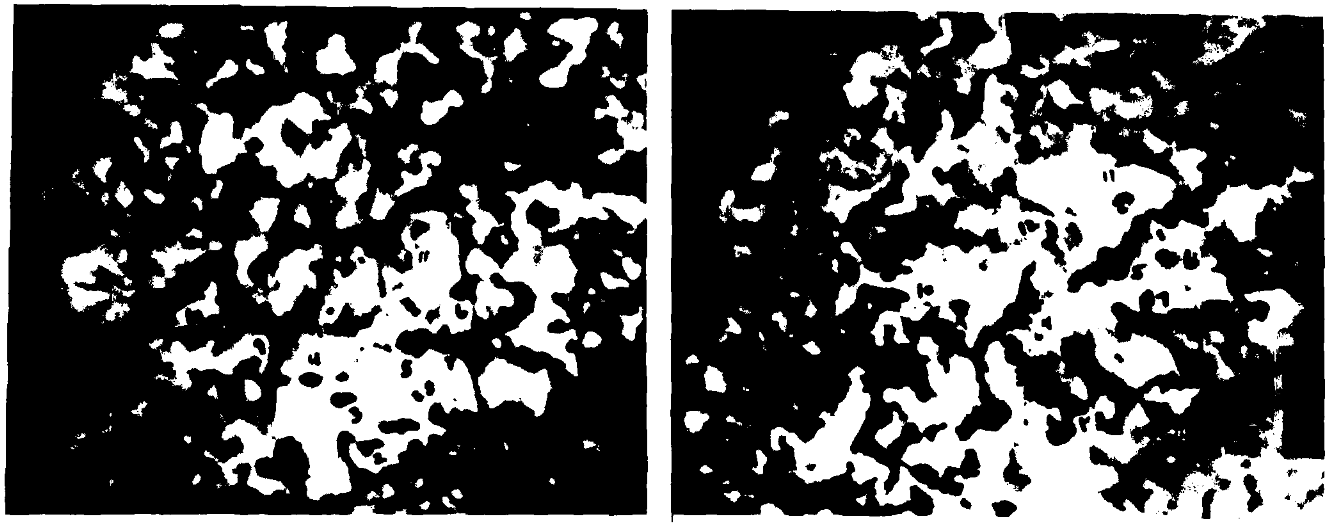

(f)

g = $[0\bar{1}1]$ 3B g = $[01\bar{1}]$

Figure A-1 (Cont.). Loops in Various Diffraction Conditions in Niobium Irradiated to 0.05 dpa at 1000°C. (f) 3B = Z near [$\bar{1}$11] Condition.

APPENDIX A-2

Loops in a Specimen Irradiated to 4.1 dpa at 800°C

TABLE A-2: Summary of Loop Contrasts Under Various Diffraction Conditions and Loop Characteristics for a Specimen Irradiated to 4.1 dpa at 800°C

		Contrast								
		1A		2A		3A		2B		
Loop Number	Trace Direction	g=$[0\bar{1}1]$	[g=$01\bar{1}$]	g=$[0\bar{1}1]$	g=$[01\bar{1}]$	g=$[0\bar{1}1]$	g=$[01\bar{1}]$	g=$[0\bar{1}1]$	g=$[01\bar{1}]$	Loop Character
1	$[\bar{2}1\bar{1}]$	0	I	0	I	0	I	0	I	Interstitial
2	$[\bar{2}1\bar{1}]$	0	I	0	I	0	I	0	I	Interstitial
3	$[\bar{2}1\bar{1}]$	0	I	0	I	0	I	0	I	Vacancy
4	$[\bar{2}\bar{1}1]$	0	I	0	I	I	0	0	I	Interstitial
5	$[\bar{2}\bar{1}1]$	0	I	0	I	0	I	I	0	Vacancy
6	$[\bar{2}\bar{1}1]$	0	I	0	I	0	I	0	I	Interstitial
7	$[\bar{2}1\bar{1}]$	0	I	0	I	0	I	0	I	Vacancy
8	$[\bar{2}\bar{1}1]$	I	0	I	0	0	I	I	0	Interstitial
9	$[\bar{2}\bar{1}1]$	0	I	0	I	0	I	0	I	Interstitial
10	$[\bar{2}\bar{1}1]$	0	I	0	I	0	I			Interstitial

I: Inside Contrast
0: Outside Contrast
1A: Zone Axis ~[011] on [111] Side
2A: Zone Axis near [122]
3A: Zone Axis near [111]

2B: Zone Axis near $[\bar{1}22]$

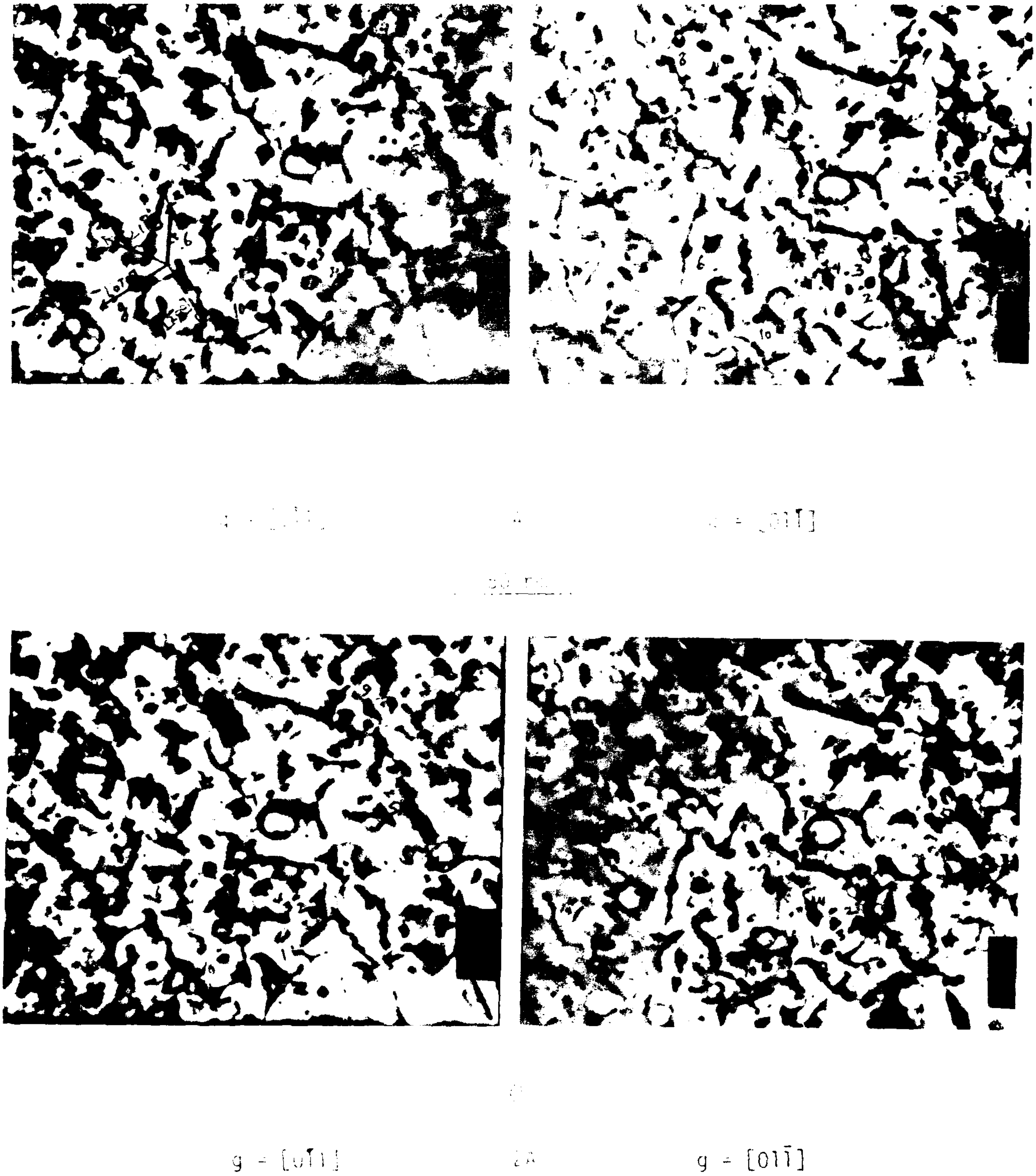

Figure A 2. Loops in Various Diffraction Conditions in Niobium Irradiated to 4.1 dpa at 800°C.

(a) 1A Z=[011] at [111] side; (b) 2A Z near [1̄22].

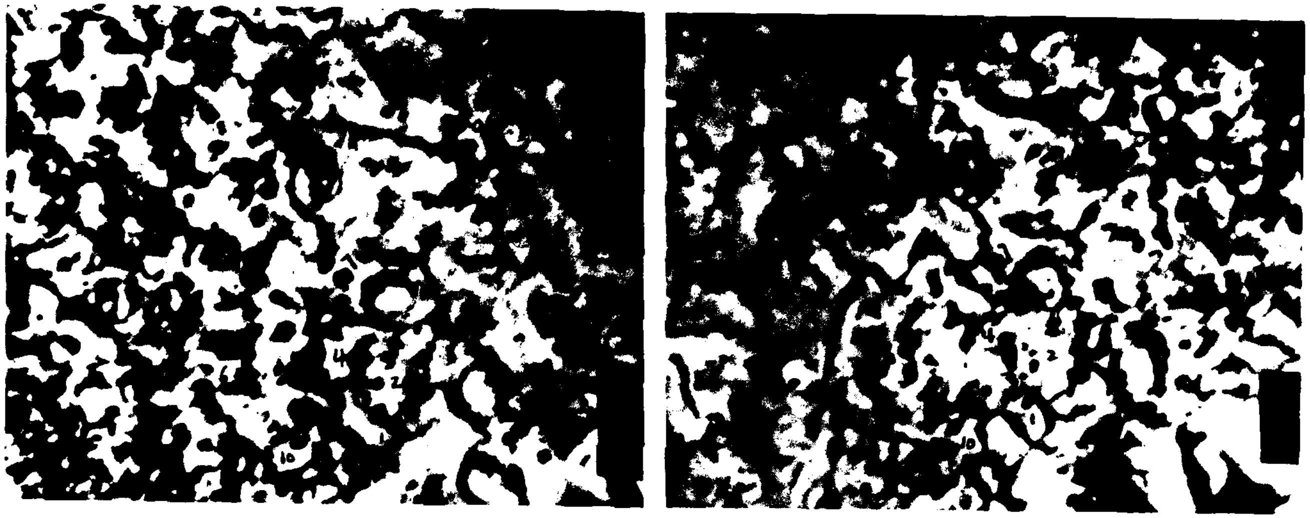

(c)

g = $[0\bar{1}1]$

3A

g = $[01\bar{1}]$

50 nm

Figure A-2 (Cont.). *Loops in Various Diffraction Conditions in Niobium Irradiated to 4.1 dpa at 800°C. (c) 3A = Z near $[\bar{1}11]$ Condition.*

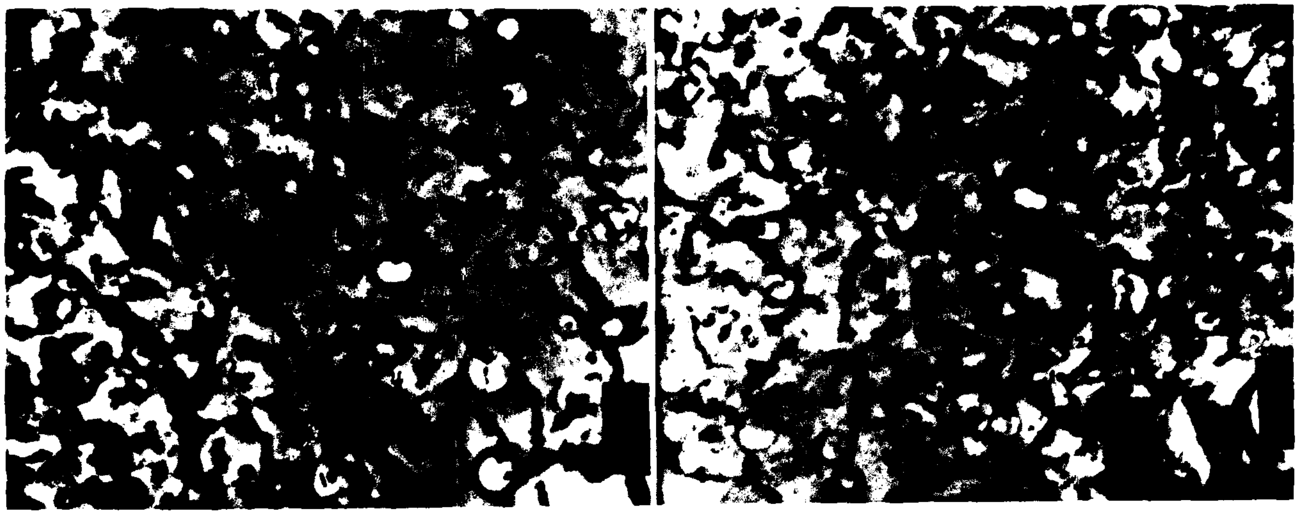

(d)

$g = [0\bar{1}1]$ 2B $g = [01\bar{1}]$

50 nm

Figure A-2 (Cont.). Loops in Various Diffraction Conditions in Niobium Irradiated to 4.1 dpa at 800°C. (d) 2B - Z near [$\bar{1}$22] Condition.

APPENDIX B

PUBLICATIONS

APPENDIX B-1

Irradiation Swelling in Self-Ion Irradiated Niobium

Space Nuclear Power Systems 1986
Edited by M. S. El-Genk and M. D. Hoover
Orbit Book Company, Malabar, FL, 1987

Chapter 29

Irradiation Swelling in Self-Ion Irradiated Niobium

Ram Bajaj and Stuart A. Shiels
Westinghouse Electric Corporation
Advanced Energy Systems Division
P. O. Box 10864
Pittsburgh, PA 15236

Barbara O. Hall
Westinghouse Electric Corporation
Research and Development Center
1310 Beulah Road
Pittsburgh, PA 15235

George R. Fenske
Argonne National Laboratory
9700 South Cass Avenue
Argonne, IL 60439

This paper presents initial results of an investigation of swelling mechanisms in a model body centered cubic (bcc) metal, niobium, irradiated at elevated temperatures (0.3 T_m to 0.6 T_m) where T_m = melting point in K. The objective of this work is to achieve an understanding of the elevated temperature swelling in bcc metals, which are the prime candidate alloys and composite matrix materials for space reactor applications. Niobium was irradiated with 5.3 MeV Nb^{++} ions, at temperatures ranging from 700°C to 1300°C, to a nominal dose of 50 dpa at a dose rate of 6×10^{-3} dpa/s. Swelling was observed over a temperature range of 700°C to 1200°C, with a peak swelling of 7 percent at 900°C. The microstructural data, obtained from transmission electron microscopy, were compared to the predictions of the theoretical model developed during this program. A reasonable agreement was obtained between the experimental measurements of swelling and theoretical predictions by adjusting both the niobium-oxygen binding energy and the incubation dose for swelling to realistic values.

Introduction

Advanced space power systems impose stringent service requirements on structural materials, including elevated temperature performance, high strength to density ratio, rigidity and low vapor pressure. Additional requirements of liquid metal coolant compatibility and neutron irradiation resistance are imposed for nuclear systems. Among the metallic materials, only refractory metal alloys and refractory metal-matrix composites based on niobium, tantalum, molybdenum, and tungsten are considered to approach meeting these requirements.

High accumulated neutron fluences, of the order of 10^{23} n/cm^2 ($E > 0.1$ MeV) at elevated temperatures to 1100°C to 1400°C, are expected in advanced multi-megawatt plants. Thus, the knowledge of neutron induced swelling behavior of these materials is vital to the design and operation of nuclear systems.

Data on the high fluence swelling behavior of refractory metals irradiated to elevated temperatures are not available because these materials were investigated primarily for their applications in fusion reactor first walls which are planned to operate at temperatures below 1000°C. Wiffen (1984) has provided an excellent state of the art review of the data on irradiation effects in refractory metals. The mechanisms of swelling in these materials, however, have not been fully understood. This paper presents the initial results of an investigation of elevated temperature swelling in a refractory metal with the purpose of achieving a better understanding of swelling mechanisms through theory-experiment coupling.

Objective and Approach

The primary purpose of this investigation is to further the understanding of high temperature cavity swelling microstructural response of refractory metals to neutron irradiation. High temperature is defined as being between 0.3 T_m and 0.6 T_m, where T_m = melting temperature in Kelvin. This goal is to be achieved by a close interaction of theory development and controlled experimental studies. The neutron induced swelling is simulated by single and dual ion irradiation with self-ions, and self-ions plus helium, respectively. Simulation techniques were chosen for this work because of their versatility, cost and time effectiveness and ease of control of irradiation variables and because they have been shown to be effective in simulating neutron induced swelling (Bleiberg and Bennett 1977, Bajaj et al. 1982, Wood et al. 1981, Johnston et al. 1976, and Bleiberg et al. 1976). Self-ions were chosen for irradiation to avoid chemical effects introduced by the injected interstitials. At the outset of the investigation, it was necessary to select a model material to fulfill the objectives effectively. The selection was based on three major considerations: (1) theoretical, (2) experimental, and (3) practical (those related to the engineering applications of these materials in space systems). Foremost among the theoretical considerations were the availability of parameters needed for theoretical modeling and the probability of formation of <100> type loops. The experimental factors considered were the availability of a self-ion beam with sufficient ion current in an energy range of 4 MeV to 8 MeV, the depth of penetration of the incoming self-ion, and susceptibility to contamination during irradiation. Application oriented considerations included the service temperature limits, fabrication and the effect of irradiation on ductile-to-brittle transition temperature (DBTT). Based on these factors, niobium was chosen as the material for study.

Theory

The aim of the theoretical portion of this investigation is to develop a model for cavity growth in body-centered cubic (bcc) metals and to calculate growth rates and swelling behavior for refractory metals. The basis for model development is provided by the chemical reaction rate formalism, which has been used extensively for treating nucleation and growth of cavities and dislocation loops in face-centered-cubic metals (Katz and Wiedersich 1971, Russell 1971, Burton 1971, Hayns 1975, Hall 1980, Wiedersich 1972, Brailsford and Bullough 1972, and Hall 1983). Since the model development has been discussed in detail elsewhere (Bajaj et al. 1985), only a brief description is presented here.

In the rate theory approach, fluctuations in the vacancy and interstitial (point defect) concentrations arising from random and inhomogeneous production processes and defect sinks are ignored, and spatially and temporally averaged vacancy and interstitial production and loss rates are assumed. The metal is, in effect, replaced by a continuum in which defects are continuously produced and annihilated at all points. Each point is characterized by averaged properties of the real material (dislocation density, grain boundary area, and solute concentration). Growth of cavities and dislocation loops are described by a set of coupled nonlinear differential equations from which the mean cavity and loop radii can be calculated as a function of time:

$$dr_c/dt = \Omega\,(D_v(C_v - C_{vc}^{th}) - D_iC_i)/r_c \text{ and} \tag{1}$$

$$dr_1/dt = a^2\,(ZD_iC_i - D_v(C_v - C_{cl}^{th}))\ , \tag{2}$$

where r_c is the mean cavity radius, r_1 is the mean loop radius, Ω is the atomic volume, D_v and D_i are the point defect diffusion coefficients, C_v and C_i are the point defect concentrations, C_{vc}^{th} is the thermal vacancy concentration at the surface of the cavity, C_{vl}^{th} is the thermal vacancy concentration at the surface of the loop, a is the lattice constant, and Z is a parameter referred to as the capture efficiency. The capture efficiency is given by the ratio of the actual point defect current to an ideal current, which would result if the sink were a perfect absorber and had no stress field to interact with that of the point defect. Theoretical capture efficiencies for both vacancies and interstitials have been evaluated for a variety of sink types (Bajaj et al. 1985), including loops and cavities. In numerical calculations, however, they are generally treated as parameters. Only the capture efficiency of interstitials at loops is retained (as above in Equation (2)) since the others are close to unity.

The swelling rate S is directly related to the time rate of change dr_c/dt of the mean cavity radius r_c by the equation:

$$S = 4\pi\, N_c r_c^2 dr_c/dt\ , \tag{3}$$

where N_c is the cavity density.

As can been seen from the equations, the rates of change of the radii are proportional to the net flux of point defects to the cavity or loop and depend on the point defect concentrations, their diffusion coefficients, and the capture efficiencies. In the treatment of swelling caused by cavity growth, the vacancy and interstitial concentrations are generally assumed to be in a quasi-steady-state, because the relaxation times for changes in their concentrations are short compared with those required to change the microstructure.

The primary difference between the rate theory model for bcc and that for face-centered-cubic metals is that in the former case equations for both <100> and <111>-type loops is needed.

Since Little et al. (1980) have proposed a mechanism for the swelling resistance of ferritic steels that is based on the differing capture efficiencies of the two types of radiation-induced loops in body-centered-cubic metals, this aspect of microstructural development is being closely examined in the current model development (Hall unpublished results). In this paper, however, the emphasis is on theoretical and experimental swelling results.

Experimental

Experimental Facilities and Procedures

The investigation of high temperature swelling in refractory metals requires a facility capable of providing a high current beam of heavy ions and helium, which can simultaneously bombard a specimen heated to high temperature (up to $0.6T_m$, ~ 1370°C for niobium). Experimental facilities capable of meeting these stringent requirements, as well as with high vacuum capability, high isotopic purity of incoming ions, and diagnostics ability, are limited in number. A survey of existing accelerator facilities was conducted to evaluate the best facility for this work, and we concluded that the HVEM-Tandem facility at Argonne National Laboratory (ANL) satisfied the program requirements. ANL was therefore selected for the performance of irradiations. Briefly, the facility, located in the Materials Science and Technology Division at ANL, consists of a National Electrostatics 2-MV Tandem Type Universal Ion Accelerator, and a Texas Nuclear 300-kV Ion Accelerator. Together, the two accelerators provide ion beams of essentially all elements with energies from approximately 10 KeV to 8 MeV. The specimen heating is accomplished by an electron beam heater designed by ANL.

The heavy ions were provided by a ANL modified NEC/University of Wisconsin SNICS (Source of Negative Ions through Cesium Sputtering) source with a metallic niobium target. The source yielded an ion current of ~ 40 nA, which is too low to perform high fluence (~ 60 displacements per atom (dpa)) irradiations in a reasonable amount of time. Therefore, a novel approach was required to achieve higher ion output. After considerable effort, a procedure analogous to that used for production of titanium ions proved successful in achieving high ion currents of niobium. This procedure requires a hydride target material. A special hydriding method was developed at ANL to obtain NbH. The process involves heating the niobium sample to high temperature under vacuum, and backfilling the vacuum chamber with high purity hydrogen at room temperature to absorb the hydrogen and form a NbH compound. The output of the SNICS source increased from about 40 nA of Nb^- with a metallic source to about 5 to 10 μA of niobium ions Nb^{++} with a a hydrided target.

The energy deposition profile for niobium was calculated using Biersack's TRIM Monte Carlo program. The maximum energy deposition for 5.3 MeV Nb^{++} ions was computed to occur at a depth of ~ 900 nm. The calculated dpa values have an accuracy of $\pm 10\%$. In calculations of dpa, a threshold displacement energy of 40 eV and an atomic density of 5.6×10^{22} atoms/cm^3 was assumed for niobium.

Niobium specimens used in this investigation were high-purity (Marz-grade) foil, 0.5 mm thick, obtained from the Materials Research Corporation. The foil was received in an annealed condition (1150°C to 200°C for 0.5 h). Chemical analysis conducted of interstitial elements showed C and O contents of 33 and 120 wppm, respectively.

The preparation of specimens for ion irradiation is a delicate and painstaking operation, requiring of a number of polishing steps and optical examination to achieve flat, scratch-free surfaces. This process is made more difficult because of the softness of niobium. Details of the mechanical polishing procedures are given by Bajaj et al. (1985). The polished specimens were individually annealed at 1200°C for 0.5 h in the vacuum chamber of the accelerator. This assured that the irradiated surface was in fully annealed condition, devoid of any deformation due to specimen preparation. The irradiations were performed with each specimen mounted in a tantalum holder in an all-metal chamber with a base pressure of 2.5×10^{-9} torr. The vacuum during the irradiation was 2.8×10^{-8} torr. The temperature was controlled and monitored by an infrared pyrometer (IRCON 300 HCS) coupled to the electron beam heater. A 5.3 MeV Nb^{++} ion beam was used to perform the irradiations, which resulted in the peak damage at ~ 0.9 μm below the specimen surface. All specimens except one (700°C) were irradiated to peak damage of ~ 60 dpa corresponding approximately to a fluence of $\sim 1.2 \times 10^{23}$ n/cm^2 ($E > 1.0$ MeV) based on stainless steel correlation. The temperature of irradiation varied from 700°C to 1300°C ($0.35\ T_m$ to $0.57\ T_m$).

The post-irradiation specimen preparation consisted of removing ~ 750 nm from the front surface by ion milling with 800 eV argon followed by back-thinning to performation. This allowed examination of material near the front surface by transmission electron microscopy. The back-thinning was accomplished by polishing in a solution containing NH_4F in methanol at − 30°C.

Transmission electron microscopy (TEM) was used to analyze the microstructure of the irradiated specimens which consisted of voids and dislocation arrays. The voids were imaged in kinematic diffraction conditions in a slightly defocused condition to obtain the true size of the voids. The dislocations were imaged in two beam (dynamic diffraction) conditions. Stereopairs were used to determine the thickness of the foils. Using enlarged micrographs (500,000 X), the diameters of the voids, number densities, average swelling, and dislocation densities were obtained. The voids were assumed to be spherical in shape in calculating the swelling. Because of their relatively large sizes, especially at high irradiation temperatures, voids exposed at the foil surface during electropolishing quickly eroded to larger sizes and more irregular shapes, losing observable contrast. Therefore, a correction factor suggested by Spitznagel et al. (1980) which alleviates the shortcomings of ASTM-recommended correction factors, was used to account for these voids.

Experimental Results

The results from the TEM examination of niobium specimens irradiated from 700°C ($0.35\ T_m$) to 1300°C ($0.57\ T_m$) are presented in Table 1. This table lists the damage level, swelling, void number density, and void size for each of the specimens examined. Additionally, ranges in swelling, void number densities and void sizes are included. These ranges were obtained from the analysis of multiple areas of a specimen.

Figure 1 shows swelling as a function of irradiation temperature. Swelling was observed at temperatures from 700°C to 1200°C. No voids were observed in the specimen irradiated at 1300°C. As seen in Figure 1, the swelling increased from 700°C to 900°C, reached a peak of 7 percent at 900°C, and decreased slowly thereafter with increasing temperature to zero swelling at 1300°C.

The void number density, expressed as voids per cm^3, is plotted as a function of irradiation temperature in Figure 2. The maximum void density was observed at the lowest irradiation temperature of 700°C, where the density was $1 \times 10^{16}\ cm^{-3}$. The void density decreased gradually, to $1 \times 10^{15}\ cm^{-3}$, over a temperature range 700°C to 900°C. From 900°C to 1000°C, the void density decreased rapidly to $5 \times 10^{13}\ cm^{-3}$ and then decreased gradually from 1000°C to 1200°C.

The decrease in void density was accompanied by an increase in the average void size as shown in Figure 3. At 700°C, the average diameter of voids was 10 nm. The void diameter increased to ~45 nm at 900°C and then increased to 110 nm at 1000°C. Thereafter, the diameter increased slowly with increasing temperature. At 1200°C, a large scatter in void diameter was obtained from area to area in the specimen. This scatter is partially attributed to the enlargement of surface voids due to the attack of the electropolishing agent on the large voids shown in Figure 3.

Figure 4 shows a typical photomicrograph of voids in niobium irradiated at 800°C. Dislocations are also shown in the inset in this figure. The dislocations were imaged in a two beam condition, mostly with a diffraction vector $\vec{g} = <110>$.

Micrographs from specimens irradiated at 700°C, 800°C, and 900°C were carefully examined under a stereoscope for void ordering (void lattice formation). No ordering was observed in any of the specimens. Void ordering was also absent in specimens irradiated at higher temperatures.

Table 1. Summary of Swelling Data for Self-Ion Irradiated Niobium.

Irradiation Temperature (°C)	Dose (dpa)	Swelling Range (%)	Swelling Average (%)	Number Density Range (cm^{-3})	Number Density Average (cm^{-3})	Diameter Range (nm)	Diameter Average (nm)
700	32 ± 4	0.6–0.8	0.7	$1–1.2 \times 10^{16}$	1.1×10^{16}	10.5–10.8	10.7
800	54 ± 9	2.3–2.9	2.6	$4.1–6.9 \times 10^{15}$	5.9×10^{15}	19.3–22.5	20.7
900	50 ± 9	2.8–7.9	7.0	$1–1.8 \times 10^{15}$	1.4×10^{15}	44.1–49.9	47.0
1000	57 ± 10	3.6–4.9	4.3	$4.1–6.3 \times 10^{13}$	5.52×10^{13}	107.5–118.3	115.9
1100	53 ± 9	2.4–3.2	2.7	$2–3.4 \times 10^{13}$	2.8×10^{13}	118.2–135.4	125.5
1200	52 ± 9	1.24–2.74	2.15	$1.9–3.1 \times 10^{13}$	2.75×10^{13}	97.7–140.8	116.5
1300	54 ± 9	—	—	—	—	—	—

Specimen irradiated at incidence angles of 10° and 45° for equal times.

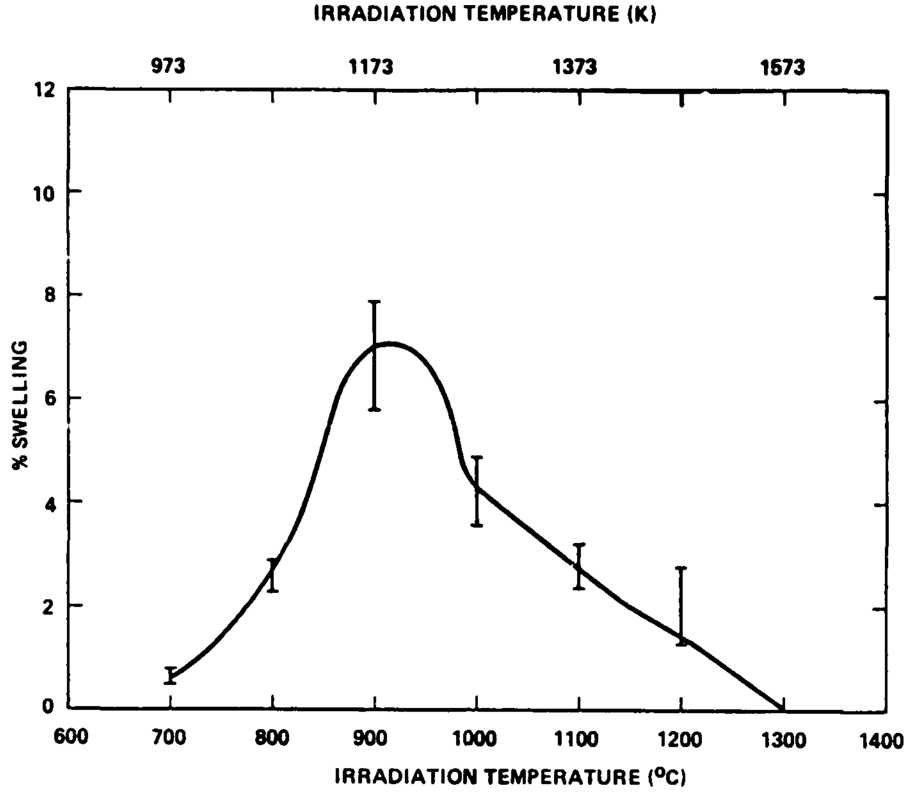

Figure 1 *Swelling as a function of Irradiation Temperature for Self-Ion Irradiated Niobium at Irradiation Exposures near 50 dpa.*

Bajaj et al. (1985) made a comparison of the present data with those reported in literature.

Discussion

Data and Model Calculations

In this section, the experimental results are compared with model calculations in order to test the validity of the theoretical assumptions, to evaluate values of critical model parameters, and to determine areas where experiments that might lead to refinement of the model can be performed.

The results of two sets of calculations are presented. The first set, a determination of the critical cavity size required for growth as a function of temperature, provides an explanation for the high-temperature cutoff observed for swelling. In the second set, calculations of swelling as a function of temperature show that swelling depends strongly on interactions of impurities with point defects and development of the dislocation structure before the onset of swelling.

Critical Size for Cavity Growth

The differential equation that describes the rate of change of the cavity radius with time contains two terms: the rate at which the cavity radius increases due to vacancy absorption, and the rate at which the radius decreases due to interstitial absorption per unit time increment. In order for a cavity to grow, the cavity radius must be greater than the "critical radius" r_c^{crit}, defined here as the radius at which the vacancy and interstitial absorption terms balance, and is given by

$$r_c^{crit} = \frac{kT}{2\,Y\Omega} \ln \frac{(D_vC_v - D_iC_i)^{-1}}{D_vC_{vc}^{th}} \qquad (4)$$

where k is Boltzman's constant, T is temperature, and Y surface energy. The value of the critical radius depends on the sink structure, the bias parameters, dose rate, and temperature. Using the average void densities given in Table 1, and the experimental temperatures and dose rate, the critical radius was calculated as a function of temperature. The results are shown in Figure 5 (curve labeled 0).

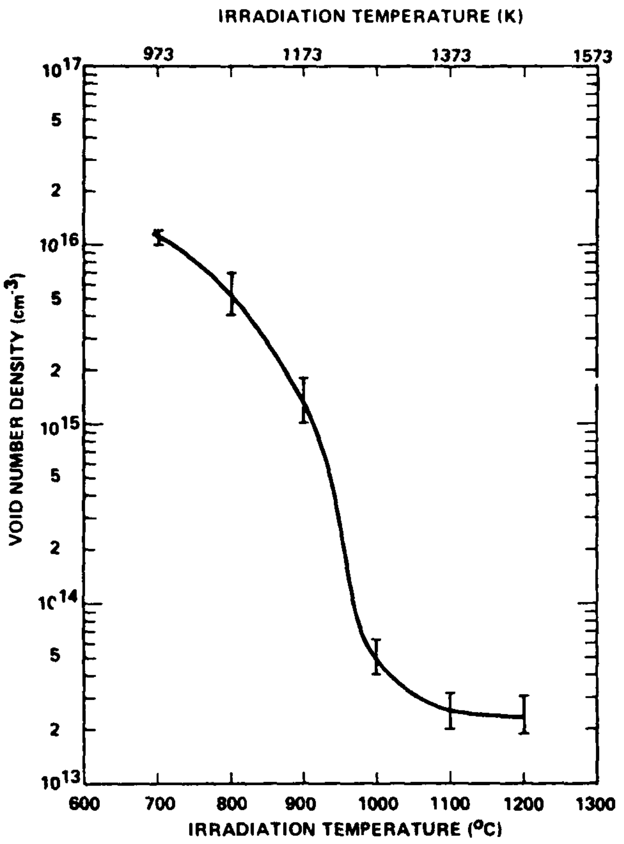

Figure 2 *Void Number Density as a function of Irradiation Temperature for Self-Ion Irradiated Niobium at ~50 dpa.*

Evaluation of the critical radius is important for analysis of the swelling data. First, it establishes the end of the nucleation process for a given set of experimental conditions. Once a cavity has attained this size, we assume it will continue growing at a rate defined by Equation (4). In a practical sense, this means that the value of r_v^{crit} is used as the initial cavity radius when the swelling equation is solved. Second, an estimate of the incubation period for swelling at each temperature can be obtained if the measured swelling values are fit to those calculated using the model equations. The difference between the actual irradiation times and the times at which the model calculations reach the measured values provide these data. Finally, the rapid increase in the critical radius at high temperatures explains the observed absence of cavities and the lack of swelling at 1300°C. No cavity embryo can reach the critical radius at this temperature in the absence of a large quantity of gas acting to stabilize the cavity by reducing thermal emission of vacancies. Therefore, the cavity nucleation rate drops to zero.

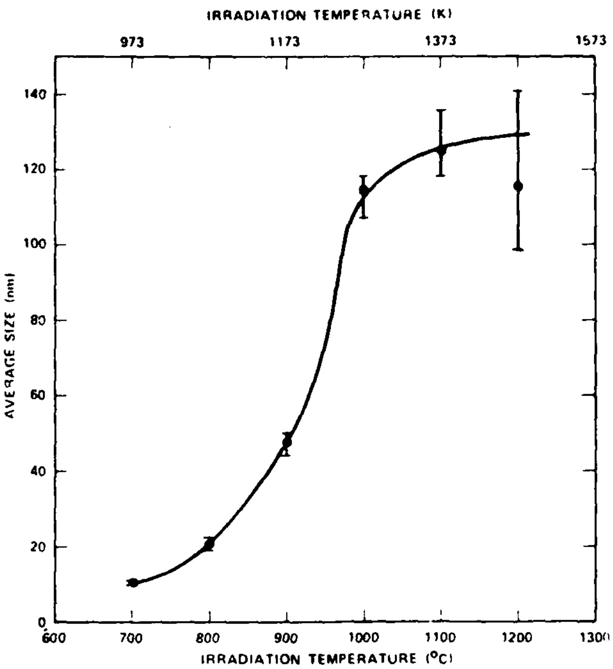

Figure 3 *Average Void Size as a function of Irradiation Temperature for Self-Ion Irradiated Niobium at ~50 dpa.*

Calculated Swelling Curves

Theoretical swelling curves were obtained from the model equations for three different sets of assumption. Each will be discussed to indicate how the analysis developed.

For the first calculation, the experimental dislocation density was taken as the value for the network density with an interstitial bias equal to 1.05. The average cavity density was used for N_c, and loop densities were assumed to be zero. The total swelling time was taken equal to the irradiation time; thus, nucleation is assumed to occur at $t = 0$. The results of this calculation are given in Figure 6 (curve labeled 0). The experimental results are indicated in Figure 6 by the dashed curve, with the measured points and error bars shown. It is apparent that the calculation does not reproduce the data, overpredicting the low temperature results by an order of magnitude, and the high temperature results by roughly a factor of three.

The first modification of the initial assumptions was the inclusion of an incubation time for swelling which is commonly seen in face-centered-cubic metals. At the onset of irradiation, a sequence of events occurs to prepare for the swelling phenomenon. This sequence includes establishment of steady state point defect concentrations, loop nucleation, loop growth,

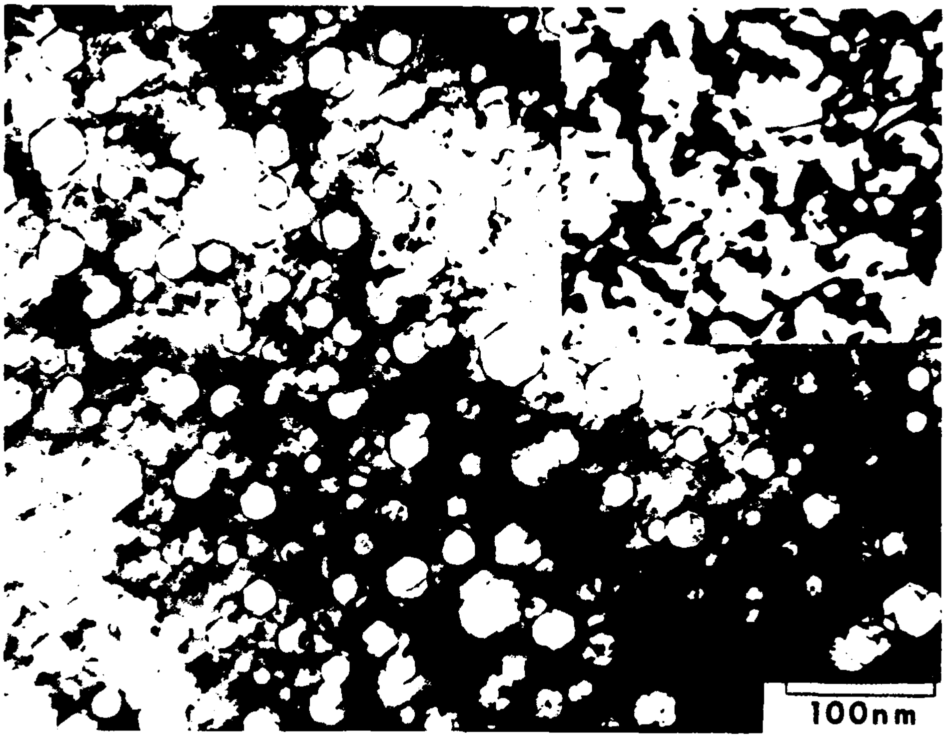

Figure 4 *Voids and Dislocations (inset) in Niobium Irradiated to 50 ± dpa at 800°C. For voids* $\vec{Z}$ ~ *[111], for Dislocations* $\vec{g}$ = *[110],* $\vec{Z}$ ~ *[111].*

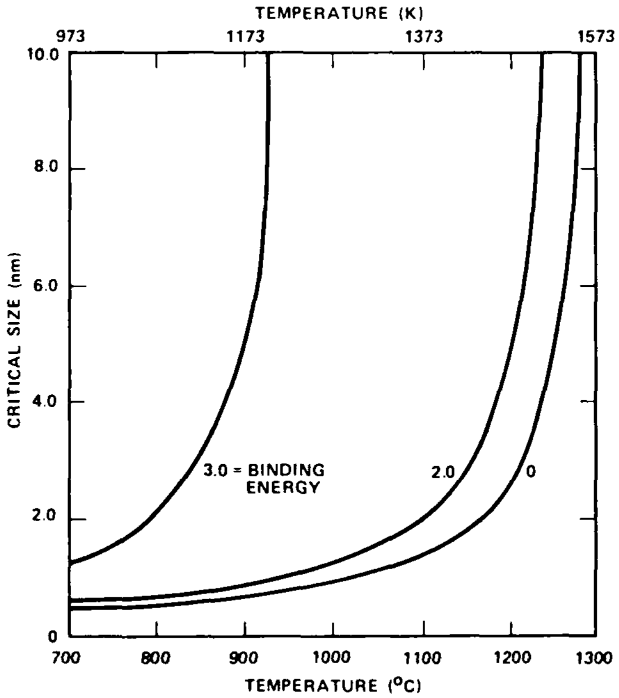

Figure 5 *Critical Radius as a function of Temperature for Three Values of the Interstitial-Oxygen Binding Energy,* E_B*. Curves are labeled by* E_B *in eV.*

and cavity nucleation. Loop growth and dislocation network formation may be completed within the initial transient period, or may extend into the cavity growth regime. Cavity growth is significant only after completion of this sequence. The initial transient period depends on temperature, dose rate, and impurity concentrations. We expect that the same phenomena also occur in bcc metals and, therefore in the present work, we assume that the initial transient period is of the order of 1–10 dpa.

To examine the effect of an incubation period on the calculated swelling, four incubation times, corresponding to doses of 1, 5, 10 and 15 dpa, were assumed, and the calculations redone. The results are shown in Figure 6, where the curves are labeled by the incubation dose. The curves show that inclusion of an incubation period does reduce the calculated swelling, but the reduction is not large enough to produce agreement between the calculations and the data. For example, with an incubation dose of 10 dpa, the calculated swelling is reduced by roughly 25 to 30 percent over the entire temperature range. At this point, two major types of effects remain to be considered within the context of the model as it has been developed to date: those due to the two types of loops and

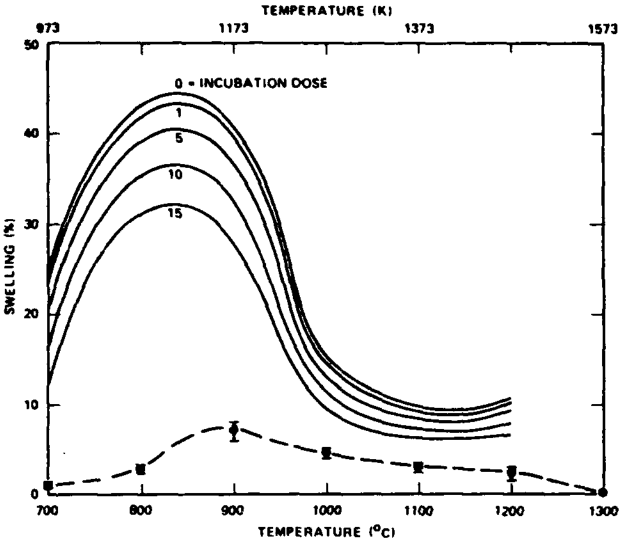

Figure 6 *Calculated Swelling as a function of Temperature. Curves are labeled by the Assumed Value of the Incubation Dose in dpa. Experimental Data are given by the Dashed Curve.*

their differing biases for interstitials, and those due to impurities. At the doses examined, it is apparent from the micrographs that the dislocation structure has evolved into the stage where the network dominates the microstructure, and data on loop types, densities, and sizes cannot be obtained. Calculation of the impact of loop properties on swelling is therefore difficult and will be deferred until low dose data are available. The third set of swelling calculations focused on impurity effects. Trapping of point defects by impurities can have a significant effect on the cavity growth rate and, hence, the swelling rate. Measured oxygen concentrations in the material used in this work are roughly 0.07 at percent. Work by Loomis and Gerber (1981 and 1982) has shown that concentrations of this order are sufficient to affect swelling, leading to a reduction in swelling relative to that in low-oxygen material. If we assume that the mechanism involved is trapping of niobium interstitials by oxygen, the diffusion coefficient D_i appearing in the model equations must be replaced by an effective diffusion coefficient given by Hall and Potter (1978) as:

$$D^+_{i,v} = D_{i,v}/(1 + 4\,\pi\, C_T R_T D_{i,v}(\tau_T - \tau_H)) \qquad (5)$$

where C_T is trap concentration, τ_H is the time spent at a host atom site during the diffusion process, τ_T is the time spent at a trap site, and R_T is the capture radius of the trap. A square-well interaction potential is assumed, with a capture radius equal to a single jump distance. The time τ_T and τ_H are given by:

$$\tau_T^{-1} - \nu_t = \nu_o \exp\left(-(E^m_{i,v} + E_B)/K_T\right) \text{ and} \qquad (6)$$

$$\tau_H^{-1} = \nu_H = \nu_o \exp\left(E^m_{i,v}\, T/K\right) . \qquad (7)$$

Use of Equation (5) introduces the interstitial-oxygen binding energy E_B as a parameter in the model, since its value has not been measured.

Preliminary calculations showed that binding energies of the order of 2 eV are needed to produce calculated swelling curves that correspond to the experimental curves. A series of calculations was made with the binding energy ranging between 1.75 and 2.1 eV. Two incubation doses were used: 0 and 10 dpa. Each experimental point was then used, along with its error bar, to determine the range of E_B values that would produce a fit. Results for all temperatures were obtained for zero incubation dose, and for an incubation dose of 10 dpa. There is some scatter in the results, with an average value of binding energy of 1.995 eV for 0 dpa and 1.943 eV for 10 dpa. These average values were used in the model equations and swelling calculated as a function of temperature, as shown in Figure 7. Triangles indicate an incubation dose of 0 dpa, and circles indicate 10 dpa.

The two combinations of incubation dose and binding energy give approximately the same fit to the data. Significant discrepancies occur at two temperatures, 800°C and 1000°C. At 800°C, the swelling is overpredicted by roughly a factor of two; at 1000°C,

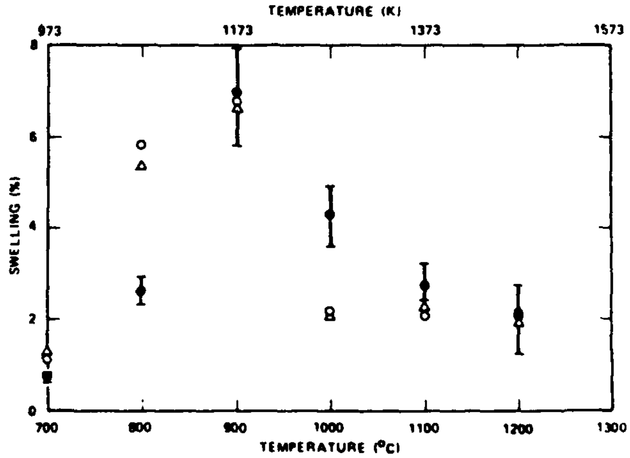

Figure 7 *Calculated Swelling as a function of Temperature for Two Combinations of Incubation Dose and Interstitial-Oxygen Binding Energy: Δ (0 dpa, 1.995 eV); O (10 dpa, 1.943 eV). Experimental Points are shown with Error Bars.*

swelling is underpredicted by the same factor. These discrepancies are not believed to be caused by the presence of grain boundaries.

Whether the values obtained for E_B are reasonable can be tested to a limited extent by observing at the effect of the binding energy on the critical radius. Trapping of interstitials by oxygen reduces the diffusivity of interstitials and changes r_c^{crit} (see Equation (4)). Calculations of r_c^{crit} as a function of temperature were done for a range of assumed binding energies, and r_c^{crit} increases as binding energy increases for a fixed temperature. Values of r_c^{crit} are plotted in Figure 5 as a function of temperature for binding energies of 2 eV and 3 eV. As can be seen from the figure, there is a large shift of the high temperature portion of the curve toward lower temperatures as the binding energy increases from 2 eV to 3 eV. The shift when E_B changes from 0 eV to 2 eV is relatively small in comparison. For example, any increase in assumed binding energy that would provide a better fit to the 800°C data point, would result in unacceptably large critical radii at high temperatures. Because cavities are observed at 1200°C, r_c^{crit} must remain relatively small until this temperature is exceeded. For binding energies near 2 eV, r_c^{crit} is 5 nm, a somewhat high value. Therefore, a reduced binding energy is more reasonable than an increased one.

Summary and Conclusions

In this study, a theoretical model based on the chemical reaction rate formalism was developed specifically for body centered cubic metals. Calculations were performed for a selected metal; that is, niobium. A special source preparation method was developed to produce a niobium hydride target material. The use of this target in the ion source resulted in an output of niobium ions of sufficient energy and flux to permit, for the first time, ion bombardment studies of niobium with self-ions. The experimental results showed:

1. A peak swelling of 7 percent was obtained at 900°C in niobium (0.07 at percent oxygen) irradiation with 5.3 MeV Nb^{++} ions at a nominal dose of 50 dpa and a dose rate of 6×10^{-3} dpa/s, and
2. Swelling occurred over a temperature range of 700°C to 1200°C. (Swelling was not observed at 1300°C.)

A comparison of model calculations with the experimental results showed a reasonable agreement between the calculated and experimental swelling values when trapping of interstitials by oxygen was included. An interstitial-oxygen binding energy of approximately 2 eV provided the best fit to the data.

Acknowledgments

This work is the result of efforts of a great many people at ANL and Westinghouse. Noteworthy amongst them are Jack Wallace, Pete Baldo, Bob Erek, Ed Johanson, Jim Emerson, Roy Kentra, Ben Loomis, Beth Beiversdorf, and Bernei Kestel of ANL, and Janet Lauer, Wesley Hughes, Jim Haugh, Bob Reese, Sam Laciak, Bob Muir, and Jim Greggi of Westinghouse. Management support provided by R. W. Buckman, M. L. Bleiberg, and S. Wood is appreciated. This work was sponsored by the U.S. Air Force Office of Scientific Research under Contract No. F49620-83-C-0120.

References

Bajaj, R., B. O. Hall, and G. R. Fenske (1985) *An Investigation of the Irradiation Swelling Mechanisms in Refractory Metals at High Temperatures*, WAESD-TR-85-005, Westinghouse Electric Corporation, Pittsburgh, PA.

Bajaj, R., S. Diamond, and M. L. Bleiberg (1982) "Optimization of Precipitation Hardened Fe-Cr-Ni Alloys Using Nickel Ion Bombardment Simulation Studies," in *Effects of Radiation on Materials, Eleventh Conference*, ASTM-STP-782, pp. 856–884, H. R. Brager and J. S. Perrin, eds., American Society for Testing and Materials.

Bleiberg, M. L., R. Bajaj, I. M. Baron, et al. (1976) "Swelling and Gamma-Gamma-Prime Particle Stability of Ion-Bombarded Iron-Chromium Nickel Alloys," in *Irradiation Effects on the Microstructure and Properties of Metal*, ASTM-STP-611, pp. 315–336, American Society for Testing and Materials.

Bleiberg, M. L. and J. W. Bennett, eds. (1977) *Proceedings of International Conference on the Radiation Effects in Breeder Reactor Structural Materials*, Metallurgical Society of AIME, held in Scottsdale, AZ.

Brailsford, A. D. and R. Bullough (1972) "The Rate of Swelling Due to Void Growth in Irradiated Metals," *J. Nucl. Mater.*, 44: 121–135.

Burton, J. J. (1971) "Effect of Mobile Interstitials on the Nucleation of Voids," *Scripta Met.*, 5: 449–458.

Hall, B. O. (1986) "Conditions for Interstitial Loop Growth/Shrinkage in Body-Centered Cubic Metals," submitted for publication in the Journal of Nuclear Metals.

Hall, B. O. (1983) "Helium Partitioning Between Voids and Dislocations," *J. Nucl. Mater.*, 117: 89–95.

Hall, B. O. (1980) "Point Defect Clustering During Irradiation," *J. Nucl. Mater.*, 91: 63–72.

Hall, B. O. and D. I. Potter (1978) "Microstructural Development During Low Dose Irradiation," in *Effects of Radiation on Structural Materials*, ASTM-STP-683, pp. 32–45, J. A. Sprague and D. Kramer, eds.

Hayns, M. R. (1975) "The Nucleation and Early Growth of Interstitial Dislocation Loops in Irradiated Materials," *J. Nucl. Mater.*, 56: 267–274.

Johnston, W. G., T. Lauritzen, J. H. Rosolowski, et al. (1976) "The Effect of Metallurgical Variables on Void Swelling," in *Radiation Damage in Metals*, pp. 227–266, N. L. Patterson and S. D. Harkness, eds., ASM, Metals Park, OH.

Katz, J. L. and H. Wiedersich (1971) "Nucleation of Voids in Materials Supersaturated with Vacancies and Interstitials," *J. Chem. Phys.*, 55: 1414–1425.

Little, E. A., R. Bullough, and M. H. Wood (1980) "On the Swelling Resistance of Ferritic Steels." in *Proceedings Royal Soc. London A*, 372: 565–579.

Loomis, B. A. and S. B. Gerber (1981) "Similar Dependence on Dilute O Concentration of Void Formation in Ion-Irradiated Nb and Some Properties of Unirradiated Nb," *J. Nucl. Mater.*, 97: 113–125.

Loomis, B. A. and S. B. Gerber (1982) "Swelling of ^{58}Ni^{+} and ^{3}He^{+} Ion-Irradiated Nb and Nb Alloys," *J. Nucl. Mater.*, 103 & 104: 1193–1197.

Russell, K. C. (1971) "Nucleation of Voids in Irradiated Metals," *Acta Met.*, 19: 753–758.

Spitznagel, J. A., S. Wood, and W. J. Choyke (1980) "Irradiation Response of Materials," in *Damage Analysis and Fundamental Studies, Quarterly Progress Report, April-June 1980*, pp. 103–114, DOE/0046, U. S. Department of Energy, Washington, D.C.

Wiedersich, H. (1972) "On the Theory of Void Formation During Irradiation," *Rad. Effects*, 12: 111–125.

Wiffen, F. W. (1984) "Effects of Irradiation on Properties of Refractory Alloys with Emphasis on Space Power Reactor Applications," in *Proceedings of the Symposium on Refractory Alloy Technology for Space Nuclear Power Applications Conference*, R. H. Cooper, Jr. and E. E. Hoffman, eds., held in Oak Ridge, TN, August 1983.

Wood, S., J. A. Spitznagel, and W. J. Choyke (1981) "Microstructural Development in Dual-Ion Bombarded 316 Stainless Steel," in *Effects of Radiation on Materials: Tenth Conference*, ASTM-STP-725, pp. 455–469, David Kramer, H. R. Brager, and J. S. Perrin, eds., American Society for Testing and Materials.

APPENDIX B-2

Conditions for Loop Growth/Shrinkage in Body-Centered-Cubic Metals

CONDITIONS FOR LOOP GROWTH/SHRINKAGE IN BODY-CENTERED-CUBIC METALS*

B. O. Hall+
Westinghouse R&D Center
1310 Beulah Road
Pittsburgh, PA 15235

---

*Research in support of Air Force Office of Scientific Research Contract F49620-83-0120, "An Investigation of the Irradiation Swelling Mechanisms in Refractory Metals at High Temperatures."

+Current address is Aluminum Company of America, Alcoa Technical Center, Alcoa Center, PA 15069.

1. Introduction

One of the features that distinguishes the irradiation-induced microstructure in body-centered-cubic metals from that found in face-centered-cubic metals is the existence of two types of interstitial dislocation loop. The type most frequently found is a perfect loop with $\frac{a}{2}$ <111> Burgers vector and a {111} habit plane. After irradiation at high temperatures, however, perfect loops with a <100> Burgers vectors and {100} habit planes are seen in α-iron (1) and ferritic alloys.(2)

Eyre and Bullough(3) first proposed a mechanism for formation of interstitial loops in the body-centered-cubic lattice. They suggested that <110> split dumbbell interstitials aggregate on {110} planes to form faulted loop nuclei with $\frac{a}{2}$ <110> Burgers vector. Due to a high stacking fault energy, the loops unfault by either of two reactions:

$$\frac{a}{2}[110] + \frac{a}{2}[1\bar{1}0] \rightarrow a\,[100]$$

or

$$\frac{a}{2}[110] + \frac{a}{2}[001] \rightarrow \frac{a}{2}[111]$$

The elastic energy of either product loop is further reduced by a rotation of the habit plane from {100} and {111} respectively. Bullough and Perrin(4) verified this model using a computer simulation of the α-iron lattice and found that $\frac{a}{2}$ <111> loop formulation was energetically favored at all irradiation temperatures. Little, Bullough, and Wood(2) subsequently calculated the relative probability of <100> loop formation at 420°C for a variety of body-centered-cubic metals. Values they obtained ranged from ~5 x 10^{-5} for niobium to ~1 x 10^{-27} for tungsten, with ~6 x 10^{-9} for α-iron.

Because several sinks with positive but differing biases for interstitials exist simultaneously in body-centered-cubic metals during irradiation, microstructural evolution is more complicated than in face-centered-cubic metals. The relative values of the bias or preference factors for network dislocations, <111> loops, and <100> loops affect loop growth rates and cavity nucleation and growth rates. There is substantial evidence that ferritic steels, for example, are much more resistant to swelling than austenitic steels. To explain this, Little, Bullough, and Wood(2) proposed a model, based on the existence of two loop types, that describe microstructural evolution in martensitic steels with high initial dislocation densities. Because the bias of a dislocation loop depends on the magnitude of its Burgers vector, <111> loops and network dislocations appear as relatively neutral when compared with <100> loops. They therefore act as vacancy sinks in the system and absorb excess vacancies, which would otherwise form void nuclei. Eventually, <111>-type dislocations disappear within domains of the material, leaving a distribution of <100> loops. These domains grow until they intersect grain boundaries, which are relatively more neutral sinks.

In their model, the presence of a high initial dislocation density is crucial. It acts to suppress initial void nucleation by enhancing the point defect recombination rate.

In the present work, we examined the conditions required for loop growth/shrinkage in body-centered-cubic metals using the formalism of chemical-reaction-rate theory. The purpose was to determine if the standard growth equations predict <100> loop growth and <111> loop shrinkage in the bias-dominated regime. Results of the analysis indicate that, contrary to the model proposed by Little, Bullough, and Wood, the difference in bias of <100> and <111> loops and a high dislocation density that decreases with time are not sufficient to explain <111> loop shrinkage in body-centered-cubic metals.

This letter is organized as follows. The conditions for loop growth and shrinkage are developed in Section 2 from the growth equations for small loops. The size-dependent bias factors derived by Wolfer and Ashkin(5,6) are incorporated in both growth and sink strength equations. The resultant boundaries of the growth and shrinkage regimes can be expressed in terms of a single materials parameter, the densities of the two loop types and network dislocations, and the loop radii. In Section 3, these boundaries are calculated as a function of the materials parameter for a variety of microstructural conditions with an assumed vacancy bias factor equal to 1. The loop growth equations were solved numerically for a variety of assumed initial conditions. Network dislocations were either constant or decreasing with time according to a modified thermal annealing equation. The results of these calculations are summarized in Section 4. Discussion and conclusions follow in Section 5.

2. Conditions for Loop Growth

In the standard rate-theory formulation,(7-9) the growth rate of small interstitial loops, treated as spherical sinks,(10,11) is described by the differential equation(9)

$$\frac{\partial r_{\ell i}}{\partial t} = \frac{2}{r_{\ell i} b_i} \left[r_I^{\ell i} D_I C_I - r_V^{\ell i} D_V \left(C_V - C_{V\ell i}^{th} \right) \right] \qquad (1)$$

where $r_{\ell i}$ is the mean radius of the loops of type i, b_i is the magnitude of the Burgers vector, $r_I^{\ell i}$ is the effective capture radius of the loop of type ℓi for interstitials, $r_V^{\ell i}$ is the effective capture radius for vacancies, C_V and C_I are fractional point defect concentrations, and $C_{V\ell i}^{th}$ is the thermal vacancy concentration at the loop.

The effective capture radii $r_I^{\ell i}$ and $r_V^{\ell i}$ are$^{(12)}$

$$\begin{aligned} r_{I,V}^{\ell i} &= \bar{r}_{\ell i} \, [(1 + \pi \, \bar{r}_{\ell i}^{\,3} \, N_{\ell i})^{1/2} + (\pi \, \bar{r}_{\ell i} N_{\ell i})^{1/2} \, \bar{r}_{\ell i}]^2 \, (1 + \delta_{I,V}^{\ell i}) \\ &= r_c^{\ell i} \, (1 + \delta_{I,V}^{\ell i}) \end{aligned} \tag{2}$$

where

$$\bar{r}_{\ell i} = \frac{\pi \, (r_{\ell i}^2 - r_d^2)^{1/2}}{\ell n \, (8 r_{\ell i}/r_d)} \tag{3}$$

where $N_{\ell i}$ is the density of loops of type ℓi, and r_d is the dislocation core radius. The preference factors $\delta_I^{\ell i}$ and $\delta_V^{\ell i}$ for interstitials and vacancies, respectively, can be considered either as model parameters$^{(13)}$ or can be calculated using the infinitesimal loop approximation.$^{(5,6)}$

When bias effects dominate, the thermal vacancy emission term in Eq. (1) can be neglected, and the growth rate of an interstitial loop is given by the difference between the first two terms, which represent the two defect fluxes. When a quasi-steady-state condition has been attained, the defect concentrations can be written as

$$C_V = \frac{K_I}{2R} \, [(1 + \frac{4RG}{K_I K_V})^{1/2} - 1] \tag{4}$$

$$C_I = \frac{K_V}{2R}\left[\left(1 + \frac{4RG}{K_I K_V}\right)^{1/2} - 1\right] \qquad (5)$$

where G is the point defect production rate per unit volume, and R is the recombination coefficient. The rate constants K_I and K_V are given by the product of the point defect diffusion coefficient and the total sink strength

$$K_\alpha = D_\alpha S_\alpha \qquad (6)$$

where α is either I or V. Using Eqs. (1) through (6) we obtain the condition that must be met for a positive loop growth rate:

$$\frac{(1 + \delta_I^{\ell i})}{(1 + \delta_V^{\ell i})} > \frac{S_I}{S_V} \qquad (7)$$

Wolfer and Ashkin$^{(5)}$ have evaluated the factors $\delta_I{}^{\ell i}$ and $\delta_V{}^{\ell i}$ for small loops in the infinitesimal loop approximation using a perturbation technique. If one neglects a strain dependent term, which is negligible for small loops ($r_{\ell i} < 100\ b_i$), one obtains

$$\delta_\alpha^{\ell i} = \delta_\alpha \left(\frac{b_i}{r_{\ell i}}\right)^2 \qquad (8)$$

for α equal to I or V. The expression that defines the proportionality constant δ_α in Eq. (8) [see Eq. (16.6) of ref. 5] depends on properties of the material; i.e., the bulk modulus and Poisson's ratio, temperature, and defect properties; i.e., elastic polarizabilities and relaxation volumes, but is independent of loop type for edge loops. Thus, for loops of the same size, the magnitude of the preference factors for loops of <100> type are larger than those for <111> loops, the ratio being $\delta_\alpha^{<100>}/\delta_\alpha^{<111>} \sim (b_{<100>}/b_{<111>})^2 \sim 4/3$.

The model system that we assume for low doses contains three types of sink--network dislocations, <111> loops, and <100> loops. The sink strength S_I for interstitials is given by

$$S_I = LZ_I^n + 4\pi\, r_c^{\ell 1}\, N_{\ell 1}\, (1 + \delta_I^{\ell 1}) + 4\pi\, r_c^{\ell 2}\, N_{\ell 2}\, (1 + \delta_I^{\ell 2}) \tag{9}$$

and that for vacancies by

$$S_V = LZ_V^n + 4\pi\, r_c^{\ell 1}\, N_{\ell 1}\, (1 + \delta_V^{\ell 1}) + 4\pi\, r_c^{\ell 2}\, N_{\ell 2}\, (1 + \delta_V^{\ell 2}) \tag{10}$$

where L is the network density, and Z_I^n and Z_V^n are bias factors for the network. Superscripts n, $\ell 1$, and $\delta 2$ are used respectively for parameters referring to network dislocations, <111> loops, and <100> loops. The preference factors $\delta_V^{\ell i}$ are generally small and will be neglected in the following development. The proportionality constant δ_I is therefore redefined as δ.

The boundary between growth and shrinkage regimes is determined by

$$\frac{S_I}{S_V} = 1 + \delta \left(\frac{b_i}{r_{\ell i}}\right)^2 \tag{11}$$

for i = 1 or 2, and therefore, the condition for shrinkage of <111> loops and growth of <100> loops is

$$1 + \delta \left(\frac{b_1}{r_{\ell 1}}\right)^2 < \frac{S_I}{S_V} < 1 + \delta \left(\frac{b_2}{r_{\ell 2}}\right)^2 \qquad (12)$$

3. Calculations

Sink strength ratios were calculated as a function of the materials parameter δ for network densities L of 10^8 and 10^{12} cm^{-2}, <111> loop densities of 10^{14} and 10^{16} cm^{-3}, and loop radii of 2.5, 10, 25, and 50 (normalized to b_1). Radii of <111> and <100> loops were assumed equal, the vacancy preference factors were assumed to be zero, and the ratio of <100> loop density to <111> loop density was taken as 10^{-5}. Results are plotted in Figs. 1 through 4 for $N_{\ell 1} = 10^{14}$ cm^{-3}. Solid curves are labeled by values of L. The dashed lines define the boundaries of the various regimes: for sink strength ratios to the left of both lines, both types of loop shrink; for those between the lines, <111> loops shrink and <100> loops grow; and for those to the right of both lines, both types of loop grow.

Several trends can be noted in the figures. In the growth/growth regime at higher values of δ in Figs. 1 through 3, S_I/S_V decreases as L increases for constant δ with a limiting value of 1.05, the assumed network bias. In the shrinkage/growth and shrinkage/shrinkage regimes, the situation is reversed with S_I/S_V increasing as L increases. The curves for differing L cross when S_I/S_V equals 1.05; as loop radius increases, the value of δ, defined as δ_c, at which this occurs increases. In Fig. 5, δ_c is plotted as a function of normalized loop radius. A necessary but not sufficient condition for

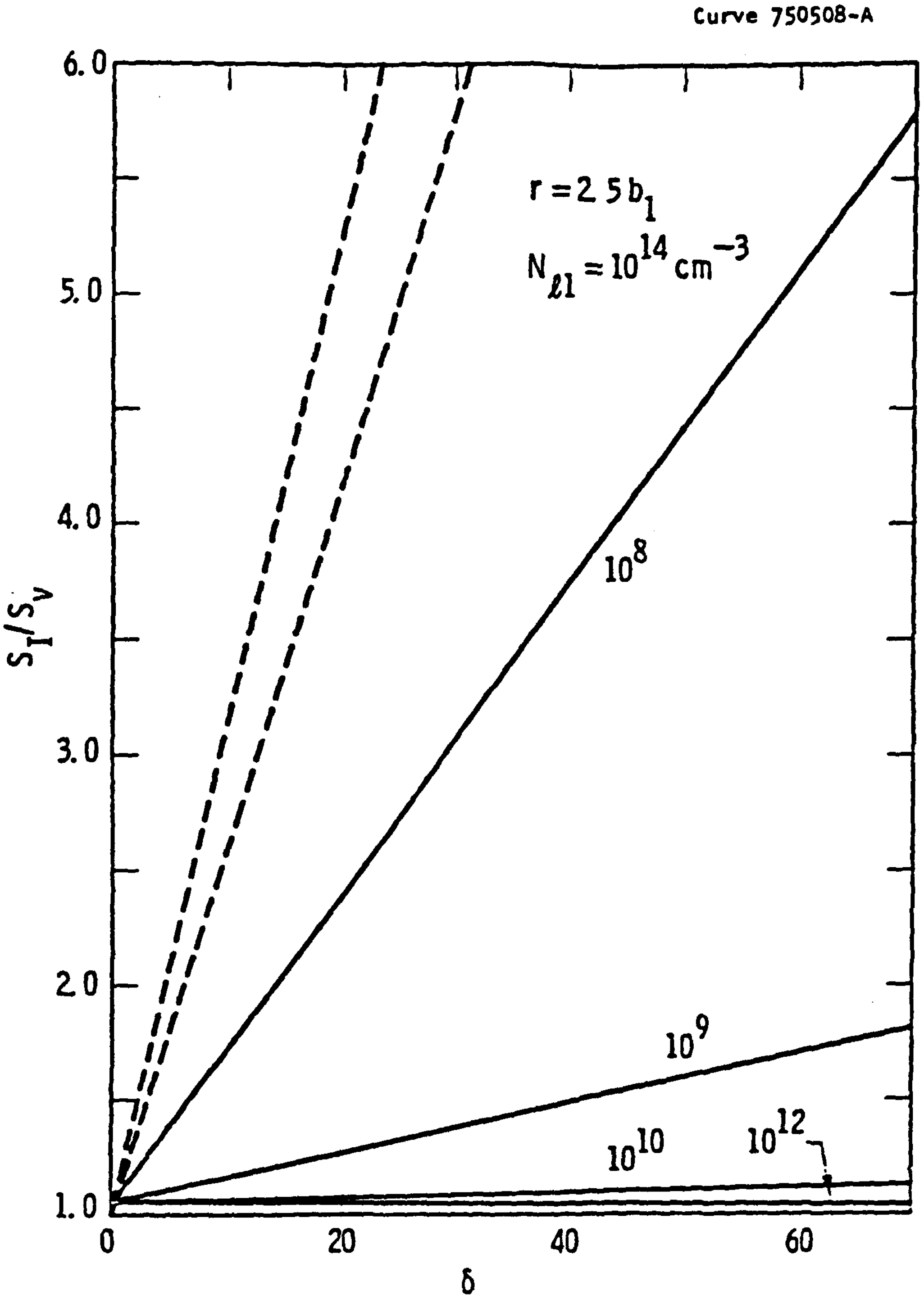

Figure 1. Sink Strength Ratio as a Function of Parameter δ for Several Network Dislocation Densities. Curves are labeled by value of L. Dashed curves define zero growth conditions for <100> (upper) and <111> (lower) loops. $N_{\ell 1} = 10^{14}$ cm^{-3}, $N_{\ell 2} = 10^{9}$ cm^{-3}, $Z_I^0 = 1.05$, and $r_{\ell 1} = r_{\ell 2} = 2.5\ b_1$.

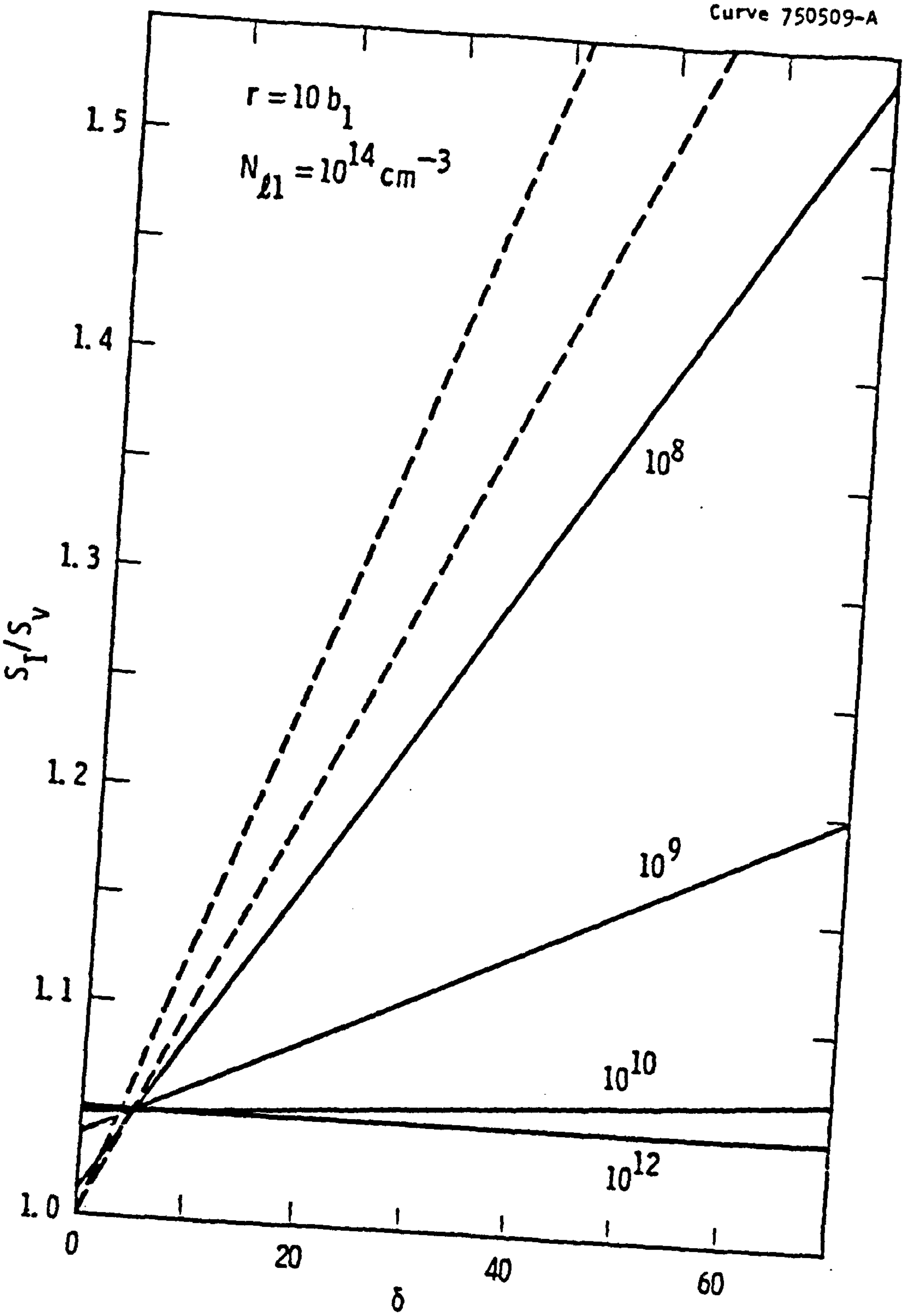

Figure 2. Sink Strength Ratio as a Function of Parameter δ for Several Network Dislocation Densities. Same labeling as Fig. 1. $r_{\ell 1} = r_{\ell 2} = 10\ b_1$.

Curve 750507-A

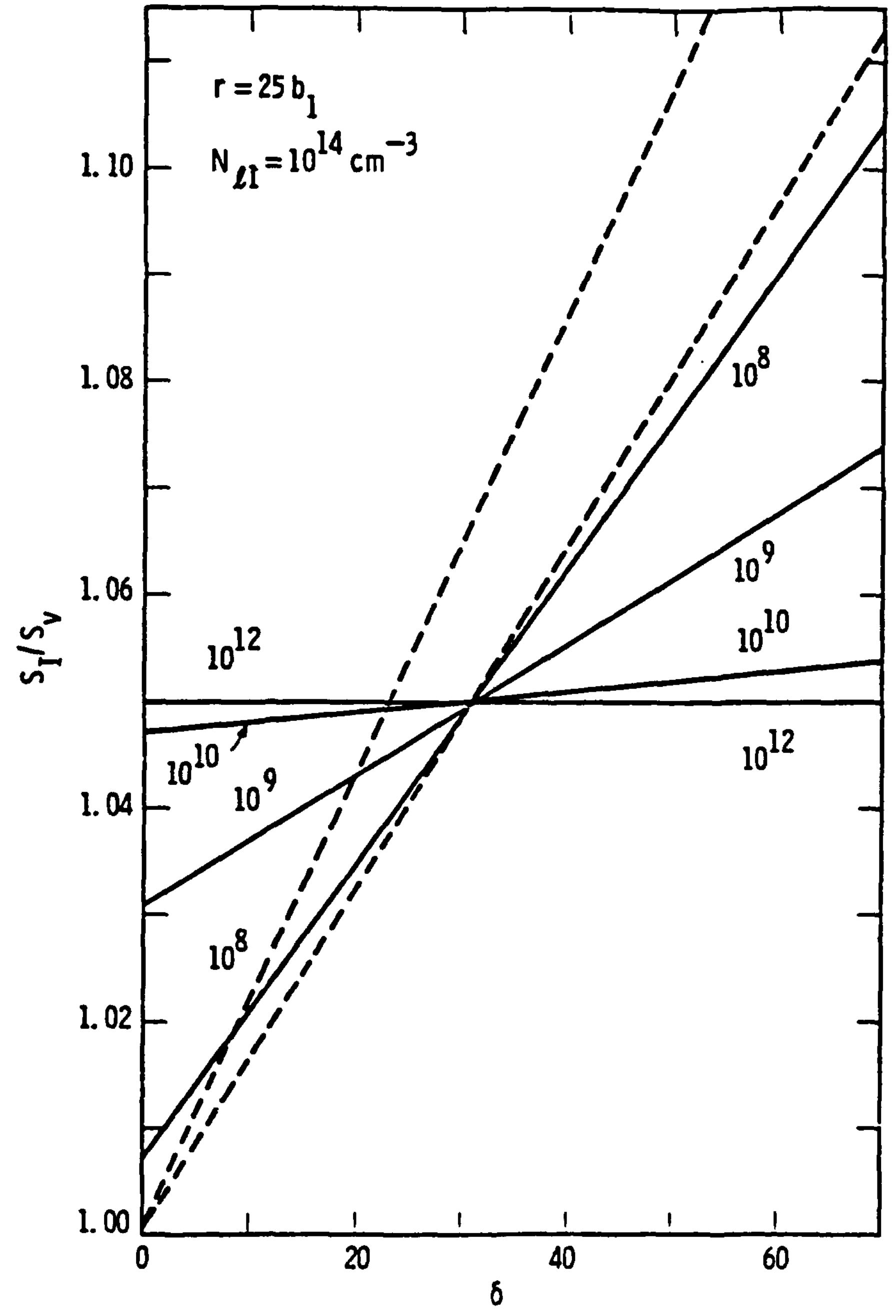

Figure 3. Sink Strength Ratio as a Function of Parameter δ for Several Network Dislocation Densities. Same labeling as Fig. 1. $r_{\ell 1} = r_{\ell 2} = 25\ b_1$.

Curve 750511-A

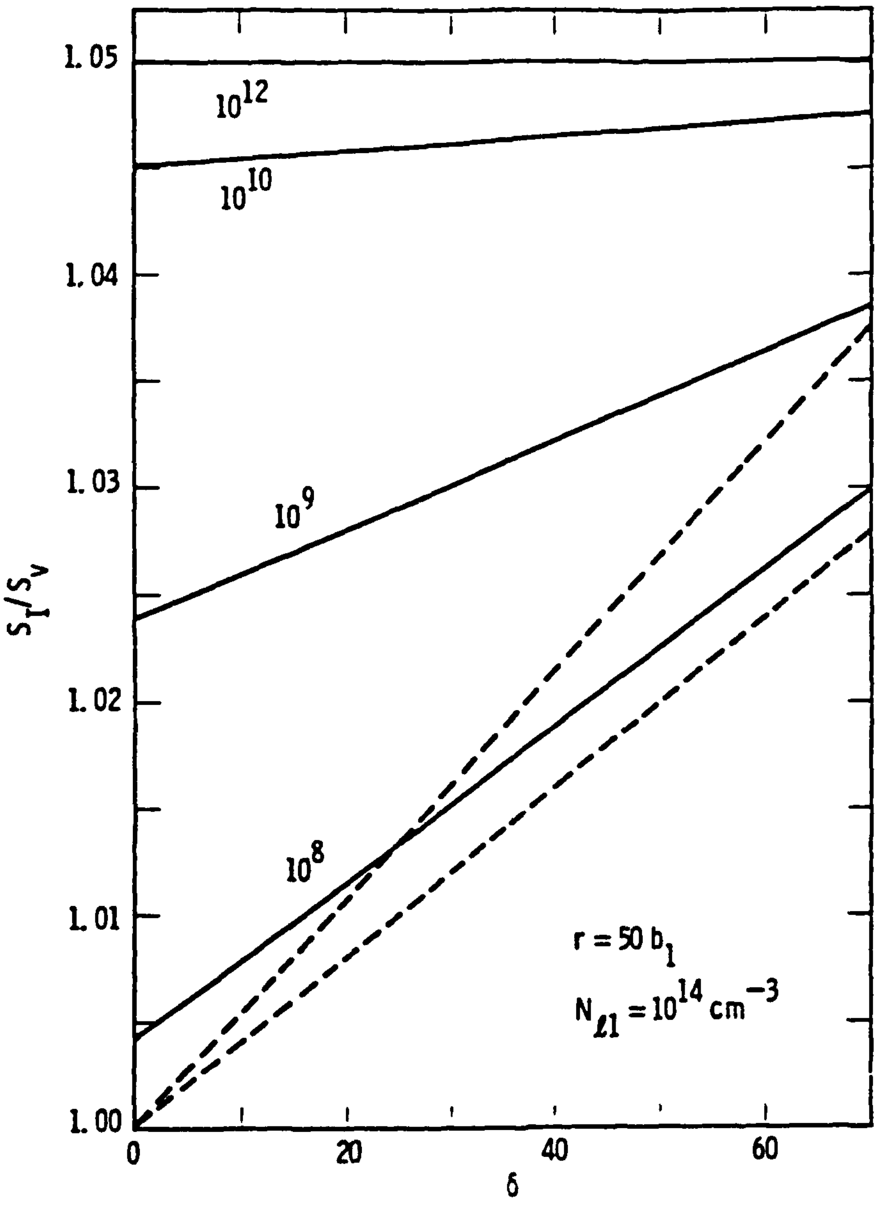

Figure 4. Sink Strength Ratio as a Function of Parameter δ for Several Network Dislocation Densities. Same labeling as Fig. 1. $r_{\ell 1} = r_{\ell 2} = 50\ b_1$.

Curve 750510-A

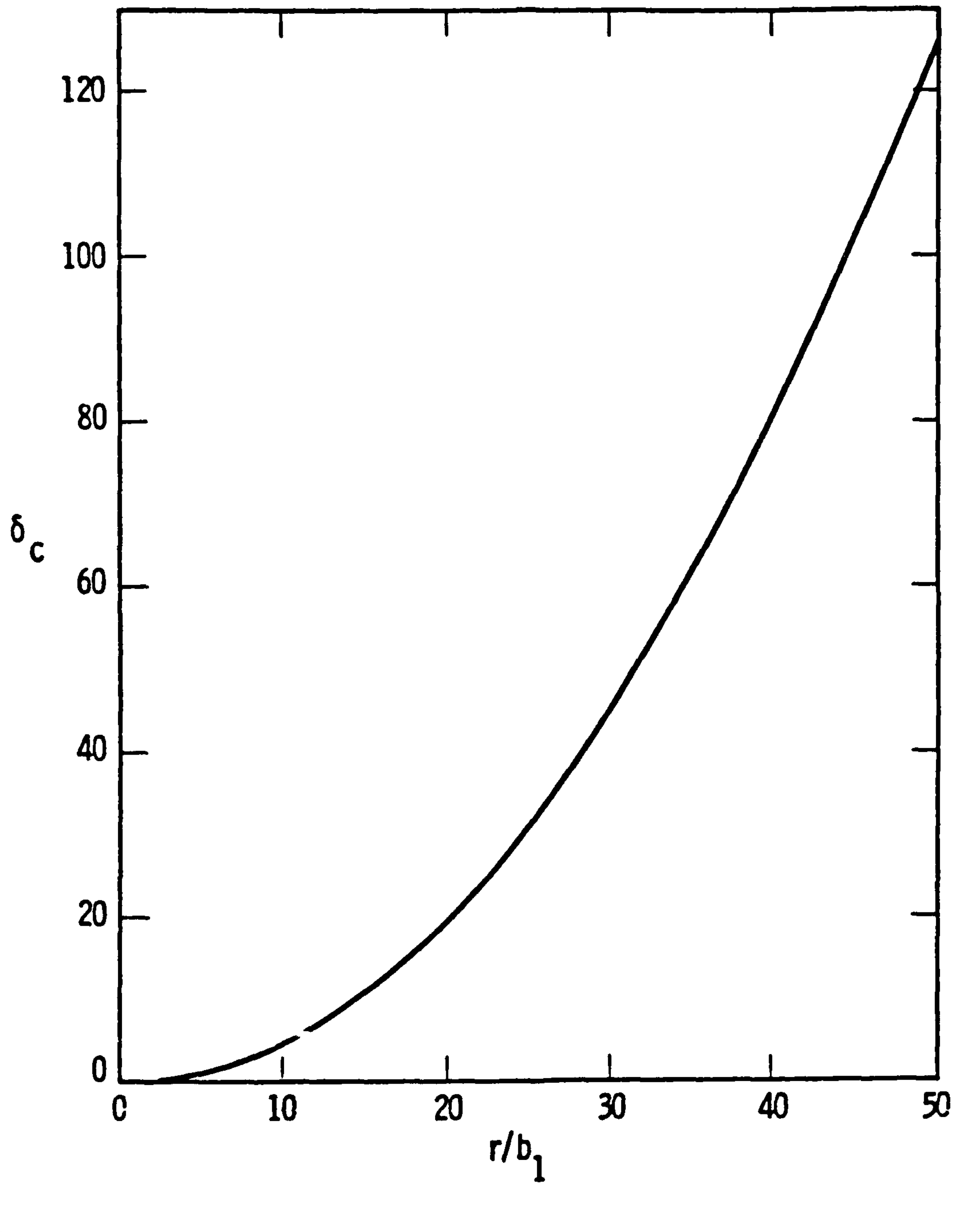

Figure 5. Critical δ as a Function of Normalized Loop Radius. $N_{\ell 1} = 10^{14}$ cm^{-3}, $N_{\ell 2} = 10^{9}$ cm^{-3}, $Z_I^n = 1.05$.

shrinkage/growth of loops of a given size is that δ be less than the critical value δ_c.

The calculated shrinkage/growth regimes for the set of 16 different conditions considered are summarized graphically in Fig. 6. The black bars indicate the range of δ for which this condition holds.

The parameter δ is fixed by the material and the loop type for small loops. Wolfer and Ashkin(5) calculated δ for edge loops in nickel and obtained a value of 27.4. If we assume a comparable value for niobium, then from Figs. 5 and 6 we find that the loop radii must be of the order of 25 b_1 or approximately 70 angstroms for the shrinkage/growth condition to be realized. These are fairly large loops, well beyond the nucleation stage. Consideration of the experimental results; i.e., <111> loop shrinkage and <100> loop growth in ferritic steels, and the results of these calculations then suggest that <111> and <100> loops nucleate and grow until the critical size is reached, after which shrinkage of <111> loops occurs with continued growth of <100> loops. The loop growth equations were solved for a variety of conditions in order to see if this behavior is predicted by the model.

4. Loop Growth

Eqs. (1) through (6) define the model. The <111> and <100> loop radii at $t = 0$ were assumed to be equal with a value of 2.5 b_1, since calculations with unequal initial values showed that the final results were unaffected by the initial conditions. Parameters for niobium were used and are given in Table I. Solutions to the system of equations were obtained for temperatures between 700° and 1100°K, with <111> loop densities of 10^{14} and 10^{16} cm^{-3}, and constant network densities of 10^8 and 10^{12} cm^{-2}. <100> loop densities were given by

Curve 750512-A

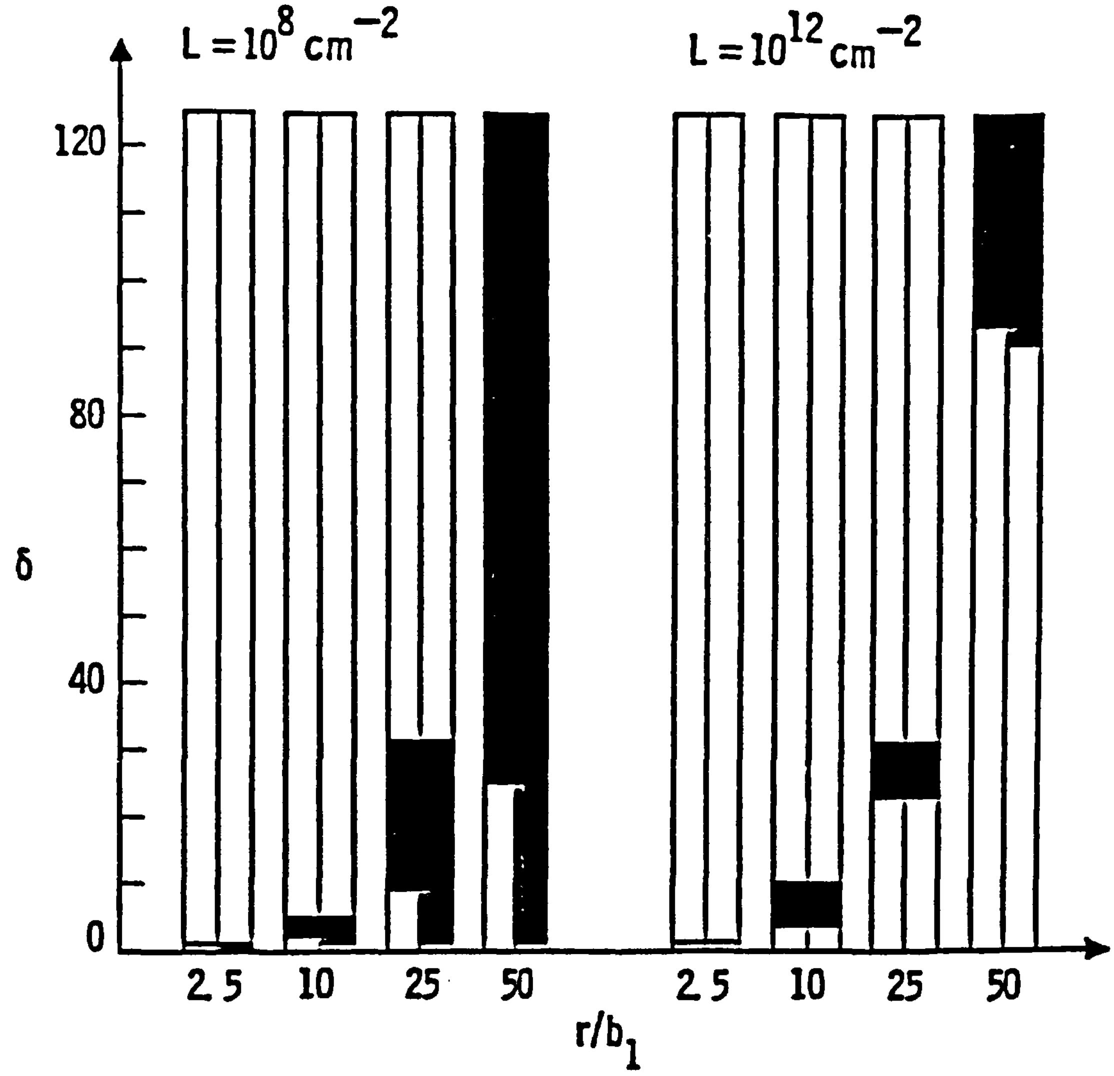

Figure 6. Summary of Growth/Shrinkage Regimes for Four Loop Radii. Sets are labeled by network density L; left bar in each pair is for $N_{\ell 1} = 10^{14}\ cm^{-3}$ and $N_{\ell 2} = 10^9\ cm^{-3}$, and right bar for $N_{\ell 1} = 10^{16}\ cm^{-3}$ and $N_{\ell 2} = 10^{11}\ cm^{-3}$. Solid region indicates range in which <111> loops shrink and <100> loops grow.

Table I. Parameters for Niobium

Quantity	Value
Lattice parameter, a	3.29×10^{-8} cm [a]
Atomic volume, Ω	1.78×10^{-23} cm^3 [a]
Nearest neighbor distance, d	2.85×10^{-8} cm [a]
Vacancy migration energy, E_V^m	1.09 eV [b,c]
Vacancy diffusion prefactor, D_{Vo}	0.008 cm^2/s [c]
Interstitial migration energy, E_I^m	0.115 eV [d]
Interstitial diffusion prefactor, D_{Io}	10^{13} $d^2/6$ cm^2/s

a. C. Kittel, Introduction to Solid State Physics, 3rd Ed. (Wiley, London, 1968), p. 29.

b. R. W. Balluffi, J. Nucl. Mater. 69/70 (1978) 240. Estimated using ratio $E_V^m/E_V^f = 0.43$ calculated from data for W and Mo.

c. N. L. Peterson, J. Nucl. Mater. 69/70 (1978) 3.

d. F. W. Young, Jr., J. Nucl. Mater. 69/70 (1978) 310.

$$N_{\ell 2} = N_{\ell 1} \exp \left(\frac{-6.97 \times 10^3}{kT}\right) \qquad (13)$$

where k is Boltzmann's constant and T is temperature. In addition, the network bias Z_I^n was varied.

The calculations showed that

(1) both types of loop grow as expected when the initial radii are 2.5 b_1;

(2) the growth rate of <100> loops is greater than that of <111> loops due to the larger preference factor of the former;

(3) the initial sink strength of the system is high because of the large values of the loop preference factors at small sizes, but falls rapidly as the loops grow;

(4) the loops grow until the radii reach steady-state values given by

$$1 + \delta \left(\frac{b_1}{r_{\ell 1}}\right)^2 = 1 + \delta \left(\frac{b_2}{r_{\ell 2}}\right)^2 = Z_I^n \qquad (14)$$

after which no further growth (or shrinkage) occurs;

(5) the steady-state radii are independent of the assumed values of L, $N_{\ell 1}$, $N_{\ell 2}$, and temperature;

(6) higher temperatures reduce the time required to reach steady state.

Based on a phenomenological model for the change in network density during irradiation$^{(14)}$, a time-dependent network density was then incorporated in our model. The instantaneous density at time t was assumed to be

$$L = L_0/(ALt + 1) \tag{15}$$

where A is an annealing constant. Several values of A were assumed. Consistent with result (5) above, the new set of calculations showed that the steady-state radii are unaffected, and therefore the decreasing network density does not lead to <111> loop shrinkage. Its primary effect is on the instantaneous sink strength, which is larger at a given time than for a constant network density.

5. Discussion and Conclusion

The major conclusion to be drawn from these results is that the difference in bias between <111> and <100> loops and a high initial network dislocation density are not sufficient conditions for <100> loop growth and <111> loop shrinkage in body-centered-cubic metals. The key to what is happening physically is given in Eq. (13): at some time in the irradiation, the bias of network dislocations, <111> loops, and <100> loops become identical. With no differential bias in the system, all of the microstructural elements act as recombination centers, absorbing equal numbers of interstitials and vacancies. No growth or shrinkage is possible in this situation.

The question then arises -- what is necessary to produce <111> loop shrinkage and <100> loop growth?

Several possible mechanisms for the change from growth/growth to shrinkage/growth regimes can be considered. The first is relatively subtle. The derivation of the preference factor using the infinitesimal loop approximation leads to an expression with a limiting value of 0 as loop radius goes to infinity, implying that the network bias is 1. In fact, the limiting value should be greater than 1. If an appropriately modified expression for the preference factor is used, it is easy to see that the steady-state condition is not attained for a finite size loop. Preference factors for both <111> and <100> loops remain greater than $Z_I^n - 1$. For this situation, however, both loop types grow, albeit slowly when the bias is close to Z_I^n.

The second mechanism is the introduction of void embryos at some finite time after loop growth is underway. This changes the sink strength ratio slightly but does not appear to affect loop growth behavior significantly. The third mechanism is an abrupt change in the network bias, possibly associated with the formation of domains or walls. From Eqs. (12) and (14) it can be seen that if Z_I^n increases so that its value lies between $1 + \delta (b_1/r_{\ell 1})^2$ and $1 + \delta (b_2/r_{\ell 2})^2$ at some time before the steady-state condition is attained, then <111> loops will shrink and <100> loops grow.

These possibilities are currently being explored, but it is apparent from our analysis that much remains to be understood about loop growth behavior in body-centered-cubic metals.

6. References

(1) E. A. Little and B. L. Eyre, J. Microscopy 97 (1973) 107.

(2) E. A. Little, R. Bullough, and M. H. Wood, Atomic Energy Research Establishment Report AERE-R9678, Harwell, Feb. 1980.

(3) B. L. Eyre and R. Bullough, Phil. Mag. 8 (1965) 31.

(4) R. Bullough and R. C. Perrin, Proc. Roy. Soc. London A305 (1968) 541.

(5) W. G. Wolfer and M. Ashkin, J. Appl. Phys. 46 (1975) 547.

(6) W. G. Wolfer and M. Ashkin, J. Appl. Phys. 46 (1975) 4108.

(7) A. D. Brailsford and R. Bullough, J. Nucl. Mater. 44 (1972) 121.

(8) H. Wiedersich, Radiat. Eff. 12 (1972) 111.

(9) L. K Mansur, Nuclear Technology 40 (1978) 5.

(10) F. Kroupa, Czech. J. Phys. B10 (1960) 284.

(11) C. P. Flynn, Point Defects and Diffusion (Oxford, Clarendon Press, 1972) 486.

(12) A. D. Brailsford, R. Bullough, and M. R. Hayns, J. Nucl. Mater. 60 (1976) 246.

(13) M. H. Yoo and J. O. Stiegler, Phil. Mag. 36 (1978) 1305.

(14) W. G. Wolfer, University of Wisconsin Report UWFDM-312, Madison, May 1979.

APPENDIX C

RECOMMENDATIONS FOR IRRADIATION FACILITIES FOR BCC MATERIALS STUDIES

ARGONNE NATIONAL LABORATORY
9700 South Cass Avenue, Argonne, Illinois 60439

October 20, 1987

Dr. R. Bajaj
Westinghouse Electric Corporation
Advanced Reactor Division
P. O. Box 158
Madison, PA 15663

Dear Ram,

The completion of the test matrix for the dual ion irradiations of Niobium and Niobium alloys at the Battelle Northwest Radiological Physics Facility represents an important step toward screening niobium alloys for space reactor applications by the ion simulation technique. To accomplish this work, a niobium negative ion source built at Argonne was fitted to the Battelle 2 MV National Electrostatics Tandem accelerator. The target holder employed was a modified unit used in the Breeder Reactor Swelling program at Argonne. Target chamber and beam line facilities were those built up by Brinhall and Kissinger for materials studies several years ago. We were indeed fortunate that all this equipment could be combined and rendered operational in a short period.

Experience in the breeder program showed that successful ion simulation experiments required a dedicated target chamber system and a knowledgeable technical staff who were aware of the critical prameter that must be controlled. This situation is even more true for work on b.c.c. refractory materials where it is essential to conduct the irradiation at elevated temperatures in ultra high vacuum conditions.

I feel that it is important to recognize that ion simulation techniques are needed for the U.S. multi megawatt space reactor program and that an irradiation facility needs to be established. The accelerator facility at Battelle contains the basic element for such work, but a considerable effort is needed to establish a reliable dual beam irradiation facility where specimens can be irradiated on a routine basis. A list of the basic equipment for such a facility is attached. I trust that one of the funding agencies will give this request their serious consideration.

Sincerely yours,

Tay

Anthony Taylor
Materials Science Division
Building 212

AT/hm
Attachment

U.S. Department of Energy The University of Chicago

Equipment Needed at Battelle Northwest Radiological Physics Accelerator Facility to Achieve Standardized Dual Ion Beam Irradiations of BCC Materials

Tandem Accelerator
- Vacuum gas lock for negative ion sources
- New Lens extractor system
- Improvement in system transmission

Van de Graaff Accelerator
- Improved Mass Resolution on 0° Beam Line

Beam Lines

Heavy Ion:
- Rastering - Steerer controller
- Rapid action Faraday Cup
- Beam Viewer
- Slit system in front of target chamber
- New vacuum pump

Light Ions:
- Quadrupole doublet focussing lens
- Rastering - Steerer Controller
- Rapid action Faraday Cup
- Beam Viewer
- Slit system in front of target chamber

Target Chamber:
- New Ion Pump > 500 ℓ/s
- New Residual gas analyzer with total pressure read-out
- He energy degrade system
- Improved beam collimation system

REPORT SUMMARY FORM

1. **SECURITY CLASSIFICATION:** None

2. **REPORT NO.:** WAES-TR-89-0010

3. **PROPRIETARY CLASS:** None

4. **AVAILABILITY:** Library - IRC

5. **ORIGINATING SOURCE:** AES - L

6. **CONTRACT NO.:** F49620-85-C-0060

7. **FUNDING SOURCE:** Air Force Office of Scientific Research

8. **NOTES:**

9. **AUTHOR(S):** R. Bajaj, G. R. Fenske, B. O. Hall, J. C. Greggi, A. T. Taylor

10. **TITLE:** An Investigation of Irradiation Swelling Mechanisms in Refractory Metals at High Temperatures - Final Scientific Report

11. **DATE--YYMMDD:** 890623

12. **PAGES, REF., ILLUS.:** 247 , 112, 70

13. **DOCUMENT TYPE:** Report

14. **KEYWORDS:** Irradiation, Swelling, Refractory Metals, Niobium + Nb Alloys, Dislocation Loops, Electron Microscopy

15. **ABSTRACT--PURPOSE, SCOPE, APPROACH, RESULTS, CONCLUSIONS, SIGNIFICANCE: (MAXIMUM: 200 WORDS)** A three-phase study of elevated temperature irradiation swelling in refractory metals was done with an objective of understanding swelling mechanisms and demonstrating practicality of swelling-resistant materials. During the first phase, a theoretical model was developed for the swelling in body-centered cubic (bcc) metals. Niobium was irradiated with Nb^{++} ions to 50 dpa and swelling was determined by transmission electron microscopy. A peak swelling at 900°C of 7% and no swelling above 1300°C was observed. Reasonable agreements were obtained between the experimental and theoretical swelling curve when niobium-oxygen interaction was included. Sink strength ratios were calculated from the data. The theoretical model during the second phase included loop growth/shrinkage in bcc metals. Experiments were performed at 800°C and 1000°C to 0.05 and 5 dpa. High densities of dislocation loops $\sim$10 nm in size were observed. Dislocation loops were predominantly interstitial in nature with a Burgers vector of $\frac{a}{2}\langle 111 \rangle$ with some vacancy loops. During the third phase, Nb-5Hf and Nb-5W were irradiated at 800°-1350°C with Nb^{++} and with $Nb^{++} + He^{+}$. Nb-5Hf showed swelling at high temperatures. Nb-5W showed no swelling up to 35 dpa, demonstrating that Nb-5W is a candidate alloy for nuclear reactor high temperature applications.

FORM AESD-00130A

DOCUMENT DISTRIBUTION LIST

INTERNAL AESD			
NAME, DEPT, LOCATION	FULL TEXT*	RSF ONLY+	COPY NO.●
R. W. Buckman Mat & Fuels Tech L	1		
W. P. Blankenship L MS & Eng.	1		
A. Boltax WM Fuels Tech	1		
E. Schmidt WM Eng. Anal.	1		
C. R. Adkins WM Engineering	1		

EXTERNAL AESD		
NAME AND ADDRESS	NO. OF COPIES	COPY NO.●
Vernita Slater Department of the Air Force AFOSR/PKO Building 410 Bolling AFB, DC 20332-6448	16	
Larry Vasko DCASMA Pittsburgh, PA	1	
B. O. Hall Alcoa Tech Center	1	
J. C. Greggi WR&D Center	1	
A. T. Taylor-Argonne Ntl Lab	1	
G. R. Fenske-Argonne Ntl Lab	1	
R. Bajaj - W Bettis	2	
Library - IRC	1	
S. Wood - W R&D Center	1	
R. Puigh - HEDL	1	
P. Ring - GE-SJO	1	

* INDICATE NUMBER OF COPIES OF FULL TEXT
\+ REPORT SUMMARY FORM ONLY
● CONTROLLED DISTRIBUTION, IF APPLICABLE

FORM NO. AESD-00130B